

Copyright Notices

Notice 1

Under the Copyright Act 1968, this thesis must be used only under the normal conditions of scholarly fair dealing. In particular no results or conclusions should be extracted from it, nor should it be copied or closely paraphrased in whole or in part without the written consent of the author. Proper written acknowledgement should be made for any assistance obtained from this thesis.

Notice 2

I certify that I have made all reasonable efforts to secure copyright permissions for third-party content included in this thesis and have not knowingly added copyright content to my work without the owner's permission.

**DEVELOPING ADVANCED PARTICLE
MANIPULATION TECHNIQUES IN
MICROFLUIDIC SYSTEMS**

LIN XU

B.ENG. (Hons.), MONASH UNIVERSITY

A THESIS SUBMITTED

**FOR THE DEGREE OF DOCTOR OF PHILOSOPHY OF
ENGINEERING SCIENCE**

LABORATORY FOR OPTICS ACOUSTICS AND MECHANICS

DEPARTMENT OF MECHANICAL AND AEROSPACE

ENGINEERING

MONASH UNIVERSITY, AUSTRALIA

3rd November 2011

TABLE OF CONTENTS

Abstract.....	v
Statement of Originality.....	vi
Acknowledgements.....	vii
List of Figures and Tables.....	viii
List of Symbols.....	xiii
1. Introduction.....	1
1.1. Background.....	1
1.2. Project Aims and Research Approach.....	3
1.3. Thesis Structure.....	5
2. Literature Review.....	7
2.1. Introduction.....	7
2.2. Contacting Methods for Particle Manipulation.....	8
2.2.1. Micropipette application.....	8
2.2.2. Micro-fabricated device application.....	9
2.2.3. Soft medium application.....	11
2.3. Non-contacting Methods for Particle Manipulation.....	15
2.3.1. Optical method.....	15
2.3.2. Magnetic manipulation.....	17
2.3.3. Ultrasonic manipulation.....	19
2.3.4. Dielectrophoretic method.....	26
2.3.5. Capillary force method.....	27
2.4. Conclusions.....	28
3. Extending the Ultrasonic Method for Particle Manipulation.....	30
3.1. Introduction.....	30
3.2. Acoustic Forces.....	31

3.2.1.	Acoustic radiation force.....	31
3.2.2.	Acoustic streaming.....	34
3.3	Degrees of Pressure Field	35
3.4.	Development of Ultrasonic Manipulation Techniques	38
3.4.1.	Piezoelectric device and experimental setup.....	39
3.4.2.	Device simulation results.....	40
3.4.3.	One-dimensional fields.....	41
3.3.4.	Two-dimensional fields.....	46
3.4.5.	Particle levitation from the bottom of the channel.	49
3.5.	Conclusions.....	51
4.	Exploring Bubbles as a Soft Method for Particle Sorting.....	53
4.1.	Introduction.....	53
4.2.	Background of Cavitation Bubbles.....	54
4.2.1.	Cavitation microstreaming.....	54
4.2.2.	Bubble oscillation modes.....	54
4.2.3.	Cavitation bubble types.....	56
4.2.4.	Cavitation bubbles applications.....	57
4.3.	Development of Ultrasonic Manipulation with Bubbles	59
4.3.1	Bubble location in the standing wave field.....	59
4.3.2	Force experienced by the bubble.....	60
4.3.3.	Piezoelectric device and experimental setup.....	63
4.3.4.	Investigation of bubble's properties.....	65
4.3.5.	Effect of microstreaming.....	74
4.3.6.	Effect of oscillation mode.....	77
4.3.7.	Particle separation.....	79
4.4.	Conclusions.....	83
5.	Improving the Capillary Force Method for Particle Manipulation.....	84
5.1.	Introduction.....	84
5.2.	Capillary Flow.....	85

5.2.1.	Minimum surface energy.....	85
5.2.2.	Contact angle.....	86
5.2.3.	Contact angle hysteresis.....	86
5.2.4.	Sharp edges.....	87
5.2.5.	Evaporation.....	88
5.2.6.	Interaction forces in a capillary chamber.....	89
5.3.	Development of Particle Assembly in a Capillary Cell	91
5.3.1.	Capillary cell and experimental setup.....	91
5.3.2.	Particles assembly investigation.....	93
5.4.	Conclusions.....	98
6.	Novel Float-sink Scheme for Particle Manipulation.....	100
6.1.	Introduction.....	100
6.2.	Background Theory and Underlying Mechanism.....	101
6.3.	The Float-sink Scheme for Single Floating Particle Selection.....	106
6.3.1.	Experimental setup.....	107
6.3.2.	Particles selected by a droplet.....	108
6.4.	The Float-sink Scheme for Particle Selection from a Floating Cluster.....	111
6.4.1.	Experimental Setup.....	112
6.4.2.	A droplet approached to a fixed particle.....	113
6.4.3.	Particles sunk from a floating cluster.....	119
6.5.	Conclusions.....	123
7.	Conclusions and Recommended Future Work...	125
	Bibliography.....	128
	Publications arising from the work.....	136
	Appendices.....	137
A.	Bubble excitation using standing waves for particle sorting.....	137
B.	Continuous particle assembly in a capillary cell.....	159

C.	Delicate selective single particle handling with a float-sink scheme.....	163
D.	Selective removal of micro-particles from a floating monolayer cluster.....	167

Abstract

Advanced particle manipulation techniques with synergistic effects of low cost, high degrees of controllability, precision, and delicateness have been developed. In particular, the one-dimensional pressure fields in a microfluidic channel device driven by a piezoelectric plate have been investigated. Particles lines were observed along the channel when corresponding resonant frequencies applied. The more complex two-dimensional pressure fields excited by one electrode in the microfluidic channel were also investigated. Single array of particles clumps have been achieved by switching between two frequencies. Additionally, two arrays of particles clumps were observed by sweeping frequency rapidly. Furthermore, particles levitation was observed under certain excitation frequency.

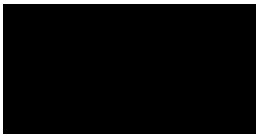
Based on the knowledge gained from the microfluidic channel, a microfluidic chamber was conducted in the development of an ultrasonic technique. Cavitation bubbles driven by the standing wave generated in the chamber have been studied. Various oscillation modes of the bubbles were also studied. Additionally, the vibrating bubbles as size-based particle selective mechanism were examined. Size varied particles either been attracted (larger particles dominated by Bjerknes force) or repelled (smaller particles dominated by drag force) by the bubble were achieved.

As an alternative to the ultrasonic particle manipulation methods, the development of particles forming in lines by capillary flow due to water evaporation has also been demonstrated in this thesis. Particles behaviour has been investigated in a capillary cell formed by a parallel glass slide and a glass cover slip. Particles remaining in hydrated while assembled and harvested in batches were shown.

Finally, the establishment of advanced strategies for using the float-sink scheme to selecting single fragile particles has been conducted. A droplet dispensed directly above the selected particle floating on the liquid surface was demonstrated to cause the particle to sink even when the particle was within a floating cluster.

Statement of Originality

I hereby declare that this thesis contains no material which has been accepted for the award of any other degree or diploma at any university or equivalent institution and that, to the best of my knowledge and belief, this thesis contains no material previously published or written by another person, except where due reference is made in the text of the thesis.



.....

LIN XU

3 November 2011

Acknowledgment

In the first place I am heartily thankful to my supervisor Associate Professor Adrian Neild, for his supervision, advice and guidance from the early stage of this research as well as giving me extraordinary experiences through out the work. It has been an honour to be his first Ph.D. student. I appreciate all his contributions of time, ideas, and funding to make my Ph.D. experience productive and stimulating. Above all and the most needed, he provided me unflinching encouragement and support in various ways.

I would also like to express my sincere gratitude to Associate Professor Ng Tuck Wah for all the patience and advice. His involvement with his originality has triggered and nourished my intellectual maturity that I will benefit from, for a long time to come. I am grateful in every possible way and hope to keep up our collaboration in the future.

Many thanks go in particular to my lab mates from Laboratory for Optics, Acoustics & Mechanics Fenfen, Priscilla, Jue Nee, Brandon, Ian, Rob, Jonathan, Mike, William and Yohannes, as well as all of my friends and colleagues for support and encouragement too.

I am extremely grateful to Dr. Liew Oi Wah and Dr. Tan Han Yen, who always greets me with kind smiles and have been tirelessly guiding me in my project. I am also very thankful to Dr. S. Oberti, without whom the work of ultrasonic particle manipulation would not be possible in the early stage of the research.

I gratefully acknowledge the funding source that made my Ph.D. work possible. I was funded by the Mechanical and Aerospace department of Monash University for my three years candidature.

Last but not the least, I would like to give my special thanks to my parents. Without your love and support, it would be impossible to write this thesis.

List of Figures and Tables

Figure 1.1	Illustration of the scope of the research work	4
Figure 2.1	Image of a mouse embryo which is held by a holding pipette during the injection with the injecting pipette, cited in Kumar <i>et al.</i> [35]	8
Figure 2.2	Schematic representation of a polymer <i>chopstick</i> microgripper, cited in Colinjivadi <i>et al.</i> [38]	10
Figure 2.3	Schematic representation of a microbubble-powered bioparticle actuator, cited in Maxwell <i>et al.</i> [21]	12
Figure 2.4	Schematic representation of a quarter-wavelength resonator: (a) cross-section view of the device; and (b) particles concentrated in the channel at the reflector layer. Based on Martin <i>et al.</i> [50].	22
Figure 2.5	Schematic representation of a half-wavelength resonator: (a) cross-section view of the device; and (b) particles concentrated along the centre of the channel. Based on Nilsson <i>et al.</i> [12].	23
Figure 3.1	Schematic description of pressure field generated in: (a) 1D channel, (b) 2D chamber, and (c) 3D cage. Grey dash lines indicate the pressure nodes.	37
Figure 3.2	Schematic view of the micro-positioning device: (a) 2-D cross-sectional device with dimensions; and (b) bottom view, where the dash lines show the channel location. Dimension not to scale	40
Figure 3.3	Simulation of the pressure field within the fluid layer: the data being calculated along a line across the lower edge of the chamber (x-axis) at a range of frequencies (y-axis).	41
Figure 3.4	Particle enrichment in the microfluidic channel. The bands show the enriched particles in resonance mode, fundamental, 1 st ad 2 nd harmonic with 1, 2 and 3 bands respectively, (a) top view microscope photographs and b) schematic description of channel cross-sections	43
Figure 3.5	Schematic description of the cross section view of the channel and the corresponding experimental images from the top view: (a) 6 μm and 1.9 μm particles full filled the channel before any excitation frequency applied, (b) 6 μm particles forming one line, while 1.9 μm particles swirling at both sides of the line when frequency of 1.305 MHz was applied	43
Figure 3.6	Schematic description of the cross section view of the channel and the corresponding experimental images from the top view by varying focusing plane: (a) the focusing plane is at top layer of the channel, 1.9 μm particles are moving outwards from the pressure nodes; (b) the focusing plane is at middle layer of the channel, 1.9 μm particles are moving towards to the pressure nodes. Images are one second apart. Red circle indicates the focal plane	45
Figure 3.7	Image of lines across the channel width that particles formed at 0.98 MHz in a non-flowing fluid volume	46
Figure 3.8	Image sequences of particle movement when frequency switching between 1.305 MHz and 0.98 MHz	47

Figure 3.9	FFT of the response frequency of 0.87 MHz	48
Figure 3.10	Image sequences of the process of clumps formation: starting with particles randomly distributed in the channel. A 20V amplitude signal at 0.87 MHz has been applied to a signal transducer. Later, particles formed clumps by rapid sweeping frequency to 0.98 MHz	49
Figure 3.11	Image sequences of particles forming patterns in the range of 2.4 MHz and 2.64 MHz	50
Figure 3.12	Schematic description and experimental images of particle elevating from the channel bottom. (a) 6 μ m particles full filled within the channel, (b) particles focused in two vertical planes when 2.66 MHz applied, (c) particles sinking to the bottom due to gravity, and (d) particles elevating from the bottom to the middle layer of the channel (zoom in image). Arrow indicates the focal plane	51
Figure 4.1	Plot of bubble resonant frequency against its resonant radius	60
Figure 4.2	Schematic description of experiment setup for particle sorting by an excited bubble, (a) the cross-section view of the device used in the experiment, and (b) the top view of the device	65
Figure 4.3	Lines forming in one dimensional standing pressure field. (a) Two of the lines shown straight without any bubble presented. (b) The affection of a bubble, circled in blue, causing one of the lines to bow around	66
Figure 4.4	Images of bubble location at the excitation frequency of 673 kHz was applied. White circles present the bubble. Image(c) and (d) are continued	67
Figure 4.5	Images of bubble effect when line forming in the pressure field of 673 kHz. (a) and (b) Images of two bubbles presented at the pressure node with 0.8s apart. (c) and (d) Images of one bubble presented with 0.76s apart	68
Figure 4.6	Image sequences of the movement of a bubble towards to the pressure node when 673 kHz was applied. The red circle presents the bubble when it remains within the particle pattern	69
Figure 4.7	Images of multiple similar sized bubbles are observed. (a) Five bubbles are attached under the glass surface; while (b) two bubbles are attached on the silicon surface where directly below. Each of the two bubbles is attached on the glass surface (c) and silicon surface (d)	70
Figure 4.8	Experimental images of bubbles with varied sizes generated in the investigation at 939.5 kHz	70
Figure 4.9	Experimental image of particle movement when two bubbles observed in the acoustic field with different size at 210.5 kHz. Particles (red circle) around the small bubbler A takes longer time to be attracted than the particles (green circle) around the large bubble B with similar distance	72
Figure 4.10	Plot of the bubble radius against time	74
Figure 4.11	Experimental image sequences of 6 μ m particles attracted by a bubble presented in the 939.5 kHz acoustic field	75
Figure 4.12	Experimental image sequences of 1.9 μ m particles repelled by a bubble presented in the 939.5 kHz acoustic field	76

Figure 4.13	Experimental image sequences of the movement of 6 μm and 1.9 μm particles in the 939.5 kHz acoustic field with a bubble presented. The 6 μm particle (with red dash circle) is attached to the bubble; while the 1.9 μm particle (with white dash circle) is following the streaming line repelled from the bubble	77
Figure 4.14	Experimental image sequences of a curve translating bubble. White curve pattern presents the bubble trace	78
Figure 4.15	Experimental images of (a) a translating and volume oscillation mode and (b) a translating oscillation mode along an axis perpendicular to the attached wall. Arrows present the direction of the streamline	79
Figure 4.16	Experimental image sequences of a translating oscillating bubble predicted by the attached particles' movement. Each image is 0.04 seconds apart. Arrows show the direction of the oscillation	79
Figure 4.17	Experimental image sequences of particles forming patterns and swirling under 939.5 kHz. (a) Time evolution of 6 μm particles forming lines. (b) Time evolution of 6 μm (circled) and 1.9 μm (squared) particles under acoustic radiation force and streaming, zoom in the red region from (a). (c) Time evolution of 1.9 μm particles under acoustic streaming, zoom in the blue region from (a)	81
Figure 4.18	Schematic and experimental images of particle movement under streaming: (a) continuous power supply, 1.9 μm particles swirling beside the pressure nodes; and (b) after apply turn on-off technique, the swirling is discontinued as seen particles moving opposite direction observed from the top plane	82
Figure 4.19	Experimental images of (a) initially applying turn on-off technique, and (b) 60s after applying turn on-off technique. The line is to help determining the distance between two streaming induced vortices	83
Figure 5.1	The geometrical definitions of the solid-liquid-vapour system	85
Figure 5.2	Droplet of water on a solid surface (dash line). 1) As liquid is added, the contact line advances, and the droplet exhibits an advancing contact angle. 2) As liquid is removed, the contact angle decreases to a receding value, and then the contact line retreats	87
Figure 5.3	Equilibrium of a water droplet at the sharp edge of a solid surface: showing a droplet approaching the edge (1), and in the critical position (2).	87
Figure 5.4	Schematic description of the fluid flow during evaporation in a drop. (a) The evaporation without flow cause a drop shrinks. (b) The outward flow to keep the contact line fixed	89
Figure 5.5	Schematic description of the Poiseuille flow in a capillary chamber	90
Figure 5.6	Schematic description of the proposed method to locate particles in position using capillary force (not to scale): (a) the top view of the device used in the experiment, and (b) the cross-section view about X-X with description of flow mechanics from droplet the meniscus	92
Figure 5.7	Schematic description of experimental setup for particle assembly in a capillary cell	93

Figure 5.8	Schematic description of the evaporation mechanics from the meniscus causing a flow that will carry particles towards it	94
Figure 5.9	Plot of velocity of particles in the cell against the time, at the location of 2.2 mm away from the free edge. The droplet was refilled by Milli-Q [®] water at 350s	95
Figure 5.10	Plot of particle concentration along the length of 1.9 mm away from the free edge after a time of 100 seconds. The distribution is clearly a uniform top hat function	96
Figure 5.11	Images with particles formed in lines. (a) and (b) show particles forming lines at the free opening, and the second image (b) occurring 2.4 seconds later than (a), clearly showing a slight retraction or the contact line towards the cover slip. (c) and (d) show particles forming lines just under the cover slip edge, with (d) having an undulating edge	97
Figure 5.12	Image sequences of particles forming a line along the glass cover edge, when water is evaporated	98
Figure 6.1	Sketch of the capillary meniscus around (a) a hydrophilic particle and (b) a hydrophobic particle	102
Figure 6.2	Sketch of a fluid neck when coalescence. (a) A fluid neck is forming when a droplet is brought into contact with fluid, and (b) a much wider neck is observed before merging	104
Figure 6.3	Sketch of partial coalescence of a droplet: (a) a droplet is brought into contact, and (b) leaving behind a smaller daughter droplet behind before total coalescence	104
Figure 6.4	Plot of the net force against the filling angle	106
Figure 6.5	Plot of the meniscus height against the filling angle	107
Figure 6.6	Schematic description of the proposed method to handle single particles delicately using a float-sink principle	108
Figure 6.7	Plot of work needed E to detach a spherical glass (hydrophilic) particle downward in water against the particle radius R_s . The inset presents the minimum values of R_d/R_s needed to sink glass and silicon (hydrophobic) particle of radius R_s in water, which is based on perfect transfer of energy from droplet to particle	109
Figure 6.8	Image sequences of a dispensed droplet that caused sinking of an originally floating glass particle in water	110
Figure 6.9	Image sequences of a dispensed droplet that failed to cause sinking of an originally floating glass particle in water	111
Figure 6.10	Schematic experimental setup: (a) a droplet approaches to a fixed particle, and (b) a droplet sinks a particle from a cluster group	113
Figure 6.11	Experimental image sequences of the liquid coalescence patterns directly over a pin head by varied droplet size. a) Time evolution of a droplet with approximate 17 nl approached to the pin head. b) Time evolution of a 103 nl droplet approached to the pin head	114
Figure 6.12	Experimental image sequences of the liquid coalescence pattern over a pin head by (a) a 4.1 nl droplet from the right, (b) a 7.1 nl droplet from the left, and (c) a 103 nl droplet from the right.	115
Figure 6.13	(a)Plot of droplet radius against offset distance measured from droplet centre to particle centre; (b) plot of droplet radius against offset distance measured from needle tip to particle centre; and (c) schematic image of alignment of droplet and particle when fluid contact line merging on only one side	118

Figure 6.14	An experimental image sequences showing the sinking of a single particle from a floating cluster sunk by a droplet. A neighbour particles movement is shown with the arrows	120
Figure 6.15	An experimental image sequence of a single particle form a floating cluster sunk by a droplet. A small particle can still be seen after the process showing the relatively small effect that the swell of fluid after merging has on the ability of nearby particles to float even when the particle in question is much smaller than the droplet	121
Figure 6.16	An experimental image sequence of a droplet misaligned with a particle fails to cause it to sink. A neighbour particles movement is shown with the arrows	122
Figure 6.17	Image sequences of surrounding particles sunk by continuous water droplet applied in a fixed position. Coloured dots presents target particles, and the sequence of the sinking particle is bottom left (red), bottom right (yellow), up left (blue) and up right (green)	123
Table 4.1	The value of bubble size under its corresponding frequency	60

List of Symbols

$\langle F \rangle$	Time-averaged acoustic force
$\langle U \rangle$	Acoustic force potential
π	PI
ρ_F	Density of a fluid
R_S	Radius of a particle
p	Acoustic pressure in a fluid
C_F	Speed of sound in a fluid
$\langle p^2 \rangle$	Mean-square-fluctuation of pressure in a incident wave
$\langle v^2 \rangle$	Mean-square-fluctuation of fluid velocity in a incident wave
v	Velocity of a fluid in a incident wave
ρ_S	Density of a particle
C_S	Speed of sound in an object
Φ	Velocity potential
\overline{F}_{elec}	Lateral electrical force
q	Net charge of a particle in an electric field
\overline{E}	Electric field
\overline{m}	Induced dipole moment
Q	Quatrapole
$\langle \overline{F}_{DEP} \rangle$	Time-averaged DEP force
ϵ_m	Dielectric constant of a suspending medium
f_{CM}	Dipolar Clausius-Mossotti factor
E_{RMS}	Root-Mean-Square value of an electric field
E_i	Magnitude of an electric field
φ_i	Phase of an electric field
Y	Displacement of a point in an acoustic standing wave
A	Amplitude of an acoustic standing wave
(x, y)	Coordinates
λ	Acoustic wavelength
t	Time
T	Periodic time
p_0	Peak acoustic pressure amplitude
k	Wave number in a fluid

ω	Angular frequency
F_r	Acoustic radiation force
V_s	Volume of a particle
β_F	Compressibility of a fluid
ϕ_c	Acoustic contrast factor
β_S	Compressibility of a particle
F_S	Acoustic streaming force
P_2	Acoustic streaming pressure
μ	Viscosity of a fluid
ω_n	Natural angular frequency of a bubble under shape oscillation
n	1,2,3...
σ	Surface tension
f_c	Frequency of a capillary wave
f_e	Frequency of excitation
R_0	Equilibrium radius of a bubble
R_{res}	Resonant radius of a bubble
λ_c	Capillary wavelength
ω_0	Resonant angular frequency of a bubble under small radial oscillation
p_g	Pressure of the gas in a bubble at rest
κ	The ratio of the specific heats of the gas (1.0 - 1.4 for air)
$p(y, t)$	Time-varying pressure in a fluid
p_A	Amplitude of a sound wave
V_b	Bubble volume
V_0	Equilibrium bubble volume
ξ_0	Bubble wall displacement with $\xi_0 \ll R_0$
α	Phase term of a bubble oscillation
∇p	Pressure gradient
R	Bubble radius
F_B	Bjerknes force
d	Distance between the centre of bubble and particle
m_b	Mass of gas and vapour inside a bubble
u_r	Relative velocity between a bubble and a liquid
A_b	Projected area of a bubble
C_d	Drag coefficient
u_b	Translational velocity of a bubble
u_l	Velocity of liquid

C_0	Saturation mass-concentration
D	Diffusion coefficient
C_∞	Mass-concentration of a gas dissolved in a liquid with a great distance from a bubble
F_D	Drag force
\overline{U}_{ab}	Unit interfacial energy between two material a and b
γ_{ij}	Interfacial tension
θ	Contact angle
θ_Y	Contact angle defined by Young's
θ_r	Receding contact angle
θ_a	Advancing contact angle
θ_0	Equilibrium contact angle
ϕ	Sharp edge angle
$\varphi(r)$	Steady-state concentration profile of a vapour
j_e	Evaporation flux
z	Distance from drop centre
R_d	Drop radius
D_v	Diffusivity of a vapour in air
J_{evap}	Total evaporation flux per unit length of a leading edge
v_f	Velocity of a flow
v_m	Peak velocity of a flow
τ	Dimensionless distance across the channel with $\tau = \frac{y}{L}$
S	Surface tension force
S_0	Surface tension between fluid and glass
\bar{v}	Mean velocity of a flow
L	Distance between two surfaces
δw	Change of work during evaporation
dA_{ij}	Interface area
r_w	Radius of wetted area on a solid surface
k	Line energy
r	Length of a wedge formed at the edge
j_0	Evaporative constant
x'	Distance from the contact line
J_s	Fluid flow
j_b	Evaporation flux outside a wedge
$\eta(x')$	Arc length of a meniscus surface

F_c	Capillary force
F_p	Pressure force
M	Mass of a particle
g	The acceleration of gravity
θ_c	Filling angle
ζ	Angle variable
B	Bond number
l_i	Dimensionless variable of density
h	Meniscus height
e	Euler constant
ϖ	Dimensionless variable with $\varpi = R_s/L_c$
ψ_i	Interface slope with a horizontal plane at the point of contact
ϑ	Inverse of capillary length
K	Modified Bessel function
E	Energy required to detach a floating particle
G	Potential energy gained by a droplet

Chapter 1

Introduction

1.1 Background

The miniaturisation of fluidic systems for chemical and biological analysis has become an important research field. The area is collectively termed micro total analysis systems (μ TAS) or “lab on a chip”, with the driving force being the goal of producing systems capable of completing full laboratory experiments with stages including sample preparation, fluid pumping, suspended particle handling, reagent mixing and sorting [1]. The advantages of reducing the size of laboratory processes include reduced reagent consumption, increased automation, reduced production costs of disposable components, smaller sample sizes and improved analysis and sensitivity [2].

The manipulation of suspended particles as a research area has been studied for many decades, and it is relevant to multiple applications including more recently microfluidics. Many investigations have also been conducted in the selective handling of fragile single particles and positioning micrometer sized particles.

Applications for microparticles handling include, for example:

- (a) Lipid particles can be separated continuously from erythrocytes in a microfluidic channel by acoustic standing wave forces [3];
- (b) The investigation of the interactions between DNA and DNA-binding proteins has been done based on the magnetic tweezers approach [4];
- (c) A flagella construction can be formed by binding thin particle patterns together due to capillary force [5].

The development of particle manipulation has become a great technological challenge for future research in areas including biomedical research and the manipulation of biological samples in solution. Generally, the techniques utilised for

particle handling in a controlled manner can be classified as either non-contacting or contacting.

The non-contacting approaches typically apply to the use of one of four methods:

- (a) Optical [6-10]. Optical methods offer the highest degrees of controllability (high accuracy of spatial control, e.g. three-dimensional particle manipulation [6]), precision, and delicateness (easy mechanical damage, such as part deformation or breakage). It is a powerful tool for handling single or a small number of particles very accurately. Unfortunately this approach has the lack of delicateness due to heating which can result in cell damage [11];
- (b) Magnetic [4, 12, 13]. Magnetic methods offer low cost, and is an excellent way to apply forces to a controlled subset of the particles or cells in a system. As only specialized materials which are affected by magnetic fields, this method has material limitations;
- (c) Ultrasonic [14-17]. An ultrasonic field is present throughout the whole fluidic volume. Therefore particles do not need to be located before manipulation when ultrasonic methods are conducted. Additionally, many particles can be positioned simultaneously in distinct location because of the periodicity of the ultrasonic standing wave field and typical larger wavelength than particle diameter;
- (d) Dielectrophoresis [18, 19]. Dielectrophoresis is the electric analogy of magnetophoresis. In fluid suspensions its properties can be used to differentiate between various particle types. But this method which offers high effectiveness operates only over short distances - in the range of a few micrometers.

In the present work another non-contacting method based on capillary flows in thin films of liquids has been developed for depositing controlled line patterns [20].

To contrast with the non-contacting methods, one of the most generally used contacting techniques employs vacuum suction via micropipettes, which offers low degrees of controllability and precision. Probes and grippers based MEMS technology offer higher degrees of controllability and precision than vacuum method; although the degree of delicateness achievable is much lower than non-contacting schemes [21, 22].

Notably, both non-contacting and contacting methods have limitations. The non-contacting methods generally offer a higher degree of controllability but are more expensive and require complex experiment setups, while the contacting methods offer lower degrees of delicateness and controllability. Therefore, methods with high degrees of controllability, delicateness and precision, simple cheap setup, moreover, low energy consumption or even obviating the use external energy sources, are the challenging tasks for current researchers.

1.2 Project Aims and Research Approach

Advanced particle manipulation techniques require the combination of low cost, high degrees of controllability, precision, and delicateness. For this reason, the broad aim of this research is to develop a range of highly specific particle separation and sorting techniques to manipulate delicate particles in an easy and highly controllable way. In this research, the specific objectives include:

- to analyse and develop acoustical methods for particle manipulation by using (a) a microfluidic channel and (b) a fluidic cell;
- to explore bubbles as a soft medium method in a new application of particle sorting by combination with ultrasonic actuation.
- to develop a method using the capillary force mechanisms to permit particles remaining hydrated, while assembling and harvesting in batches;
- to establish a new method to sink particles based on a sink-float scheme. A droplet is dispensed directly above a selected particle floating on the liquid surface to cause it to sink.

A roadmap of the research approach is summarized as shown in Fig. 1.1.

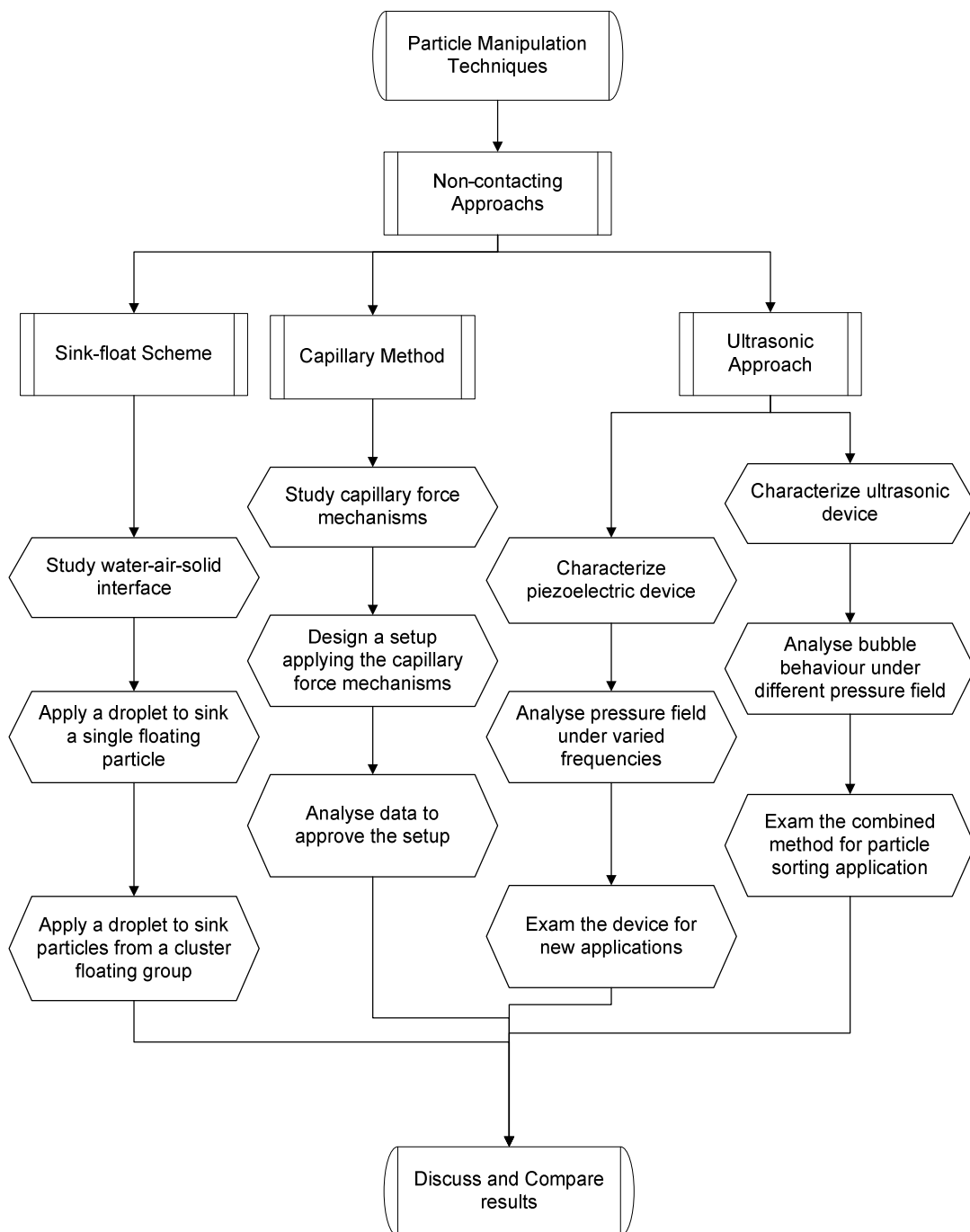


Figure 1.1 Illustration of the scope of the research work

1.3 Thesis Structure

Background information is presented as a Literature Review in Chapter 2. Section 2.2 presents previous research concerning contacting methods for particle manipulation, including micropipette, microrobots and soft medium application. Section 2.3 presents researches in the area of non-contacting methods. Such methods including optic, magnetic, ultrasonic and dielectrophoresis offer higher controllability, precision and delicateness. Research gaps are identified in Section 2.4.

Chapter 3 extends the technique of using ultrasonic methods for particle manipulation. A brief introduction is presented followed by the background theory. Experiments presented in this chapter include: (a) simple pressure field analysis in a microfluidic channel, (b) two-dimensional field observation in a microfluidic channel. The piezoelectric device and experimental setup are characterised in Section 3.3. The microfluidic channel consists of an etched silicon substrate bonded to a glass wafer, and subsequent adhesion of a piezoelectric actuator with electrode shapes designed to excite the modes required in the investigations. Both acoustic radiation force and acoustic streaming are studied. In experiment (a), line formation is observed under resonant frequencies. Furthermore, particle clumps are achieved in the form of an array in the microfluidic channel. Experiment (b) shows that under certain region of actuation frequency, a two-dimensional pressure field is obtained by a single electrode actuator.

By way of further developing the ultrasonic method, vibrating bubbles within the acoustic field are demonstrated as a mechanism for particle sorting in Chapter 4. The microstreaming flow pattern around the oscillating bubbles and its applications are discussed in Section 4.2. The piezoelectric driven chamber and experimental setup are characterised in Section 4.3. The size based particle sorting demonstrated operates by use of the secondary Bjerknes force between the bubble and particles, and the drag force on the particles due to streaming flow. Experiments on the behaviour of different sized bubbles in varied pressure field are presented. Two sizes of particles are used to examine the sorting application. Larger particles ($6\ \mu\text{m}$) are caught by a oscillating bubble while small particles ($1.9\ \mu\text{m}$) aren't; whilst at a lower resonant frequency, both sizes of particles are repelled from the oscillating bubble.

In Chapter 5, capillary force mechanisms are discussed with a view to developing a new method for particle assembling. A brief theoretical background is presented in Section 5.2. Section 5.3 describes the simple setup of the experiment, which has a fluid cell created by a glass slide and a glass cover slip. This method offers the advantage of keeping particles hydrated and obviating the use external energy source. Experimental results are discussed in Section 5.4.

In Chapter 6 a delicate method, that of using a droplet to sink a selected floating particle from a liquid surface, is discussed. This method is based on the sink-float scheme, which is broadly used in the recycling industry with macro objects. Section 6.2 presents summarised background information. Section 6.3 presents the experimental setup and discussion for selecting single floating particle from water surface. A single particle located within the vicinity of a droplet can be sunk due to the sink-float scheme. Moreover, in Section 6.4, the development of the sink-float scheme to select particles from a floating cluster group is presented. It is necessary to find a droplet size such that the objectives of sinking an individual particle within a floating cluster can be achieved, whilst the neighbouring particles remained floating and the cluster itself stays largely undisturbed. This is shown to be possible. Section 6.5 presents a brief conclusion of the sink-float scheme.

In the final chapter, conclusions of the research project are presented, as well as the recommended further work from the research.

A collection of the relevant journal articles that have been published, or submitted for publication has been included in the appendices.

Chapter 2

Literature Review

2.1 Introduction

The reduction in scale of fluidic based chemical and biological processes offers significant analytical and sensitivity improvements as well as reduced reagent usage, increased automation and reduced manufacture costs [2], these advantages motivate interest in “lab-on-a-chip” or micro total analysis systems (μ TAS) [1]. Most microfluidic systems involve enclosed fluidic channels. These can be fabricated in a range of manners including etching in silicon and sealed with glass [23], hot embossed in plastics [24], or moulding in PDMS [25]. An issue which arises when using such enclosed systems is that they must be filled, if the samples need to be handled as otherwise pumping mechanisms fail [26]. When attention is turned to very small volumes of sample, this requires separation in an immiscible buffer solution [27], or the switching from using enclosed volumes to be use of droplets deposited on plane surfaces [28]. In this switch, some of the key technological building blocks required remain the same including the manipulation of suspended matter [29, 30], sample mixing [31] and fluid motion [32] (whether pumping or droplet movement).

Generally, the techniques utilised for particle handling in a controlled manner can be classified as contacting or non-contacting methods. Section 2.2 will introduce the contacting methods which include one of the most generally used technique which employs vacuum suction via micropipettes offering low degrees of controllability and precision; as well as probes and grippers based on MEMS technology which offer higher degrees of controllability and precision. Section 2.3 will summarise the non-contacting methods which include optical methods, magnetic methods, ultrasonic methods and dielectrophoretic methods, as well as the capillary methods. The degrees of delicateness achievable by non-contacting methods are much higher than contacting methods.

2.2 Contacting Methods for Particle Manipulation

Contacting methods require direct surface contact. The most generally used contacting approaches include vacuum suction via micropipette, and probes and grippers based on MEMS technology.

2.2.1 Micropipette application

A micropipette aspiration technique applied to cells detached from the substrate was reported by Sato *et al.* [33]. During the experiments, the tip of the micropipette was made to approach the surface of a cell by manipulation of both the cell chamber and the stage of the microscope. A negative pressure was applied to the tip, to draw the cell toward and into the pipette; this pressure gradient was set by using the difference of the height between two reservoirs. As a result, the aspirated part of the cell continued to deform after the application of pressure, but an almost steady state was observed to occur within 8-10 minutes of investigation.

The micropipette suction technique was also used to investigate the adhesion of normal and carcinoma hepatic cells on a membrane containing collagen IV [34], and applied to robot/human cooperative microinjection [35] as shown in Fig. 2.1.

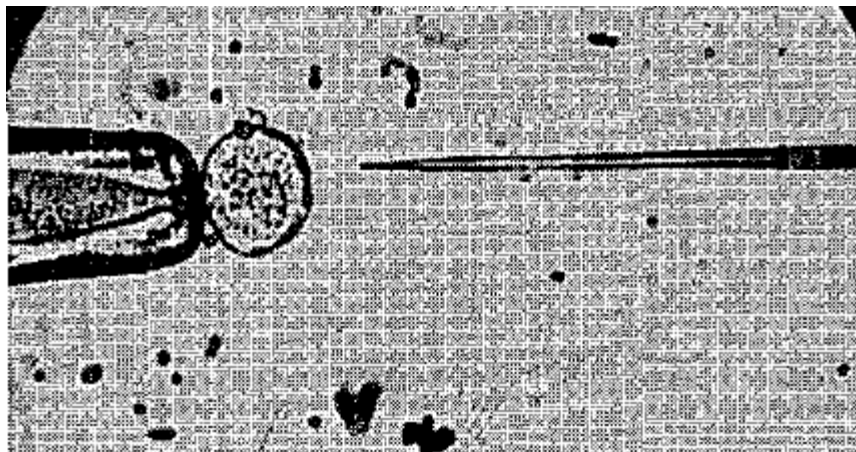


Figure 2.1: Image of a mouse embryo which is held by a holding pipette during the injection with the injecting pipette, cited in Kumar *et al.* [35].

Although, the basic principle of this technique is very simple (the use of the aspirating pressure produce by the micropipette), effective results are achieved quite well. In biological investigations, some issues are raised however. For example, due to its low degree of controllability, it is relatively difficult to achieve precise cell

manipulation. For this reason, other contacting methods for particle manipulation have been developed as discussed in the following.

2.2.2 Micro-fabricated device application

The use of micro-fabricated devices, such as microgrippers and microprobes, is undergoing rigorous development currently. These types of MEMS devices provide a wide range of options in terms of design, performance and material compatibility. Though such MEMS based grippers solve the problem of low controllability, a new challenge of the best achievable delicateness is introduced.

Applying Microrobots

Jager *et al.* [36] reported a microrobotic arm operating in an aqueous environment, with dimensions suitable and scalable for the manipulation of cells. The microfabricated devices are individually controlled by microactuators based on polypyrrole-gold bilayers. Patterning of active and passive elements defines the geometry of a microrobot, whose individual bending beams are addressed separately and are therefore capable of more complex motions. For the microactuators, polypyrrole (PPy) doped with dodecyl benzene sulfonate ions in a bilayer configuration with Au acting as both a structural layer and an electrode was normally used. Unlike the polysilicon microrobots, PPy/Au bilayers microactuators are suitable for operating in salt solutions, blood plasma, urine, and cell culture medium; therefore, these micro-robots are most interesting for operations in biological fluids. The robots could be used for single-cell diagnostics. The robot arm could arrest biological entities from a sample and then transfer them sequentially to different measurement stations of a multisensors area. An array of standing micro-robots, whose fingers are treated with adhesion molecules, could be used to select given cells or bacteria in a sample and then transfer them to the multisensor area. In the report they demonstrated the gripping and positioning of a 100 μm glass bead by a maximum displacement of 270 μm with this microrobotic arm.

Applying grippers

Generally, the contacting methods have limitations on the application of life science investigations. This is due to the fragile nature of the cell membrane. The utmost caution is required in order to ensure its healthiness during and after manipulation. Alternatively, operating temperature, force and voltage are the major factors that could cause non-viability of the cells. As a solution, the development of a SU-8-

based microgripper can operate in physiological ionic solutions which was presented by Nikolas and Luke [37]. The electrothermally activated polymer gripper consists of two “hot-and-cold-arm” actuators that are fabricated in a two-mask surface micromachining process. The high thermal expansion coefficient of SU-8 compared to silicon and metals, allows the actuation of the microgripper with small average temperature elevations at low voltages. These properties make the microgripper a suitable device to be used for the manipulation of single cells and other biological species in solution with minimal undesired interactions.

More recently, Colinjivadi *et al.* [38] presented the development of an optimized contact technique for viable cell manipulation utilizing a high aspect ratio polymer *chopstick* gripper. This gripper, as shown in Fig. 2.2, consists of a 2 μm thick metal heater layer and a 60 μm thick SU-8 layer and is fabricated by a typical UV-LIGA process using SiO_2 as sacrificial layer. For such a gripper, Ansys simulations show an average 7°C increase when a 10 μm displacement is required in air; however an average 18°C temperature raise occur when a similar displacement in phosphate buffered saline solution. Critically, there is negligible temperature rise near the tips of the gripper. Additionally, the material of the gripper with a relatively low value of Young’s modulus of 4Gpa and consequently low stiffness improves the handling force. The results of the experiment show that the microgripper is capable of picking, moving and placing a suspended cell in a solution without any damage.

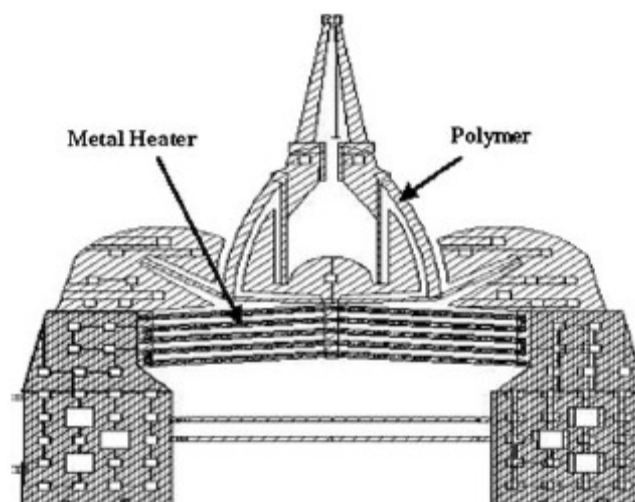


Figure 2.2: Schematic representation of a polymer *chopstick* microgripper, cited in Colinjivadi *et al.* [38].

The particle manipulation techniques with micro-fabricated device are demonstrated to be suitable for single cell manipulation. Microtechnical structures or particles are usually produced in large numbers; therefore individual handling will be very time-consuming. Moreover this technique can damage the fragile structure of the cell due to the dimensions poorly controllable contact forces. The degree of delicateness is still questionable.

2.2.3 Soft medium application

Unlike the vacuum suction and micro-robots methods, soft medium applications using microbubbles or hydrogel beads to attach to particles provide a solution to improve delicateness. Unfortunately, this method can result in problem associated with particle harvesting.

Microbubble actuation

The earliest use of bubble formation to create a jet of fluid was in the inkjet printer industry [32, 39]. The work by Lin in 1998 [39], addressed the thermophysical phenomena of bubble formation by using solid-state microheaters and recommended specific directions for future applications. Characterization of microbubble formation mechanisms leads to new scientific research in microscale heat transfer and provides design guidelines for bubble-powered micromachines. Experimentally, individual, spherical vapour bubbles with diameters of 2 to 500 μm have been generated, and unusual characteristics such as stable and controllable bubbles have been demonstrated. Lin [37] also suggested some challenging applications based on microbubble formation. Later, Geng *et al.* [32] presented a potentially useful pumping device without moving mechanical parts. The principle of this device is based on the periodic generation and collapse of a single vapour bubble in a channel. The channel shape is such that it creates an asymmetry in the surface tension forces, which results in a pumping effect. Under certain conditions, the device develops a head of a few centimetres of water with typical flow rates in the range of 100 μl per minute. Both head and flow rate can be increased by adjusting geometrical parameters and operating conditions. In a similar manner, by using a thin-film heater to form a vapour bubble, thermal inkjet pens fire drips of ink out of chambers due to the volume expansion created by the bubble. The explosive vaporization used in the inkjet printing industry already has been proven as an effective, reliable fluid actuation mechanism.

Using a Bubble Jet ink jet device, a similar approach also described by Okamoto *et al.* [40] has been used to eject precise volumes of a solution containing DNA onto a glass surface, thereby creating a DNA microarray for biological screening. By using this method, they fabricated DNA microarrays that carried 64 groups of 18-mer oligonucleotides, encoding all possible three-base mutations in the mutational “hot spot” of the *p53* tumor-suppressor gene. These were screened with a fluorescently labelled synthetic 18-mer oligonucleotide derived from the *p53* gene, or segments of the *p53* gene that had been PCR amplified from genomic DNA of two cell lines of human oral squamous cell carcinoma. This allowed discrimination between matched hybrids and 1 bp-mismatched hybrids.

Another controllable bubble actuation method used to manipulate particles is a microbubble-powered bioparticle actuator demonstrated by Maxwell *et al.* [21], as shown in Fig. 2.3. In the report, they described that using resistive heaters with micromachined nucleation sites, bubbles can be formed in precise locations, at temperatures that are repeatable to within 20-30 degrees, and then can dissipate completely within seconds of formation. This technology and method for yielding a rather deterministic bubble formation process demonstrates the potential for using bubbles as a robust actuation scheme. One advantage of this actuator is that the fabrication technology involves materials that are biocompatible and processes that are scalable. In a proof-of-concept device, they also demonstrated that bubble actuation could be used to actuate cell-sized particles.

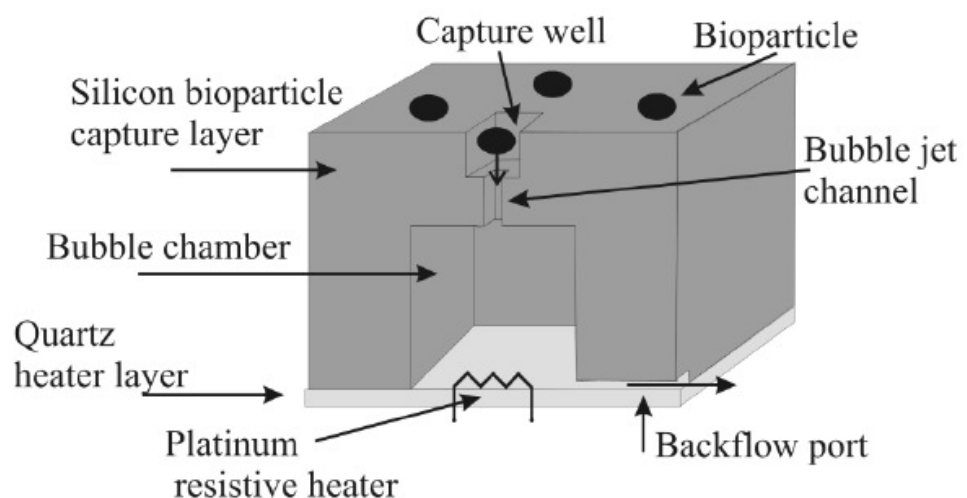


Figure 2.3: Schematic representation of a microbubble-powered bioparticle actuator, cited in Maxwell *et al.* [21].

As an alternative to the resistive heater generated bubble, Taylor and Hnatovsky [22] used low power continuous wave laser radiation coupled into an etched optical fibre to heat a metallized microtip to generate a stable bubble by spontaneous and highly localized boiling of the liquid. During the microbubble formation stage it was also possible to trap material onto the bubble surface which was dispersed within the fluid. As the result, the microbubble, which is firmly attached to the end of the fiber probe, can be easily manipulated in 3-D and used to delicately extract small particles from a surface. Furthermore, the microbubbles were remarkably resilient and could withstand penetration by an external probe. This opens up the possibility of positioning probes on either side of biological material trapped on the surface of the bubble. While mixing biological material on the surface of a bubble without thermal damage is also described in their paper. A special control over the temperature distribution on the probe surface permitted by new probe designs like the focussed ion beam nanomachined probe is required. The hollow tip fiber probe design provides control over the microbubble both in space and in time and should be very useful for the further studies of bubble formation, growth and collapse and on the role of trapped gases and surfactants on these processes. Therefore, the microbubble experiments are interesting in studying immobilized biological material, since a bubble membrane provides an alternative medium compared to glass slides.

Furthermore, a mixing technique based on the principle of bubble-induced acoustic microstreaming was developed by Liu *et al.* [41]. The mixer consists of a piezoelectric disk that is attached to a reaction chamber, which is designed in such a way that a set of air bubbles with desirable size range is trapped in the solution. Fluidic experiments showed that air bubbles resting on a solid surface and set into vibration by the sound field generated steady circulatory flows, resulting in global convection flows and thus rapid mixing. From the report, numerical simulations showed that the induced flowfield and thus degree of mixing strongly depend on bubble positions. Optimal simulated mixing results were obtained for staggered bubble distribution that minimizes the number of internal flow stagnation regions. Alternatively, immunomagnetic cell capture experiments showed that acoustic microstreaming provided efficient mixing of bacterial cell matrix suspended in blood with magnetic capture beads, resulting in highly effective immunomagnetic cell capture. Furthermore, bacterial viability assay experiments showed that acoustic microstreaming has a relatively low shear strain field since the blood cells and

bacteria remained after mixing. As a result, acoustic microstreaming has many advantages over most existing chamber micromixing techniques, including simple apparatus, ease of implementation, low power consumption, and low cost.

Consequently bubbles have been used for pumping, printing, jetting, biological capture and mixing. In this thesis, bubbles as a soft medium method is explored for a new application. A vibrating bubble in an acoustic field is used for particle sorting in Chapter 4.

Hydrogel beads

A bead-based dynamic cell microarray is also a successful contacting technique for particle manipulation. Recently, Tan and Takeuchi [42] reported a selective retrieval method for arrayed monodisperse hydrogel beads containing cells. Modifications were implemented including: the incorporation of cavities as nucleation sites; indirect retrieval using bubble powered jets; and the use of low boiling point fluid in the device to realize a gentle optical-based retrieval method. Parametric studies confirmed that these modifications dramatically reduced both the intensity and duration of applied laser pulses required for bubble formation. They also demonstrated for the first time the formation of a bead-based dynamic cell microarray by introducing cell-encapsulating alginate beads into the dynamic microfluidic system, and successfully retrieved an alginate bead from a fluidic trap. Two types of devices were used in their experiments. Design 1 was used to study the effects of incorporating cavities as nucleation sites and the feasibility of indirect retrieval using a bubble-powered jet. This device is easier to control and required less complicated fabrication than Maxwell *et al.* used [21]. Design 2 was used to study the effect of using low boiling point fluid. Instead of working with single cell types, this device is a trend toward “animal on a chip” devices that incorporate cells from different tissues and organs, resulting in a system that better mimics metabolism in the body. The platform can be a high-throughput tool to study pathological and physiological phenomena in cells with parallelization and automation in the future.

Contacting “soft medium” approaches based on hydrogel beads or bubbles offer solution to the delicateness problem but will likely incur some difficulties in particle harvesting when the operation is completed.

Above all, the micropipette suction technique is a simple way to handle a single cell; but its poor controllability gains difficulties for the accuracy. While the micro-fabricated device give the solution to the controllability. Grippers and micro-robots can damage the fragile structure of the cell because of the hardly controllable contact forces. The degree of delicateness is quite low. In addition, the delicateness that soft medium application achieved is very interesting. Unfortunately, all these methods are not suitable for particles manipulation in a bulk solution containing many particles. The difficulty of particle harvesting is the big issue. Therefore, an idea of incorporating the bubble method with the ultrasonic method is introduced, and demonstrated for particle sorting in Chapter 4.

2.3 Non-contacting Methods for Particle Manipulation

In contrast to the contacting method discussed previously, non-contacting methods avoid direct surface contact. The most widely-used non-contacting methods for particle manipulation are optical micromanipulation, magnetic tweezers, acoustic manipulation and dielectrophoresis. In this Section, a detailed review of these non-contacting methods is presented.

2.3.1 Optical method

The first observation of acceleration of freely suspended dielectric particles and atoms by the forces of radiation pressure was reported by Ashkin in 1970 [43]. Historically, the main problem in studying radiation pressure in the laboratory has been the obscuring effects of thermal forces. These are caused by temperature gradients in the medium surrounding an object and, in general, are termed radiometric forces. When the gradients are caused by light, and the entire particle moves, the effect is called photophoresis. These forces are usually orders of magnitude larger than radiation pressure. Even with lasers, photophoresis usually completely obscures radiation pressure. In Ashkin's report [43], radiometric effects were avoided by suspending relatively transparent particles in relatively transparent media. Even more, the thermal effects that Ashkin used are 10^3 times the power densities of Rawson and May in 1966 [44]. One of the experimental result from Ashkin's work [43] when a sphere of $r = 1.34 \mu\text{m}$ in water with $P = 19 \text{ mW}$, $w_0 = 6.2 \mu\text{m}$, is $25 \pm 5 \mu\text{m}/\text{sec}$ which is good agreement with the computation's result of $v = 29 \mu\text{m}/\text{sec}$.

Based on the first investigation of particle acceleration by light, Ashkin and Dziedzic [45] reported that optical trapping and manipulation of viruses and bacteria by laser radiation pressure was achievable by single-beam gradient traps. In this report, individual tobacco mosaic viruses and dense oriented arrays of viruses were trapped in aqueous solution with no apparent damage using 120 milliwatts of argon laser power. The sensitivity of laser trap effectiveness to optical absorption and particle shape is of particular importance for the trapping of biological particles. Absorption can cause an excessive temperature rise or additional thermally generated forces as a result of temperature gradients within a particle. In general, the smaller the particle size the less the temperature rise and the less the thermal gradients for a given absorption coefficient. For the case of a large particle and a small beam, it is clearly the local shape of the particle that dominates the net force. There are some disadvantages from their experiments. Firstly, during the experiments the power needed to be down to 5 mW to reduce the possibility of optically damaging, once the bacterium had been captured. Secondly, for complex shaped particles, a complete description of the trapping forces was not provided.

Unfortunately, as mentioned earlier, cells can be damaged by cell manipulation using optical traps. As reported by König *et al.* in 1995 [11], the extremely high fields of trapping intensities and photon flux densities may induce two-photon absorption processes and anomalous biological effects. From their investigation, the continuous-wave near-infrared micro-beams can stimulate multi-photon processes in single living cells. The consequences of micro-irradiation include membrane permeability changes, alterations in cloning efficiency and UVA-like stress.

However, optical tweezers are a very widely-used technique for a range of applications. Optical tweezers offer high resolution for trapping single particles, but have a limited manipulation area owing to tight focusing requirements. Ferrari *et al.* [6] demonstrated both direct and indirect optical manipulation using completely customizable multi-trapping systems in 2005. They found that direct trapping is a powerful method for force measurements and indirect cell manipulation can be used to simulate mechanical stresses in cells in order to monitor reactions to controlled stimuli.

Chiou *et al.* [46] presented an optical image-driven dielectrophoresis technique (OET) for high-resolution patterning of electric fields on a photoconductive surface for manipulating single particles which achieved both high resolution and high throughput at the same time. By exploiting the dielectric differences between different particles or cells, DEP techniques have been able to discriminate and sort biological cells that have differences in membrane properties, internal conductivity, and size. The OET technique not only inherits these DEP advantages, but also provides the capability of addressing each individual cell. Dholakia [47] also summarised the OET work and pointed that a much larger potential-energy landscape in which microscopic objects can be arranged can be achieved by the absence of wires.

Most recently, holographic optical tweezers for applications in lab-on-chip environments was reported by Padgett and Leonardo [48]. Such holographic optical tweezers use a commercially available spatial light modulators (SLM) to act as a programmable diffractive optical element (DOE) to split a single laser beam into many optical traps. One of the advantages is that the independently position in 3-dimensional can be achieved, and each of the traps can be independently controlled. In their paper, the applications such as alternative configurations, micromachines, and microdynamics have been discussed. Furthermore, they showed that optical tweezers are not limited to use in controlling lab-on-chip systems under the microscopes, rather that full chip level integration of multifunctional optical tweezers for controlling, driving and sensing lab-on-chip system is also possible.

Above all, optical methods arguably offer the highest degrees of controllability, precision, and delicateness; even though it can result in cell phototoxicity [11]. Optical tweezers offer high resolution for trapping single particles, but have a limited manipulation area owing to tight focusing requirements; on the other hand, electrokinetic forces and other mechanisms provide high throughput, but lack the flexibility or the spatial resolution necessary for controlling individual cells.

2.3.2 Magnetic manipulation

Magnetic tweezers were first introduced by Crick and Hughes in 1950s, using micro-sized magnetic particles and permanent magnets to probe the physical properties of the cytoplasm of adherent cells [49]. The magnetic material used was in a finely

divided form and added to the culture medium of the original explant for three days before subcultivated into the normal medium. In applying the magnetic field to the particles within the cells, three types of movement were involved in their experiments, which were twisting, dragging and prodding.

Through their experiments, some advantages and disadvantages of the magnetic particle method are apparent. Firstly, it is possible to apply a stress which varies swiftly with time. This has enabled to distinguish small elastic effects which would be difficult to demonstrate by any other method. Secondly, the stresses can be applied locally. It is not necessary to apply them intensely to the cell as a whole, as in centrifuging. Thirdly, the stresses in the case of dragging of large particles can conveniently be made high, and for twisting, less conveniently, very high.

The disadvantages are the difficulty of getting the particles into the cell, since only certain types of cells will phagocytose them; the possibility that they may modify the neighbouring cytoplasm; and the care needed to perform some of the magnetic measurements without artefacts. For small particles the accuracy is low, though this could probably be improved for larger particles. The fundamental disadvantage of the magnetic method is that the properties can not be measured at constant stress.

Fifty years later, Haber and Wirtz [4] utilized magnetic coils instead of permanent magnets to apply forces of controlled amplitude, direction, and time dependence on super-paramagnetic microspheres. Magnetic tweezers were generally utilized to measure the force produced by individual motor proteins as well as the micromechanical and transport properties of individual DNA molecules; to evaluate binding of proteins which including histones, TATA-box binding proteins, and elastic protein, when DNA is under tension.

Recently, Yan, Skoko and Marko [50] developed a near-field magnetic tweezers by using a small permanent magnet moved to within 10 μ m of the particle. This instrument provided a significantly large force for micromanipulation of single DNA molecules. They described a hybrid method for manipulation of single DNA molecules, using a truly transverse magnetic-tweezer system where the magnet is in solution and thus can be very close to the end-attached particles being manipulated, allowing large and constant forces to be generated if needed. Either fixed-position measurements as in GM or fixed-force MT measurements are possible by this

approach. One “bead-catching” micropipette and the magnet particle are mounted on motorized three-axis micromanipulators. A “loading” pipette is mounted in a manual three-axis manipulator, and a fourth “force-measuring” micropipette is mounted on the microscope in a fixed position in the sample cell. With this setup, bead + DNA structures can be injected into the sample cell, and the catching pipette can grab them using fluid suction. Then, by using the pipettes to stretch DNAs strung between a pair of beads, measuring forces uses deflection of the force-measuring pipette. Alternately, the small magnet can be used to apply a constant force to the paramagnetic optics.

In general, magnetic tweezers are very cost-effective, and they can be used as a versatile tool to characterize the physical properties of complex living cell system [49]. Furthermore, they are shown to be very efficient in spinning small scaled objects [13]. But the devices used are usually too bulky for collaboration with other components and result in difficulties in terms of visualisation, they also require considerable amount of energy to generate strong local magnetic field gradients.

2.3.3 Ultrasonic manipulation

The manipulation of suspended particles within microfluidic systems is a big challenge as it has many applications, such as flow cytometry, cell sorting, cell fusion, and systems where cells need to be divided into clumps to be treated differently whilst being kept under observation. One effective method of doing this is to use acoustic radiation forces generated by an ultrasonic pressure field.

Acoustic radiation forces arise as a second order effect when an ultrasonic wave interacts with a suspended particle. The ultrasonic wave, a pressure wave within a compressible fluid oscillating at high frequency (>20 kHz), can simply propagate through the fluid, or more usually be multiply reflected and result in a standing wave when a suitable resonant frequency is selected. The advantage of the second scenario is that the large amplitudes and hence forces can be achieved. When these ultrasonic waves impinge on a suspended particle a force is produced, calculated by integration of momentum terms in the Navier Stokes equation over the surface of the sphere and time averaging. The time averaging is important as the oscillations are at high frequency so there is insufficient time for the particle to overcome inertial effects within single cycles, hence no response would be expected from linear terms,

however these second order terms are non-zero over a complete cycle, hence a force field exists which is not oscillating. The result is that particles (denser and more compressible than the host fluid) are collected at the pressure minima of the standing wave. Since the ultrasonic wavelength is typically much larger than the particle diameter, the periodicity of the ultrasonic standing wave field can be used to simultaneously position many particles in distinct locations.

Gor'kov [51] has considered the force arising from an arbitrary pressure field, and states the time-averaged force as

$$\langle F \rangle = -\nabla \langle U \rangle, \quad (2.1)$$

where $\langle U \rangle$ is the force potential, which is given by

$$\langle U \rangle = 2\pi\rho_F R_s^3 \left(\frac{1}{3} \frac{\langle p^2 \rangle}{\rho_F^2 C_F^2} f_1 - \frac{1}{2} \langle v^2 \rangle f_2 \right). \quad (2.2)$$

The terms $\langle p^2 \rangle$ and $\langle v^2 \rangle$ refer to the mean-square-fluctuations of the pressure and fluid/particle velocity in the incident wave at the point where the particle is located,

$$f_1 = 1 - \frac{\rho_F C_F^2}{\rho_S C_S^2} \quad \text{and} \quad f_2 = \frac{2(\rho_S - \rho_F)}{2\rho_S + \rho_F}. \quad \text{The terms } \rho_F \text{ and } \rho_S \text{ are the density, and}$$

C_F and C_S are the speed of sound in the fluid and objects respectively. The linear

equation of the sound field is used to calculate $\langle p^2 \rangle$ and $\langle v^2 \rangle$; therefore, $p = \rho_F \frac{\partial \Phi}{\partial t}$

and $v^2 = v_x^2 + v_y^2 + v_z^2$, where $v_x = -\frac{\partial \Phi}{\partial x}$, etc. The particles collect at the areas of

minimum force potential.

A rapid growth has been witnessed in this field since the year 2000, with the focus being shifted to micromachined devices, following the ongoing trend of miniaturization of biochemical processes to be performed on chips. These microfluidic systems possess the distinct advantages of shortened analysis times, reduced sample and reagent consumption, low cost as a consequence of their reduced geometrical size and the possibility of integrating different functions on the same system in series. Moreover, the use of ultrasound to position particles has some advantages over optical tweezers because the particles do not need to be located prior to manipulation. In addition, since the ultrasonic wavelength is typically much larger

than the particle diameter, the periodicity of the ultrasonic standing wave field can be used to simultaneously position many particles in distinct locations.

The majority of devices described in the literature are acoustic filters, built using conventional techniques, which can partially separate two phases from each other, provided that at least one is liquid or gaseous. The devices consist of multiple layer resonators, in which one layer is a fluid. The device is in contact with a piezoelectric plate, in which there are thin metal electrodes on the bottom and top surface of the plate. When modelled, they are treated as 1-D systems. However, there are an increasing number of microfabricated devices being studied.

Trapping planes parallel to a transducer

In one-dimensional resonators, the thickness of the layers is designed carefully, so that a standing pressure field of half or a quarter acoustic wavelength can be established in the fluid. The trapping plane parallel to the transducer is termed “parallel mode”, and is depicted in Fig. 2.4. Quarter wavelength resonators, were first reported by Hawkes *et al.* [52]. In these multilayer resonators, particles can be positioned at the centre of a cavity or pushed against the walls. In order to fulfil the boundary conditions set to the pressure, half wavelength resonators required quarter wavelength thick reflectors and quarter wavelength resonators are used in combination with half wavelength reflectors. When operated in continuously flowing fluid mode, by pumping fluid into an inlet defined in the silicon substrate and removing it through two outlets at different ratios, particles can be focused at half or quarter channel depth in a channel etched in glass [53-55]. As a result, all the particles are left the device from one outlet, whilst the particle-free fluid is removed from the other.

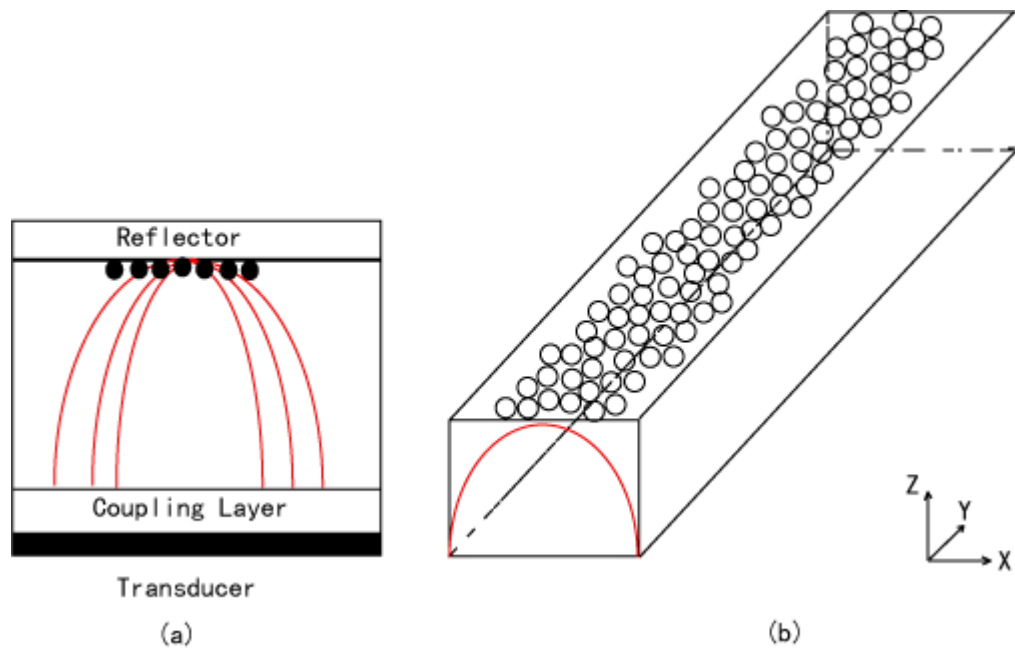


Figure 2.4: Schematic representation of a quarter-wavelength resonator: (a) cross-section view of the device; and (b) particles concentrated in the channel at the reflector layer. Based on Martin *et al.* [50].

Hill *et al.* [55] also have investigated the possibility of varying materials and hence adopts a different, more standard fabrication approach independent of silicon micromachining facilities. As a result, it is found out that the material choice played a minor role in the definition of the node position and in the amplitude of the pressure field. Furthermore, Haake and Dual [56] have reported that by varying electronic parameter (voltage magnitude and voltage phase), the pressure node position can be changed.

Trapping planes perpendicular to a transducer

In contrast to the parallel mode is the perpendicular mode, where the acoustic standing field is set up in the plane of the silicon substrate, leading to trapping planes parallel to the side walls, as seen in Fig. 2.5. The excitation is still produced by a transducer mounted parallel to the cavity bottom surface. The major advantage with respect to the previous devices lies in the fact that there is no longer a need to carefully design the layer thickness to match multiples of quarter or half acoustic wavelength. Additionally, multiple trapping planes resulting in multiple particle lines are visually accessible from the top.

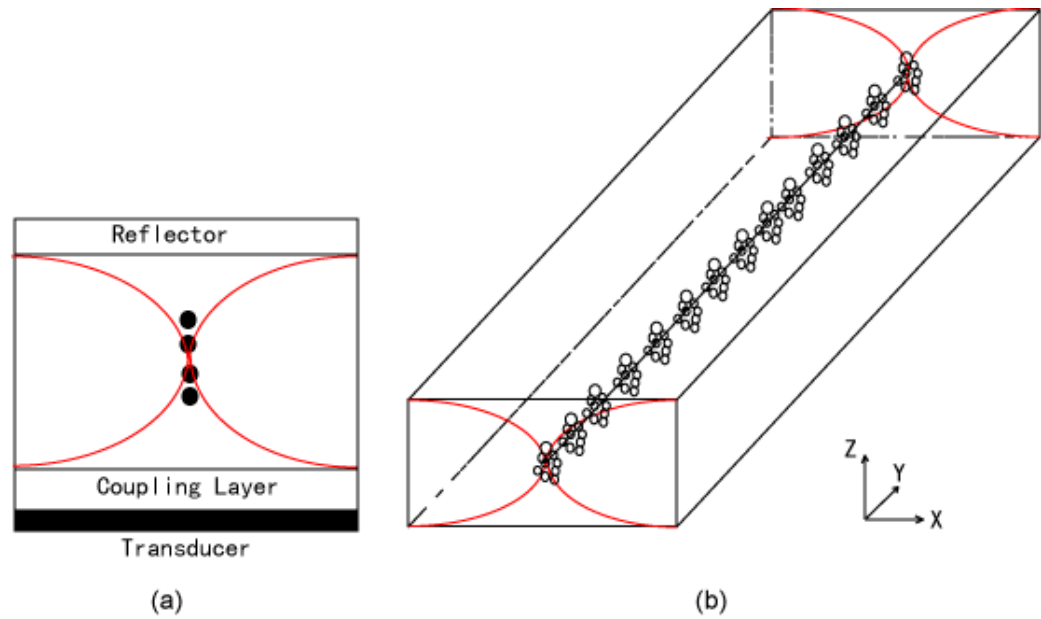


Figure 2.5: Schematic representation of a half-wavelength resonator: (a) cross-section view of the device; and (b) particles concentrated along the centre of the channel. Based on Nilsson *et al.* [12].

Dougherty *et al.* [57] have demonstrated a standing pressure field with a single node plane along the centreline of a wet etched channel by out-of-phase excitation of two half-channel-width electrodes patterned on the lower surface of a piezoelectric transducer. In the 750 μm wide, 250 μm deep and 13mm long channel by Nilsson *et al.* [14], the excitation is given by a transducer largely exceeding the channel size, pressed against the silicon chip, coupled using ultrasonic gel and tuned to the frequencies at which standing pressure waves across the channel are established in the liquid. In 2005, Petersson *et al.* [3] reported on bovine blood separation into its component erythrocytes and lipids using the same system. Lipid particles are responsible for disorders after cardiac surgery and therefore it would be of advantage to separate them from the rest of the blood. The experiment takes advantage of the spatial separation given by their different mechanical properties when exposed to ultrasound. Whilst the erythrocytes are focused along the centreline and exit through the central outlet, the lipids are gathered at the antinodes along the channel walls and removed through the two external branches.

Multiple piezoelectric transducers device

Lilliehorn [58] described a particle trapping device, which uses multiple trapping sites which are controlled by a multilayer ultrasonic transducer individually. Such ultrasonic microarray device has the potential to create two-dimensional pressure fields.

Continuous separation and size sorting of particles in a microfluidic channel with two transducer paralleled mounted to the channel is reported by Kapishnikov *et al.* [59]. The phase difference between signals generated by the two transducers determined the field of the ultrasonic standing wave with the force anti-nodes. A half wavelength resonator was used as a separator. The antinodes located near the wall allow the particles to be concentrated and separated from the solution. A multi-stage device provided a significant improvement of the purity. While size sorting, a quarter wavelength resonator was used. Such a size sorting device was designed based on the idea of the particle velocity strongly depends on its size, which means that the larger particles move faster.

Recently, particles being trapped and moved in one dimension using three piezoelectric transducers have been demonstrated by Courtney *et al.* [60]. The transducer attached on the bottom of the device creates a parallel trapping plane which levitates particles against gravity. The other two transducers are located on the side walls in an opposing position which create vertical planes. In their investigations, the grid pattern of particles is observed due to the coupling of the parallel and vertical trapping plane. Furthermore, by varying the relative phase of two signals generated by the pair transducers, 140 μm displacement can be achievement in one dimension.

Using wedge transducers

Besides using piezoelectric directly attached to the microfluidic chip, Manneberg *et al.* [61-63] investigated more than one-dimensional particle manipulation by using specially designed wedge-mounted transducers. A two-dimensional ultrasonic manipulation in a microfluidic chip was designed in terms of actuation frequency, wedge angle and the coupling effects in orthogonal directions between single- and dual-frequency ultrasonic actuation [61]. As a result, they demonstrated arraying and alignment of particles in two dimensions. Another scheme for achieving two-dimensional spatial control for flow-free ultrasonic transport and positioning cells was discussed by combining a rapid (1 kHz) linear frequency sweeping around 6.9 MHz, and a slow (0.2-0.7 Hz) linear frequency sweeping around 2.6 MHz. Additionally, a three-dimensional ultrasonic cage was design by Manneberg *et al.* [62]. The cage is designed as a dual-frequency resonant filled square box integrated

in the fluid channel. Based on this, a microplate for parallelized manipulation of particles was demonstrated. The device enables aggregation, positioning and high-resolution microscopy of cells distributed in an array of 100 microwells centred on the microchip. And the cells continuously exposed to ultrasound were able to divide and remain viable for at least 12 hours inside the device. This demonstrates the potential for long-term biocompatibility.

Combination with other techniques

Due to their different action ranges, it is sensible to think that acoustic manipulation can be combined with other manipulation methods discussed in this chapter. To the possibilities of simultaneous parallel handling of large number of particles offered by the long range acting standing pressure fields, the benefits of the localized, more accurate manipulation using electric, optic or magnetic fields could be added.

The combination of acoustic manipulation and dielectrophoresis is reported by Wiklund [64]. The spatial accuracy is improved by applying the long range ultrasonic forces and short range dielectrophoretic forces. This method is suitable for particle and fusion of particle subgroups.

Another device capable of trapping particles within a fluid volume, in which there is no bulk flow, has been described by Neild [16]. A pressure field is excited by coupling the movement of a shear piezo to the fluid using a bending glass plate. It has been shown to collect cells in lines and points effectively. Based on this device, Neild [17] investigated the combination of ultrasonic standing wave and microgripper for particle manipulation. In the acoustic field, particles are positioned in predictable locations. In this experiment, particles are concentrated in the line along the centre of the channel. The microgripper is designed to remove the last particle in the line.

Advantages of the ultrasonic method include the fact that many particles can be manipulated at the same time, and prior pre-location is not necessary. The ultrasonic method is also a cost-effective method which allows the experiments to be done on a lab-on-chip device. Moreover, particle manipulation such as particle trapping, sorting, concentration and separation, particle switching can be demonstrated by using ultrasonic method. In Chapter 3, experimental results are included show the development of new ultrasonic particle manipulation schemes.

2.3.4 Dielectrophoretic method

Dielectrophoresis (DEP) is widely used in microsystems as a mechanism for particle manipulation. It is appealing because dielectrophoretic forces are quite large when small devices are employed, and the dielectrophoretic forces on a particle scales with the characteristic length scale of the system to the cubic power. Moreover, the particle response varies based on the frequency and phase of the applied field. In contrast to linear electrophoresis, DEP is the controlling forces of an electrically polarized object in a non-uniform electric field, it does not require that the object have a net charge and has a non-zero time-averaged effect even if AC electric fields are used [65].

A particle experiences a lateral force \overline{F}_{elec} , when it is placed in an electrical field.

$$\text{Such force [66, 67] is given by } \overline{F}_{elec} = q\overline{E} + (\overline{m}\nabla)\overline{E} + \frac{1}{6}\nabla(Q:\nabla\overline{E}) \quad (2.3)$$

Pohl [18] was one of the first to study the dielectric force, recognize and explore it to be used for the manipulation of particles, particularly living cells. The movement of particles induced by them is called dielectrophoresis (DEP), and the polarization forces are strong enough to move particles towards regions of higher or lower field strength.

The time-averaged DEP force $\langle \overline{F}_{DEP} \rangle$ acting on a particle in an imposed electrical field $\overline{E}(\omega)$, can be approximated in terms of dipole effects from Eq. (2.3) as

$$\langle \overline{F}_{DEP} \rangle = 2\pi\epsilon_m R_s^3 \left\{ \begin{array}{l} \text{Re}(f_{CM}(\omega))\nabla E_{RMS}^2 \\ + \text{Im}(f_{CM}(\omega))(E_x^2\nabla\varphi_x + E_\theta^2\nabla\varphi_\theta + E_\xi^2\nabla\varphi_\xi) \end{array} \right\}, \quad (2.4)$$

where ϵ_m is the dielectric constant of its suspending medium, R_s is the particle radius, and f_{CM} is the dipolar Clausius-Mossotti factor that embodies the frequency-dependent dielectric properties of the particle and its surroundings that give rise to the induced dipole moment \overline{m} in Eq. (2.3), ω is the angular frequency and E_{RMS} is the root-mean-square value of the applied electric field. E_i and φ_i ($i = x, \theta, \xi$) are the magnitudes and phases of the electric field, respectively.

DEP enables electrically-controllable trapping, focusing, translation, fractionation and characterization of particulate mineral, chemical, and biological analyses within

a fluid suspending medium, it helps in developing means to manipulate and discriminate particles and analysis efficiently in microfluidic and micrototal analysis systems. DEP is particularly well suited to applications at the small scales of microfluidic devices, is amenable to integration by inexpensive fabrication methods, is easily and directly interfaced to conventional electronics, and can reduce or eliminate the need for complex, expensive, and potentially unreliable sample manipulation methods involving microfabricated mechanical pumps and valves. Dielectrophoretic forces access a much richer set of particle properties than electrophoresis, because the dielectric properties of a particle depend on both its structure and composition.

DEP has been used in many applications, but the short-range effect of the DEP device requires the electrodes need to be located next the trapping sites. For manipulating particles simultaneous within the microfluidic channel, many electrodes are needed which makes the device more complex. In contrast to DEP, the ultrasonic pressure field acts throughout the whole fluidic volume using a single actuator. In addition, the periodicity of the standing wave field and typical larger wavelength than particle diameter allows particles to be positioned simultaneous in distinct locations.

2.3.5 Capillary force method

From the physical point view, another kind of force capable of being used for individual cells manipulation is the hydrodynamic force. For particle solutions in a capillary cell, the hydrodynamic force is the key factor between the particles and solid surfaces. When a coffee drop evaporates on a table, ring-shaped coffee stains remain on drying [68]. In this case, the boundary between air, solid, and liquid, the contact line, is pinned, that is, immobilized on surface defects. The capillary flows push coffee particles to the boundary. Recently, Vyawahre, Craig and Scherer [20] demonstrated a way to create and control line patterns using capillary flow. In their experiments, they found, under certain conditions, lines are formed instead of rings. Three main conditions are necessary: 1) evaporating solutions between partially wetting surfaces, 2) the presence pinning points, and 3) the presence of foaming surfactants, molecules with a lyophilic or solvent-liking and lyophobic or solvent-repulsing part. Surfactant molecules prefer to aggregate at surfaces and tend to lower surface tension. This process is not very sensitive to concentration, and solutions of

BSA from 10nM to 10mM all formed lines. Higher concentrations render the solution gellike because of an increase in viscosity; low concentrations are too dilute and waterlike, unable to form stable lines. The two surfaces may be peeled apart. This leaves a pattern on one surface that is the mirror of the pattern on the other surface; the lines seem to break at the centre, leaving behind material on each surface with approximately half the height.

The most significant advantage of the capillary method is that there is no external energy consumption during the process. Unfortunately, particles in the resultant patterns are dry, which is not suitable for application to biological investigations. For these reasons, it is worth while to develop this method for cell manipulation. In Chapter 5, a capillary cell which can leave the particle patterns hydrated when process is completed is demonstrated.

Above all, non-contacting methods generally offer higher degrees of controllability, precision and delicateness than contacting methods. Optical tweezers and dielectrophoresis are excellent in single particle manipulation with high spatial accuracy. Magnetic method offers the most cost-effective solution, but the bulky appearance limits the collaboration with other techniques and cause visualisation problem. In contrast to magnetic methods, ultrasonic methods are applied on Lab-on-a-chip techniques with advantages which include simultaneously positioning large groups of particles in the whole microfluidic channel. And the dielectrophoresis enables controllable trapping, focusing, translation, fractionation and characterization of particles within a fluid medium, but the short-range effect of the DEP requires the electrodes to be located next to the trapping site which makes the device more complex. Finally, the capillary force avoids any external energy requirement for particle manipulation. Unfortunately, this method results in particle patterns which are in dry, which is not suitable for biological investigation.

2.4 Conclusions

In this chapter, a review of both contacting and non-contacting approaches of particle manipulation has been presented. The previous studies have reported the non-contacting approaches provide higher controllability, delicateness and precision than contacting approaches. But many methods from the non-contacting approaches require large energy supply, complex setup, bulky and expensive device. The

ultrasonic method is used in lab-on-a-chip investigations. Such experiments can reduce pollution, sample used, energy consumption, and duration time.

Ultrasonic methods provide a wide range of options in device design, material used, actuator chosen, and excitation frequencies applied. Varied one or a combination of some options gives different effectiveness of particle manipulation. In this research project, we have investigated two piezoelectric devices under varied excitation frequencies. A simple two-layer structure is studied in Chapter 3. Two strategies to achieve two-dimensional trapping planes in the microfluidic system are also demonstrated.

Furthermore, a bubble within the ultrasonic standing wave field can be used for particle sorting is discussed in Chapter 4. A combination of the soft medium contacting method and an ultrasonic non-contacting method providing a new effective particle manipulation technique is thereby achieved. The size-based particle sorting by a vibrating bubble is demonstrated depending on the dominant force acting on the particles, as illustrated in Appendix A.

Capillary force method for particle alignment, as discussed in this chapter, requires no external energy during the process. However, this method results in dried particles, which is not suitable for cell manipulation. A capillary cell is designed and demonstrated in Chapter 5, which allows the particles to remain hydrated during the process and when the process is completed. The publication detailing the developments is included in Appendix B.

Additionally, a scheme which is more often used for macro-scale manipulation method, is applied for the first time in micro-scale particle manipulation. This is demonstrated in Chapter 6. This method applying of a water droplet to select floating particles based on sink-float method is a simple, low energy, and highly delicate method. The publication detailing the adaption and developments is in Appendix C, and Appendix D.

In this thesis, the ultrasonic, vibrating bubble, capillary force and sink-float methods are demonstrated and discussed in the following chapters.

Chapter 3

Extending the Ultrasonic Method for Particle Manipulation

3.1 Introduction

Particle manipulation by ultrasonic approaches has been studied for decades. There are a number of reasons which have encouraged researchers to utilise ultrasonic forces. In an ultrasonic system, the acoustic standing wavelength and the particle size would typically differ by two or more orders of magnitude; hence the periodicity of the standing wave field can be used to simultaneously position many particles in several locations. In addition, as the ultrasonic field is present throughout the fluidic volume, it is not necessary to first identify the location of particles prior to handling. Furthermore exposure to large electrical or intense optical fields is not required. Another advantage of using an ultrasonic system is that due to fabrication issues the simplest visual access is obtained through the top of the device. In recent studies, the use of acoustic radiation forces for the manipulation and positioning of micrometer sized particles has been demonstrated [30].

This chapter presents experimental studies of the acoustic radiation forces actuated by a piezoelectric driven device. In Section 3.2, a brief background of acoustic radiation forces and streaming is presented, which provides a theoretical framework of the field. Section 3.3 summarises the varied types of pressure field achieved by researchers based on varied geometry of the device and/or actuation signals. In Section 3.4, a microfluidic channel is designed, modelled and examined over a range of frequencies in this research project. The one-dimensional (1-D) vertical pressure fields in the fluidic channel, i.e. parallel to the side wall, are presented. An advantage of this approach is that due to fabrication issues the simplest visual access is obtained through the top of the device. In addition, two-dimensional (2-D) acoustic planes are investigated using two strategies, switching between two frequencies and rapidly sweeping frequencies.

3.2 Acoustic Forces

The forces in an acoustic field can be categorized into three major types: acoustic radiation forces, secondary forces and drag forces due to acoustic streaming. Acoustic radiation forces arise from the interaction of one object with the surrounding medium, and secondary forces arise between two objects within the medium. Acoustic streaming is the movement of the entire fluid, usually in swirling patterns, which exert forces on particles due to drag. By establishing a relatively high intensity ultrasonic field in a small fluid volume, it is possible to cause any of these effects, the dominance of one over the others will depend on factors such as particle size [69], frequency and system geometry. Here we discuss the acoustic radiation forces and streaming only. The secondary forces, such as secondary Bjerknes forces arising between solid particles, are not considered here, but are discussed in Chapter 4.

3.2.1 Acoustic radiation force

In this section, only acoustic radiation forces arising as a primary force will be considered. This is a second order effect when an ultrasonic wave interacts with a suspended particle. An acoustic standing wave is commonly described as

$$Y = A \cdot \cos\left(\frac{2\pi x}{\lambda}\right) \cdot \sin\left(\frac{2\pi t}{T}\right). \quad (3.1)$$

This equation expresses the displacement (Y) of a point in the standing wave corresponding to a certain position (x) and time (t). The amplitude of the standing wave (A), the wavelength (λ) and the periodic time (T) affects the displacement as well. By looking at the cosine part of the equation it becomes evident that the distance between two consecutive nodes is $\lambda/2$.

When ultrasonic waves impinge on a suspended particle, a force is produced, calculated by integration of momentum terms in the Navier-Stokes equation over the surface of the sphere and time-averaging. The time averaging is important as the oscillations are at high frequency so there is insufficient time for the particle to overcome inertial effects within single cycles; hence no response would be expected from linear terms, however these second order terms are non-zero over a complete cycle, hence a force field exists which is not oscillating. The result is that particles (denser and more compressible than the host fluid) are collected at the pressure minima of the standing wave. Since the ultrasonic wavelength is typically much

larger than the particle diameter, the periodicity of the ultrasonic standing wave field can be used to simultaneously position many particles in distinct locations.

If particles in a liquid are subjected to an ultrasonic field they experience pressure fluctuations. These fluctuations arise from the displacement of the molecules of the medium. If the acoustic field is in the form of a standing wave, the pressure can be written as

$$p = p_0 \cdot \sin(kx) \cdot \cos(\omega t). \quad (3.2)$$

The constants $k = \frac{2\pi}{\lambda}$ and $\omega = \frac{2\pi}{T}$ have been introduced and the phase difference has been omitted since it only results in a lateral displacement of the wave. Sonic acoustic waves in a liquid are longitudinal which means that the particles are displaced along the wave. This results in compression and decompression of the particles in the medium. At the pressure nodes the molecular displacement is at its maximum and at the pressure anti-nodes at its minimum. The pressure fluctuations result in forces that act laterally on the particles in the x-direction. According to the acoustic force theory presented by Yosioka and Kawasima [70] the force on a particle can be expressed in the following way:

$$F_r = -\left(\frac{\pi p_0^2 V_S \beta_F}{2\lambda}\right) \cdot \phi_c(\beta, \rho) \cdot \sin(2kx), \quad (3.3)$$

$$\phi_c = \frac{5\rho_S - 2\rho_F}{2\rho_S + \rho_F} - \frac{\beta_S}{\beta_F}, \quad (3.4)$$

where V_S is the volume of the particle, p_0 is the pressure amplitude from Eq. (3.2) and ϕ_c is defined by Eq. (3.4). The density of the particle and medium are denoted ρ_S and ρ_F respectively and the corresponding compressibility β_S and β_F . Small particles can generally be trapped in an acoustic standing wave. The first criterion is that the particle diameter must be less than half the wavelength for this analysis to hold. The second criterion is that ϕ_c must not equal to zero, otherwise there will be no net force exerted on the particle.

To predict the location where the particles are trapped in a multidimensional field, the Yosioka and Kawasima's theory, restricted as it is to 1-D, cannot be applied. Here the more comprehensive description by Gor'kov [51] has to be used. The ultrasonic wave, a pressure wave within a compressible fluid oscillating at high frequency (>20 kHz), can simply propagate through the fluid, or more usually for this application be

multiply reflected and result in a standing wave when a suitable resonant frequency is selected. The advantage of the second scenario is that large amplitudes and hence forces can be achieved.

The time average force acting on a particle of radius R_s can be expressed as the negative gradient of a force potential U as has been define by Gor'kov [51]:

$$\langle F \rangle = -\nabla U = -\nabla \left[2\pi R_s^3 \rho_F \left(\frac{1}{3} \frac{\langle p^2 \rangle}{\rho_F^2 C_F^2} f_1 - \frac{1}{2} \langle v^2 \rangle f_2 \right) \right], \quad (3.5)$$

where $f_1 = 1 - \frac{\rho_F C_F^2}{\rho_S C_S^2}$, and $f_2 = \frac{2(\rho_S - \rho_F)}{2\rho_S + \rho_F}$; ρ is the density and C the speed of sound in the particle(S) and in the fluid(F). The $\nabla \langle p^2 \rangle$ term and $\nabla \langle v^2 \rangle$ represent the spatial gradients of the time average pressure and fluid velocity fluctuation and can be interpreted as spatial gradients of the time average kinetic and potential energies.

To compare the force predicted by Yosiola and Kawasima's theory Eq. (3.3) and Gor'kov Eq. (3.5), firstly, taking the time-average of p^2 defined by Eq. (3.2), gives:

$$\langle p^2 \rangle = \frac{1}{2} p_0^2 \sin^2(kx). \quad (3.6)$$

Calculating $\langle v^2 \rangle$ from governing the following equations:

$$\begin{aligned} \Phi &= \frac{1}{\rho} \int p dt = \frac{p_0}{\rho \omega} \sin(kx) \sin(\omega t), \\ v &= -\nabla \Phi = -\frac{kp_0}{\rho \omega} \cos(kx) \sin(\omega t), \\ \langle v^2 \rangle &= \frac{k^2 p_0^2}{2\rho^2 \omega^2} \cos^2(kx). \end{aligned} \quad (3.7)$$

On substituting Eqs. (3.6) & (3.7) into Eq. (3.5), we get:

$$\langle F \rangle = -\frac{1}{3} k \pi R_s^3 p_0^2 \left(\frac{1}{\rho_F^2 C_F^2} f_1 + \frac{3k^2}{2\rho^2 \omega^2} f_2 \right) \cdot \sin(2kx). \quad (3.8)$$

Finally, expressed Eq. (3.8) in terms of β and ρ by substituting $f_1 = 1 - \frac{\rho_F C_F^2}{\rho_S C_S^2}$,

$$f_2 = \frac{2(\rho_S - \rho_F)}{2\rho_S + \rho_F} \text{ and } C = (\beta\rho)^{-\frac{1}{2}} = \frac{\omega}{k}, \text{ leads to:}$$

$$\langle F \rangle = -\frac{1}{3}k\pi r^3 p_0^2 \left[\beta_F \left(\frac{5\rho_S - 2\rho_F}{2\rho_S + \rho_F} - \frac{\beta_S}{\beta_F} \right) \right] \cdot \sin(2kx). \quad (3.9)$$

On the other hand, expressed Eq. (3.3) by substituting $V_c = \frac{4}{3}\pi r^3$ and $\lambda = \frac{2\pi}{k}$, gives:

$$F_r = -\frac{1}{3}k\pi p_0^2 r^3 \beta_F \cdot \phi(\beta, \rho) \cdot \sin(2kx), \quad (3.10)$$

$$\text{where } \phi(\beta, \rho) = \left(\frac{5\rho_S - 2\rho_F}{2\rho_S + \rho_F} - \frac{\beta_S}{\beta_F} \right).$$

Thus we obtain the same expression of acoustic radiation force equation based on Yosiola and Kawasima's theory and Gor'kov respectively, and demonstrate how Gor'kov's expression can be used.

3.2.2 Acoustic streaming

From previous studies, it has become clear that streaming is fairly weak compared to the much stronger acoustic radiation forces (ARF) within enclosed channels. However, streaming might be the limiting factor for the possibility to separate sub-micrometer particles, as the drag forces it induced become more significant when compared to ARF for small particles. Acoustic radiation force is proportional to the cube of the particle radius. Hence, for a large particle, acoustic radiation force is the dominant force; while for a small particle (usually $\leq 1 \mu\text{m}$), acoustic streaming is the dominant force.

Acoustic streaming is the bulk fluid flow arising due to acoustic vibration. Basic equations are governed from the Navier-Stokes equation by considering a small volume [71]. The force balance equation is given:

$$F_s = \rho \left[\frac{\partial v}{\partial t} + (v \cdot \nabla)v \right]. \quad (3.11)$$

And if the fluid is subject to shear and bulk viscosity:

$$F_s = -\nabla P + \left[\mu' + \frac{4}{3}\mu \right] \nabla \nabla \cdot v - \mu \nabla \times \nabla \times v. \quad (3.12)$$

The well known equation of continuity is expressed as:

$$\frac{\partial \rho}{\partial t} + \nabla \cdot \rho v = 0. \quad (3.13)$$

Combining Eqs. (3.11) and (3.13), this gives:

$$F_s = \frac{\partial(\rho v)}{\partial t} + \rho(v \cdot \nabla)v + v \nabla \cdot \rho v. \quad (3.14)$$

In order to cause a bulk flow of the fluid, time independent terms are required rather than terms varying at frequencies. These can be obtained by time averaging:

$$\langle X \rangle = \frac{1}{T} \int_0^T X dt, \text{ where } T = \frac{2\pi}{\omega}.$$

For $x = \sin(\omega t)$, $x^2 = \sin^2(\omega t) = \frac{1}{2}[1 - \cos(2\omega t)]$, and

$x \frac{\partial x}{\partial t} = \sin(\omega t) \cos(\omega t) = \frac{1}{2} \sin(2\omega t)$, the first order harmonic terms time-averaged is

zero. Therefore, Eq. (3.12) expresses up to second order and time-averaged:

$$\langle F_s \rangle = -\nabla P_2 + \left[\mu' + \frac{4}{3} \mu \right] \nabla \nabla \cdot v_2 - \mu \nabla \times \nabla \times v_2. \quad (3.15)$$

The ∇P_2 term in Eq. (3.15) presents the streaming pressure, while v_2 presents streaming flow. The force $\langle F_s \rangle$ is given by expressing Eq. (3.14) to second order and the time-averaged as:

$$\langle F_s \rangle = \left\langle \frac{\partial(\rho_0 v_2 + \rho_1 v_1)}{\partial t} + \rho_0 (v_1 \cdot \nabla) v_1 + v_1 \nabla \cdot \rho_0 v_1 \right\rangle = \langle \rho_0 (v_1 \cdot \nabla) v_1 + v_1 \nabla \cdot \rho_0 v_1 \rangle. \quad (3.16)$$

Furthermore, from the previous studies, there is no direct relation between the strength of acoustic streaming and acoustic radiation force [69]. This is indicated by investigating both circular and square chambers using full-image micro-PIV (Particle Image Velocimetry) analysis under acoustically resonant excitations. For the large beads (5 μm), the acoustic radiation force dominates exactly in both chambers. An inhomogeneity in the strength of the streaming vortices across the square microfluidic chamber was observed when a slightly shifted resonant frequency was applied. However, the same inhomogeneity was not seen in the acoustic radiation force vector plot.

3.3 Degrees of Pressure Field

Besides the acoustic forces presented on the particles, spatial control due to pressure planes is also a key factor for particle manipulation. A plane of standing wave field arises from the superposition of two waves of equal wavelength and amplitude travelling in opposite directions. The interference between the waves results in the formation of parallel stationary planes of maximum pressure amplitude (antinode

planes) and zero pressure amplitude (node planes) [72]. These two travelling waves are coupled by the original acoustic wave and its reflection by the side walls. Therefore, the factors affecting the degrees of pressure field achieved in the acoustic device include: the device dimensionality, the transducer types and the excitation frequencies applied.

Generally, the relationship between fluid restrictions and the dimensionality of the field/device limits the degrees of the pressure field, as seen in Fig. 3.1. A one-dimensional (1-D) trapping plane such that isolated lines (when viewed from above) are observed, can be generated in a microfluidic channel [16]. As seen in Fig. 3.1 (a), the ultrasound frequency matches half of the wavelength to the channel width, which results in a pressure nodal plane along the centre of the channel. Such device has been studied and applied in particle separation applications [3, 14, 73, 74]. Lipid vesicles as focused at the pressure antinodes were separated from erythrocytes which gathered in the pressure node [3]. Furthermore, increasing excitation frequencies to match 1st, 2nd, and 3rd harmonic mode of the device, two, three and four particle bands can be observed [14].

By adding another two side walls, a chamber (usually the depth of the chamber is not larger than half the wavelength) has been widely used for achieving a two-dimensional (2-D) pressure field, as seen in Fig. 3.1 (b). A half-wavelength thick fluidic chamber has been investigated by Townsend *et al.* for a 2-D modal analysis [75]. The lateral forces due to lateral variations in the acoustic field by the geometry and materials can result a 2-D pressure field by coupling with the axial radiation force effect.

Other methods to generate a 2-D pressure field include applying a pair of ultrasonic transducers attached on the chamber as demonstrated by Saito *et al.* [76, 77]. In their investigations, two transducers were attached on both the top and bottom of the chamber. Microorganisms were trapped at the intersections of the nodes in the two orthogonal standing waves at 3.1 MHz. In contrast to the two transducers conducted devices, one piezoelectric plate with two orthogonally aligned strips electrodes defined on the surface was examined by Neild *et al.* [78] to achieve 2-D manipulation. As a result, a diagonally aligned grid of cells were observed in the microfluidic chamber when two electrodes actuated by two similar signals (2.6 MHz and 2.6 MHz+10 Hz).

In contrast to the use of piezoelectric transducers, wedge transducers have also been investigated for 2-D particle manipulation. Manneberg *et al.* [62, 63, 79] have studied ultrasonic manipulation in microfluidic chip based on oblique coupling of ultrasound from external transducers combined with refractive wedges. Two-dimensional continuous alignment of particles based on combining horizontal (focusing) and vertical (levitation) was demonstrated. Alternatively, flow-free particle transport along a microchannel was demonstrated by combining rapid frequency sweeping for stabilized particle alignment in 2-D (6.90-7.00 MHz; rate 1 kHz), and slow frequency sweeping (2.60-2.64 MHz; rate 0.5 Hz) [79].

Instead of sweeping the device frequency, trapping and moving particles at arbitrary positions has also been shown by varying the relative phase of two applied signal [60]. In the experiments, three transducers were attached to the device with one located horizontally and the other two were vertically facing each other. On the one hand, a grid pattern is induced by the orthogonal arranged piezoelectric transducers. On the other hand, the phase difference which generated by the facing transducers control the nodal positions which can result in particles movement.

Three-dimensional (3-D) trapping planes can also be generated by using ultrasonic method in a cage, as seen in Fig. 3.1 (c). A designed 3-D resonant cage was demonstrated to enrich, control aggregation, and manipulate of microparticles and cells by Manneberg *et al.* [62]. The ultrasonic cage was simultaneously excited at two different frequencies corresponding to half wavelength resonances in three orthogonal directions. Therefore, individual particles can be trapped three dimensionally. Wedges were used to actuate the fluidic chamber in their investigation which is further discussed in the next section.

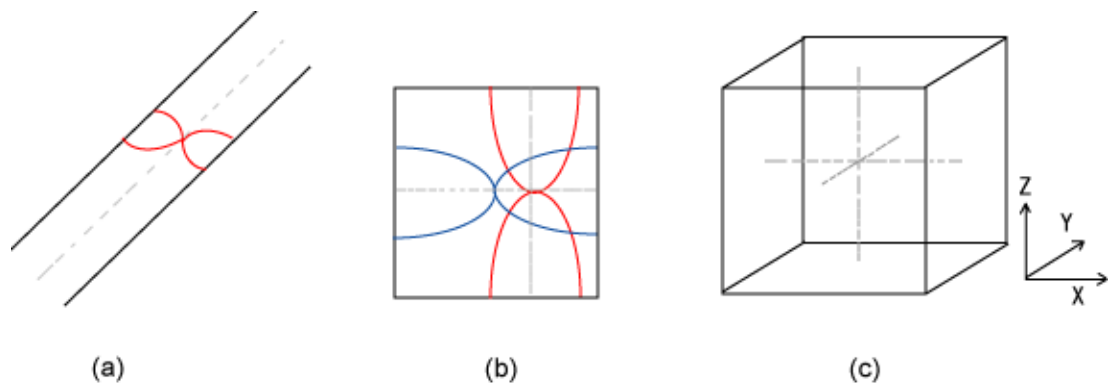


Figure 3.1: Schematic description of pressure field generated in: (a) 1D channel, (b) 2D chamber, and (c) 3D cage. Grey dash lines indicate the pressure nodes.

Moreover, frequency-modulated ultrasonic actuation can break the fluid restrictions and the dimensionality of the field relationship. Therefore, it is possible to generate a 2-D pressure field in a microfluidic channel. One way to achieve that is when different frequencies are applied (1.97 MHz and 6.90 MHz). Manneberg *et al.* [61] demonstrated a 2-D manipulation generated by coupling two orthogonal standing wave actuated by two wedges attached to the fluidic channel. Therefore, the orthogonal components of the generated 2-D field are strongly coupled and the result is an unpredictable and/or complicated pattern of the manipulated particles. The other way to achieve 2-D field based on the frequency-modulated is to apply linear frequency sweeping. Manneberg *et al.* [79] demonstrated a slow (0.2-0.7 Hz) linear frequency sweep around 2.6 MHz for particle transport in a flow-free microfluidic channel. A degree of constraint on particle motion in the length direction of the channel is added, so a 2-D field is achieved.

Above all, a 2-D ultrasonic field can be generated in a microfluidic chamber when two orthogonal standing waves presented, no matter if the waves are generated by two actuators or two electrodes. Furthermore, frequency sweeping is also a suitable method to add a degree on the particle movement along the channel. Here we present a more complicated force field by exciting one electrode in a microfluidic channel which usually generates 1-D field.

3.4 Development of Ultrasonic Manipulation Techniques

Application of ultrasonic standing waves to microfluidic systems began by using one-dimensional fields, orientated such that isolated lines (perpendicular planes seen from above) can be observed [16]. However, it is also possible to obtain more complicated ultrasonic fields. In this research project, a piezoelectric actuated microfluidic channel has been investigated for particle manipulation. In this section, both 1-D and 2-D ultrasonic fields which are observed in the same microfluidic system are discussed.

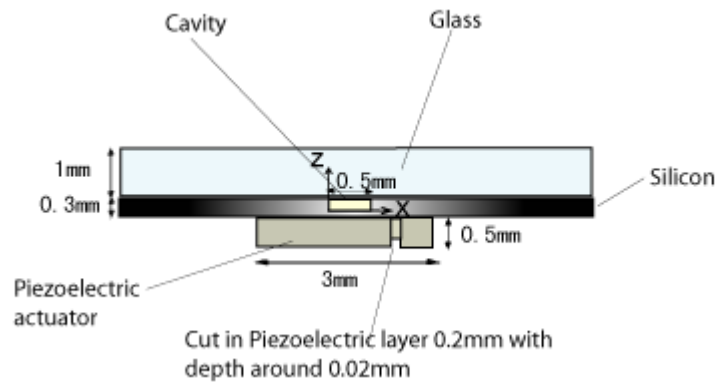
By putting a droplet of the solution at one of the ends of the channel, the channel is filled by capillary forces. The fluid used was distilled water with copolymer particles of 6 μm diameter (density = 1050 kg/m^3). Three resonant frequencies found for forming isolated lines were discussed in Section 3.3.3. More complicated 2-D ultrasonic fields were discussed in Section 3.3.4.

3.4.1 Piezoelectric device and experimental setup

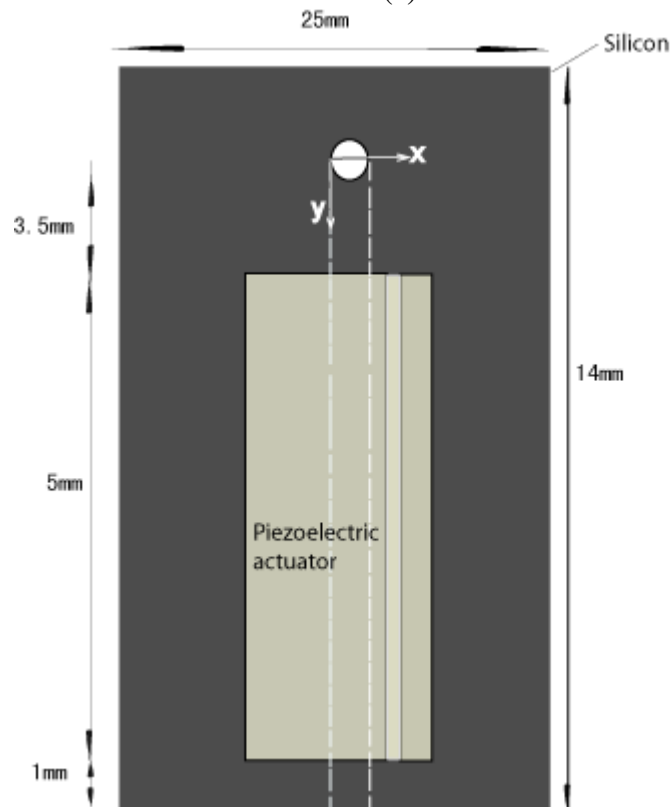
Acoustic manipulators in microfluidic channels, with both flowing fluid and non-flowing fluid, have been used. An etched silicon substrate bonded to a glass wafer, and subsequent adhesion of a piezoelectric actuator with electrode shapes designed to excite the modes required formed the device [15-17]. The anisotropic deep reactive-ion etching (DRIE) properties of silicon provide a low surface roughness, furthermore this micro machinery process offers a high accuracy and so good wall alignment is easily achieved (far better repeatability than a coalitional fabrication method in offer). Advantages of this design also include the visual access from above the device, easy manufacture and processing.

A similar silicon-glass micro-positioning device is introduced here with non-flowing fluid. Details of the device, with dimensions, are shown in Fig. 3.2. It consists of a 1mm thick piece of glass, which is adhered to a deep reactive ion etching etched silicon wafer, such that a channel is formed with a cross-section of 0.5×0.2 mm. This channel contains the fluid and particles. The silicon wafer is 0.3 mm thick. On the underside of the silicon wafer, a 0.5 mm thick piezoelectric plate is attached. The device was made by a collaborator in ETH Zurich, using their cleanroom facilities.

A 5mm long piece of piezoelectric is used to excite the channel. The electrode on the underside of the piezoelectric plate is cut. The signal is then applied to this strip and the rest of the bottom electrode and the upper electrode are grounded. When a signal is applied, a wave propagates along the plate consisting of the piezoelectric itself and the 0.1 mm silicon layer to which it is attached. This wave couples to the water and so the system is set into vibration. A strong field occurs over the short length of the channel covered by the piezoelectric, which gives a rise to a localised minimum in the force potential. The 14 mm long device is supported at one end.



(a)



(b)

Figure 3.2: Schematic view of the micro-positioning device: (a) 2-D cross-sectional device with dimensions; and (b) bottom view, where the dash lines show the channel location. Dimension not to scale.

3.4.2 Device simulation results

Numerical modelling of the device has been performed by a fellow group member using COMSOL in order to simulate its acoustic behaviour as a result of the electrical excitation of the piezoelectric transducer. In this way it can be determined under which conditions a resonant pressure field can be established in the channel. The pressure field can be studied and hence conclusions about its suitability for the particle manipulation can be formed. A normal acceleration to the channel wall and a

pressure based force were applied to the interfaces to set the boundary condition in the simulation. Instead of presenting data over the cross section of the channel (2-D simulation), a 1-D data set taken from the bottom line of the cross section is presented. Figure 3.3 shows the pressure field within the fluid layer, at a range of frequencies. The colour indicates the pressure variation with minimum value in dark blue and maximum in red. Within this frequency range the pressure field within the fluid is essentially 1-D varying only in the x -direction (across the channel width). It can be seen that the resonant frequency (frequency at which the amplitude of the pressure variation in the fluid is greatest, which is shown as red line near the channel edges) is 1.33 MHz.

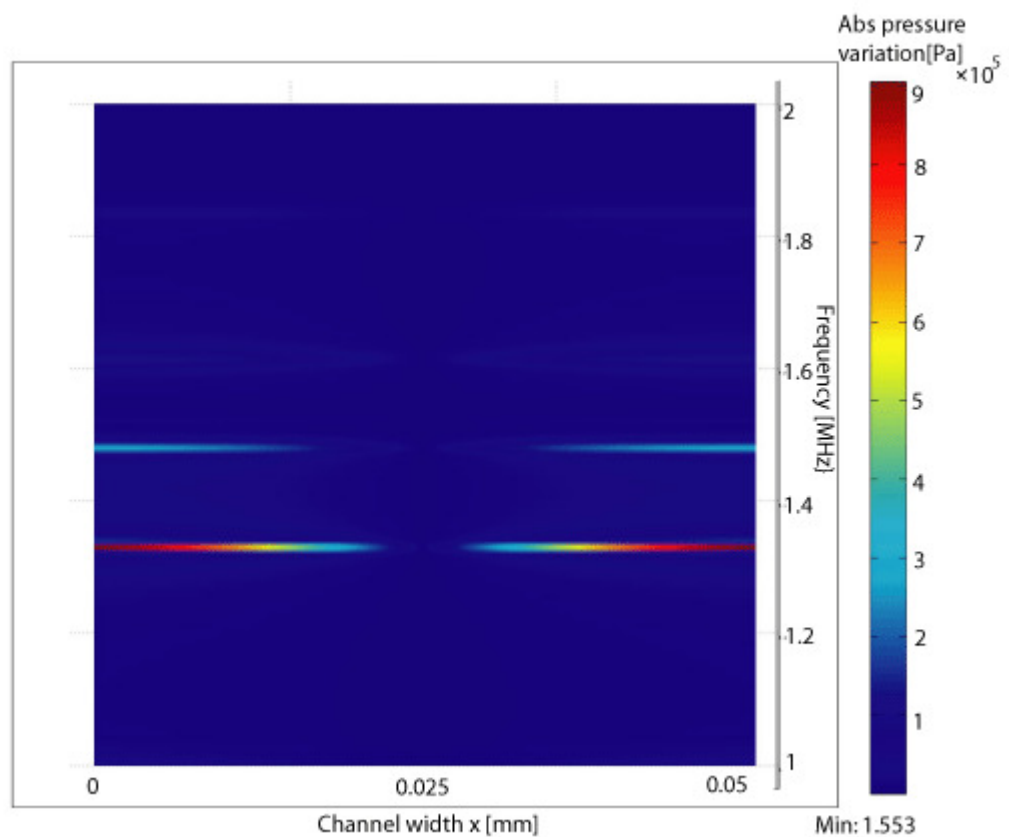


Figure 3.3: Simulation of the pressure field within the fluid layer: the data being calculated along a line across the lower edge of the chamber (x -axis) at a range of frequencies (y -axis).

3.4.3 One-dimensional fields

In one series of experiments, with the channel filled by 6 μm particles solution, the frequency applied was slowly increased over a range of 1.27-1.49 MHz, in steps of 1 kHz. It was clearly observed that a better line was formed within the channel at the central location, when the excitation frequency of 1.305 MHz was applied. In the other series of experiments with smaller steps in the same frequency range, a better

line was obtained in the range of 1.305-1.308 MHz. This experimental result is in reasonable agreement with the simulation result which predicted 1.33 MHz. Further investigation of the pressure field with the channel under different frequencies, showed two lines being formed at 2.66 MHz, and three particle lines were observed at 4.17 MHz. All the experiments were done by using a 20 V amplitude signal, and lines were formed within a few seconds. If a simple model is used, in which the resonances are predicted by considering just the wave propagation in the fluid in the horizontal direction, which means if the chamber is assumed to be a certain number of half wavelengths wide, then the frequencies which would be predicted for one, two and three lines are 1.48 MHz, 2.96 MHz, 4.49 MHz. It can be seen that such a simplified model is insufficient.

Figure 3.4 shows images of 6 μm particles which have been positioned within the chamber, in each case the images are in the xy-plane as defined in Fig. 3.2. Figure 3.4 (left) shows the image taken when the device was driven with a 20 V amplitude signal at 1.305 MHz, when one vertically orientated line was observed. Figure 3.4 (middle) shows the image taken when the device was driven at 2.66 MHz, when two vertically orientated lines were observed. Figure 3.4 (right) shows the image taken when the device was driven at 4.17 MHz, when three vertically orientated lines were observed. On both sides of the image, the dark strip is un-etched silicon viewed through the glass. At the edges of the channel the bright lines are particles which are stuck to the walls of the channel.

As discussed previously, in the acoustic field both acoustic radiation force and streaming exist. For large particles, acoustic radiation force is the dominant force, while for small particles acoustic streaming is the dominant force. To demonstrate this, a series of experiments were performed in which the device was driven at 1.305 MHz with both 6 and 1.9 μm particles present in the channel, both acoustic radiation force and acoustic streaming are observed, as shown in Fig. 3.5. The 6 μm particles as in Fig. 3.5 (b), the acoustic radiation force dominates exactly as in Fig. 3.4 (left), which results in particle accumulation at the pressure nodal lines. The motion of the smaller particles of 1.9 μm is dominated by the acoustic streaming of the water.

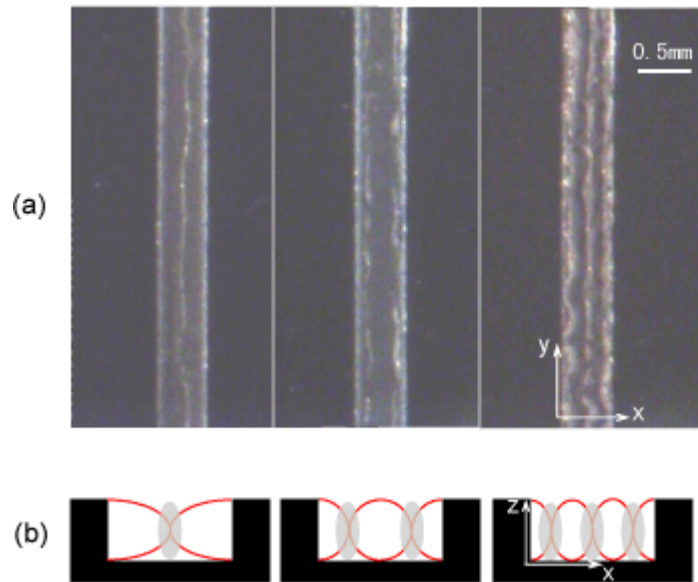


Figure 3.4: Particle enrichment in the microfluidic channel. The bands show the enriched particles in resonance mode, fundamental, 1st and 2nd harmonic with 1, 2 and 3 bands respectively, (a) top view microscope photographs and b) schematic description of channel cross-sections.

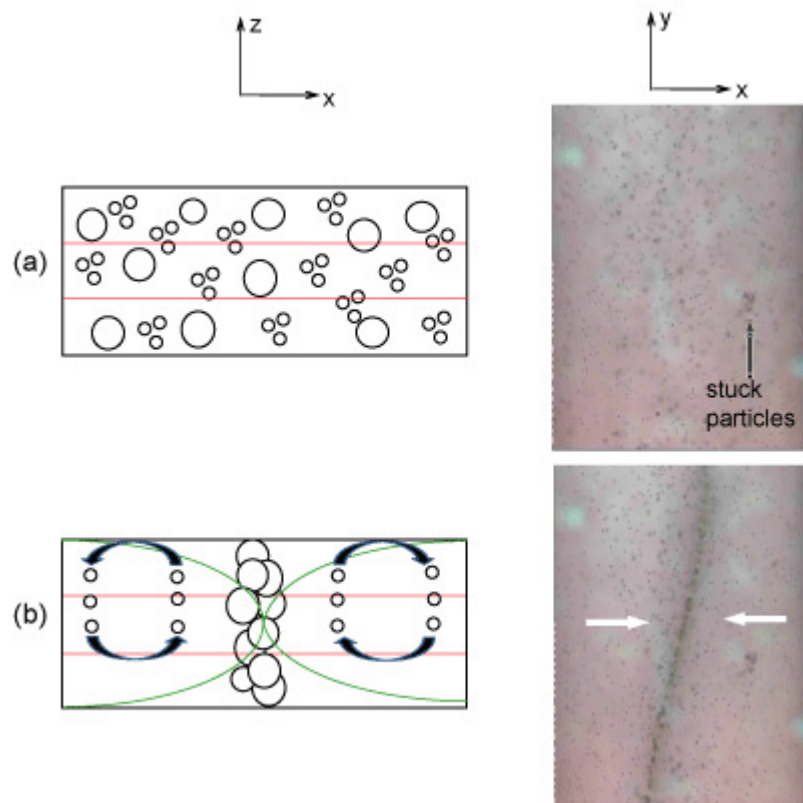


Figure 3.5: Schematic description of the cross section view of the channel and the corresponding experimental images from the top view: (a) 6 μm and 1.9 μm particles full filled the channel before any excitation frequency applied, (b) 6 μm particles forming one line (white arrows indicate the acoustic radiation force direction), while 1.9 μm particles swirling at both sides of the line when frequency of 1.305 MHz was applied.

In order to investigate the motion of the streaming which occurred in the acoustic field, a strategy of using different focusing planes was applied. Figure 3.6 (a) shows the images taken from the top layer of the channel, the images are one second apart. The dark dots (indicated by the black arrow) are a few 6 μm particles which have stuck on the glass surface. The line formed by the 6 μm particles appears as a dark shadow along the centre of the image. This is caused by the particles sinking down to the channel bottom due to gravity. The 1.9 μm particles which were affected mostly by the streaming were moved away from the line; and two vortex patterns along each side of the line were visible. The motion of the 1.9 μm particles is not clear from the images as the 1.9 μm particles are much smaller compared to 6 μm particles. This motion is clearly visible from the video taken of the experiment, by way of showing the effect using still images, we use a blue box to trace the 1.9 μm particle movement. The 1.9 μm particles inside the blue box are highlighted to compensate for the visual problem caused by size reduction and poor print quality. The blue boxes remain static across the images to allow easy comparison. From the top layer of the channel, as shown in Fig. 3.6 (a), particles inside the blue box are moving leftwards, as the particles are much closer to the left edge of the box one second later. The streaming orientation is opposite to the acoustic radiation force direction as indicated by the red arrows. While from the middle layer of the channel, as shown in Fig. 3.6 (b), 1.9 μm particles are moving towards to the pressure nodes, which has the same direction as the acoustic radiation force. Again, the particle motion is shown by using a blue box. The swirling motion of the acoustic streaming is confirmed.

Additionally, from the experiments, the acoustic radiation force on the large particles leads to a much larger particle velocity than the acoustic streaming velocities of the smaller particles. More investigations of the acoustic streaming have been done by using another ultrasonic device with different geometry; this will be discussed in Chapter 4.

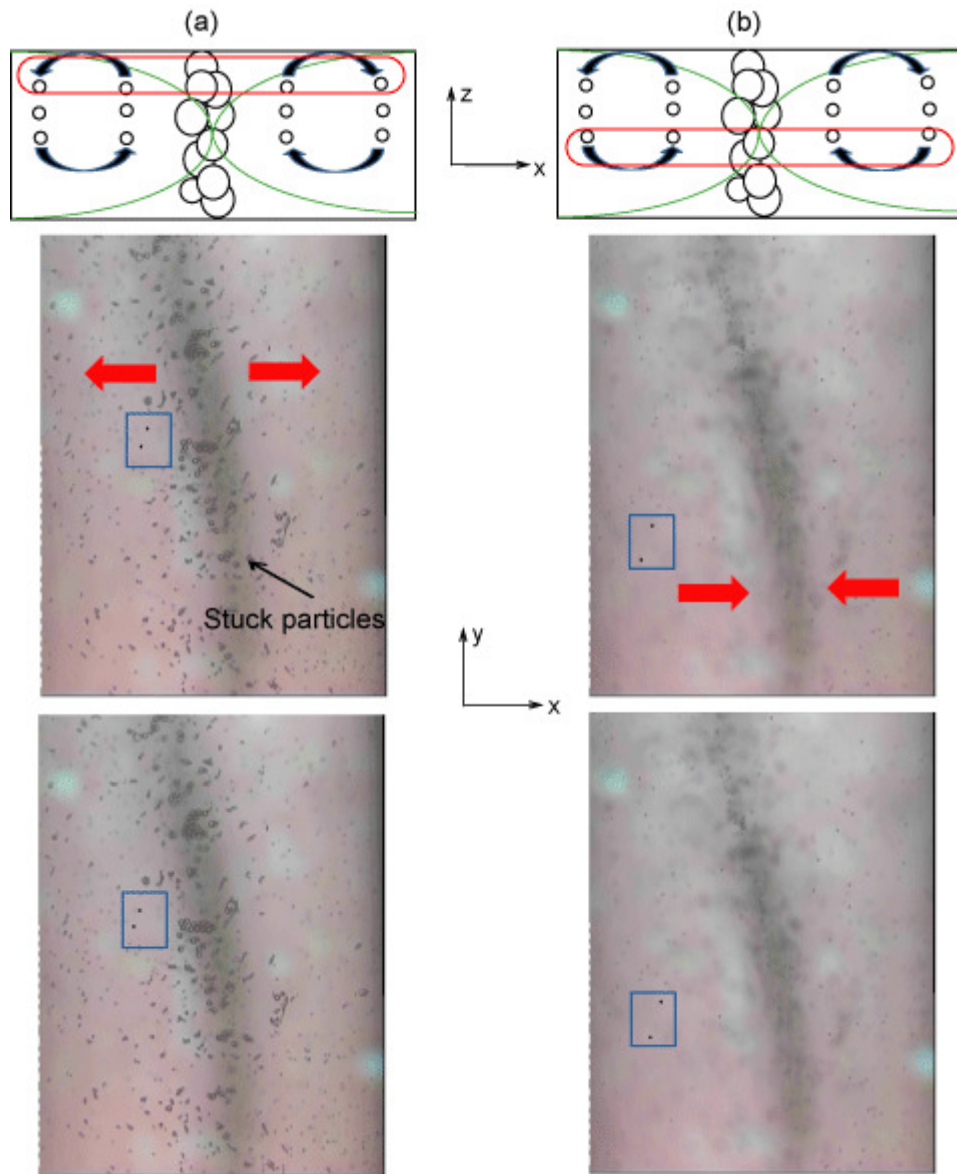


Figure 3.6: Schematic description of the cross section view of the channel and the corresponding experimental images from the top view by varying focusing plane: (a) the focusing plane is at top layer of the channel, $1.9 \mu\text{m}$ particles are moving outwards from the pressure nodes; (b) the focusing plane is at middle layer of the channel, $1.9 \mu\text{m}$ particles are moving towards to the pressure nodes.

Images are one second apart. Red circle indicates the focal plane.

The frequency range of well above that required to form one line has been studied by other researchers using similar devices [14-16, 80]. With this device, the frequency range of 0.9-1.3 MHz was examined, which is below the single line frequency. The expectation was that little movement would be observed across the channel, however along the length of the channel clear vertically orientated particle clusters formed. This is caused by the resonance which exists along the channel instead of crossing the channel as it is less than the width ($w = \frac{\lambda}{2}$). The particles indicate the locations

of minimum force potential. Figure 3.7 shows the image when a 0.98 MHz excitation frequency was applied. The particle clusters, which are across the channel, are parallel to each other with a uniform separation distance.

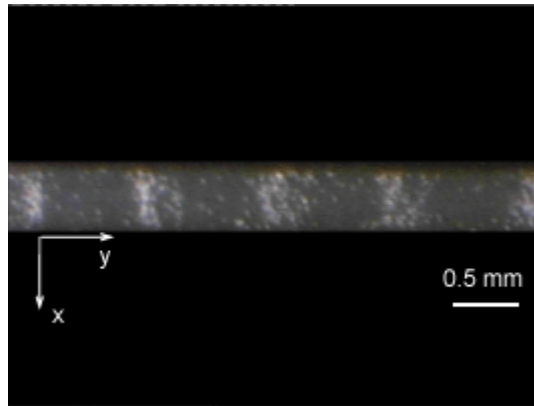


Figure 3.7: Image of lines across the channel width that particles formed at 0.98 MHz in a non-flowing fluid volume.

Both 1-D fields achieved in the experiments are vertical planes. The particle lines are presented in the yz -plane (perpendicular to the channel bottom and along the channel), while the particle clusters are presented in the xz -plane (perpendicular to the channel bottom and across the channel, also refer to Fig. 3.2).

3.4.4 Two-dimensional fields

Most recently, Glynne-Jones *et al.* [81] reported a new technique to achieve the controllable agglomeration position in a multi-mode chamber. Such technique uses mode-switching between the half and quarter-wave mode. Particles are able to be positioned between the half and quarter-wave node position by controlling the percentage of the quarter-wave mode used. Notably, the source mode which includes the half and quarter-wave mode, and the resulted mode provide 1-D field which is parallel to the transducer.

In contrast, we have investigated 2-D particle manipulation by using mode-switching between two 1-D source modes.

Switching between resonant frequency method

From the previous investigation, we found that particles can be focused at the centre of the channel (horizontally in xz -plane) to form one line at 1.305 MHz; while particles can be concentrated across the channel (vertically in xz -plane) to form

clusters at 0.98 MHz. By combining these two focusing forces, a 2-D manipulation field can be generated. Instead of applying two signals as reported by Neild *et al.* [78], one signal actuator was studied. In order to have the same effect as two signals applied, switching the frequencies between 1.305 MHz and 0.98 MHz in a suitable rate was studied. As a result, a 2-D field was successfully achieved.

Figure 3.8 shows a series of images taken when the device was driven by switching the frequency between 1.305 MHz and 0.98 MHz every 2 seconds. The transducer was actuated from 10 seconds at 1.305 MHz, one particle line was observed at the centre of the channel. By switching the frequency between 1.305 MHz and 0.98 MHz, particles started to move horizontally (in xz-plane), to form clumps. This was clearly observed after 22 seconds. Continually switched the frequency between 1.305 MHz and 0.98 MHz constantly, an array of dots allocated at the middle of the channel with uniform distance to each other was obtained. This shows the ability to position particles in distinct point location.

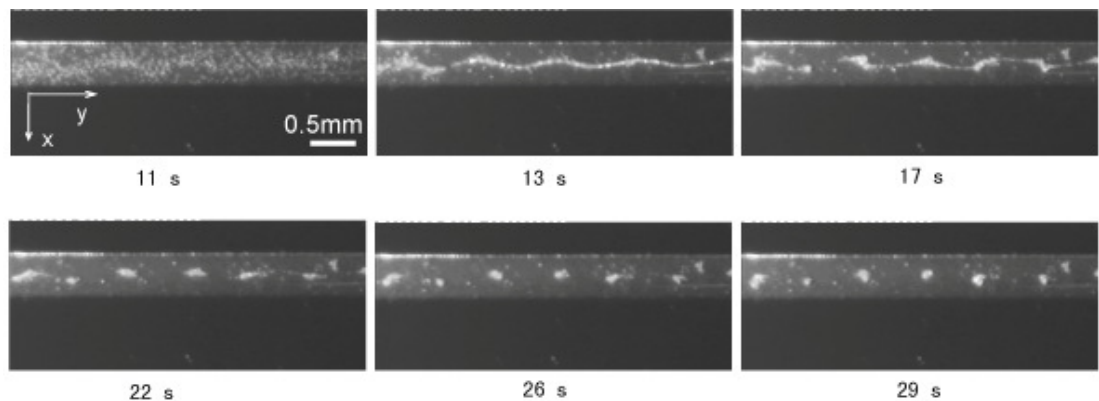


Figure 3.8: Image sequences of particle movement when frequency switching between 1.305 MHz and 0.98 MHz.

Rapid frequency sweeping method

An alternative method to the strategy used above, aimed at achieving 2-D manipulation field is by sweeping frequencies [79]. Unexpectedly, at 0.87 MHz, two particle lines were observed along the channel. Later investigation was shown that this is caused by the distortion of the signal from the amplifier. Figure 3.9 is the FFT of the response frequency of 0.87 MHz from the signal amplifier during the experiment. From the FFT diagram, the second harmonic resonance frequency of 2.6

MHz is observed, which gives the effect of two lines formed along the channel. This explains why we obtained two particle lines at frequency of 0.87 MHz.

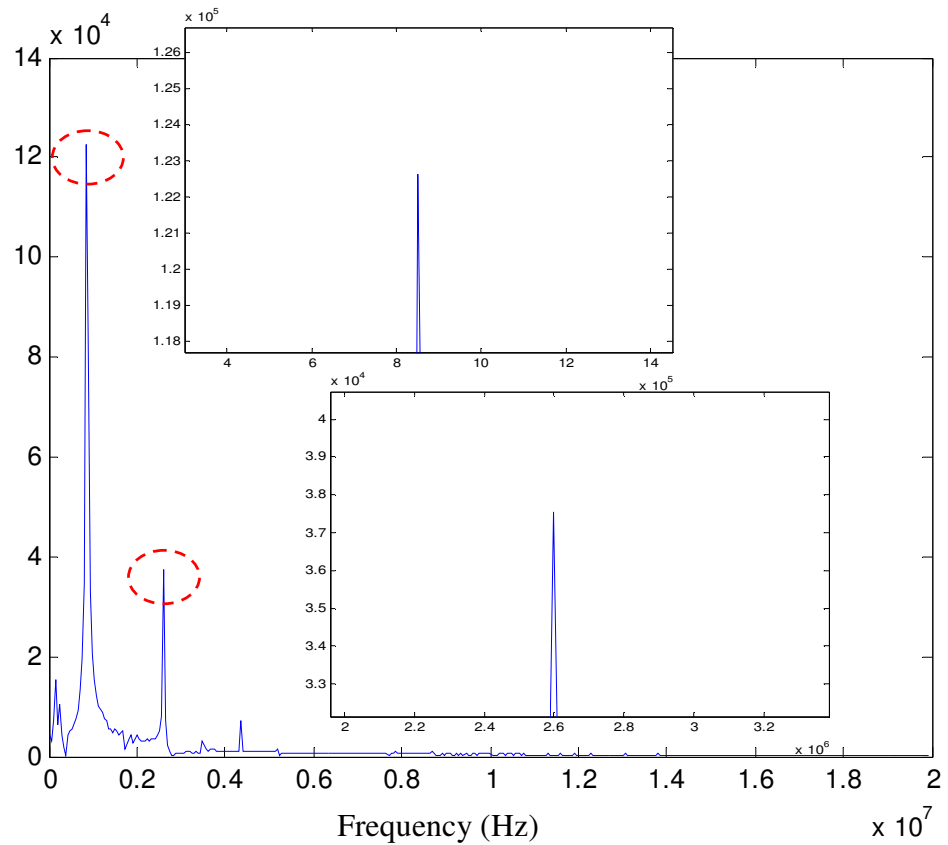


Figure 3.9: FFT of the response frequency of 0.87 MHz.

To illustrate how the rapid frequency sweeping method can generate a 2-D acoustic field, the particle patterns are shown in Fig. 3.10 at 10s. Applying a 20 V amplitude signal at 0.87 MHz, particles have been collected into lines, as shown in Fig. 3.10 at 62s. Here a longer time required to form lines is noticed. This is because the device was under second harmonic resonance; the acoustic radiation force was weaker than in the case when 2.6 MHz actuation frequency was applied.

Sweeping with a rate of 1 kHz, particles started to move into the lowest potential position (pressure nodes), as shown in Fig. 3.10 at 78s. Continuously sweeping frequency, particles kept moving into the pressure nodes and formed circular shaped clumps, as shown in Fig. 3.10 at 86s. Eight dots formed in 2×4 arrays in the xy-plane, and were observed until 0.98 MHz was achieved.

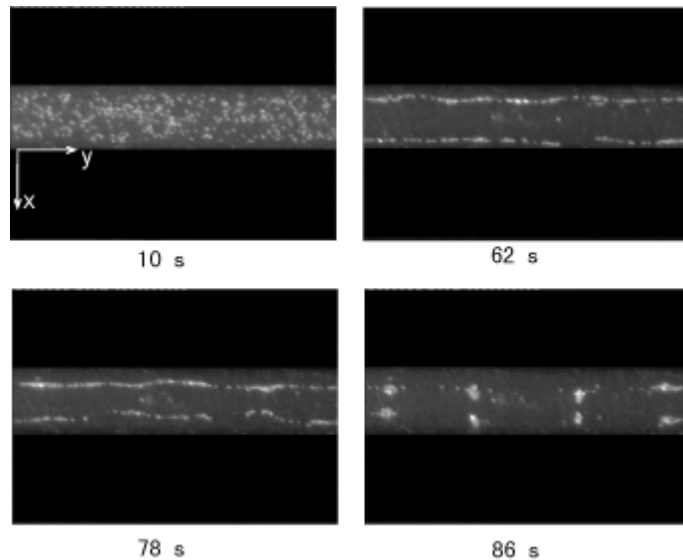


Figure 3.10: Image sequences of the process of clumps formation: starting with particles randomly distributed in the channel. A 20 V amplitude signal at 0.87 MHz has been applied to a signal transducer. Later, particles formed clumps by rapid sweeping frequency to 0.98 MHz.

Above all, 2-D fields have been created to cluster particles within a microfluidic channel excited by a piezoelectric device. One array of particle clusters is achieved by applying switching frequencies between 1.305 MHz and 0.98 MHz. Furthermore, two arrays of particle clusters are achieved by rapidly sweeping frequency from 0.87 MHz to 0.98 MHz. Both strategies for achieving 2-D fields are resulted in the combination of two vertical planes, xz -plane and yz -plane. Besides that, a 2-D field of focusing (xz -plane) and elevating (xy -plane) can also be created by this device, discussed in the next section.

3.4.5 Particles levitation from the bottom of the channel

Most of the previous studies reported that near-one-dimensional ultrasonic fields are focusing particles into vertically oriented pressure node plates of the standing wave. However, a less desired effect with this arrangement is that the particles settle to the bottom of the chamber due to gravity. In pressure-driven flows with near-parabolic flow profiles, the results is a large variation in particle speeds and a significantly increased risk of adhesion of particles or cells to the channel surfaces that may cause problems such as sample loss, sample contamination and channel clogging. In the discussion of strategies to achieve 2-D particle manipulation, Manneberg *et al.* [61-63, 79] have reported a combination of focusing and levitation can be generated by using wedges. This gives one solution to the problem. In this part of research, we investigated a possible way to achieve a 2-D field by combing the levitation plate with the focusing plate by a single transducer actuated resonator.

Experiments of varying frequencies from 2.4 MHz to 2.8 MHz have been done in two sweeping rate, 1 kHz per 0.28 second and 5 kHz per 2 seconds. Applying excitation frequency range from 2.4 MHz to 2.64 MHz, particles formed patterns under 1 kHz sweeping, as shown in Fig. 3.11. Due to the gravity, particles sunk to the bottom. Two vertical particle lines were observed once the frequency reached 2.66 MHz. This is due to the 1-D vertical plane generated with two pressure nodes in the channel. As frequency further increased, particles lines remained mostly steady until 2.73 MHz was applied. Particles started to elevate from the bottom. Later on, particles formed patterns as the frequency was increased.

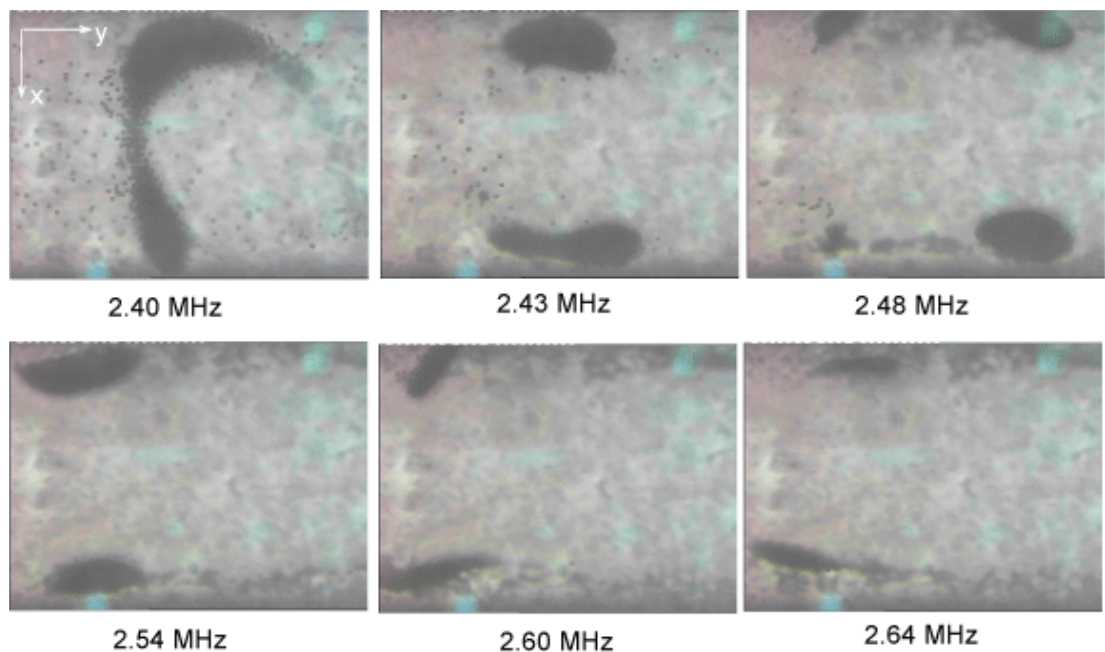


Figure 3.11: Image sequences of particles forming patterns in the range of 2.4 MHz to 2.64 MHz.

Figure 3.12 shows image sequences of particles behaviour under varied frequencies from 2.66 MHz to 2.7 MHz under three focus planes. Initially, particles randomly filled in the channel, as seen in Fig. 3.12 (a). Once a 2.66 MHz excitation frequency was applied, particles formed two lines along the channel, shown in Fig. 3.12 (b). Due to gravity, the particle then sank to the bottom, as seen in Fig. 3.12 (c). As frequency increased to 2.73 MHz, particles started to elevate from bottom, as seen in Fig 3.12 (d). This motion was observed as the individual particles are visual clear bringing the focusing plane up to the middle layer.

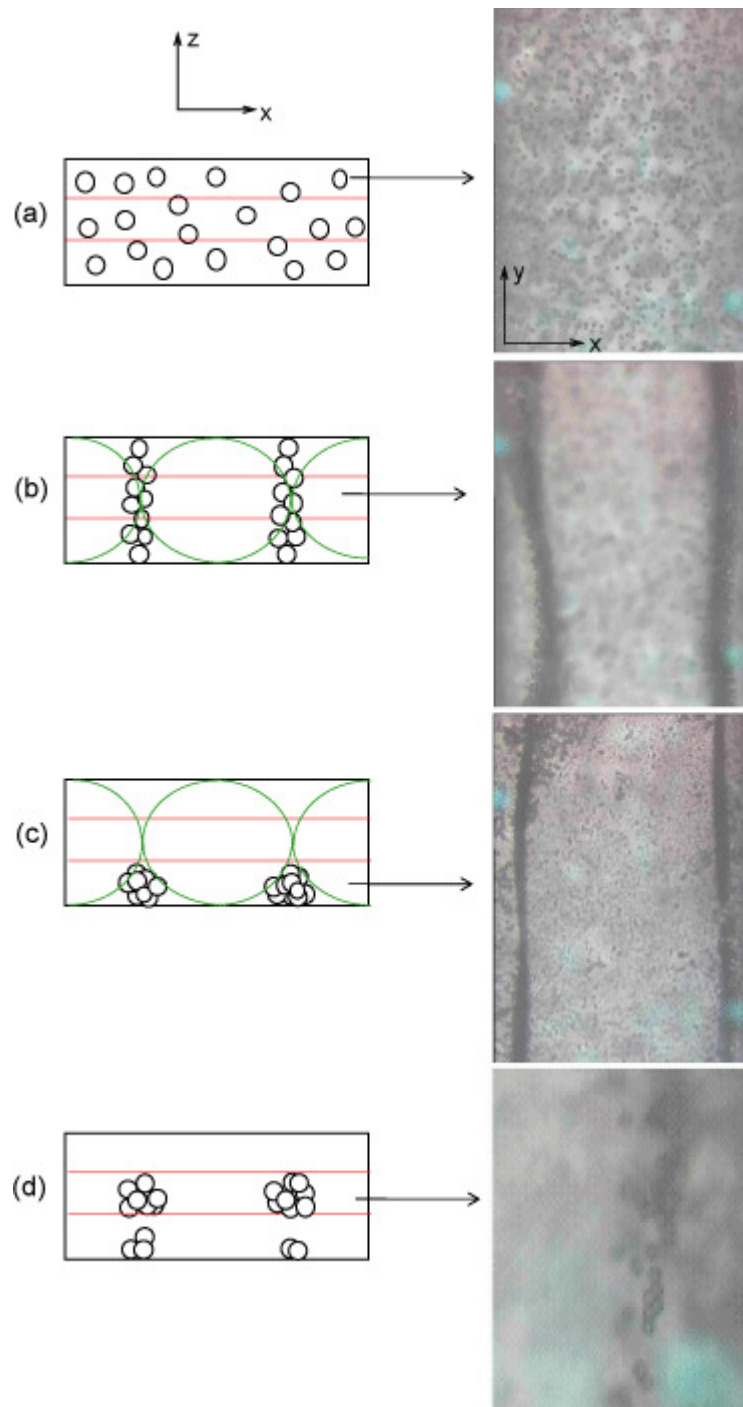


Figure 3.12: Schematic description and experimental images of particle elevating from the channel bottom. (a) $6\ \mu\text{m}$ particles full filled within the channel, (b) particles focused in two vertical planes when $2.66\ \text{MHz}$ applied, (c) particles sinking to the bottom due to gravity, and (d) particles elevating from the bottom to the middle layer of the channel (zoom in image). Arrow indicates the focal plane.

3.5 Conclusions

In this chapter, acoustic radiation forces actuated by a piezoelectric device have been investigated in detail. Particles forming lines are observed from the top of the device when 1-D vertical acoustic plane is presented. Switching between two excitation frequencies of $1.305\ \text{MHz}$ and $0.98\ \text{MHz}$, one array of particle clumps is formed

along the centre of the channel. While rapidly sweeping frequency from 0.87 MHz to 0.98 MHz, particle clumps in the form of 2×4 arrays is observed. Both the particle clumps arrays are formed in the plane parallel to the bottom, controlled by xz - and yz -plane. In the region of 2.66 MHz to 2.8 MHz, particle elevating from the bottom of the channel is observed due to the 2-D acoustic field (xz -plane and xy -plane). Such levitation can reduce particle waste by avoiding adhesion to the surface. The results are repeatable.

To develop the ultrasonic method for other applications, a vibrating bubble is introduced to the standing wave field. This method explores bubbles as the contacting method for particle manipulation to a new application for particle selection due to the particle size. Demonstration of this method is discussed in Chapter 4.

Chapter 4

Exploring Bubbles as a Soft Medium

Method for Particle Sorting

4.1 Introduction

A bulk fluid flow around an air bubble is induced by the frictional forces generated at the air/liquid surface when a bubble undergoes vibration within an acoustic field. Such fluid motion called cavitation microstreaming or acoustic microstreaming has been studied since the 1950s. The mode of oscillation and the flow pattern have been investigated in the early stage by Elder [82, 83]. Recently, the effects of the flow pattern by the oscillation motion have also been studied by Tho *et al.* [84]. The presence of micro-scale acoustic streaming gains lots of interest due to applications such as rupture of lipid membranes [85] and drug delivery [86, 87]. Furthermore, violent flow patterns have been studied for effectively mixing [41, 88, 89].

Cavitation microstreaming is most pronounced for bubbles undergoing resonance. This is very difficult when multi-bubbles are presented in the field, as the size of the bubbles is not likely to be exactly the same. Therefore, a way to actuate multi-bubbles with slightly different sizes is very useful. Here we present the method of using standing waves to drive the bubbles. The microstreaming achieved is much weaker, but importantly varied sized bubbles can be excited under one excitation frequency. Furthermore, in this chapter a vibrating bubble in a standing wave field as a particle selecting mechanism is demonstrated. The particles experience both the secondary Bjerknes force which acts between the bubble and particles, and drag force introduced by the streaming lines. The behaviour of the varied size particles (6 and 1.9 μm) in the acoustic field varies according to which of these two forces is dominated. For large particles, excitation can be such that the Bjerknes force between the bubble and the particle is dominant; while for small particles, the drag force induced by the acoustic streaming is dominant. As a result, the large particles

are attracted by the bubble; while the small particles are repelled from the bubble as they follow the streamlines of the acoustic streaming.

4.2 Background of Cavitation Bubbles

4.2.1 Cavitation microstreaming

As early as 1954, Elder *et al.* [82] observed the small-scale acoustic streaming around a bubble attached on the inner wall of a liquid container, present within in an acoustic field. A violent streaming pattern was noticed when the bubble matched its resonant size. Later, Elder [83] has investigated cavitation microstreaming caused by cavitation bubbles located near solid boundaries further. In his investigations, cavitation microstreaming was observed to obtain some stable regimes under certain sound amplitudes, while other parameters remained the same.

Additionally, cavitation microstreaming differs from conventional acoustic streaming. Previous research shows that the microscopic bubbles existing in fluids could increase the flow velocity of acoustic streaming [90, 91]. This is mainly caused by acoustic bubbles, which are induced by ultrasonic waves, which absorb the energy of these ultrasonic waves. Cavitation microstreaming is predicted to be much faster than conventional acoustic streaming [92]. Elder [83] also found that the microstreaming is most pronounced for bubbles undergoing breathing mode (pulsation) resonance. Furthermore, later research shows that the microstreaming pattern is affected by the mode of oscillation of the bubble [84]. Several different types of oscillation may be observed including translating oscillations, radial oscillation, volume oscillation and shape oscillation which is discussed in the following section.

4.2.2 Bubble oscillation modes

Cavitation microstreaming can be influenced by the type of oscillation mode. The translation, radial oscillation, volume oscillation and shape deformation of a gas bubble in a liquid may be observed in an acoustic field. An erratic dancing motion of a spherical bubble trapped in an acoustic standing wave was observed by Eller and Crum [93]. They suggested that the erratic dancing motion was caused by the presence of shape oscillations that were parametrically excited by the bubble pulsations when the pressure amplitude exceeded a threshold. Recently, Doinikov [94] has studied the dancing motion in the context of translational instability which is

the special case of the nonlinear coupling between the volume pulsation, translational motion and shape modes. These are described below:

Translational and radial motions

Generally, both translational and radial motions can exist for a bubble in an acoustic standing wave field. Temporal and spatial variations of an ambient fluid pressure induce the translational motions of a bubble in an acoustic field [95]. Under this motion, bubbles move periodically along one or more different axes. Furthermore, the temporal variation of the pressure induces radial oscillation. Hence it introduces a change in bubble volume, which also affects the translational motion. Watanabe & Kukita [95] reported that the bubble size would affect both its location and oscillation mode. Their experiments showed that a bubble which is larger than the resonance size moves to a pressure node position and its radial oscillations becomes small; in contrast, for a sufficiently small bubble, it moves to a pressure antinode position and radially oscillates under the maximum pressure amplitude. A chaotic oscillation was observed in both the radial and translation directions when a slightly smaller than the resonance size bubble was presented.

Volume oscillation

Volume oscillation, sometimes also referred to as radial oscillation, refers to a bubble which expands and contracts radially while maintaining its spherical shape. This mode is also known as breathing mode and its behaviour is a consequence of the compressibility of the gas and is forced by the fluctuating acoustic pressure field. This oscillatory mode is most pronounced when the bubble is excited near its natural frequency [83]. Therefore, the volume oscillation mode has been investigated in the applications of sonoporation of cells by the shear stress caused by microstreaming near pulsation oscillating bubbles [87, 96].

Shape oscillation

Unlike the volume oscillation, shape mode oscillations distort the bubble from its usual spherical shape into various polygonal shapes depending on the particular shape mode [97]. It is observed when a bubble is excited into higher-order modes of oscillation. However, it is difficult to secure a bubble in any particular mode of oscillation. Part of an investigation by Tho *et al.* [84] showed that the bubbles usually remain stable shape oscillation for around 30s and most often would change

into another mode of oscillation or occasionally would detach from its fixed position and move around erratically.

For a bubble with fixed radius R_0 , the expression for the natural frequency of the n th mode of the shape oscillation is given as:

$$\omega_n^2 = \frac{(n-1)(n+1)(n+2)\sigma}{R_0^3 \rho_F}. \quad (4.1)$$

Such modes have been shown by Matsumoto and Ueno [98]. This can be reduced to the dispersion relation for capillary waves on a flat surface if R_0 and n tend to infinity whilst $\lambda_c = 2\pi R_0 / n$ is held constant. The capillary wavelength is given by:

$$\lambda_c^3 = \frac{2\pi\sigma}{\rho_F f_c^2} = \frac{8\pi\sigma}{\rho_F f_e^2}, \quad (4.2)$$

where f_c is the frequency of the capillary wave, and f_e is the frequency of excitation. This takes into account that the capillary waves are one half the frequency of the excitation [99].

Above all, cavitation microstreaming is one of the most significant phenomena observed around an oscillating bubble. Such microstreaming is depended on the bubble oscillation mode which can be varied from one type to another during the oscillating period. In the investigations of microstreaming patterns, the oscillation modes need to be considered. Besides that, a stable cavitation bubble is also the key factor.

4.2.3 Cavitation bubble types

Generally speaking, there are two types of cavitation bubbles that can be generated in an acoustic field: stable cavitations and transient cavitations. Stable cavitations are bubbles that oscillate usually in a non-linear function around some equilibrium size. They are relatively permanent and may continue oscillating for many cycles of the acoustic wave. In contrast, transient cavitations generally exist for less than one cycle. During this one cycle, they expand to a size which often to many times of their original size, and then collapse violently [100]. Factors that affect the type of cavitation generated include the driving frequency, the type of transducer and the type of acoustic wave.

The accuracy of one type of bubble is dependent on the ultrasound frequency. At high frequencies, stable cavitation is dominant, where bubbles oscillate for hundreds of acoustic cycles. At low frequencies around 20kHz, transient cavitation bubbles are generated. However, by using plate type transducers, at low frequencies a significant amount of stable cavitation can be generated [101].

Another factor, as shown by Calvisi [102], is that bubbles are more unstable in a travelling ultrasonic wave than in a standing wave. For a bubble located at the pressure antinode of a standing acoustic wave field, an approximately uniform pressure field causes the bubble to remain spherical. By contrast, a travelling acoustic wave generates a time-dependent pressure gradient along its direction of travel. This induces non-spherical shape modes to grow.

4.2.4 Cavitation bubbles applications

Mixing

Recently, interest in the application of biological systems and engineering applications to microfluidics has grown. Cavitation microstreaming has been demonstrated by Liu *et al.* [41] as a mechanism for mixing fluids in microscale. The experimental system consists of a microchamber with a piezoelectric plate attached to one of its walls. The oscillating multi-bubbles inside the chamber induce the microstreaming when excited by a piezoelectric transducer. Furthermore, a low frequency (~5 kHz) and low voltage (~ 10 Vpp) is used to provide almost no heating to the liquid. As a result, their chamber mixing technique reduces the time to fully mix liquid solutions in a 22 μl chamber from hours to tens of seconds.

A more efficient mixing technique was introduced later by Ahmed *et al.* [89]. In their experimental system, a polydimethylsiloxane based microchannel was used with a “horse-shoe” shaped microstructure fabricated inside it. A single bubble was induced in the horse-shoe structure and can be securely trapped even when a high flow rate was applied. An adjacent piezoelectric transducer was used to drive the membrane of the trapped bubble at a frequency and voltage of 70.1 kHz and 8 V. Ahmed *et al.* [89] also examined the mixing effectiveness with the flowing fluids with the flow rate range from 3 $\mu\text{l}/\text{min}$ to 10 $\mu\text{l}/\text{min}$. As a result, a further reduced mixing time of ~7 ms was achieved with excellent mixing across the entire width of the channel.

Transportation

The flow field around an oscillating bubble has been studied by Marmottant & Hilgenfeldt [85]. In their earlier work, lipid vesicles were used to track the streamlines around an oscillating bubble. Bubbles were generated by syringe injection of air into a quartz cuvette. The near resonant frequency (180 kHz) for the bubble of radius of 1 μm was applied to the system. The streaming flows then observed consisted of a vortex ring around the bubble. Additionally, in one experiment, a vesicle was ruptured due to the shear forces. This result can be applied to sonoporation which is discussed in the next section.

Based on their previous observations, Marmottant & Hilgenfeldt [86] then reported a bubble-driven technique to transport particles in a microfluidic device. The bubble adsorbed at the bottom of the cuvette was driven to oscillate by a piezoelectric transducer attached the side wall at frequencies ranging from 40 to 200 kHz. A doublet – bubble/particle combination was introduced to develop a steady streaming flow around it when placing in the vicinity of an oscillating bubble. The flow field of the bubble/particle combination- doublet is easily obtained in the present small scale regime, where inertial forces are negligible compared to viscous forces.

Sonoporation

A growing area of interest is in biomedical applications. By maintaining a single stable oscillating gas bubble at 20 kHz, hydrodynamic stresses resulting from acoustically induced small-scale eddying motion near the bubble may be the mechanism of hemolysis [103]. One of the observations from the investigations provides a method for determining the mechanical strength of cell membranes by measuring the critical threshold for release of cell contents.

As early as 1970, Rooney [103] studied sonically induced shear as a mechanism for biological application. In his investigations, the shearing stresses due to cavitation microstreaming were observed to cause haemolysis of erythrocytes, which supporting the observation made by Marmottant & Hilgenfeldt [85]. Numerical calculations of the shear forces induced by cavitation microstreaming have been found to be large enough to generate reparable sonoporation of cells [104, 105]. Further studies of ultrasound contrast bubbles induced cell deformation and enhanced cell membrane permeability were also carried out for the application of drug transfer via sonoporation [87].

Micro-rotor/ actuators

A micro-rotor provided a rotation speed of 625 rpm was reported by Kao *et al.* [106], which was powered by the microstreaming generated in the vicinity of a micro-bubble excited by ultrasound. In their experiments, three types of micro-rotor were designed with diameter of 65 μm and examined. The rotor floating on the solution in a cuvette was attracted to the bubble which was attached on the surface of a millimetre-size heater by the microstreaming generated. The rotor then was self-centred on the top of the bubble. Finally, the symmetrical flow of the microstreaming drove the rotor rotating. Clearly, when the excitation frequency matches the resonant frequency of the bubble-cuvette system, the maximum rotational speed is achieved. Furthermore, a misalignment of the rotor can reduce the maximum rotational speed.

4.3 Development of Ultrasonic Manipulation with Bubbles

The previous section shows that vibrating bubbles' studies in the literature have been focused on the violent microstreaming patterns around a resonant bubble in an acoustic field. In order to excite the bubble in its resonant mode, some difficulties have been raised during these investigations. One of the difficulties is that the bubble size is unstable due to the bubble growth. Additionally, in the case of many bubbles presented in the acoustic field which may have a wider application field, it is difficult to create bubbles with exactly the same size.

In this project, we investigate the standing wave driving of bubbles for particle sorting. Some key factors need to be considered, which include the resonant bubble size and its location, the surface friction, the drag force presented on the particles due to the streaming and the Bjerknes force between the bubble and the particle.

4.3.1 Bubble location in the standing wave field

An ultrasonic standing wave is established by exciting the fluidic chamber in its resonant frequency which results in a one dimensional pressure field. Within the pressure field Watanabe and Kukita found that a bubble sufficiently smaller than the radius, which would allow resonance at the given drive frequency ($R_0 / R_{res} < 0.87$), will move to the pressure anti-node within the standing wave, whilst a bubble radius larger than the resonant size will move to the pressure node ($R_0 / R_{res} > 1.03$) [95].

The relationship between resonant angular frequency and bubble radius is given, assuming a permanent bubble undergoing small radial oscillations, by [107]:

$$\omega_o^2 = 3\kappa \frac{p_g}{\rho_F R_o^2} - \frac{2\sigma}{\rho_F R_o^3}, \quad (4.3)$$

where a polytropic law of compression has been assumed with exponent κ (the ratio of the specific heats of the gas, which takes a value between 1 and 1.4 for air), p_g is the pressure of the gas at rest, σ is the surface tension and ρ_F is the density of liquid. The plot of the relationship between the resonant angular frequency and the bubble radius is shown in Fig. 4.1. Thus, for the excitation frequencies used in the investigation, the resonant bubble size is in the range 2.68 μm to 15.4 μm . The bubble size and its corresponding frequency values are listed in the Tab. 4.1.

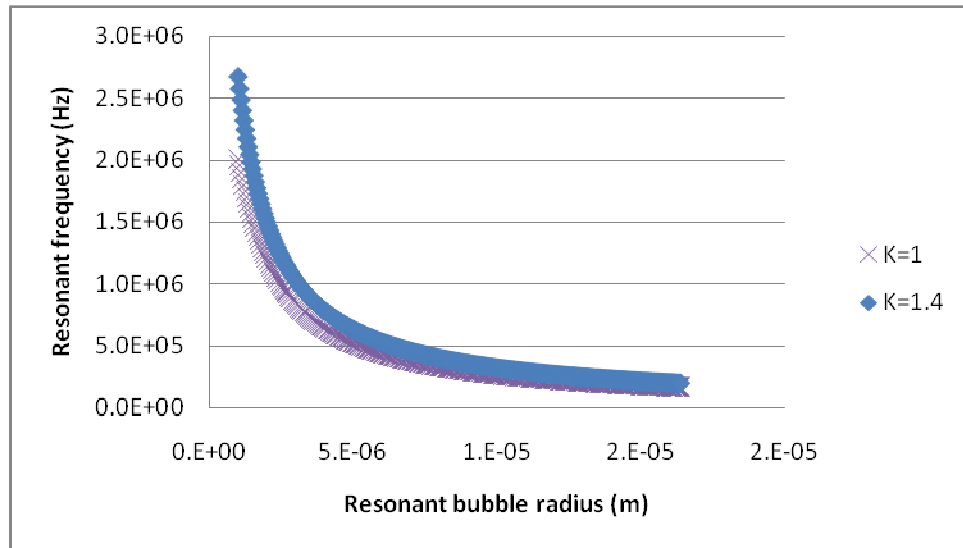


Figure 4.1: Plot of bubble resonant frequency against its resonant radius.

Table 4.1: The value of bubble size under its corresponding frequency

Frequency (kHz)	210.5	673	939.5
Bubble radius (μm) K=1	12.95	3.85	2.68
Bubble radius (μm) K=1.4	15.4	4.7	3.31

4.3.2 Forces experienced by the bubble

In an acoustic pressure field, acoustic radiation force and drag force due to streaming were discussed previously in Chapter 3. When a gas bubble is present within the

acoustic field, Bjerknes forces have been brought to the attention of researchers. There are both primary Bjerknes forces and secondary Bjerknes forces existing in the field. Furthermore, for bubbles attached to a solid wall, the surface friction needs to be considered as well during the investigation.

Primary Bjerknes forces

When a gas bubble in liquid exposed to an acoustic pressure field, it can undergo volume pulsations. A non-zero acoustic pressure gradient can couple with the bubble oscillations to produce a translational force on the bubble. This is the primary Bjerknes force which influences the bubble due to the “primary” (external) sound field. According to the size, bubbles which are larger than the resonance size travel to pressure nodes; otherwise, they travel to pressure antinodes. This is also shown by the equation provided by Leighton *et al.* [108].

Firstly, assume time-varying pressure formulation as:

$$p(y,t) = p_0 + 2p_A \sin(ky)\cos(\omega t), \quad (4.4)$$

where y the spatial distance, p_A the amplitude of the sound wave and ω the circular frequency.

$$\nabla p(y,t) = 2kp_A \sin(ky)\cos(\omega t), \quad (4.5)$$

$$R(y,t) = R_0 - \xi_0 \sin(ky)\cos(\omega t + \alpha), \quad (4.6)$$

where the phase term α equals zero for bubbles size smaller than resonance, and equals π for bubble larger than resonance.

Therefore, the bubble volume for approximate to first order as:

$$V_b(y,t) = V_0 \left[1 - \left(3 \frac{\xi_0}{R_0} \right) \sin(ky)\cos(\omega t + \alpha) \right], \quad (4.7)$$

when $V_0 = 4\pi R_0^3 / 3$.

A body of volume V_b in a pressure gradient ∇p experiences a force $-V_b \nabla p$.

$$F = -\langle V_b(t) \nabla p(r,t) \rangle, \quad (4.8)$$

$$F = [3p_A k \xi_0 V_0 \sin(2ky)] / (2R_0), \quad (4.9)$$

for bubbles smaller than resonance; and

$$F = -[3p_A k \xi_0 V_0 \sin(2ky)] / (2R_0), \quad (4.10)$$

for bubbles larger than resonance.

Clearly, from the above equations, for bubbles of less than resonance size, a positive force is presented which forces bubbles' travelling to the pressure antinodes; while for bubbles larger than resonance size, a negative force is presented which forces bubbles' travelling to the pressure nodes.

Secondary Bjerknes forces

In contrast to a single bubble, theoretical and experimental work has been done on the forces between bubbles and bubbles/particles due to the “secondary” sound field emitted by other bubbles/particles, which called secondary Bjerknes force. Theoretical and numerical models describing the interaction forces between two or more gas bubbles in acoustic field have been in development for decades [109-112]. Several models for the interaction between bubbles and immovable solid objects are also being studied [113]. Coakley and Nyborg [114] derived an expression for the time-averaged force generated between a spherical bubble and a rigid, immovable sphere, both bubble and particle are free to move.

Recently, using Lagrangian mechanics, Hay *et al.* [113] derived the time-average secondary Bjerknes force equation at fifth-orders of a spherical gas bubble and a rigid spherical particle, at which both are free to translate. By assuming the small periodic bubble pulsation of

$$R(t) = R_0 + \xi_0 \sin \omega t, \quad \xi_0 \ll R_0. \quad (4.11)$$

The time-averaging interaction force over one acoustic cycle is given:

$$\langle F_B \rangle = 4\pi\rho \left(\frac{\rho - \rho_s}{\rho + 2\rho_s} \right) \frac{R_0^4 R_s^3}{d^5} \omega^2 \xi_0^2, \quad (4.12)$$

where ρ_s and R_s is the density and radius of the particle respectively, d is the separation distance between the centres of the bubble and particle, ω is the angular frequency of the bubble vibration, and ξ_0 is the bubble wall displacement. From this equation, the secondary Bjerknes force depends on both size and density. Additionally, it indicates that for a denser particle than that of the liquid, the interaction force is negative, and the bubble and particle are attracted toward one another; on the other hand, for a lighter particle, the force between the bubble and particle is repulsive.

Surface friction force

Early experimental and theoretical studies of oscillation modes and their microstreaming flow have been completed for a free sphere air bubble in liquid [113, 115, 116]. Only a few works have been reported of a bubble resting on a solid surface, where it often becomes hemispherical in shape. The forces acting on the hemispherical bubble are more complicated than for the free bubble, which includes the acoustic radiation force, drag force and Lubricated friction force.

For a spherical bubble in an acoustic field, the translational motion of the bubble in the direction of the pressure variation is given by

$$m_b \frac{du_b}{dt} = -V \frac{dp}{dx} - \frac{1}{2} \rho_F \frac{d}{dt} (V_b u_r) - \frac{1}{2} \rho_F |u_r| u_r A_b C_d, \quad (4.13)$$

where m_b is the mass of gas and vapour inside the bubble, u_b is the translational velocity defined by $\frac{dx}{dt} = u_b$, V_b is the bubble volume, u_r is the relative velocity between the bubble and the liquid, A_b is the projected area of the bubble, and C_d is the drag coefficient.

The relative velocity is given by

$$u_r = u_b - u_l, \quad (4.14)$$

and the velocity of the liquid u_l is assumed to be

$$u_l = \frac{k \Delta p}{\omega \rho_F} \cos(\omega t) \cos(kx). \quad (4.15)$$

Here we consider two cases: the acoustic radiation force exceeds the drag force (which includes the friction force), and the acoustic radiation force is less than the drag force.

4.3.3 Piezoelectric device and experimental setup

The apparatus used for the experiments is depicted in Fig. 4.2. The actuator for the system is a piezoelectric plate this is driven by a signal generator (Stanford Research SDR 345) via a power amplifier (Amplifier Research 25A250A). The particles suspended in the enclosed fluid chamber are viewed using an Olympus BX51 upright microscope fitted with a charge coupled device camera (Hitachi HV-D30) operating at 25 frames per second. The video signal is sent to a DVD recorder and monitor.

Subsequent image capture is achieved by playing the DVD recordings back into a frame grabber (National Instruments 1411) housed in a PC.

The device itself is fabricated in two parts. The lower (main) part is made by attaching a 5 mm square piezoelectric transducer with a thickness of 0.5 mm to a 20 mm square piece of silicon wafer. These are mounted on support structures which hold the electrical connections to the upper and lower surfaces of the piezo. The second part consists simply of a 2 mm thick piece of glass (5 mm square). This piece of glass and the silicon substrate form the upper and lower surfaces of the fluidic chamber.

A 0.5 mm diameter wire is used as a spacer to define the chamber height and lateral dimensions as 4.7 mm × 4 mm. These values are different so that the resonant frequencies causing mode shapes of one dimensional pressure fields occur at different frequencies in each of the two lateral directions. The chamber is filled by depositing 9.3 µl solution of copolymer microspheres onto the silicon surface, and covered with a glass cover slip. The process of placing the cover slip on the fluid needs to be carefully performed so that no air bubble is trapped inside (bubbles formed at this stage tend to be too large). The approach allows subsequent successive raising and lowering of the cover slip to ensure the formation of small bubbles as required in this work. In the experiments two sizes copolymer microspheres, 6.0 µm and 1.9 µm diameter (Bangs Laboratories, density = 1050 kg/m³), are used to provide the size contrast.

One important parameter of the chamber is the depth. From the experiments, we found that most of the bubbles which were generated in the fluid chamber were around 20 to 50 µm in radius. To give extra space for bubble growth, as well as to identify the bubbles which are attached on the glass surface (upper layer, separated from the lower part of the device) or the silicon surface (bottom layer), the depth of 0.5 mm is chosen. Another important parameter is the lateral dimensions of the chamber. In the situation with fixed air concentration in a fluid (e.g. water at room temperature), the generation of a cavitation bubble within the fluid depends on the volume of the chamber. From the experiments, the case of chamber dimension with 4.7 mm × 4 mm × 0.5 mm can easily generate cavitation bubbles. Thus, the dimension of the chamber was chosen.

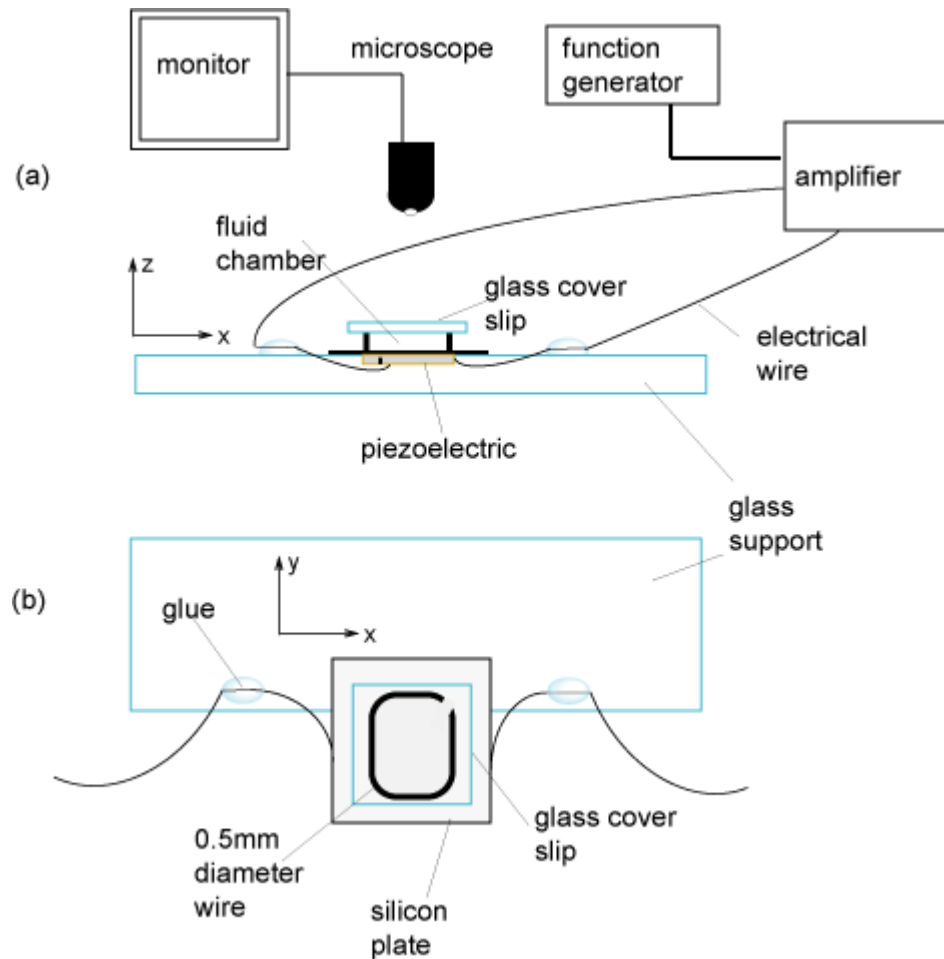


Figure 4.2: Schematic description of experiment setup for particle sorting by an excited bubble, (a) the cross-section view (x-z plane) of the device used in the experiment, and (b) the top view (x-y plane) of the device.

4.3.4 Investigation of bubble's properties

A novel method of using an ultrasonic standing wave excited bubble to sort particles, which has not been reported before, is discussed in the following sections. As we are using the standing wave to drive the gas bubble in the microfluidic chamber, we need to establish the standing wave field first. This has been done by actuating the device at its resonant frequency. All experimental images are captured in x-y plane.

Bubble location

Frequencies which cause an ultrasonic standing wave resulting in a quasi one-dimensional standing wave across the shorter lateral dimension of the chamber were found experimentally to occur at 939.5 kHz and 673 kHz. The existence of these resonant modes was inferred from the patterns formed by suspended 6 μm microspheres in the form of a series of parallel lines. At 939.5 kHz four lines are

formed. Figure 4.3 (a) shows two of these lines which approximately confirm to a one dimensional standing pressure field.

When a bubble of 25 μm in radius (R_o), well above the radius accompanying resonance, is introduced into the 939.5 kHz pressure field, it should be aligned with the pressure node (refer to Section 4.3.1). This can be seen in the two lines of particles of Fig. 4.3 (b). Interestingly, the presence of the bubble has the effect of causing one of the lines to bow around the bubble in this experiment. The bubble is the only large object within the chamber which is much larger than the particle; however it is difficult to be identified from the image. It is much clearer in the video which can be indicated by the movement of the surrounding 6 μm particles due to the microstreaming.

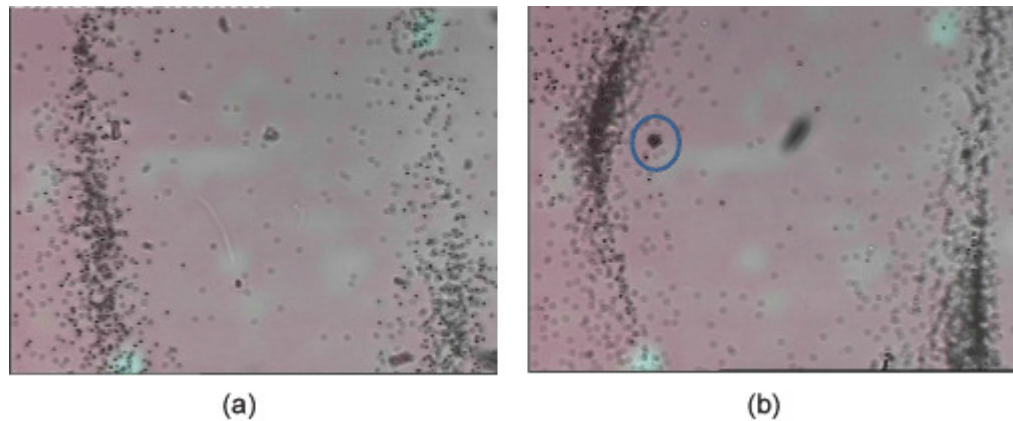


Figure 4.3: Lines forming in one dimensional standing pressure field. (a) Two of the lines shown straight without any bubble presented. (b) The effect of a bubble, circled in blue, causing one of the lines to bow around.

Alternatively, a series of experiments with a resonant frequency of 673 kHz were examined. Instead of forming lines, particles formed more complex patterns at 673 kHz. The bubbles radius generated are around 25 μm which is again far beyond the resonant bubble size between 3.85 μm and 4.7 μm at the 673 kHz (refer to Tab. 4.1). Without doubt, these bubbles are observed at the pressure nodes, shown in Fig. 4.4. Three similar size bubbles are observed from Fig. 4.4 (a), which located at the end of the particle pattern shown in the image. Figure 4.4 (b) shows a bubble located in a particle pattern. A white circle is added in Fig. 4.4 (b) to indicate the bubble as it is difficult to be identified in the pattern.

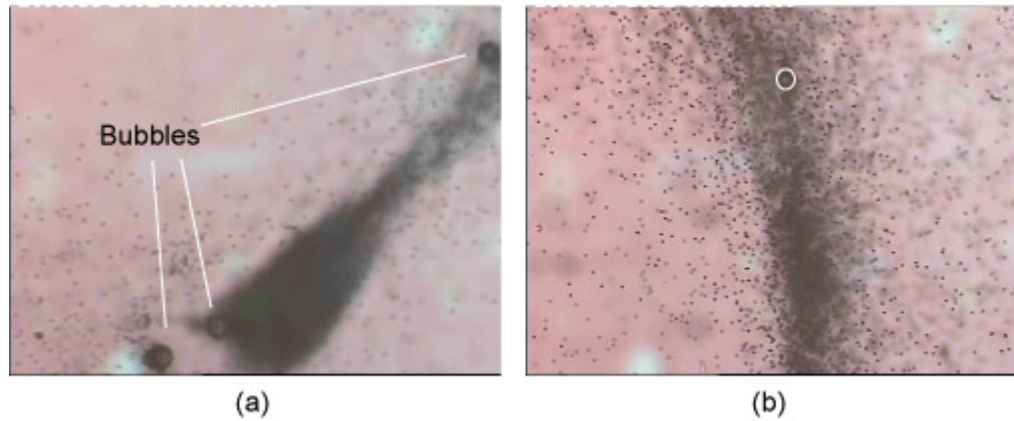


Figure 4.4: Images of bubble location at the excitation frequency of 673 kHz was applied. White circles present the bubble within the particle pattern.

The bow around effect caused by the oscillating bubble was also observed in the experiments, shown in Fig. 4.5. Two large bubbles present at the pressure node, as seen in Fig. 4.5 (a), many particles are attached on the bubble surface. The particles which form the pattern are shifted to the left. The particle movement shown by the arrows is due to the microstreaming flow. Figure 4.5 (b) shows 0.8s later, where a slight bow effect is shown as the particle pattern becoming more curved at the edge. The bow effect is clearly shown in Fig. 4.5 (c) and (d), when a 25 μm bubble is presented. The particle line is discontinued by a bubble within it. The particles original from the line are pushed to one side. Therefore the bow around is observed. Interestingly, the particles within the bow pattern are supplied by bringing the particles along the line due to the microstreaming.

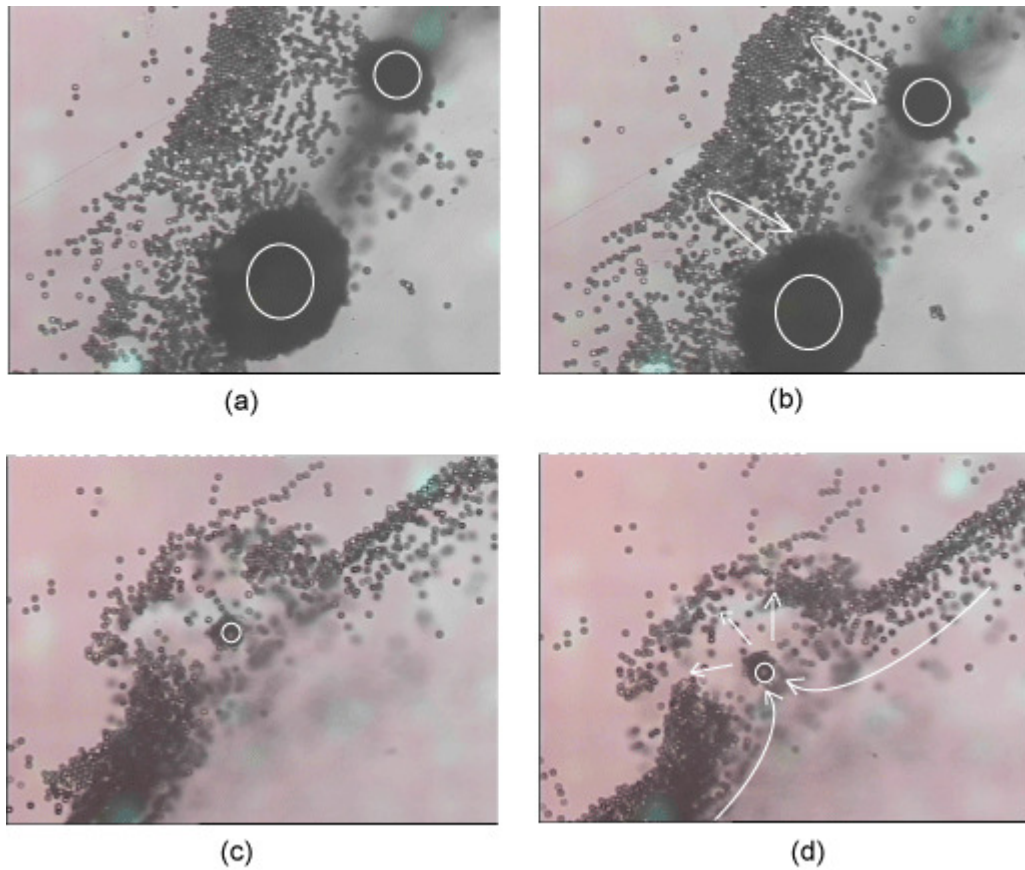


Figure 4.5: Images of bubble effect when line forming in the pressure field of 673 kHz. (a) and (b) Images of two bubbles presented at the pressure node with 0.8s apart. (c) and (d) Images of one bubble presented with 0.76s apart.

Bubble movement

In contrast to the bubble originally generated at the pressure node, a movement of bubble towards to the pressure node was observed from the investigation. In the case when a bubble with larger than resonant size is generated near pressure antinodes, the bubble experiences a maximum force due to acoustic pressure. For the larger acoustic radiation force presented on the bubble, the movement of the bubble towards to the pressure node can be observed. Clearly, Fig. 4.6 shows a bubble of 40 μm diameter moving towards a pressure node. Initially, the bubble was generated at the place between the pressure antinodes and the pressure node. Forced by the acoustic radiation force, the bubble started to move to the low energy position - the pressure node. The average speed of the bubble movement is measured as 10.53 $\mu\text{m}/\text{second}$.

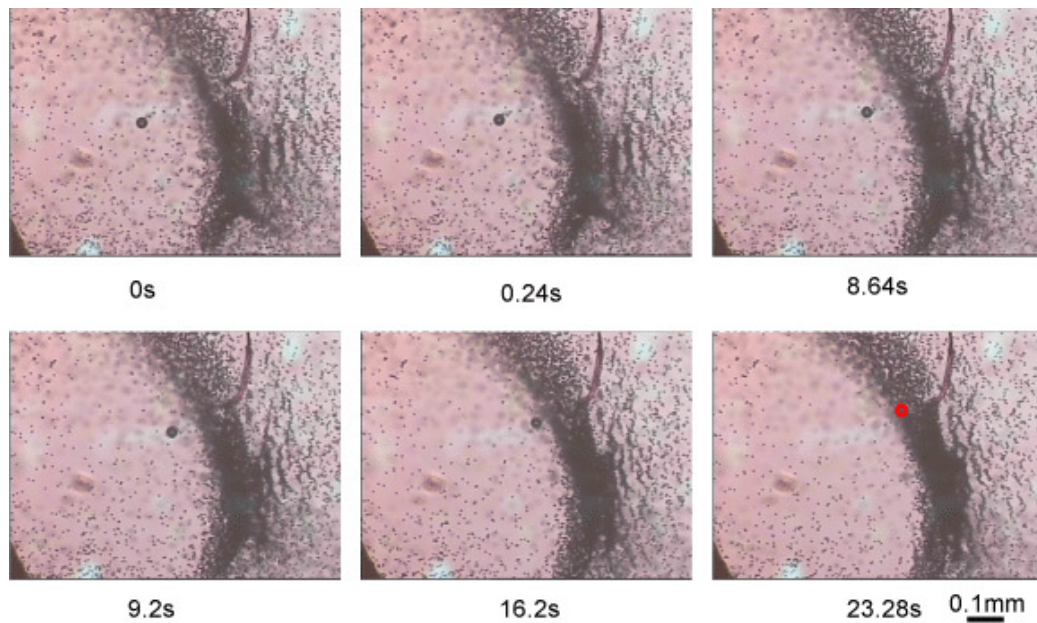


Figure 4.6: Image sequences of the movement of a bubble towards to the pressure node when 673 kHz was applied. The red circle presents the bubble when it remains within the particle pattern.

Varied bubble size

If we wish to have many bubbles vibrating in the acoustic field in some investigations, we must bear in mind that to achieve exactly the same size of bubbles is highly problematic. As observed in the investigation, more than one acoustic bubble can be generated. These bubbles can be observed on the glass surface or/and silicon surface at the pressure node position as their size is well above the resonant size.

Figure 4.7 shows multiple bubbles observed at the pressure nodes from two experiments. In one experiment, a total of seven bubbles were observed at the pressure node position. Five of them were attached under the cover glass surface (see Fig. 4.7 (a)), while another two were attached on the silicon surface where directly below the five bubble group (see Fig. 4.7 (b)). In another experiment, two bubbles were generated. One was attached to the glass surface, Fig. 4.7 (c); and the other was attached on the silicon surface, Fig. 4.7 (d). Both experiments were excited at 939.5 kHz, and the bubble sizes observed were around 50 μ m diameter. Notably, the microstreaming around these bubbles are similar in both strength and type.

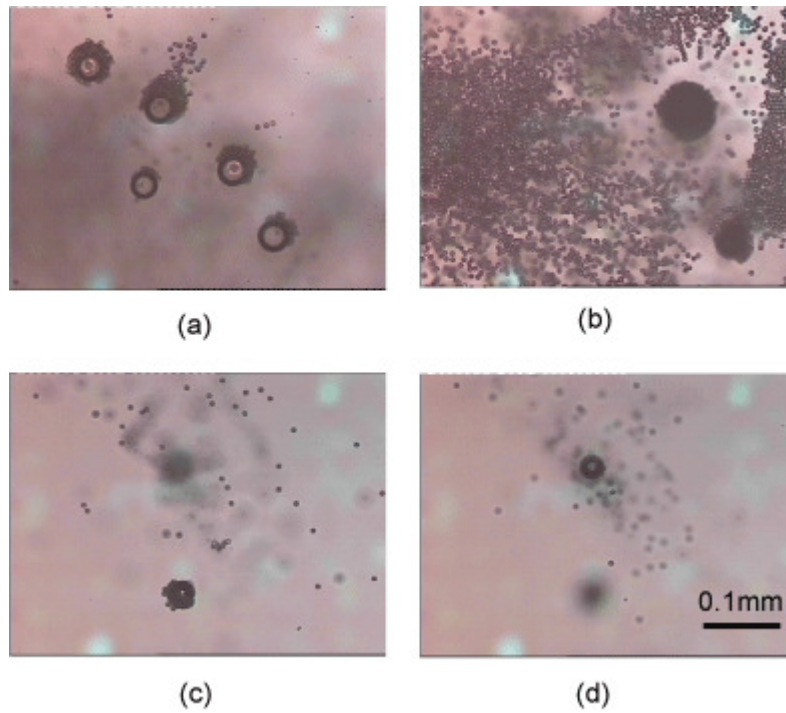


Figure 4.7: Images of multiple similar sized bubbles are observed. (a) Five bubbles are attached under the glass surface; while (b) two bubbles are attached on the silicon surface where directly below. Each of the two bubbles is attached on the glass surface (c) and silicon surface (d).

Therefore, using the standing wave to actuate the bubble is very helpful. Some bubble sizes generated in the investigation are shown in Fig. 4.8. The bubbles' diameters were varied from 20 μm to 50 μm .

These images were taken when an excitation frequency of 939.5 kHz was applied. At one resonant frequency, the varied size bubbles all experienced the same oscillating mode. As seen from the Fig. 4.8, all images show that the bubble is able to attract the 6 μm particles at 939.5 kHz. Alternatively, the strength of the oscillation is different. For a large bubble, the oscillation is stronger compared to the smaller bubble.

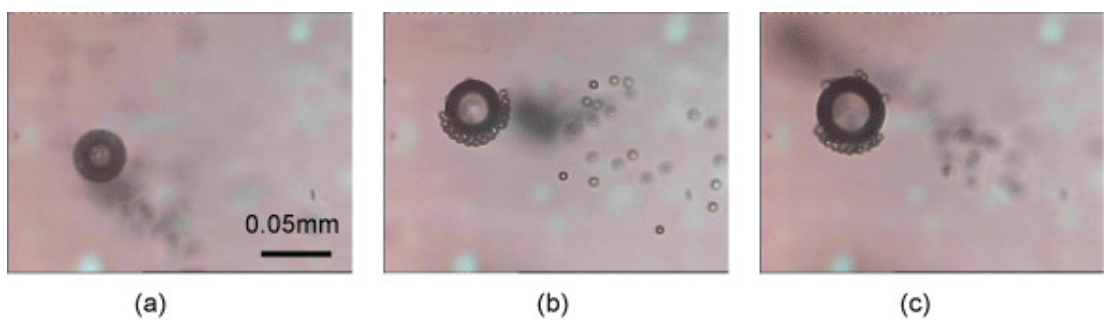


Figure 4.8: Experimental images of bubbles with varied sizes generated in the investigation at 939.5 kHz.

In another experiment, two different bubble sizes were observed. Figure 4.9 shows two bubbles with different size presented in the acoustic field. The excitation frequency of 210.5 kHz was applied in this experiment (acoustic streaming is dominant in this case rather than acoustic radiation force, therefore no particle patterns were observed). The bubble A is sufficiently smaller than bubble B. The strength of the microstreaming around the bubble is varied by the bubble size. As seen from Fig. 4.9 with red circle, particles around the bubble A takes 1.88s to become attached. While for the particles around bubble B, with green circle, less time of 1.08s is required for particles to be attracted from a similar distance. The particles were observed to be moving faster near bubble B. This indicates that the microstreaming flow is stronger for a larger bubble presented. This is because the Bjerknes force $\langle F_B \rangle = 4\pi\rho \left(\frac{\rho - \rho_s}{\rho + 2\rho_s} \right) \frac{R_b^4 R_s^3}{d^5} \omega^2 \xi_0^2$ is proportional to R_b^4 . For a larger bubble, a larger Bjerknes force is presented on the particle with certain distance apart.

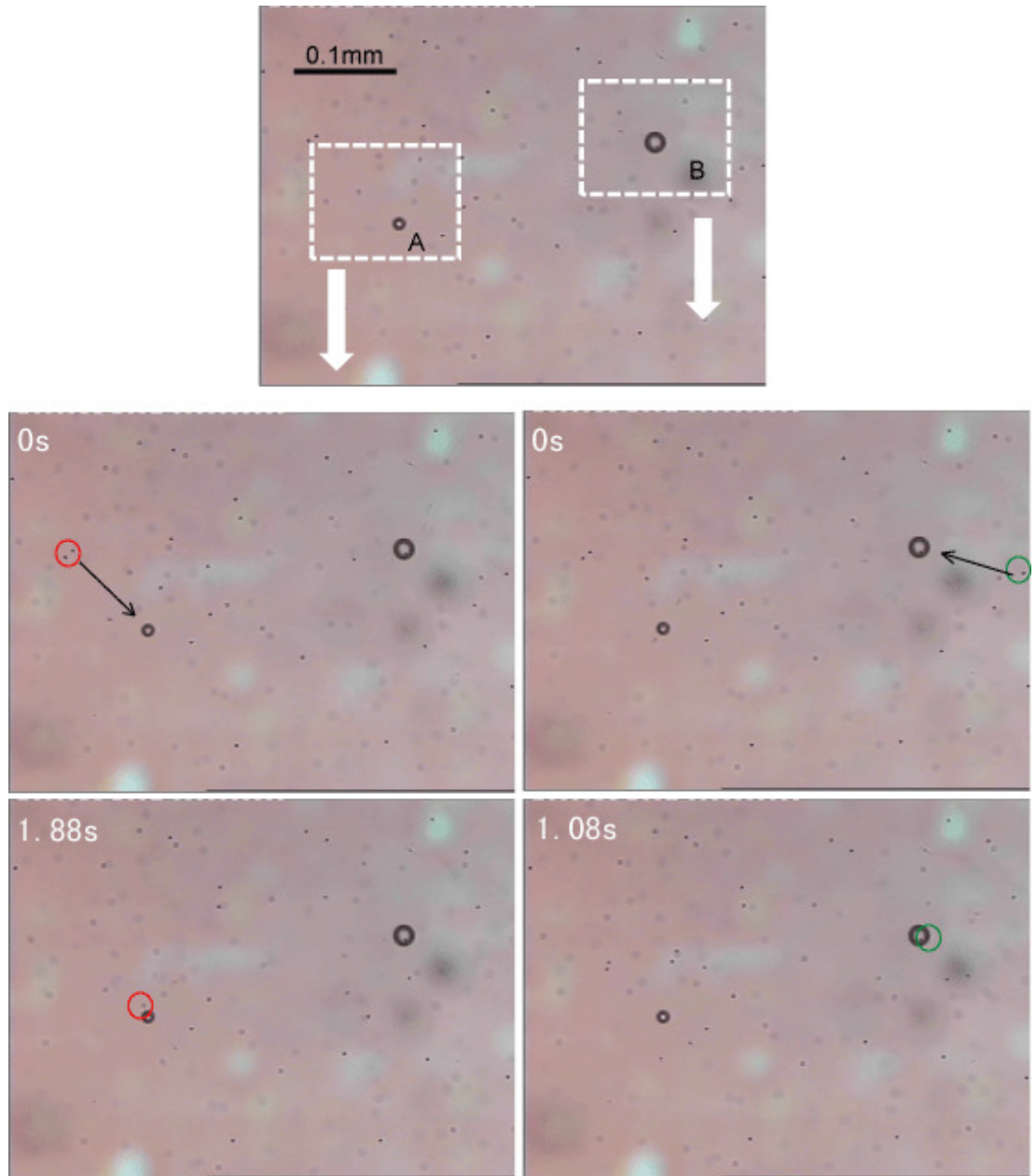


Figure 4.9: Experimental image of particle movement when two bubbles observed in the acoustic field with different size at 210.5 kHz. Particles (red circle) around the small bubbler A takes longer time to be attracted than the particles (green circle) around the large bubble B with similar distance.

Bubble growth rate

Clearly, there is an enhancement in the growth rate of a bubble due to the presence of microstreaming flows. The rate of increase in bubble size by diffusion is given [100]:

$$\frac{dR_b}{dt} = \frac{C_0 D}{\rho_F} \left(\frac{C_\infty}{C_0} - 1 - \frac{2\sigma}{R_0 p_0} \right) \left[\frac{1}{R_0} + (\pi D t)^{-\frac{1}{2}} \right], \quad (4.16)$$

where C_∞ is the mass-concentration of gas dissolved in the liquid at a great distance

from the bubble and C_0 the saturation concentration under the prevailing conditions, D is the diffusion coefficient, ρ_F is the liquid density.

From this equation, the surface tension term ensures that the bubble will eventually dissolve away even when the liquid is saturated with dissolved gas ($C_\infty = C_0$). Furthermore, the “rectified diffusion” allows the bubble to grow even when the relative concentration $\frac{C_\infty}{C}$ is well below unity. This is envisaged physically as: on the positive pressure half-cycle, the gas in a small bubble will be compressed, while the relative concentration of dissolved gas in the liquid is reduced. Gas diffuses outwards from the bubble into the liquid; conversely, during the negative half-cycle of pressure, while the bubble is expanded, gas diffuses from the liquid into the bubble. However, these two rates are not equal as the surface area of the bubble is greater during the negative half-cycle, and the bubble must gain some gas over a complete cycle due to the diffusion rates are proportional to the exposed area.

The bubble, excited at 939.5 kHz, shows the growth rate during the experiment period is approximately 0.165 $\mu\text{m/s}$. It is calculated as the gradient of the linear line which is shown in Fig. 4.10. The data is an average value taken from three experiments. This growth rate is much higher than any type of oscillating bubble discussed in Tho *et al.* [84] with the largest value of 0.0285 $\mu\text{m/s}$. This may be caused by the higher excitation frequency used in our investigation compared to 20 kHz. However, the linear type growth rate is matched to the linear translating bubble.

The enhancement in growth rates appears to be related to the microstreaming flows accentuating diffusion by improving the mixing of fluid near the bubble’s surface. This ensures that “new” fluid with a high concentration of gas is transported near the air-water interface to maintain the diffusion process. Therefore, the sizes of bubbles generated in the investigation are also depended on the size of the microfluidic chamber.

The bubble growth shown in the experiments is another reason to apply a standing wave to drive the bubble.

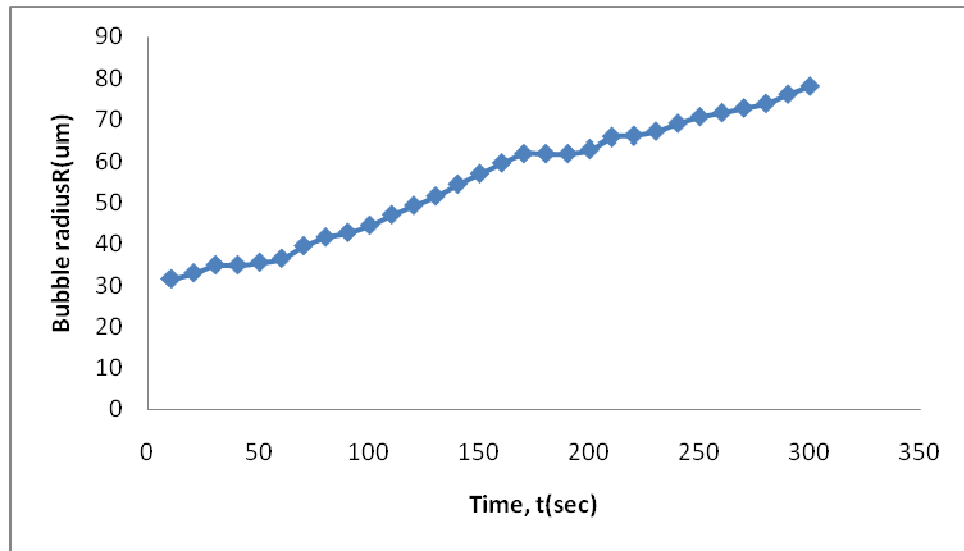


Figure 4.10: Plot of the bubble radius against time.

4.3.5 Effect of microstreaming

Previously, we discussed the bubble properties such as the location, the bubble size and the growth rate. Now we need to investigate the behaviour of rigid particles in the acoustic field. When a permanent gas bubble is excited within an acoustic field, cavitation microstreaming is generated around the bubble. For a solid particle suspended within the microstreaming flow field, a steady drag force is experienced as well as the secondary Bjerknes force. In microfluidic systems the drag force F_D , as known as Stokes drag, is defined as

$$F_D = 6\pi\mu u_r R_s, \quad (4.17)$$

where μ is the liquid viscosity, u_r is the relative fluid velocity and R_s is the particle radius.

Another important force between bubble and particle is the secondary Bjerknes force, which is not considered in the presence of strong microstreaming usually. This was discussed in section 4.3.2. The time-averaged force expression is given as Eq. (4.12).

In the same acoustic field, different size particles experience the drag force and the secondary Bjerknes force with varied values. As seen from the equations, $F_D \propto R_s$

and $F_B \propto \frac{R_s^3}{d^5}$. Furthermore, F_B is negative when the particle is denser and the force between them is attraction, otherwise the force is repulsion.

A driving bubble to attract particles

Particles used in the investigation are polymer microspheres with density of 1.06 g/ml. Theoretically, particles will be attracted to the bubble due to the secondary Bjerknes force. Firstly, a series of experiments have been conducted to investigate the 6 μm particle behaviour in a 939.5 kHz ultrasound standing wave field. Figure 4.11 shows a series of images taken from an experiment in which a 25 μm radius bubble sits within the standing wave. The particles in the vicinity of the bubble are in motion due to the acoustic streaming established by the standing wave. When they enter the proximity of the bubble the more localized streaming draws the particle towards the bubble. The particle then meets the liquid-gas interface where it remains trapped.

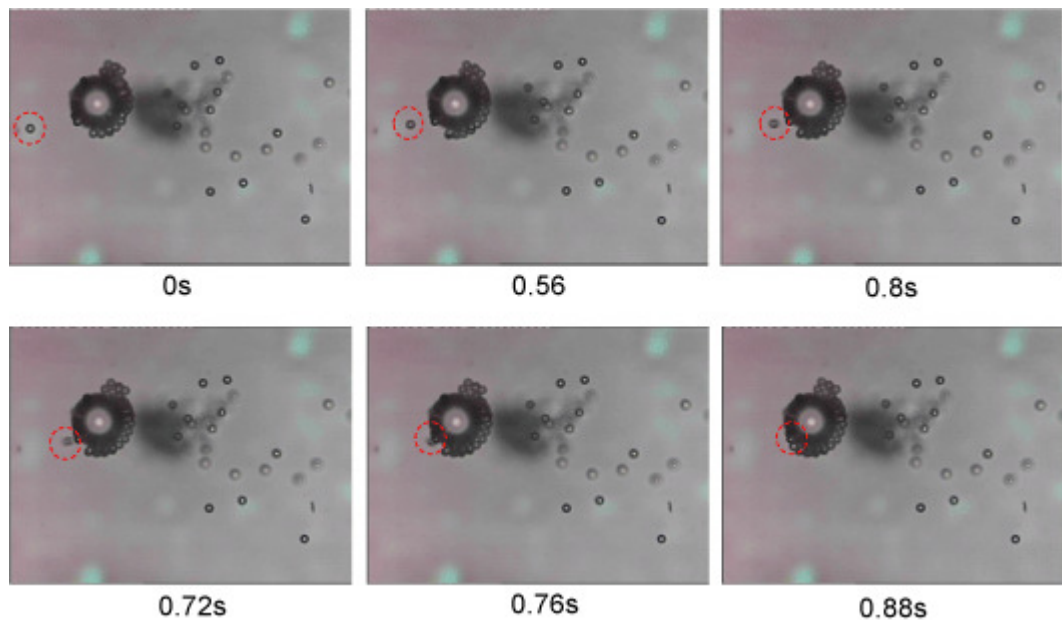


Figure 4.11: Experimental image sequences of 6 μm particles attracted by a bubble presented in the 939.5 kHz acoustic field.

A driving bubble to repel particles

This result can be contrasted with the situation where 1.9 μm particles were used. The particle which is indicated with a white dash circle is drawn towards the bubble before being repelled, as shown in Fig. 4.12. The difference in behaviour between the 6 μm particles and 1.9 μm particles depends on the comparison of the drag force and the secondary Bjerknes force they experienced. Clearly, in this case, the drag force is stronger than the secondary Bjerknes force. Thus the 1.9 μm particles are able to follow the streaming line.

These experiments showing partial balancing change due to the varying particle size have been done separately. In the next section, we show that the different behaviour between the 6 μm particles and 1.9 μm particles is still observable when both of the particles are presented in the same acoustic field.

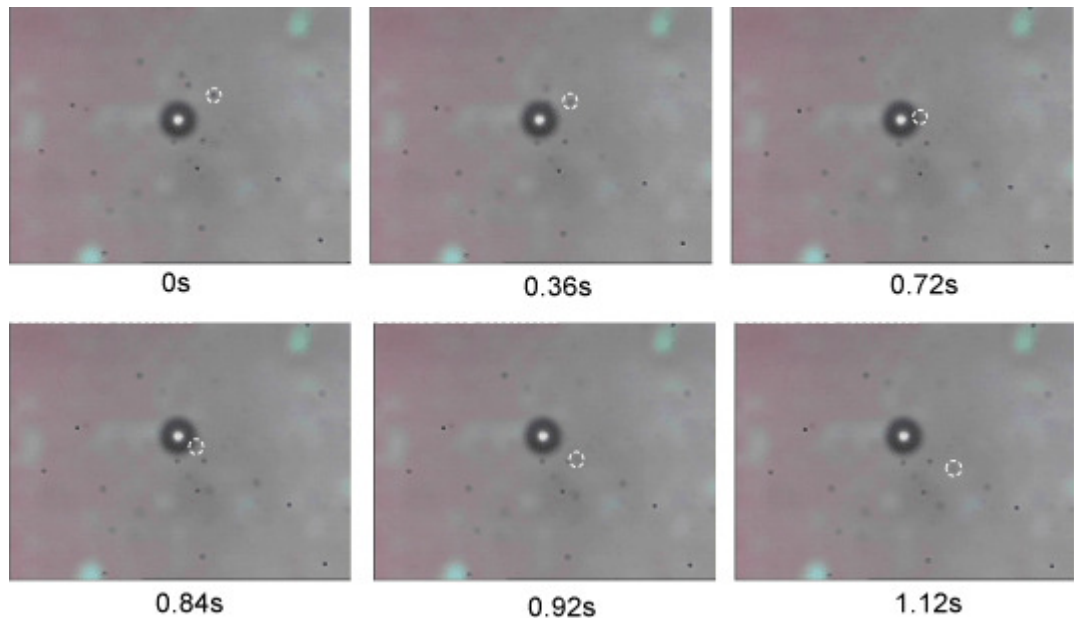


Figure 4.12: Experimental image sequences of 1.9 μm particles repelled by a bubble presented in the 939.5 kHz acoustic field.

A driving bubble as a sorting mechanism

Finally, a series of experiments have been done for both size particles in the standing wave field. Figure 4.13 shows the experimental image sequences of both size particles influenced by the effect of the microstreaming. Clearly, under the same excitation frequency applied, both size particles experienced the drag force due to the local streaming which bring the particles towards the bubble. Once the distance between the bubble and particle is small enough, which means the secondary Bjerknes force is stronger than the drag force; particles can be caught by the bubble. Another important factor is the particle size: a larger/smaller particle experienced stronger/weaker secondary Bjerknes force than drag force. Therefore, the 1.9 μm particles are able to follow the microstreaming flow lines due to the drag force as the dominant force, as seen from Fig. 4.13 with white dash circle. In contrast, the 6 μm particles are attracted by the bubble due to the secondary Bjerknes force as the dominant force, as seen from Fig. 4.13 with red dash circle.

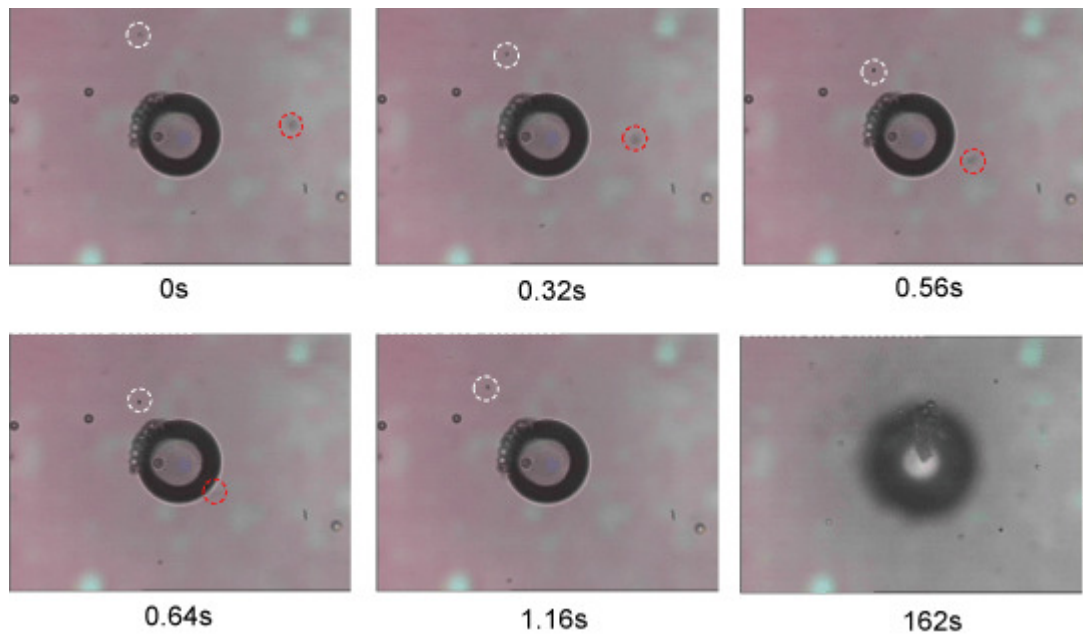


Figure 4.13: Experimental image sequences of the movement of $6\ \mu\text{m}$ and $1.9\ \mu\text{m}$ particles in the $939.5\ \text{kHz}$ acoustic field with a bubble presented. The $6\ \mu\text{m}$ particle (with red dash circle) is attached to the bubble; while the $1.9\ \mu\text{m}$ particle (with white dash circle) is following the streaming line repelled from the bubble.

The differing behaviour of the two particle sizes clearly portends the possibility of a sorting mechanism using a vibrating bubble. The effect is that the larger particles become attached to the bubble whilst the smaller ones do not. The process is totally reversible. Once the actuation is turned off, the captured particles fall away from the bubble (the final image in the sequence of Fig. 4.13) to allow the system to be refreshed and operate anew. It is worth noting that the trapped particles in the bubble are held at a hydrated state [117]; which is useful if the approach is translated to the case of cells. In a practical situation, it should be conceivably possible to operate in an externally imposed bulk fluid flow to affect an almost automated process.

4.3.6 Effect of oscillation mode

The oscillation mode is another factor that influences the microstreaming pattern. In one of the experiments at $673\ \text{kHz}$, as shown in Fig. 4.14, a translating oscillating mode of a vibrating bubble was noticed. A smooth translation as depicted by the white curve pattern shown in the last image was observed. Such translating motion is due to the high acoustic pressure in the field. The bubble moves towards to the minimum energy position. As discussed in section 4.2.2, a particular oscillation mode is hard to secure. A changing from translating and volume oscillation to

translating along an axis perpendicular to the wall was observed, as seen in Fig. 4.15. A symmetrical microstreaming flow pattern with flow being recirculated from one end of the bubble to the other was observed. From Fig. 4.15 (a), attracted $6\mu\text{m}$ particles are concentrated at one side of the bubble, which indicates that the streaming flow moves towards to the bubble from one direction and leaves in the same direction. Such a microstreaming flow pattern is called a “dipole”. In contrast to the “dipole” flow structure, which was also discussed by Tho [84], a microstreaming flow pattern drawn towards the bubble near the plane wall where the bubble was attached was observed. As seen from Fig. 4.15 (b), $6\mu\text{m}$ particles are attached around the bubble evenly in all the direction.

The translating of an oscillating bubble along an axis perpendicular to the wall is the dominant mode in our investigations. This may be caused due to the unsealed glass cover where the bubbles attached. When the device is under a resonance mode, the glass cover is also driven into oscillation, which induces bubbles to oscillate in the same direction as that of the glass cover.

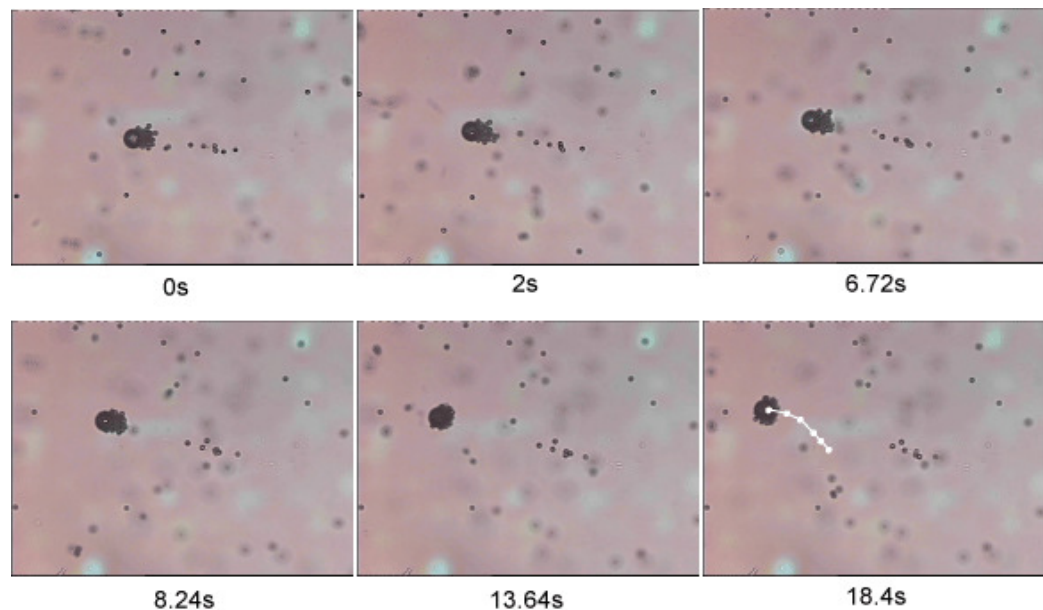


Figure 4.14: Experimental image sequences of a curve translating bubble. White curve pattern presents the bubble trace.

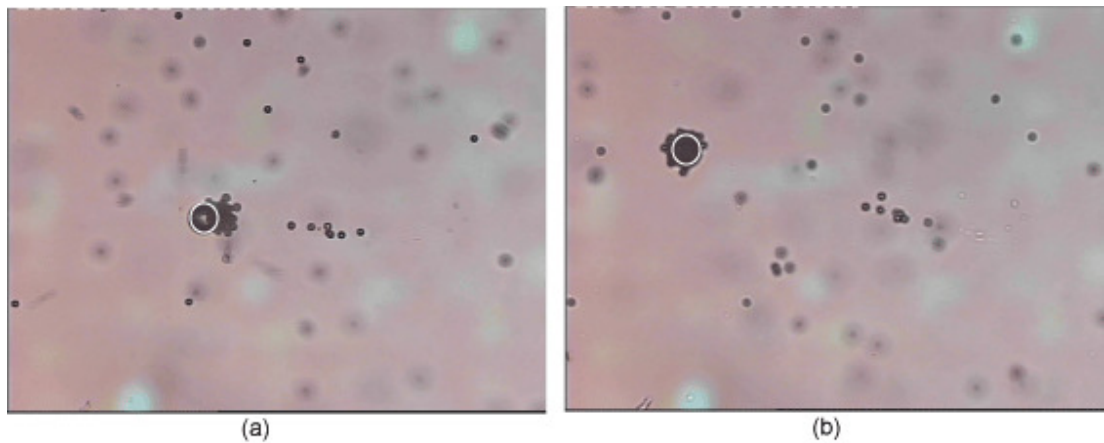


Figure 4.15: Experimental images of (a) a translating and volume oscillation mode and (b) a translating oscillation mode along an axis perpendicular to the attached wall. Arrows present the direction of the streamline.

An alternative oscillation mode was also observed during the investigation. As shown in Fig. 4.16, 6 μm particles are attracted by the bubble due to the secondary Bjerknes force. Interestingly, the attached particles are concentrated at one side and rotate clockwise and anticlockwise at a small angle. Such a micro-sized torque may be useful in application of biological investigations.

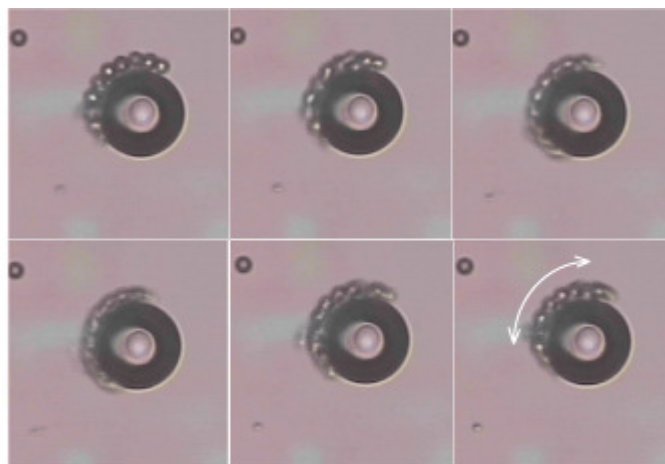


Figure 4.16: Experimental image sequences of a translating oscillating bubble predicted by the attached particles' movement. Each image is 0.04 seconds apart. Arrows show the direction of the oscillation.

4.3.7 Particle separation

In contrast to the microstreaming that resulted in the vicinity of a vibrating bubble, the acoustic streaming as discussed in Chapter 3 exists in the acoustic field together with the acoustic radiation force. The acoustic streaming affects small particles while large particles experienced the radiation force as their dominate force.

In this series of experiments, both 6 μm and 1.9 μm particles were used when 939.5 kHz excitation frequency applied. As the radiation force is the dominant force for large particles, 6 μm particles are moving towards to the pressure nodes, as seen in Fig. 4.17 (a) as forming the particle line, and (b) the particles moving towards the pressure node which are indicated by red circle. In contrast to 6 μm particles, 1.9 μm particles started to swirl between the pressure node and pressure antinodes position which is dominated by the drag force. The 1.9 μm moves towards to the pressure node, as seen in Fig. 4.17 (b). As the result of swirling, the 1.9 μm moves away from the pressure antinode, as seen in Fig. 4.17 (c). The images are taken at the bottom focusing plane from one experiment, and the boxes remain static across the image sequences. The motion difference between the acoustic radiation force and streaming is much clear when the focal plane is at the top layer, which is discussed below.

A continuous supply of power maintains the streaming within the microfluidic chamber, as seen in Fig. 4.18 (a). A turn on-off technique with a discontinuous power supply was applied in a series of experiments to investigate the effect to the acoustic streaming. Clearly, Fig. 4.18 (b) shows an opposite direction of movement observed on the 1.9 μm particles, once the power was on from one second discontinued prior. From the top layer view, instead of moving inward to the pressure antinodes position, small particles moving outward with the same direction as radiation force. In this experiment, the turn on-off is typically using 3s period (2 second on and 1 second off). This is due to the stronger radiation force being dominant instantly. The streaming becomes dominate when the power is on for a while. As a result, Fig. 4.19 shows a large different in the distance between two streaming induced vortices. Initially, the distance of the gap is around 0.11 mm with continuing power supply; after 60 seconds on-off, the distance is measured about twice wider as 0.21 mm. This technique offers a possibility to separate small particles due to the acoustic radiation force by breaking the streaming flow.

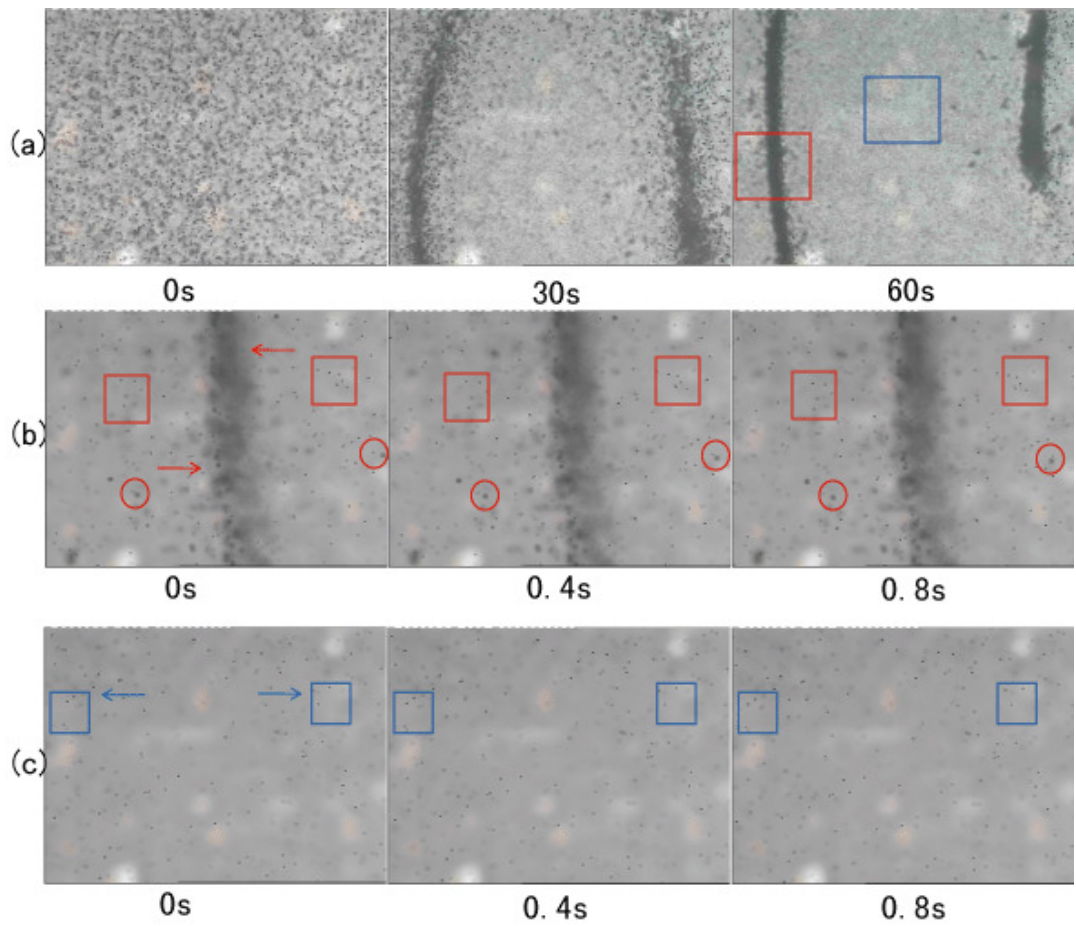


Figure 4.17: Experimental image sequences of particles forming patterns and swirling under 939.5 kHz. (a) Time evolution of 6 μm particles forming lines. (b) Time evolution of 6 μm (circled) and 1.9 μm (squared) particles under acoustic radiation force and streaming, zoom in the red region from (a). (c) Time evolution of 1.9 μm particles under acoustic streaming, zoom in the blue region from (a).

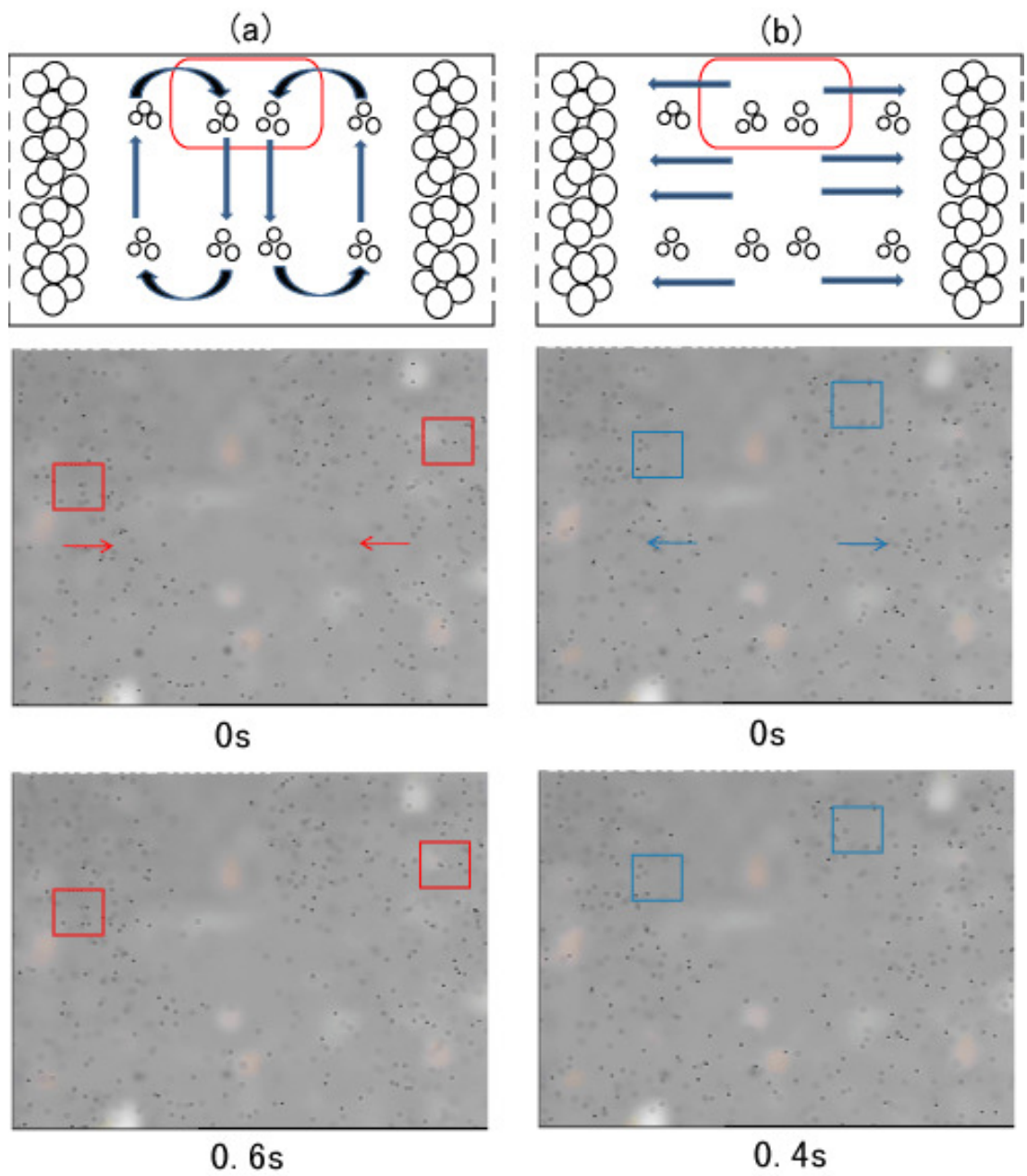


Figure 4.18: Schematic and experimental images of particle movement under streaming: (a) continuous power supply, 1.9 μm particles swirling beside the pressure nodes; and (b) after apply turn on-off technique, the swirling is discontinued as seen particles moving opposite direction observed from the top plane.

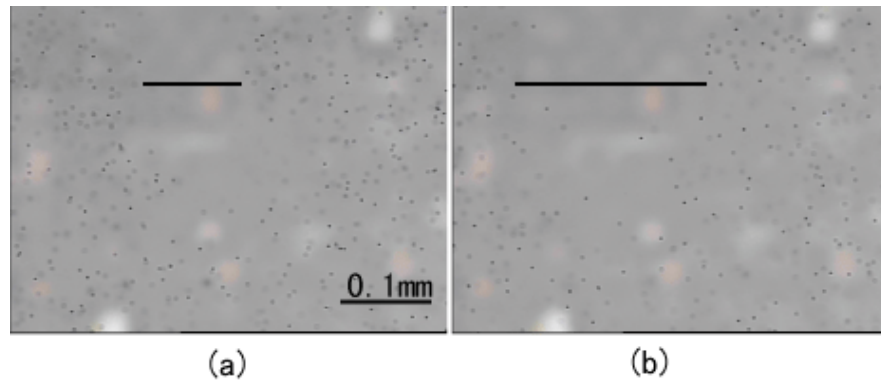


Figure 4.19: Experimental images of (a) initially applying turn on-off technique, and (b) 60s after applying turn on-off technique. The line is to help determining the distance between two streaming induced vortices.

4.4 Conclusions

This chapter demonstrates the ability to use vibrating bubbles in an acoustic standing wave field for size based particle sorting. The operating mechanism involves exciting a bubble within an acoustic chamber at the device resonance, resulting in strong recirculatory microstreaming in the vicinity of the bubble. Depending on the bubble size, particles can be selectively attracted and sorted by comparing the secondary Bjerknes and drag forces. For the large particles ($6\ \mu\text{m}$) which are the secondary Bjerknes force dominated, the particles deviate from the microstreaming lines generated by the oscillating bubble and attach to the bubble. The system can also be refreshed. By contrast, for the small particles ($1.9\ \mu\text{m}$) which are drag force dominated, the particles follow the microstreaming line. The results are also presented in the manuscript which has been submitted to Journal of Acoustical Society of America as in Appendix A.

Furthermore, it has been demonstrated that acoustic streaming force which causes the small particles to circulate in the entire chamber can be broken by discontinuing power supply. As a result, a two fold increase in the gap between two particles can be achieved for small particle sizes.

Particle manipulation using ultrasound techniques has many advantages, such as that large groups of particles can be positioned simultaneously. However, this method consumes energy supply. A more environmental friendly technique required no energy is one of the most interesting research areas nowadays. Therefore, in the next chapter, a developed approach of particle sorting and manipulation by capillary forces is presented.

Chapter 5

Improving the Capillary Force Method for Particle Manipulation

5.1 Introduction

In contrast to the ultrasonic method and other methods which require actuation, capillary forces are naturally occurring. Self-assembly, defined as the autonomous organization of objects into ordered structure, is one of the most efficient methods to order large numbers of small particles. It usually relies on the interaction forces between particles and/or particles and surfaces to drive the formation of ordered arrangements [118]. A wide variety of methods exist including convective assembly [118], capillary assembly [119-121], free-floating sheet assembly [122], and vertical deposition method [123]. The capillary interaction forces between particles which allow self-assembly can also cause the formation of two-dimensional patterns. One well known example is when a coffee drop evaporates on a surface, ring-shaped coffee stains remain on drying [68]. In this case, the boundary between air, solid, and liquid (the contact line) is pinned. The capillary flows push coffee particles to the boundary as fluid flows to replace that lost by evaporation. Based on this, Vyahre, Craig and Scherer [20] demonstrated a way to create and control line patterns using capillary flow. In their experiments, they find, under certain conditions, lines are formed instead of rings, and the process is not sensitive to concentration.

The general techniques for particle manipulation, especially the non-contacting approaches, provide delicacy and a means to move and hold groups of particles at certain locations. An alternative goal is to remove the need for external energy sources. Capillary forces can allow controlled particle assembly, or cause droplets to fill cavities acting as micro-plate wells. As such, capillary forces have intriguing potential in low power applications, such as hand-held diagnostic systems for use in

remote locations. However, when applied to biological applications, the challenge is to keep the cells alive.

In this chapter, a capillary force method that permits particles to remain hydrated, while they are assembled and harvested in batches using a single setup is investigated. Furthermore, the possibility of this method to assemble of different sizes/types of particles is discussed.

5.2 Capillary Flow

In particle manipulation using capillary force, the key factors which can affect the results include: the line tension and the intrinsic contact angle in a solid-liquid-vapour system [124], pinned contact line [68], the Poiseuille flow [125], and the hydrodynamic interaction forces between particles and surfaces [126]. These factors are discussed in this detailed introduction.

5.2.1 Minimum surface energy

To explain how capillary force act on particles causing self-assembly, a solid-liquid-vapour system, see Fig. 5.1, is a good starting point. Calculation of the line tension in a solid-liquid-vapour system is presented by Marmur [124]. The system consists of a solid (S), a liquid (L), and a fluid (F). Imagine that these components are separated and moved to an infinite distance from each other. As a result, each interface ij turns into two individual surfaces i and j . The initial energy of interaction of the three phases is U_{SLF} , and the final energy of interaction is zero.

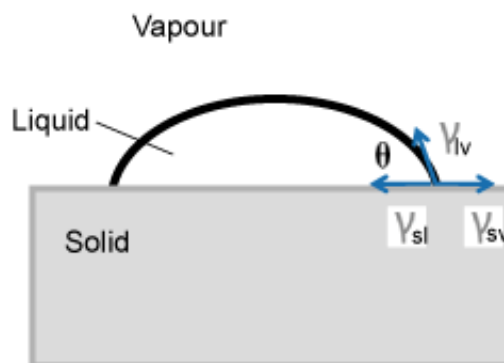


Figure 5.1: The geometrical definitions of the solid-liquid-vapour system

The work of adhesion is related to interfacial and surface tensions by the relationship

$$-\bar{U}_{ab} = \sigma_a + \sigma_b - \sigma_{ab} , \quad (5.1)$$

where \bar{U}_{ab} is the energy per unit area of the interaction of two semi-infinite bodies made of materials a and b , which are touching each other.

In the solid-liquid-fluid system, the interfacial energy of the system would have been the sum of the products of each interfacial tension multiplied by the corresponding interfacial area.

5.2.2 Contact angle

Contact angle, θ , is a quantitative measure of the wetting of a solid by a liquid. It is defined geometrically as the angle formed by a liquid at the three phase boundary where a liquid, vapour and solid intersect. A solid-liquid-vapour system (see Fig. 5.1), consists of a spherical liquid cap (L) sitting on a semi-infinite ideal solid (S), and a vapour (V) which the liquid and solid are immersed.

The well known contact angle theory is the Young equation [127]:

$$\cos \theta_Y = \frac{\gamma_{SV} - \gamma_{SL}}{\gamma_{LV}} , \quad (5.2)$$

where γ_{ij} are the interfacial tensions.

5.2.3 Contact angle hysteresis

The measurement of a single static contact angle to characterize the interaction is no longer thought to be adequate. For any given solid-liquid interaction there exists a range of contact angles which may be found. For example, a surface usually shows two extremes to the range of stable values. When adding additional liquid to a drop on a solid surface, the contact line advances and the drop exhibits an advancing contact angle θ_a , as seen in Fig. 5.2 in grey. Alternatively, if liquid is removed from the drop as in the case of evaporation, the contact line remains pinned until the contact angle decreased to a receding value θ_r , as seen in Fig. 5.2 in black, and then the contact line retreats [128].

The difference between the advancing contact angle and receding contact angle is referred to as the contact angle hysteresis, $\Delta\theta$:

$$\Delta\theta = \theta_a - \theta_r . \quad (5.3)$$

Hysteresis can arise from molecular interactions between the liquid and solid or from surface anomalies, such as roughness or heterogeneities [129].

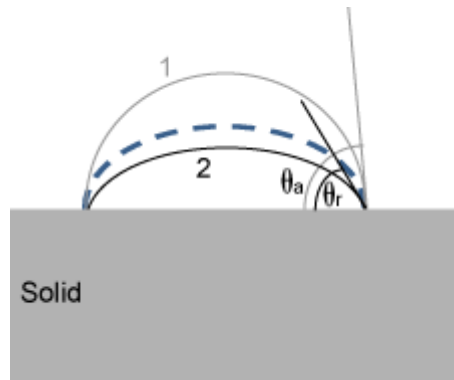


Figure 5.2: Droplet of water on a solid surface (dash line). 1) As liquid is added, the contact line advances, and the droplet exhibits an advancing contact angle. 2) As liquid is removed, the contact angle decreases to a receding value, and then the contact line retreats.

5.2.4 Sharp edges

An additional factor which affects the contact angle is a sharp edge. In the case of floating spherical particles, the contact line is fixed by the Young-Dupre law [130] which states that the contact line must move when the contact angle is fixed. In the case of floating cylinders (or other objects with a sharp edge), when the contact line is pinned at the sharp edge, the contact angle must change. In this case, Gibbs [131] has extended the Young-Dupre law to provide the case for the contact angle at the corner, as shown in Fig. 5.3.

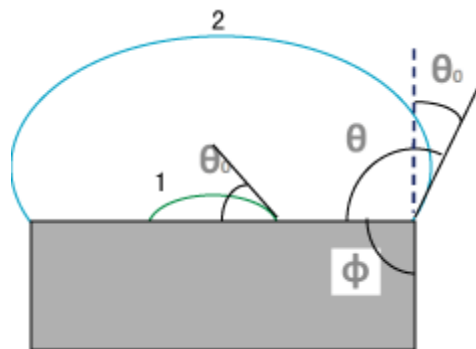


Figure 5.3: Equilibrium of a water droplet at the sharp edge of a solid surface: showing a droplet approaching the edge (1), and in the critical position (2).

The range of the contact angle specified by the Gibbs extension to the Young-Dupre law is then given:

$$\theta_0 < \theta < 180 - \phi + \theta_0, \quad (5.4)$$

where ϕ is the edge angle and θ_0 is the equilibrium contact angle for the vertical face [131].

Unfortunately, the derivation of the Gibbs condition which is given above assumes the edge to possess mathematical sharpness which has no physical reality. However, if one is unable, optically, to resolve the finite curvature of the real edge then, the advance of the liquid drop around that curvature will be indistinguishable from the mathematical edge treated above - the contact line appearing to halt at the edge and the contact angle to increase until the Gibbs criterion is satisfied [132].

5.2.5 Evaporation

The minimum surface energy, the contact angle and especially the contact angle hysteresis all can be affected by evaporation in the solid-liquid-vapour system. In the case of coffee stain formation, the liquid drop wets the solid surface with a certain contact angle value. Initially, the evaporation would alter the height profile, as shown in Fig. 5.4 (a), from the blue profile to the red profile. Such reduction of the liquid volume would cause the drop to shrink. But as the contact line is pinned, the radius of the drop cannot be reduced. Therefore, outwards fluid motion to prevent the shrinkage occurs [68]. As seen in Fig. 5.4 (b), the fluid moving outwards to compensate for evaporative losses results in the particles in the solution being brought to the edge of the droplet. Such fluid flow is also caused by the rate of evaporation, which differs over the drop. Finally, as evaporation continues, the contact angle reaches its receding value, and the interfacial tensions are unbalanced. Thus shrinkage of the drop occurs and the particle patterns are observed.

The evaporative flux depends only on the shape of the drop [68]. At the surface of the drop, the vapour quickly approaches a steady-state concentration profile $\phi(z)$. The steady-state diffusion equation gives:

$$\nabla^2 \phi = 0. \quad (5.5)$$

The desired evaporation flux is given by the derivative at the surface:

$$j_e(z) = -D_v \nabla \phi, \quad (5.6)$$

where D_v is the diffusivity of the vapour in air.

For a drop with contact angle θ , the evaporative flux at the distance z which is from the drop centre approaches to the contact line has the form:

$$j_e(z) \propto (R_d - z)^{\frac{\pi-2\theta}{2\pi-2\theta}}, \quad (5.7)$$

where R_d is the drop radius.

The total evaporation flux per unit length of the leading edge is the integral of along the axis x , gives [119]:

$$J_{evap} = \int_0^{\infty} j_e(z) dz. \quad (5.8)$$

Therefore, the evaporation flux is increased as the distance is increased. In the case of the drop evaporation, the outer range evaporates faster than the inner centre.

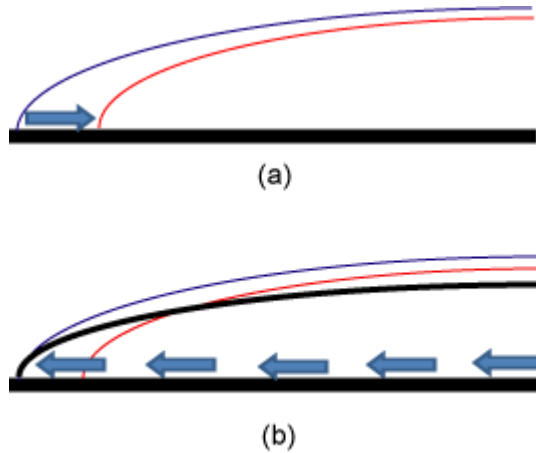


Figure 5.4: Schematic description of the fluid flow during evaporation in a drop. (a) The evaporation without flow cause a drop shrinks. (b) The outward flow to keep the contact line fixed.

5.2.6 Interaction forces in a capillary chamber

There is a difference to the open fluid case when the fluid lies between two parallel sheets, such as in a capillary chamber. Some unique features need then to be considered as well.

Poiseuille flow

Poiseuille flow describes laminar flow in a tube or between parallel sheets [125]. The latter is exactly the flow type that occurs when a sample is loaded into a capillary chamber.

To discuss this x is defined as the direction of flow, y is the direction perpendicular to the walls, and L is the wall spacing, see Fig. 5.5. Assuming that the transverse width of the chamber is very much greater than the chamber depth, the width is effectively infinite. If the dimensionless distance across the channel is defined as $\tau = y/L$. Then the fluid velocity v_f at any distance y from the wall is given by

$$v_f = 4v_m(\tau - \tau^2), \quad (5.9)$$

where the peak central velocity at $\tau = 1/2$ is v_m .

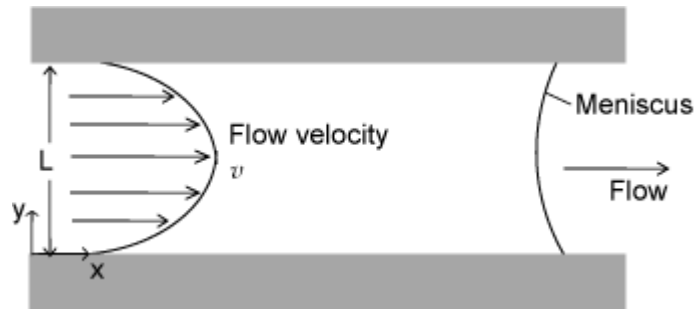


Figure 5.5: Schematic description of the Poiseuille flow in a capillary chamber.

The surface tension force, $S = S_0 \cos \theta$ draws fluid into the chamber, where S_0 is the surface tension between fluid and glass and θ is the contact angle. After the fluid has travelled a distance x into the chamber, the pressure gradient will be $\frac{dp}{dx} = \frac{2S}{Lx}$, where p is the pressure, and the factor 2 is used because there are 2 surfaces separated by distance L .

The peak velocity and the mean bulk velocity are given by

$$v_m = \frac{L^2}{8\mu} \frac{dp}{dx} = \frac{1}{4} \frac{SL}{\mu x} \text{ and } \bar{v} = \frac{2}{3} v_m \text{ respectively,} \quad (5.10)$$

where the viscosity μ is independent of velocity and the pressure gradient is the driving force of the capillary flow. From Eq. (5.9), flow velocity reaches the maximum value at the centre of the channel, which is parabolic in δ . The fluid velocity will be a maximum at the point of entry, proportional to chamber depth, and decreases as the meniscus proceeds into the chamber, which is linearly with the meniscus penetration distance x [125].

Hydrodynamic interaction

Previously, we considered the forces between the fluid and solid surface mostly. However, the hydrodynamic interaction force between particles and solid surface has also been studied by researchers. In confined environments, swimming cells are attracted by surfaces, as reported by Berke *et al.* [126]. The distribution of nontumbling *E. coli* cells swimming between two glass plates in a density-matched fluid was measured. Based on long-range hydrodynamic interactions between swimming cells and surfaces, the hydrodynamic interactions of the swimming cells with solid surfaces leads to their reorientation in the direction parallel to the surfaces, as well as their attraction by the closest wall.

Above all, in a solid-liquid-vapour system, the varying evaporative rate over the drop causes the particles to move towards the edge due to the fluid flow. The contact line moves when it reaches the receding angle. Additionally, the range of the contact angle is extended by conducting a sharp edge. In contrast, in a capillary chamber the pressure gradient is the driving force of the capillary flow. Moreover, the hydrodynamic interactions between the particles and solid surfaces direct particles to be parallel to the surfaces. Therefore, a capillary chamber with sharp edges is a suitable device for particle sorting due to capillary force which is discussed below.

5.3 Development of Particle Assembly in a Capillary Cell

As mentioned in both the Literature Review and the Introduction to this chapter, the capillary method requires no external energy, and particles can be assembled orderly and controllably. Unfortunately, these particles are in a dry condition in the resultant patterns, which is not suitable for cell investigation. To maintain the particles in a hydrated state, liquid needs to be added into the drop regularly to avoid reaching the receding contact angle. By introducing a capillary chamber with a sharp edge, the contact angle hysteresis is extended. This sharp edge allows the particles at the contact line to be hydrated for a much longer period. Additionally, a short travelling distance (short chamber length) is required to limit the solid surface attraction to the particles and maximise the fluid velocity in the chamber. For these reasons, we have developed a capillary cell which leaves the assembled particles in a hydrated state effectively.

5.3.1 Capillary cell and experimental setup

A fluid cell is formed by a cover slip and a glass slide. Firstly, the cover slip is cut into a certain size for preparation. Secondly, deposit a droplet of Milli-Q[®] water (purified water by dispensing through a 0.22 μm membrane filter) on the middle of a glass slide and lowering the cut cover slip until fully wetted. The liquid spreads until it balances the weight on top of it to form a thin film. Three sides of the cell were sealed (Fig. 5.6(a)) in order to avoid evaporation from these sides. Varnish is used carefully to seal the sides of the cover slip, leaving one long side free and an opening in the middle of the opposite side. The small opening was left at the centre of the sealed edge so that a droplet of particles in suspension can be introduced during the experiment.

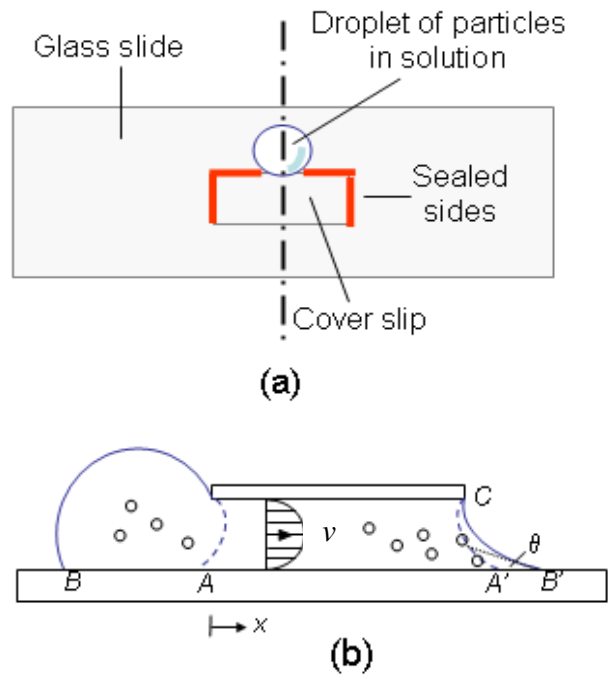


Figure 5.6: Schematic description of the proposed method to locate particles in position using capillary force (not to scale): (a) the top view of the device used in the experiment, and (b) the cross-section view about X-X with description of flow mechanics from droplet the meniscus.

The solution droplet deposited at the opening creates a continuous fluid body, combining the droplet and the cell contents. This body must re-establish equilibrium, clearly observed by a movement of the contact line at the free edge of the cell (depicted as being from A' to B' in Fig. 5.6 (b)). The sharp edge of the cover slip (C) allows a large range in the contact angle, hence the meniscus can deform as shown [131]. As evaporation progresses, the droplet free surface and meniscus combination will recede gradually before eventually falling back to the original position of A and A' respectively. In the intervening time a flow occurs within the cell which causes particle collection and assembly, which is governed by two effects - the quasi-static maintenance of equilibrium of surface forces acting on the fluid, and the replacement of evaporated fluid. We consider them separately, though they are interrelated.

The particles chosen were 6 μm diameter copolymer microspheres, as they are clearly visible under magnification levels offering a suitable field of view. A droplet of 1.3 μl Milli-Q[®] water was released on the middle of a glass slide this forms a thin film when a cut cover slip (3 by 22 mm) is placed on top of it creating the liquid cell. This gives a cell height is 10 μm [126, 133]. Varnish was used carefully to seal the

sides of the cover slip, leaving one length side free and opening in the middle of the opposite side. Then, a 1.4 μl solution droplet was placed carefully at this opening. A CCD camera (Hitachi HV-D30) attached to a microscope permitted viewing and recording from the top of the device (Fig. 5.7).

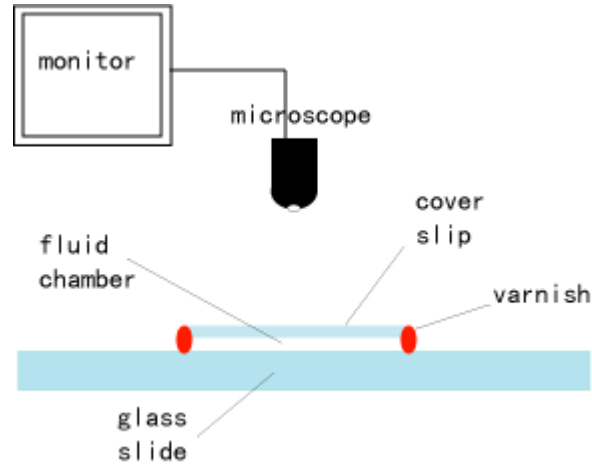


Figure 5.7: Schematic description of experimental setup for particle assembly in a capillary cell.

5.3.2 Particles assembly investigation

The flow rate

The addition of a droplet causes a short time scale flow through the chamber, as equilibrium is sought. Subsequently, as fluid evaporates this equilibrium needs to be maintained resulting in further flow. The equilibrium of a small scale open fluid system is most easily considered as the minimization of the surface energies of the liquid vapor interface and the solid liquid interface, and the line energy related to the movement of the contact line (during which the equilibrium contact angle, θ_0 , may alter through a range between the receding angle, θ_r , and the advancing angle, θ_a). This can be expressed as [124]:

$$\delta W = 0 = \gamma_{LV} dA_{LV} + (\gamma_{SL} - \gamma_{SV}) dA_{SL} - 2\pi k dr_w, \quad (5.11)$$

where δW represents the work change, γ_{LV} , γ_{SL} and γ_{SV} are the surface energies (subscripts being liquid, solid and vapour), and k is the line energy. The other variables are geometric, dA_{LV} and dA_{SL} are the interface areas, and r_w is the radius of the wetted area of the solid surface. So the fluid will seek to minimize surface areas and contact line length.

The second important physical mechanism, evaporation as discussed broadly in section 5.2.5, also affects the flow rate. By idealizing the bottom tip of the meniscus B' as a wedge with a length r , typically order 1mm, [68] (Fig. 5.8) the evaporative flux in a droplet at distance x' from the contact line is given by (refer to Eq. (5.6))

$$j_e(x') = j_o x'^{-((\pi-2\theta)/(2\pi-2\theta))} , \quad (5.12)$$

where j_o is an evaporative constant. The evaporation flux outside this region j_b is a constant for the bulk suspension in which x' is replaced by r . In a quasi-static situation of a flow at reasonably low speeds, the shape of the meniscus is kept by a fluid flow J_s towards the contact line in which [119] (refer to Eq. (5.7)):

$$J_s = \int_0^r (j_e - j_b) \eta(x') , \quad (5.13)$$

where $\eta(x')$ is the arc length of the meniscus surface. Again in the case of a droplet, this causes a net flow to the perimeter of the droplet.

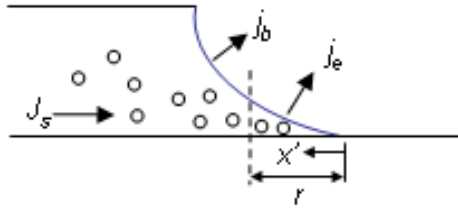


Figure 5.8: Schematic description of the evaporation mechanics from the meniscus causing a flow that will carry particles towards it.

The varying ability of vapour to diffuse (allowing further vapour to be removed) causes the changes in evaporative rates across a droplet [68], so the addition of the cell which creates a wedge of narrow width (ideal for enhanced diffusion) and a long length should prove to be an efficacious evaporative structure.

In the case of the cell, we see that a shift in the meniscus shape from B' to A', whilst the contact angle at the lower edge remains the same, causes the surface area of the meniscus varies greatly. We can thus expect that the evaporation will be faster in the case of B' (possessing the larger area), so the change of meniscus shape affects J_s – which drives particle deposition capability, in contrast to methods such as vertical evaporation colloidal deposition (VECD) [123]. In our approach, the continual droplet deposition at the inlet ensures that particle collection and concentration can

be maintained at a fixed location; making it also accessible for harvesting and without the need for drying.

Figure 5.9 tracks individual particle speeds over time at a distance of 2.2 mm from the free edge. Speeds of about 0.4mm/s were measured initially, reducing to 0.007 mm/s, as evaporation progressed over the next 312 seconds. At 350 seconds, another particle solution droplet of 1.3 μl volume was placed at the input; the speed was restored to 0.2 mm/s and again reduced rapidly. It is evident that no backflow (into the droplet) occurs.

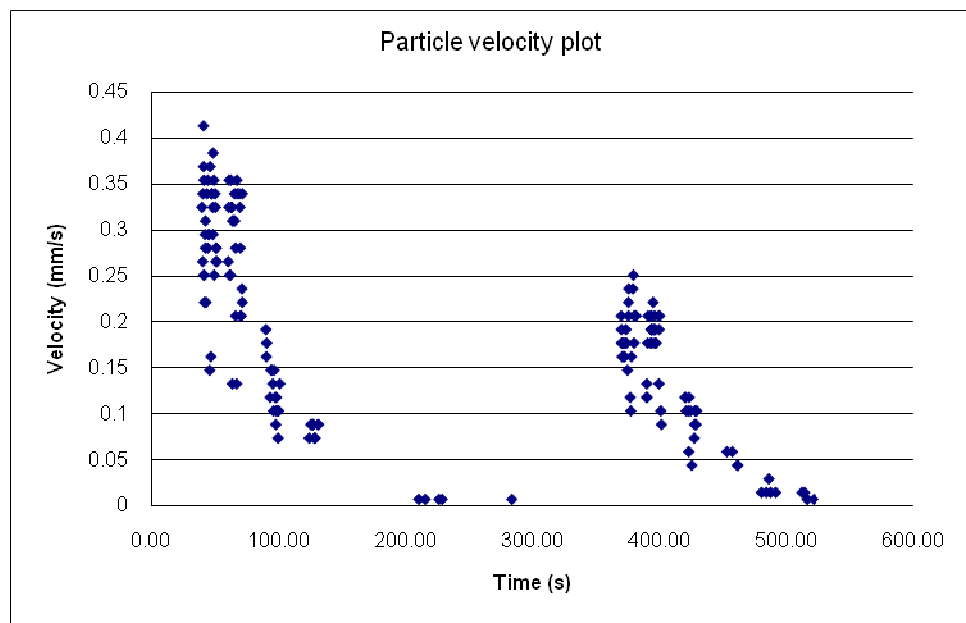


Figure 5.9: Plot of velocity of particles in the cell against the time, at the location of 2.2 mm away from the free edge. The droplet was refilled by Milli-Q[®] water at 350s.

Particle concentration across the chamber

Figure 5.10 gives a plot of particle concentration at 1.9 mm from the free edge after 100 seconds, approximately uniform concentration was achievable across a span length of about 11.5 mm. This illustrates the suitability of the technique in providing a steady throughput of particles to be collected, concentrated or assembled. Outside this span the particle concentration fell to almost zero this is attributed to the limit of the flow fanning out from the narrow entry opening.

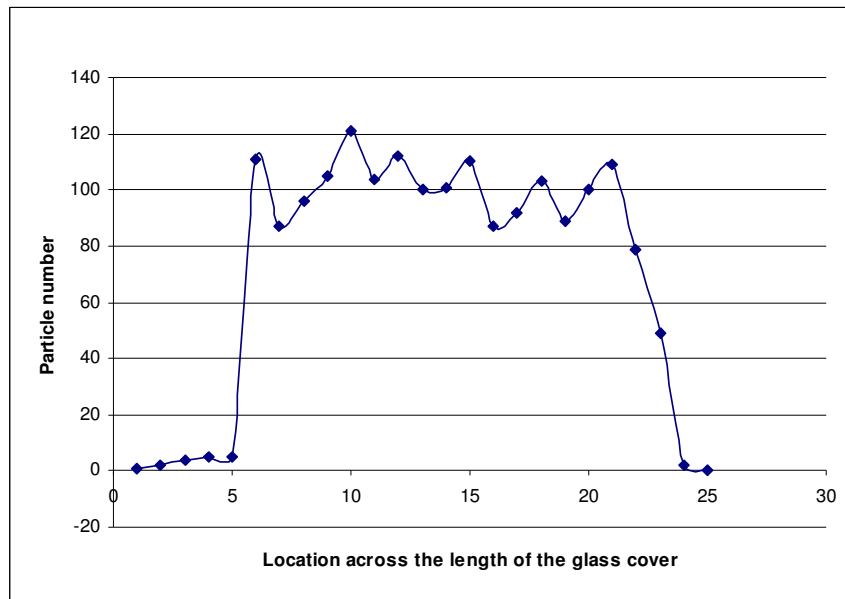


Figure 5.10: Plot of particle concentration along the length of 1.9 mm away from the free edge after a time of 100 seconds. The distribution is clearly a uniform top hat function.

Particle assembling at the meniscus

Figure 5.11 shows the particles collected at the meniscus. As the particles are introduced to the system via the droplet deposited externally to the cell, the aligned particles have passed from this droplet through the cell. It is easily conceivable that assemblies of multiple particles sizes can be achieved by changing the suspensions added in each subsequent droplet. It is clear that the surface tension is able to hold the particles in place. Figure 5.11 (a) and (b) have the time difference of 2.4 seconds apart. Note the minor retraction of the particles back into the solution region in Fig. 5.11 (b), as they follow the retreating meniscus due to water evaporation. That the particle concentration appears somewhat unchanged between the two illustrates that the retreating meniscus is not dominant in the particle collection. The ability to line the particles despite the non smoothness of the cover slip edge in Fig. 5.11 (d) implies the capability to shape the assembly of particles.

The results shown enlighten the interplay between the two mechanisms governing the fluid flow. The following evidence allows this, we note that the maximum flow detected was 0.4 mm/s, furthermore from Fig. 5.11 (a) we conclude the meniscus moves over a distance of approximately 60 μm , shown by the deposition of two particles at this outermost extent (something we observed rarely), the volume of fluid required for this change can be estimated to be transferred in less than a fifteenth of a second at a flow rate of 0.4 mm/s. So, clearly flows arising from maintaining quasi-static equilibrium are negligible, instead evaporation rates dominate. Of course, the

evaporation may be greater in the droplet, but this will not affect flow in the chamber other than by equilibrium maintenance.

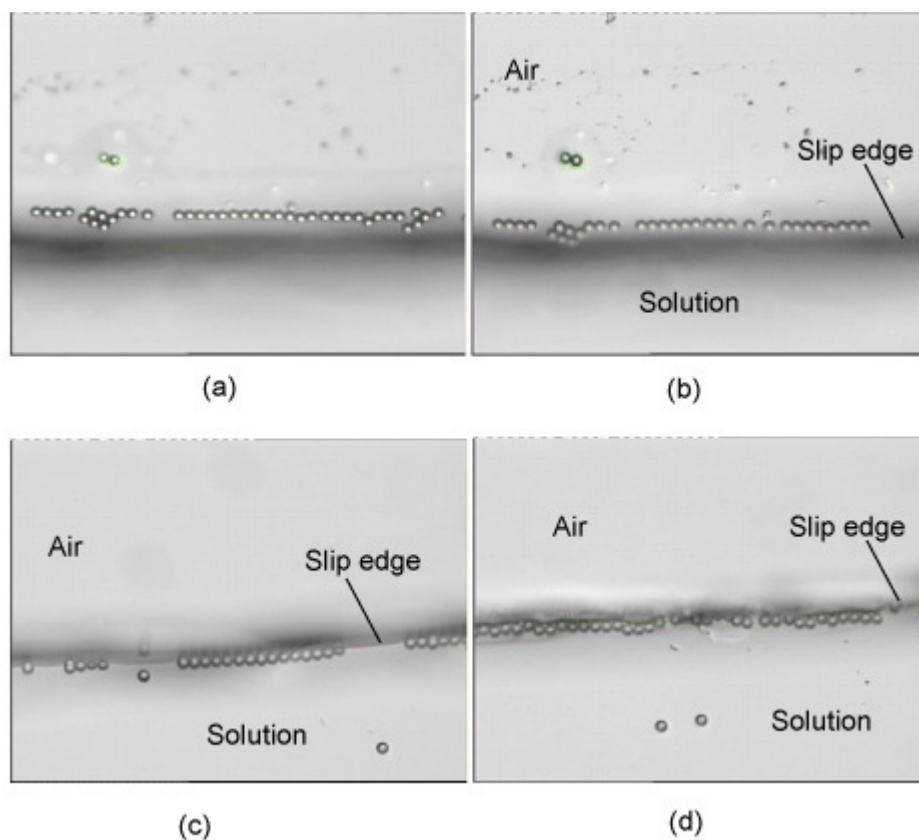


Figure 5.11: Images with particles formed in lines. (a) and (b) show particles forming lines at the free opening, and the second image (b) occurring 2.4 seconds later than (a), clearly showing a slight retraction of the contact line towards the coverslip. (c) and (d) show particles forming lines just under the coverslip edge, with (d) having an undulating edge.

Continuous particle assembling along the batch

In one of the experiments, during the stage of evaporation, both the contact lines (upper and bottom) were receding towards to the cover slip edge. Particles in the solution between these lines were pushed and narrowed. The hydrodynamic force created by the flow dragged particles to the contact line and led to a line formation. Once there was a line formed, the solution in the line was constantly evaporating, and a new supply of fluid must be maintained to prevent line from drying up. This flow brought with it additional solutions that tended to concentrate in the line. The pressure gradient created by the parabolic shape, combined with the flow due to the receding contact line, created a flow pattern.

Figure 5.12 shows the image sequences of the flow pattern at the end of the process when all the solution in the capillary cell was evaporated. After 5 seconds later of the

parabolic formed, from the figure, a particle line is observed. A particle line along the cover slip edge is show clearly in Fig. 5.12 at 9.2s.

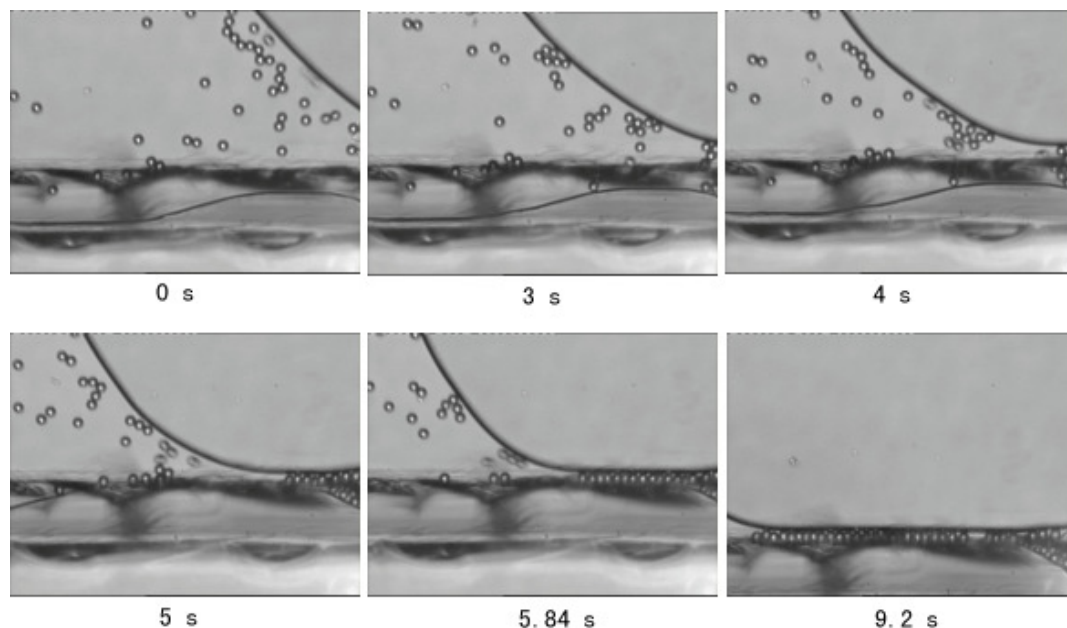


Figure 5.12: Image sequences of particles forming a line along the glass cover edge, when water is evaporated.

5.4 Conclusions

In this chapter, a capillary chamber has been designed and examined by applying capillary force for (a) particles to be hydrated constantly, (b) assembled particles to be harvested in batches and rebuilt with additional particles using the same setup, and (c) particles of different sizes or types to be assembled at specific compositions. This process is very sensitive to concentrations. Previous capillary force studies allow particles to be sorted after staining; and other particle manipulation approaches require energy consumption. For the first time, the particles being sorted in a hydrated state have been developed, and such method avoids any external energy usage. We also demonstrated that the particles can be assembled along the undulating edge resulting in additional control of the patterns formed. Such assembled shapes can be used for functional biosensors and flagella constructions once particles are bound together with agents such as proteins. The phenomenon in Fig. 5.12 happens rarely. The conditions caused this phenomenon should be further investigated. Furthermore, the result that Fig. 5.12 showed is very interesting and useful for particle sorting. Some results are also presented in the paper published in Applied Physics Letters as in Appendix B.

Future progress of self-assembly driven by capillary force has the ability to accurately control the particle arrangement (e.g., lattice spacing control, defect-free, and long-range order) in three dimensions and in two dimensions for a board range of particle sizes, shapes, and types. When certain particles in the lattice itself being defective (such as the wrong size or different shape), it is difficult to use general methods like using surface standing wave or applying an external electrical field normal to the interface to remove these particles. In this case, a sink-float method is more effective. In the next chapter, the method required low energy for particles selecting by applying sink-float scheme is demonstrated.

Chapter 6

Novel Sink-float Scheme for Particle Manipulation

6.1 Introduction

The selective handling of fragile single particles is a challenging task. Cells, for example, have membranes that damage easily and are susceptible to environmental conditions. The ability to handle fragile single particles in a repeatable and convenient manner is vital in the context of operations such as sorting, isolation, and placement. The float sink principle is well known and widely used in the large scale separation of macro-sized items, especially in the recycling industry. There are no previous studies about the float sink scheme used for micro-sized particle manipulation.

Additionally, the formation of ordered two dimensional particle arrays has important uses in the creation of desired surface structures in materials, and sensors in biomedicine. The ability to do this in the form of a floating monolayer via self assembly from inter-particle forces possesses distinct advantages [120, 122]. Some key desirable features in the creation of these structures include the ability to control lattice spacing in a defect-free and long-range order fashion. One convenient method is to use the inter-particle forces which occur between particles of similar characteristics which float at a fluid gaseous interface. However, within populations of particles it is often beneficial to be able to remove rogue units.

In this chapter, a float sink scheme is demonstrated for the first time for delicately handling selective fragile single micro-sized particles. In the following section, a brief background of solid-fluid-gas interface and underlying mechanisms is presented for a better understanding. In the next section, two investigations are conducted: the experimental setup and results of selecting single fragile particle using float sink scheme. A droplet is used to sink a floating particle from water surface. This

approach enables automation capabilities to be incorporated without difficulty; particle selectivity via the deposition of droplets in close vicinity to the particle whilst leaving the rest of the cluster largely undisturbed. With the accurate dispensing of droplets now achievable using technologies developed around the ink jet printer, this portends a useful method of altering removing rogue particles from clusters that form naturally due to capillary forces.

6.2 Background Theory and Underlying Mechanism

Capillary forces of floating particles

One of the most commonly employed particle types in many researches are the spheres particles. They are either presented hydrophilic or hydrophobic. For a particle to sit in equilibrium at a fluid/gaseous interface three forces must be balanced in the vertical direction, these are the capillary force, F_c , the pressure force F_p and the weight of the particle itself. In balancing these forces a deformation of the fluid surface normally occurs, characterized by h , and depicted in Fig. 6.1. The forces are given by [134]

$$F_c + F_p = Mg \quad (6.1)$$

The vertical component of capillary force F_c and pressure force F_p is given respectively:

$$F_c = -2\pi(R_s \sin \theta_c)\sigma \sin(\theta_c + \theta) \quad (6.2)$$

$$F_p = \int_0^{\theta_c} p \cos \zeta (2\pi R_s \sin \zeta) R_s d\zeta \quad (6.3)$$

where R_s is the particle radius, σ is the surface tension coefficient, θ_c is the filling angle and θ is the contact angle.

Substituting Eqs. (6.2) and (6.3) with $M = \frac{4}{3}\pi R_s^3 g \rho_s$, Eq. (6.1) can be simplified in a dimensionless form as

$$\begin{aligned} \sin \theta_c \sin(\theta_c + \theta) = & -\frac{1}{2}B \left[\frac{4}{3}l_1 - \left(\frac{2}{3} - \cos \theta_c + \frac{1}{3} \cos^3 \theta_c \right) \right. \\ & \left. - l_2 \left(\frac{2}{3} + \cos \theta_c - \frac{1}{3} \cos^3 \theta_c \right) + (1 - l_2)(\cos \theta_1 - \cos \theta_c) \sin^2 \theta_c \right] \end{aligned} \quad (6.4)$$

where $B = \rho_F R_s^2 g / \sigma$ is the Bond number [135], $l_1 = \frac{\rho_s}{\rho_F}$ and $l_2 = \frac{\rho_g}{\rho_F}$ are the density ratios.

$$F_P = \rho_F g \pi R_s^3 \left(\frac{2}{3} - \cos(\theta_C) + \frac{1}{3} \cos^3(\theta_C) \right) + \rho_g g \pi R_s^3 \left(\frac{2}{3} + \cos(\theta_C) - \frac{1}{3} \cos^3(\theta_C) \right) - (\rho_F - \rho_g) g h \pi R_s^2 \sin^2(\theta_C) \quad (6.5)$$

where R is the particle radius, θ_C is termed the filling angle, θ is the contact angle of the particle, σ is the surface tension, ρ_F and ρ_g are the densities of the liquid and gas respectively. The deformation, h , itself being given by [136]:

$$h \approx R_s \sin(\theta_C) \sin(\theta_C + \theta) \left[\ln \left\{ \frac{4}{\varpi \sin(\theta_C) (1 - \cos(\theta_C + \theta))} \right\} - e \right], \quad (6.6)$$

where, $\varpi = R_s / L_c$, L_c being the capillary length ($= \sqrt{\sigma / \rho_F g}$), and as such ϖ is the square root of the Bond number, e is the Euler constant. Such an approach allows both unknowns, θ_C and h , to be found, and has been applied for example to surface cleaning [137] and coffee stain deposits [138].

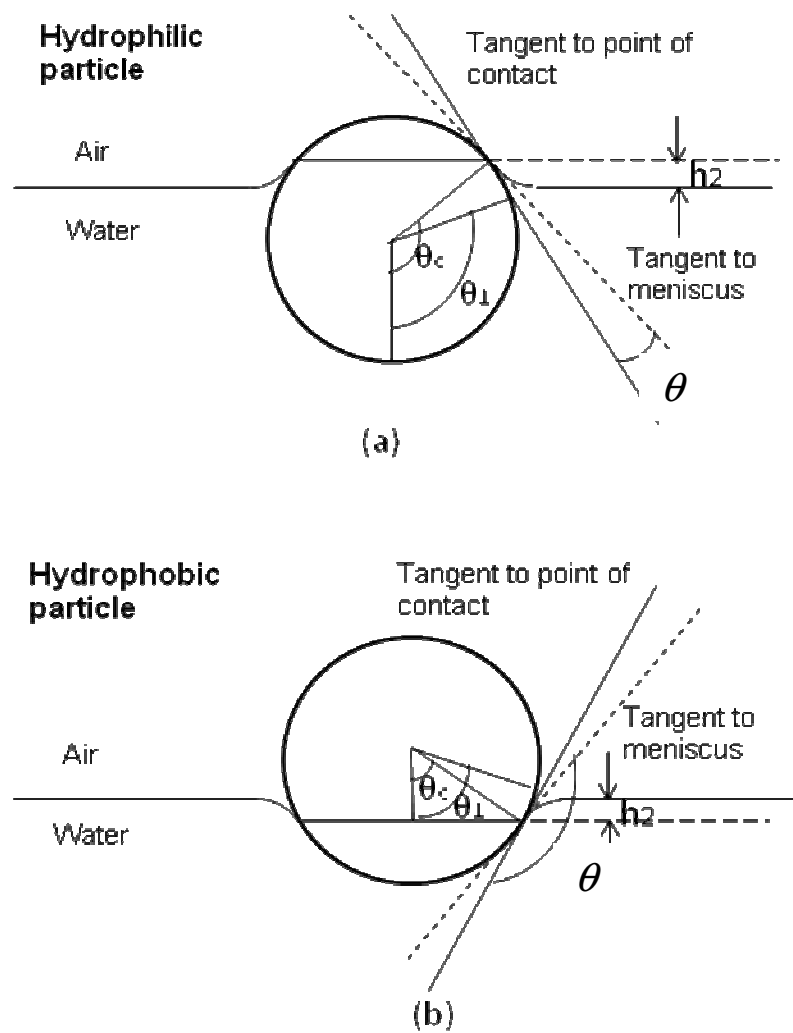


Figure 6.1: Sketch of the capillary meniscus around (a) a hydrophilic particle and (b) a hydrophobic particle.

With more than one particle present at the surface, the deformation causes a capillary force between the particles to occur [139]. The analytical description of the capillary force between two floating bubbles was furnished by Nicholson [140] using the superposition approximation to solve the Laplace equation of capillarity. Similar approximated methods have been furnished by others [141, 142]. For the case where the meniscus slope and particle size are small, the Laplace equation for the interface shape can be solved using bipolar coordinates [143, 144]. The lateral force acting of particles of radii R_{s1} and R_{s2} separated by a distance d is equal in magnitude and opposite in sign and is given by [145]

$$F_{12} = -2\pi Q_1 Q_2 \vartheta K(\vartheta d) [1 + O(\vartheta^2 R_{Si}^2)], \quad (6.7)$$

In this equation, $r_i = R_{Si} \sin(\theta_c)$, ($i = 1, 2$ are the radii of the two contact lines), $Q_i = R_{Si} \sin(\psi_i)$, ψ_i is the interface slope with the horizontal plane at the point of contact, $\vartheta = \sqrt{(\rho_{s1} - \rho_{s2})g / \sigma}$ is the inverse of the capillary length, and $K(x)$ is the modified Bessel function of the first order. The dynamical behaviour of particles floating on fluid can be analysed using Eq. (6.7) and incorporating the relevant drag forces. Simulations of these have been performed [134]. The result of this lateral force is to cause an attractive force between hydrophilic particles [145].

Drop coalescence at fluid interfaces

As Thoroddsen and Takehara [146] mentioned, when a drop is deposited gently onto the surface of a layer of the same liquid, it sits momentarily before coalescing into the bottom layer. High speed video imaging reveals that the coalescence process is not instantaneous, but rather takes place in a cascade where each step generates a smaller drop. This cascade is self-similar and up to six steps are observed. The time associated with each partial coalescence scales with the surface tension time scale. The cascade will, however, not proceed *ad infinitum* due to viscous effects, as the Reynolds number of the process is proportional to the square root of the drop diameter. Viscous effects will therefore begin to be important for the very smallest drops.

When a drop is gently placed on a reservoir of the same fluid, gravity draws the drop downwards and eventually the drop and reservoir interfaces become sufficiently close that attractive Van der Waals forces initiate coalescence. The ensuing

coalescence involves a fluid neck or bridge forming that rapidly opens up (see Fig. 6.2). When the liquid has low viscosity, capillary waves propagate away from the initial point of contact [136]. This induces two possible outcomes; total coalescence in which the drop merges completely with the reservoir, or a fraction of the drop merges with the reservoir and a daughter drop is left behind (see Fig. 6.3). For the latter (partial coalescence) to occur, the horizontal constriction of the interface, which is driven by surface tension on the sides of the drops, must overcome the vertical collapse driven by the curvature at the top of the drop. When capillary waves are able to reach the drop's summit before being damped, they interfere with the vertical collapse and allow the horizontal stretch to dominate and cause the daughter droplet to form [137]. A similar process proceeds with the daughter droplet until coalescence completes. The process of coalescence is extremely fast (in the order of milliseconds) and can only be viewed using high speed cameras.

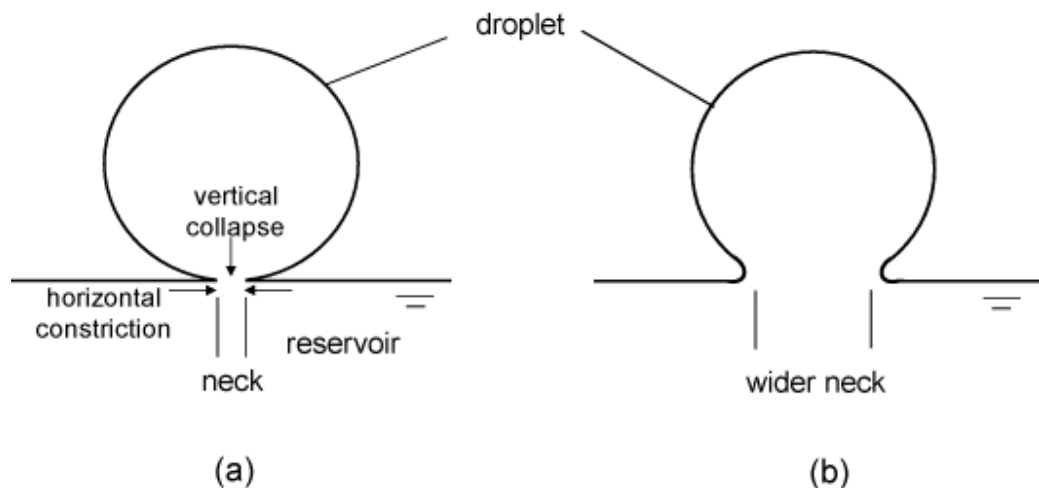


Figure 6.2: Sketch of a fluid neck when coalescence. (a) A fluid neck is forming when a droplet is brought into contact with fluid, and (b) a much wider neck is observed before merging.

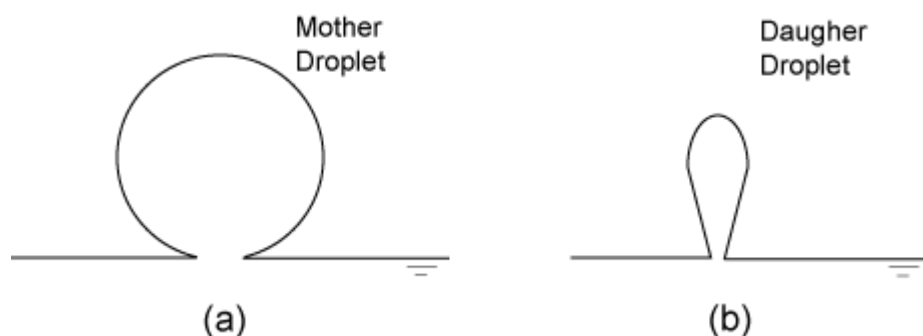


Figure 6.3: Sketch of partial coalescence of a droplet: (a) a droplet is brought into contact, and (b) leaving behind a smaller daughter droplet behind before total coalescence.

When two separate masses of the same fluid are brought gently into contact, they are expected to fully merge into a single larger mass to minimize surface energy.

However, when a stationary drop coalesces with an underlying reservoir of identical fluid, merging does not always proceed to completion. Occasionally, a drop in the process of merging apparently defies surface tension by ‘pinching off’ before total coalescence occurs, leaving behind a smaller daughter droplet. Moreover, this process can repeat itself for subsequent generations of daughter droplets, resulting in a cascade of self-similar events. Such partial coalescence behaviour has implications for dynamics of a variety of systems, including the droplets in clouds, ocean mist and airborne salt particles, emulsions, and the generation of vortices near an interface. Although it was first observed almost half a century ago, little was known about its precise mechanism. F.Blanchette and T.P. Bigioni [147] combined high-speed video imaging with numerical simulations to determine the conditions under which partial coalescence occurs, and to reveal a dynamic pinch-off mechanism. This mechanism is critically dependent on the ability of capillary waves to vertically stretch the drop by focusing energy on its summit. They have shown that partial coalescence of liquid drops is a dynamically driven process, and does not result from the Rayleigh-Plateau instability [147]. The occurrence of pinch-off is determined by a competition between the vertical and horizontal collapse of the connected drop. When the vertical collapse is sufficiently delayed by converging capillary waves, the horizontal collapse succeeds in pinching off the neck and producing a daughter droplet. However, if the waves are strongly damped before converging on the summit, so that the drop is not sufficiently stretched, the drop will fully coalesce with the underlying fluid. The phase boundary between partial and total coalescence is characterized by the critical Ohnesorge number, which depends weakly on the Bond number.

Chen, Mandre and Feng [135] in their report detailed the daughter drop phenomenon with different size of droplet. This phenomenon is governed primarily by inertia and interfacial tension, and three regimes can be further delineated depending on the roles of viscosity and gravity. Scaling relationships are developed for the drop size ratio and the coalescence time. For drops that are too large or too small, partial coalescence is arrested by gravity or viscosity, respectively.

6.3 The Sink-float Scheme for Single Floating Particle Selection

We envisage a method based on float sink scheme, whereby droplets can be released on selected micron-sized single particles floating on the surface of a liquid in order to cause them to sink. Two investigations are presented in this chapter. One is based on the energy transfer from the droplet to the floating particle to cause it to sink, which is discussed in this section. Another is based on the wetting process over the floating particle area which is exposed to the air, see Section 6.4.

According to the force balance equation (refer to Eqs. (6.5) and (6.6)) for a particle floating on the water surface, a hollow glass microsphere with diameter of $120\mu\text{m}$ (density of 2.19 g/ml) is examined for floating on the water surface. Figure 6.4 shows that situation when the particle is in static state, which means the net force is zero, and the filling angle θ_c is 2.67. From Fig. 6.5, as the filling angle is 2.67, the meniscus height is $2\times 10^{-8}\text{ m}$. As a result, such a glass microsphere is predicted to float.

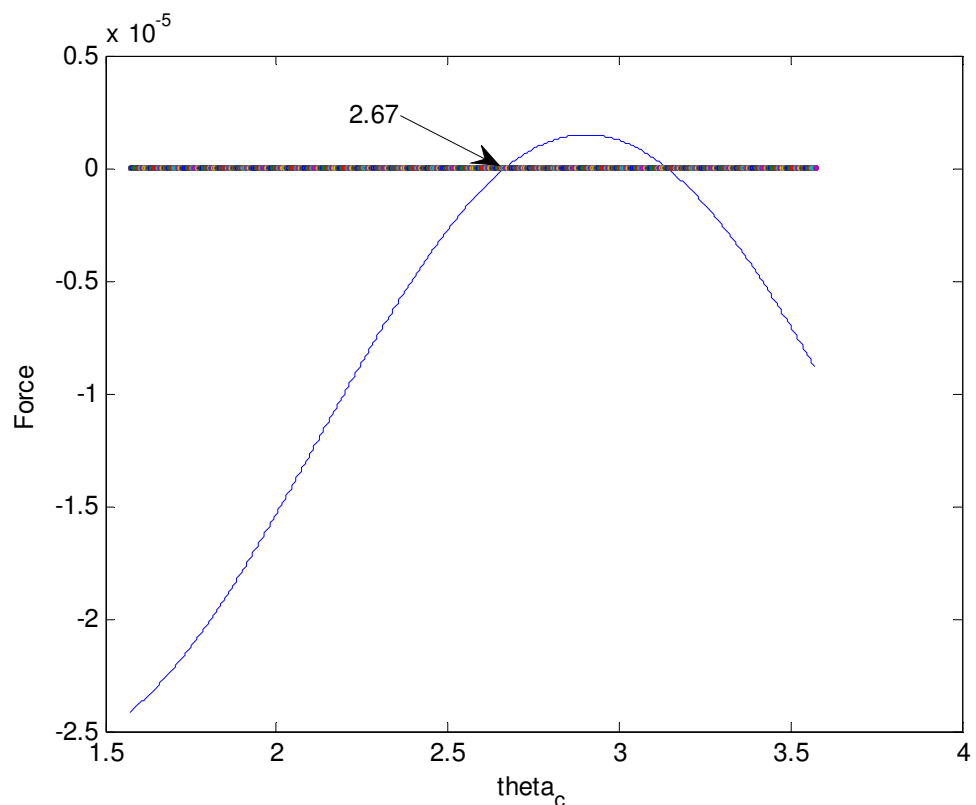


Figure 6.4: Plot of the net force against the filling angle.

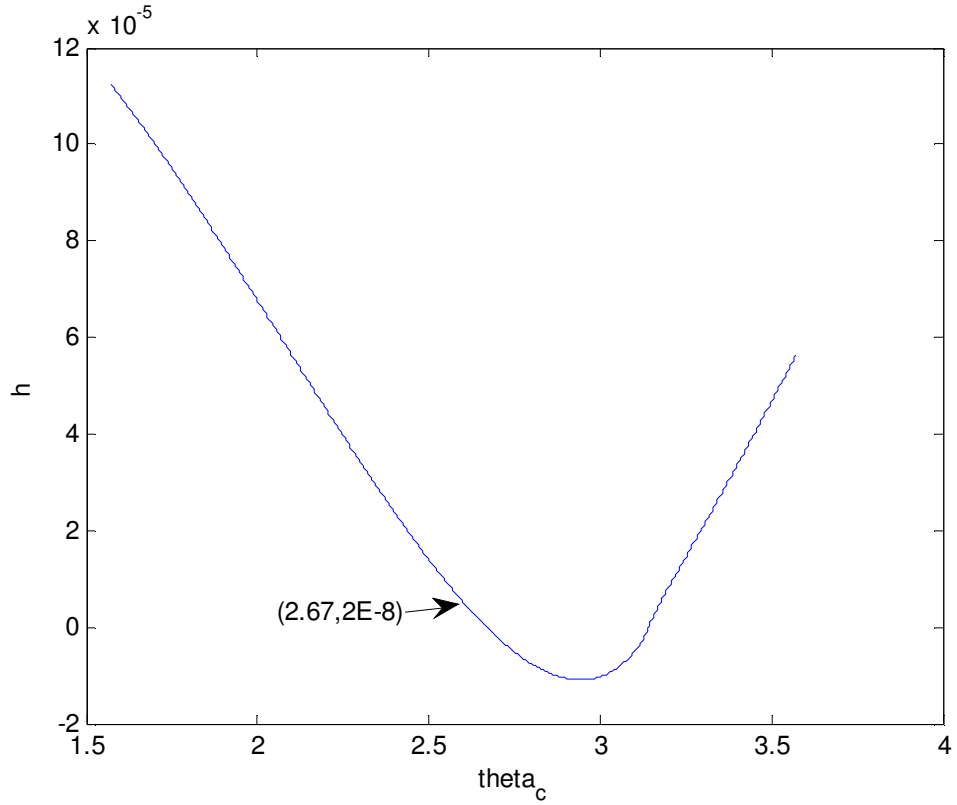


Figure 6.5: Plot of the meniscus height against the filling angle.

Additionally, the work necessary to detach the particle downward from the surface under an applied force has been found to be [136]

$$E = 2\pi\sigma R_s^2 \left[\frac{1}{4} \left(1 - \cos \frac{\theta}{2} \right)^2 \left(7 \cos^2 \frac{\theta}{2} + 8 \cos \frac{\theta}{2} + 3 \right) + \frac{1}{2} \sin^4 \frac{\theta}{2} \left(\log \frac{4}{B \sin \frac{\theta}{2} \left(1 + \cos \frac{\theta}{2} \right)} - e \right) \right], \quad (6.8)$$

where σ is the surface tension, R_s is the radius of the particle, θ is the contact angle, B is the Bond number, and e is Euler's constant.

6.3.1 Experimental setup

The experimental set up is shown in Fig. 6.6. In order to visualize the particle sinking, single particles were placed carefully in the viewable region of a microscope attached to a CCD camera. The particles were glass microspheres with diameters of 103-125 μm . These particles were floated on the surface of Milli-Q[®] water filled in a Petri dish. A flat end needle was positioned using a manual three-axis opto-mechanical. The output from the camera was sent to a computer to monitor the

process and a mirror placed under the CCD camera at an angle in order to be able to visualize both the particle and water droplet at the same time. To minimize splashing, the needle was placed as close as possible to the water surface. Nevertheless, placing the needle too close to the water may cause the droplet to prematurely attach to the water surface. In the experiments, we estimated the droplet dispensed to be $0.3 \mu\text{l}$ giving a radius of $415 \mu\text{m}$.

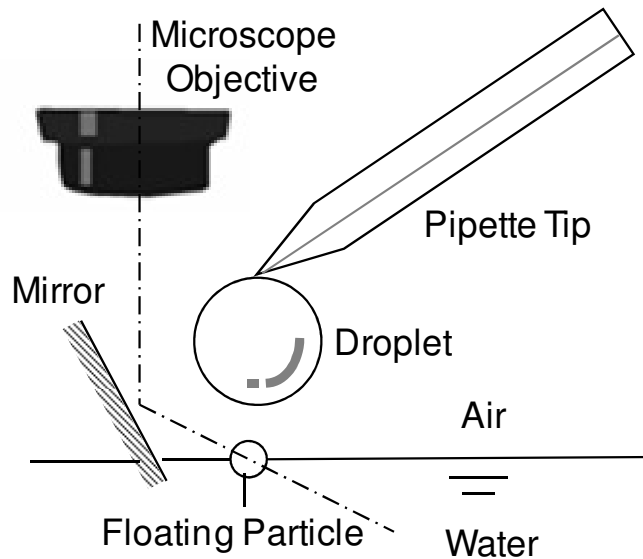


Figure 6.6: Schematic description of the proposed method to handle single particles delicately using a sink-float principle

6.3.2 Particles selected by a droplet

Figure 6.7 presents a plot of E (refer to Eq. (6.12)) against R_s for hydrophilic glass spheres in water. The application of a water droplet on the floating spherical particle can result in sinking in two ways. Obviously, a droplet released directly from an altitude posses a large potential energy that is higher than E ($G > E$), assuming that all the potential energy of the drop is transferred to the particle, will cause the floating particle to sink. Misalignment will necessitate a larger radius droplet or greater height of release to be used for sinking to occur, as imperfect transfer of energy from droplet to the particle and the viscous dissipation by the surrounding fluid. Conversely, if a small droplet engaged in lower release position with the potential energy smaller than E , will still cause sinking, then the droplet wetting the region of

the floating particle exposed to air is considered, which is discussed later in Section 6.4.

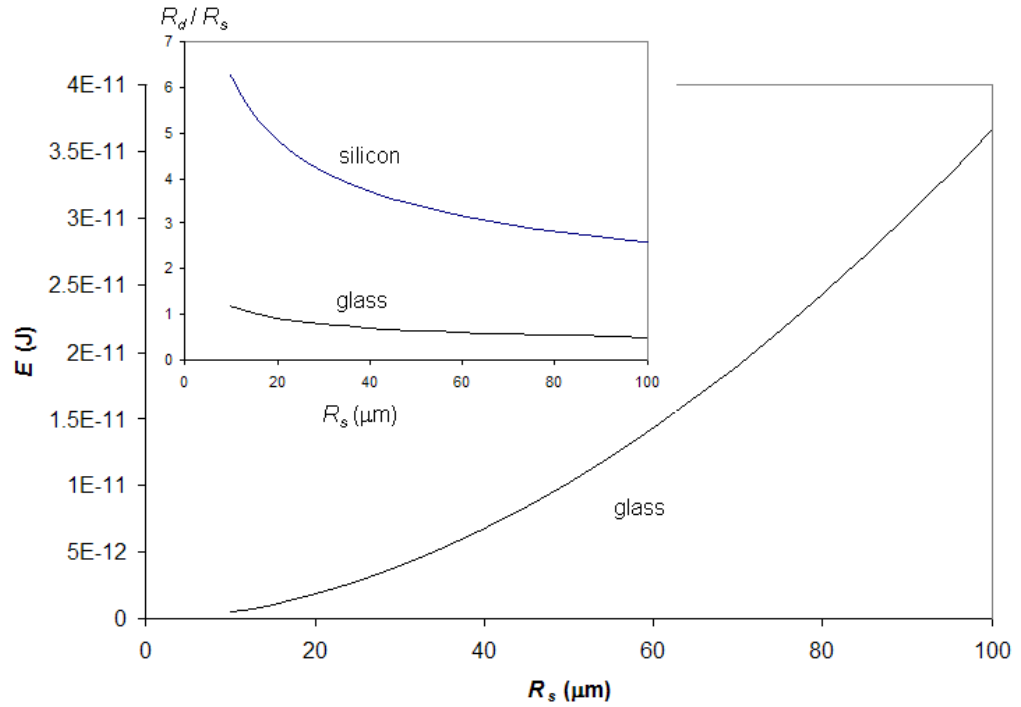


Figure 6.7: Plot of work needed E to detach a spherical glass (hydrophilic) particle downward in water against the particle radius R_s . The inset presents the minimum values of R_d/R_s needed to sink glass and silicon (hydrophobic) particle of radius R_s in water, which is based on perfect transfer of energy from droplet to particle.

Particle Sinking

A series of experiments have been done when the droplet is more in alignment with the floating particle. Figure 6.8 presents image sequences of an originally floating particle that was sunk with a droplet paced above it. The particle was clearly moving toward the needle apex during the first 0.64s of observation. From 0.4s after observation, the droplet began to be ejected from the needle tip. At 0.72s, both the droplet and particle were seen to disappear from view, indicating that the particle had sunk into the liquid as a result of a droplet released close to just above it. As the centre of the droplet was approximately 0.5mm above the liquid surface, this amounted to a potential energy G of 14.7×10^{-10} J. This was clearly higher than values of E depicted in Fig. 6.7 for particle radius between 50 and 60 μm , confirming sufficiency of the $G > E$ condition for sinking by droplet-particle energy transfer.

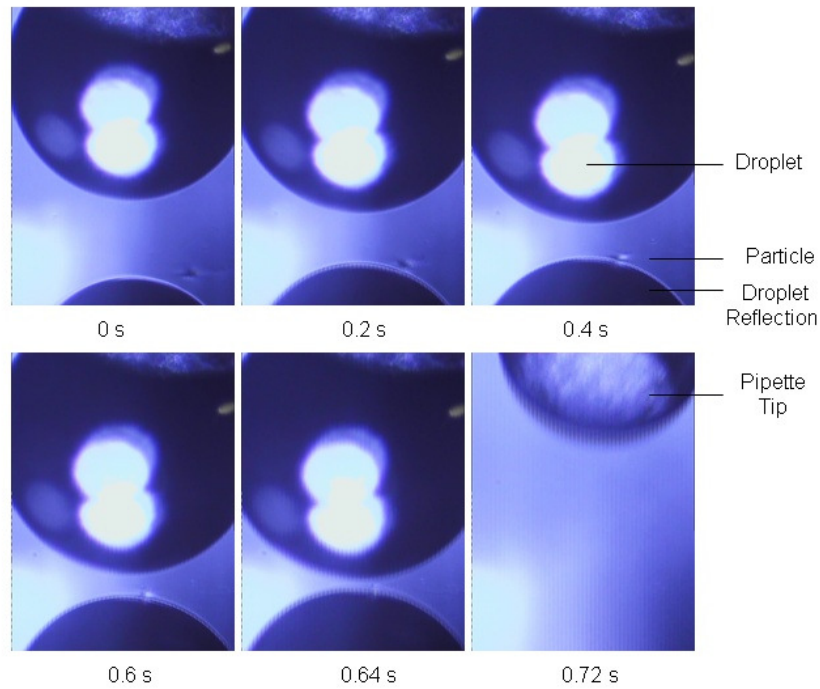


Figure 6.8: Image sequences of a dispensed droplet that caused sinking of an originally floating glass particle in water.

Particle not Sinking

Clearly in the case of $G > E$, the particle may not to sink is also investigated. A series of experiments have been done when the droplet is more in misalignment with the floating particle. Figure 6.9 presents image sequences of an originally floating particle that did not sink when a droplet was dispensed. The particle in this case was visibly more misaligned to the droplet than in Fig. 6.8. Nevertheless, sinking via wetting – if it was the mode of operation - should have occurred considering that the droplet was much larger than the particle, and the particle was located well within its vicinity of influence. This result appears to indicate that detachment with an applied force is the dominant mode of action. If so, this offers considerably greater resolution in selecting which particles to remove from the liquid surface. The results shown indicate the viability of using this scheme in selectively sink particles from the liquid surface. Receptacles placed under the selected particle can be used as a convenient collection tool.

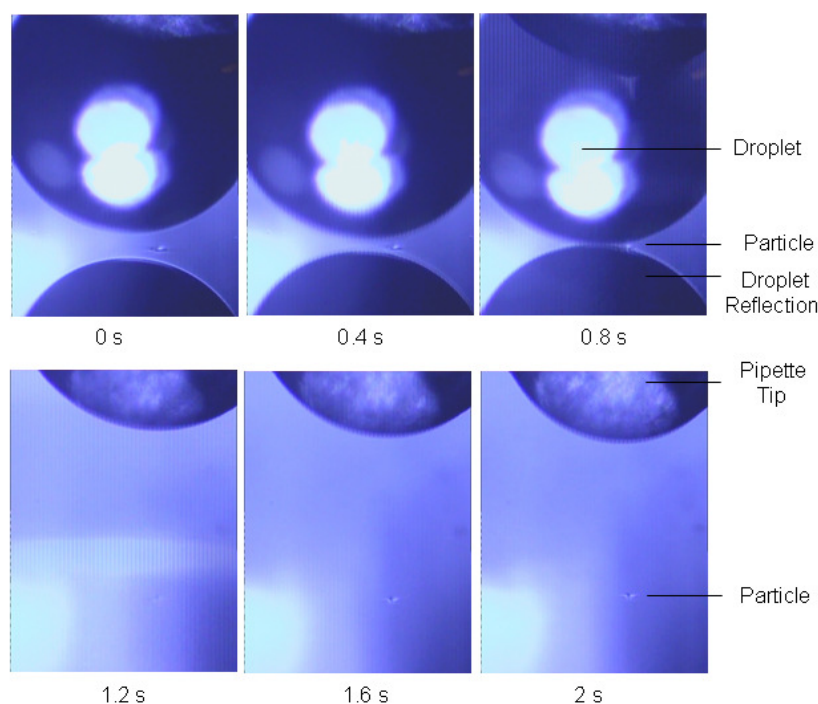


Figure 6.9: Image sequences of a dispensed droplet that failed to cause sinking of an originally floating glass particle in water.

6.4 The Sink-float Scheme for Particle Selection from a Floating Cluster

A single floating particle selection was demonstrated in Section 6.3. In this section, particle selection from the floating monolayer is discussed. Unlike the single particle case, when large group of particles floating on the water surface, capillarity offers a convenient means of congregating particles. This arises because particles floating close to each other deform the interface around them to minimize the interfacial energy [134, 140-145]. Capillarity-induced clustering, while advantageous in that no external energy source need be applied, suffers from the inability to achieve the assembly features mentioned earlier (lattice spacing control, defect-free and long range order) effectively. One approach that can overcome this somewhat is via the use of surface standing waves [148]. However, a method that is more amenable for particles in the micro and nano scale involves applying an external electric field normal to the interface after capillary induced clustering has occurred [121]. Whilst lattices that are defect-free can be created this way, it does not overcome the limitation arising from certain particles in the lattice itself being defective. The context of defective here include situations where the particle may be of the wrong size, differently shaped (e.g. ellipsoidal instead of spherical), chemically incompatible (e.g. improper coating in the case of functionalized particles), or

inappropriate in terms of physical properties (e.g. low density). Typically, if such a particle can be identified, it will be necessary to introduce some means to selectively remove it; preferably in the most gentle manner possible. The application of the sink-float method has been demonstrated to accomplish this well in the context of selectively removing a floating isolated particle [117], see Section 6.3. Typically, a droplet that is significantly larger is dispensed directly above the particle to do so. The question of whether this is workable in terms of removing one particle from a cluster formed by capillarity is intriguing as well as functionally important; and on the surface appears unlikely in view that the droplet to particle size ratio used has to be rather large. Yet, we conclusively show that this is possible; wherein we uncover that the process is influenced strongly by the dynamics of drop coalescence at fluid interfaces.

6.4.1 Experimental Setup

Two series of experiments were conducted. In the first set (Fig. 6.10 (a)), a hollow glass microsphere with a diameter of 120 μm (Whitehouse Scientific GP0116) was attached to the side of a 100 μm thick cover slip in order to create a pin head. This glass slide was then fixed vertically onto a Petri dish filled with Milli-Q[®] water. The water covered the slide and approximately half of the particle, therefore the pin head can be observed above the water surface. The liquid coalescence pattern was investigated by releasing the droplet (of the same fluid) gently on the pin head. The entire process was monitored by a high speed camera (Fastec Imaging) at [500 frames/second] and saved as a digital video file in a computer. The purpose of making the particle static was to align the droplet more accurately with the particles. Such an alignment is especially necessary in the sense perpendicular to the focal plane as video detection is not possible in this direction. This setup also allowed the lighting and alignment of the camera to be better controlled so that high speed images from the side can be recorded for experiments that are inherently difficult to perform. A flat-ended needle (Eppendorf AG) with an inner diameter of 10 μm was positioned using a manual three-axis mechanical translator. A droplet was then produced at the needle tip and lowered gently towards to the pin head. Varied size droplets were introduced in a series of tests that allowed investigation of the nature of liquid coalescence over a particle at the fluid interface.

In the second series of experiments (Fig. 6.10 (b)), clusters of the same hollow glass microspheres were set floating on the surface of Milli-Q[®] water contained in a small Petri dish. A droplet (of the same fluid) generated from the needle was positioned carefully on them by using a Micro-controller (Newport). The output from the CCD camera integrated with a microscope was sent to a computer to monitor the process. The needle was left static in the vertical direction with the tip of the needle positioned 30 μm from the fluid surface. This allowed the distance between needle tip and liquid surface to approximately define the size of the droplet formed, and ensured that the tip will not contact the fluid surface as doing so will cause a sudden movement of nearby particles. Whilst the distance defined the droplet size, it should be noted that the droplet will tend to move up from the tip of the needle, rather than simply hang downwards, thereby causing the resulting drop size to be slightly larger than a diameter of 30 μm .

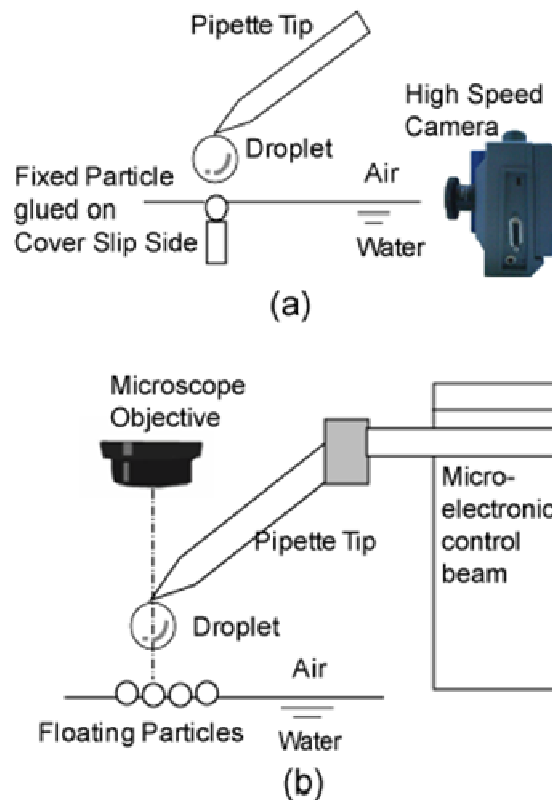


Figure 6.10: Schematic experimental setup: (a) a droplet approaches to a fixed particle, and (b) a droplet sinks a particle from a cluster group.

6.4.2 A Droplet approached to a fixed particle

We consider first results investigating the coalescence of the droplet with the fluid surface with a fixed particle. Figure 6.11 provides images taken using backlighting which allows the edge of the droplet to be more defined. The smaller shape at the centre of the droplet is the bright spot due to light focused through the droplet, whilst

the hump at the bottom of each image (outlined in red) is the particle protruding through the liquid surface. The bulk fluid surface which partially submerges the particle is aligned with the lower edge of the image. In terms of causing a given particle to sink in a given fluid, there are two key parameters: the alignment and size of the drop.

In the image sequences of Fig. 6.11, the centres of the descending droplet and particle were closely aligned (the offset much lower than one particle diameter distance). As the droplet was lowered slowly towards the fluid surface, it first met the particle and then merged with the fluid itself. This process occurred much faster than the speed with which the needle was moved. It can be seen from Fig. 6.10, that a contact line was formed for both the 17 nl and 103 nl droplets on the static particle as they descended until contact was made with the fluid surface itself. After this, the droplet quickly merged with the bulk fluid volume. The transient liquid swells above the surface that appeared on both sides of the static particle clearly demonstrate that fluid from the droplet had passed over both the left and right (with reference to the images) sides of the particle. This can be imputed to indicate that at some stage during the process the particle will have been enveloped by liquid (no contact with the fluid/air interface) and should submerge fully underwater. Under such conditions, the capillary forces assisting a free particle to remain at the fluid surface will disappear and the downward momentum imparted onto the particle due to the rapid fluid motion that occurs as the two unequal fluid volumes merge.

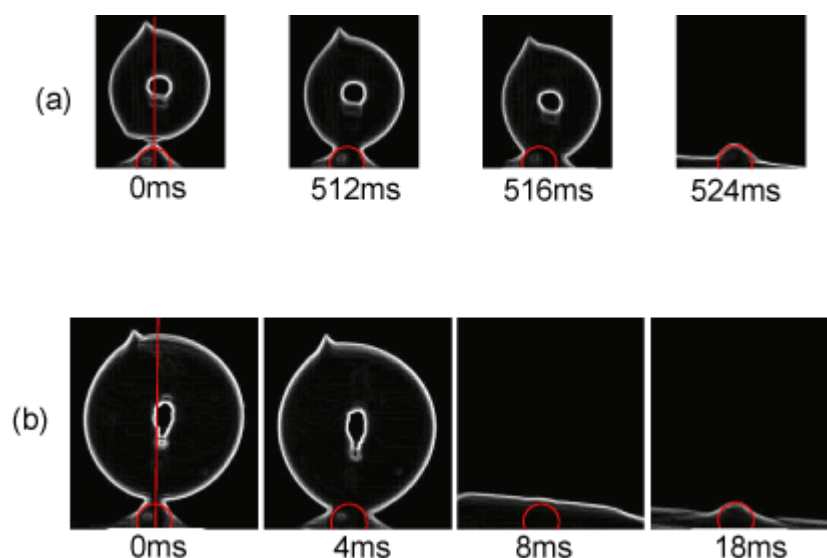


Figure 6.11: Experimental image sequences of the liquid coalescence patterns directly over a pin head by varied droplet size. a) Time evolution of a droplet with approximate 17 nl approached to the pin head. b) Time evolution of a 103 nl droplet approached to the pin head.

Cases of three droplets that were not sufficiently aligned to cause fluid to cover both sides of the tethered particle are shown in Fig. 6.12. A droplet of 4.1 nl (Fig. 6.12 (a)) positioned such that its centre aligned with the particle's center to a degree slightly higher than the cases in Fig. 6.11 did not produce the same outcome. With the droplet lowered to a height close enough to the particle and fluid below such that merging started to take place, the contact line formed between the droplet and the particle was seen to descend on one side (right). The swell of fluid formed as merging completed was entirely to the same side of the particle. This result showed the dependence of the sinking process on the alignment between particle and droplet centers. The second sequence with a 7.1 nl droplet, shows the liquid merging asymmetrically more clearly as the misalignment was increased. With the droplet offset to the left by a distance of 55 μm , the descending droplet made a contact line on the particle which remained high up on the right hand side. When merging began, this contact line remained stationary and the fluid passed to the left of the particle. The third sequence shows the same process with a much larger 103 nl droplet. Even with this volume that was well in excess of the particle size, an offset of 110 μm was sufficient for the fluid to merge almost entirely on one side. Once again the contact line remained high on the particle and ensured that the swell was predominately on the right hand side of the particle.

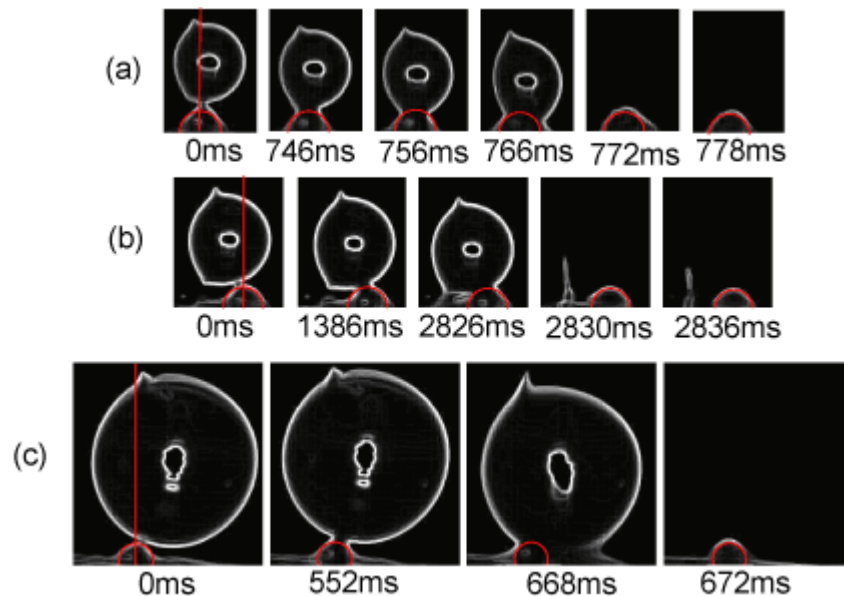


Figure 6.12: Experimental image sequences of the liquid coalescence pattern over a pin head by (a) a 4.1 nl droplet from the right, (b) a 7.1 nl droplet from the left, and (c) a 103 nl droplet from the right.

For the series of experiments the static particle was aligned such it was half submerged when compared with the fluid surface. However, Eq. (6.6) shows that at

the vicinity of the particle itself, the fluid surface will deform to the extent that it interfaces with the particle at its contact angle. For example, a 60 μm radius particle, with 27° contact angle can exact a local deformation of as much as 36 μm in the vertical direction. As the droplet is lowered, a second contact line is produced on the particle. A local deformation can also be expected, though it would be expected to be considerably lower than from that of a flat surface, since any deformation of the spherical droplet will involve a larger surface area change and as such a larger surface energy gradient is associated with this case. It can be seen from the images that there is indeed a tight curve as the droplet meets the particle; again this deformation being such that the contact angle formed is dictated by the three phases present (air, water, and solid). It is when these contact lines meet that merging between the droplet and main fluid body occurs. Such a consideration is largely one of geometry and can be treated as quasi-static. However, it can be seen from the images, that once one side merges, two options can occur: either liquid flowing to one side, or to both sides (within the image plane). It can be seen from Fig. 6.12 (a) that prior to merging, the height of the droplet contact line on the particle is slightly higher on the left than on the right. This meant that flow had occurred on both sides. It can also be seen between the second and third images of Fig. 6.12 (c) that the droplet merged with the liquid such that its contact line drops downwards on the left hand side without allowing flow to develop. Hence whilst the two contact lines must meet to effect merging on that respective sides, this geometrical consideration is not sufficient to predict how merging will take place. In Fig. 6.12 (a) it would predict flow to the right, while in Fig. 6.12 (c) the contact line changed on the left such that a bit greater merging could have occurred on both sides. Clearly, it is the widening of the neck forming between the two fluids which ultimately dictates the nature of the merging process.

It is clear that for the contact line to be removed from the particle by the droplet, which obfuscates the capillary forces maintaining the particle at the interface and ensures downward momentum transferred to the particle from the liquid, the alignment has to exceed critical maximum offset value. Not surprisingly, this value is droplet size dependant. To examine this dependency further, a series of experiments were performed with varying alignment and droplet size, again using a fixed particle in the same arrangement. The needle used had a hooked end. This provided additional control over the droplet. When a droplet of small size is produced at the

tip of a needle, surface tension can cause the droplet to form around the needle tip rather than dangle from it as would be expected at the macro scale. By using a needle with a slight bend, the way in which the droplet clings to the needle is more repeatable (always preferring, based on surface energy minimization, one side). Figure 6.13 (a) shows the behaviour of the various droplets and offset (measured as the distance from the centre of the drop to the centre of the particle) combinations. The outcomes have been classed as either causing sinking (fluid passes over both sides of the particle) or allowing floating (fluid passing over one side only). These outcomes were again determined from inspection of images taken with a high speed camera. It can be seen that for both needle arrangements (bent leftwards – case 1, and bent rightwards – case 2) a change of behaviour occurs once a critical value of offset is exceeded and that this critical value is droplet size dependant. In Fig. 6.13 (b) we correct for the bend of the needle, which causes the tip of the needle to be offset by 32 μm from the shaft (measured from images of the needle after the droplet has coalesced). Hence in this image the offset of the droplet with respect to the particle is measured from the tip of the needle producing the droplet, and it can be seen that the data sets now map over each other. Effectively what this shows is that the offset should be measured with respect to the needle tip. When the droplet merges with the bulk fluid it remains attached to the needle tip until the last moment. Hence it is the location of the tip which is critical. In Fig. 6.13 (c) a diagram of the alignment for cases in which the fluid contact line merges on only one side is shown, it can be seen that the contact line (with no surface deformation) is higher up the particle for larger droplets indicating that in these cases, in which a greater fluid volume is involved, the momentum of the flow which occurs when the fluids merges is sufficient to displace the contact line further than for the small droplet cases.

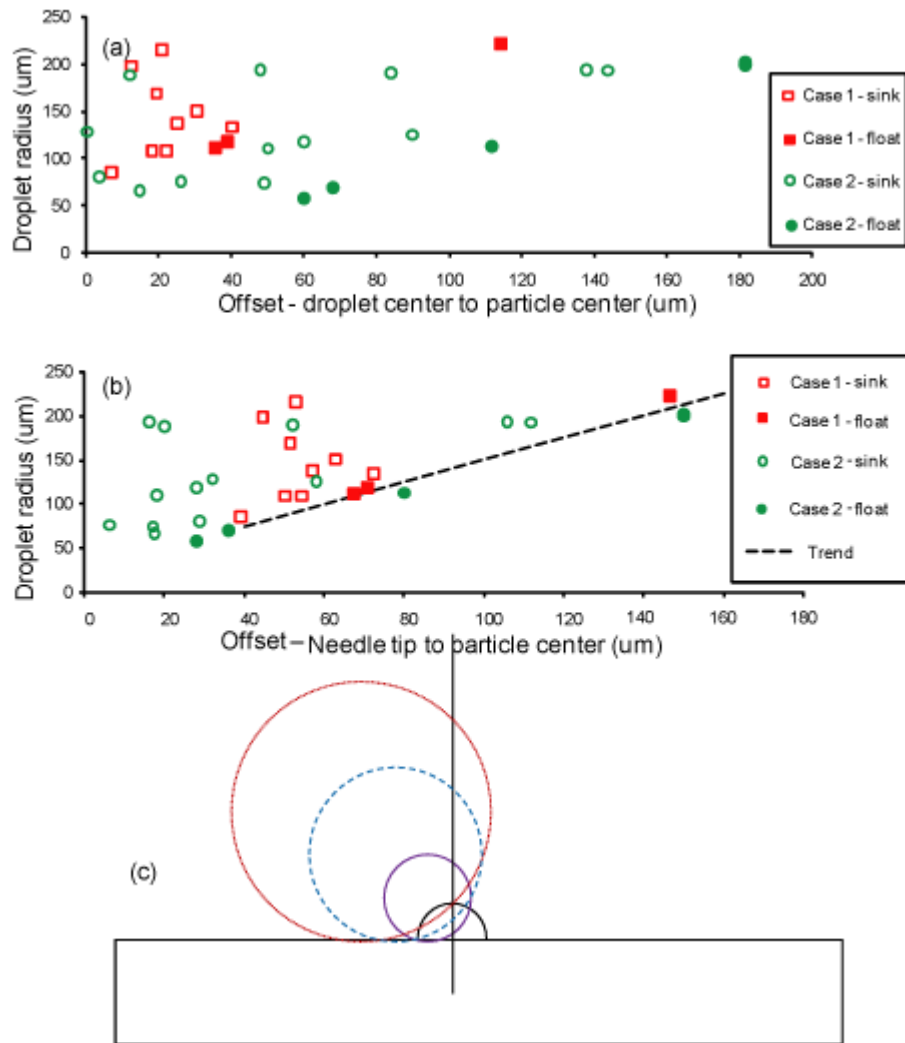


Figure 6.13: (a) Plot of droplet radius against offset distance measured from droplet centre to particle centre; (b) plot of droplet radius against offset distance measured from needle tip to particle centre; and (c) schematic image of alignment of droplet and particle when fluid contact line merging on only one side.

In extrapolating the preceding consideration to that of a free particle within a cluster, we must examine three factors. Firstly, in fixing the particle we have reduced it to a zero degree of freedom object, whilst a particle on the fluid/air interface has 5 degrees of freedom (our aim here is to selectively overcome the sixth direction, that perpendicular to the interface). For a particle in a cluster, the proximity of other particles means that translation within the plane of the interface is hindered; however the three rotational degrees of freedom remain. The effect of the asymmetric flow of fluid over the particle as described above will be to cause some rotation of the particle due to shear forces. In terms of the contact line, this will cause a change in contact line angle based on the contact angle hysteresis of the solid surface. However, as the main body of fluid contact line advances (recedes) due to rotation

the droplet contact line will recede (advance), limiting the role that rotation plays. The second key difference is that due to the presence of the surrounding particles, a limit must be imposed on the maximum droplet size. This is to ensure that contact is predominantly made on the particle selected for removal. As a limit is also imposed on the minimum size due to the need to create flow around the whole particle to cause sinking, it is not assured that removal of individual particles would be possible. Thirdly, it is clear from the previous experiments that as the fluid volumes merge the air/bulk fluid interface raises, whilst for the case of the static particle this plays no major role, the effect will be more sensitive when the particle to be sunk is part of a cluster, possibly hindering the removal of individual particles. Despite these factors, the following experiments demonstrate that the goal of dingle particle removal is in fact possible.

6.4.3 Particles sunk from a floating cluster

To investigate the effectiveness of this method in removing individual particles from a cluster, single droplets are used to sink single particles and then multiple droplets used for multiple targets. In each case the needle is not moved in height, rather the merging of the fluid volumes occurs due to the droplet's growth (at a droplet volume of 3.5 nl). In the case of the multiple targets, this simply means that a larger liquid volume is syringed in to create the multiple droplets continuously.

A single particle sunk by a droplet from a floating cluster

The series of experiments of a single particle sunk by a single droplet from a floating cluster have been done, as shown in Fig. 6.14. Figure 6.14 (a) shows that a target particle is labelled with a black dot, and is surrounded by four almost adjacent particles denoted with red dots. The dots remain static across the images to allow easy comparison. Again from (a) it can be seen that the neighbouring particle furthest to the right is closest to the target. A drop as shown as a bright dot in (a) is initially generated beside to the target. As the drop grows prior to merging as shown in (b) it can be seen that the particles drifted leftwards. There is a net shift by most particles in this direction even by those well away from the droplet, as can be seen from the particle labelled with a blue dot. The shift of the closest particle to the target however is significantly greater, showing a degree of interaction with the droplet (perhaps with a contact line being formed). As the fluid volumes merge the target particle disappears (c). The erstwhile closest neighbour continues to drift leftward, with the

other red labelled particles also moving towards the original location of the target. The most significant movement was made by the red dot labelled particle second from the left, which is also the least constrained by the neighbouring particles in contact. It seems that, as well as the standard drift of the whole cluster, there is also a net movement towards the location from which the target was removed. Clearly, this was most significant for particles in closest proximity.

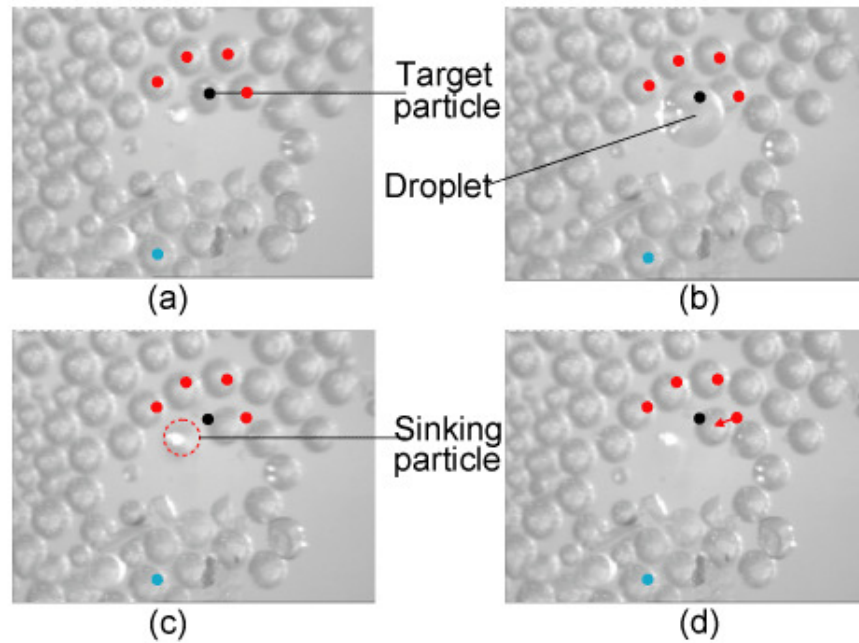


Figure 6.14: An experimental image sequence showing the sinking of a single particle from a floating cluster sunk by a droplet. A neighbour particles movement is shown with the arrows.

Figure 6.15 shows a similar sequence, in this instance three of the surrounding particles move significantly towards removed target particle once it has sunk. The fourth of the adjacent particles continues its drift after merging without a change in direction. This is likely caused by collisions with the other particles. This sequence of events includes a very small particle, which despite its small size does not sink due to the brief rise in the fluid interface height associated with the fluids merging.

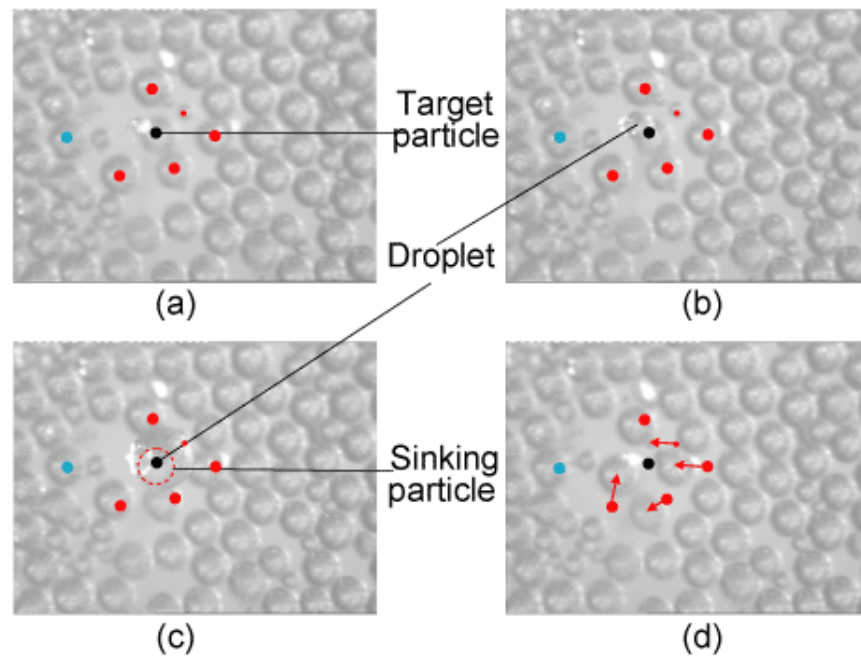


Figure 6.15: An experimental image sequence of a single particle from a floating cluster sunk by a droplet. A small particle can still be seen after the process showing the relatively small effect that the swell of fluid after merging has on the ability of nearby particles to float even when the particle in question is much smaller than the droplet.

A misaligned particle failed to sink from a cluster

Figure 6.16 shows a sequence of images from an experiment in which the droplet was misaligned with the nominal target particle, again labelled with a black dot. It can be seen in (a) that the droplet is formed above five particles, labelled with black and red dots, and is aligned close with the centre point between these particles. The droplet merges with the fluid in (b) without sinking any of the particles. Instead the surrounding particles remain in their position. Note that the bright spot initially appears in (b) is the needle tip. Through images (c) and (d) the drifting demeanour of the cluster labelled with a black arrow with reference to the particle labelled with a blue dot is clearly shown. This steady drift meant that the droplet was further misaligned to the black dot particle when the fluid merged in image (b) as opposed to when it first appeared to be the case in (a). At the time of merging, the droplet was in the middle of the red and black labelled particles. It can be seen in (d) that the neighbouring particle labelled with a red arrow, naturally moves inwards with subsequent fluid merging. This experiment shows that accurate alignment is

required, as was expected from the static particle experiments. Whilst the drifting shown in the experiments can cause misalignment to occur during the process of droplet formation, we see from this experiment that the initial alignment must be poor. Furthermore, droplets can be created rapidly and accurately using technologies developed around the application of ink-jet printing.

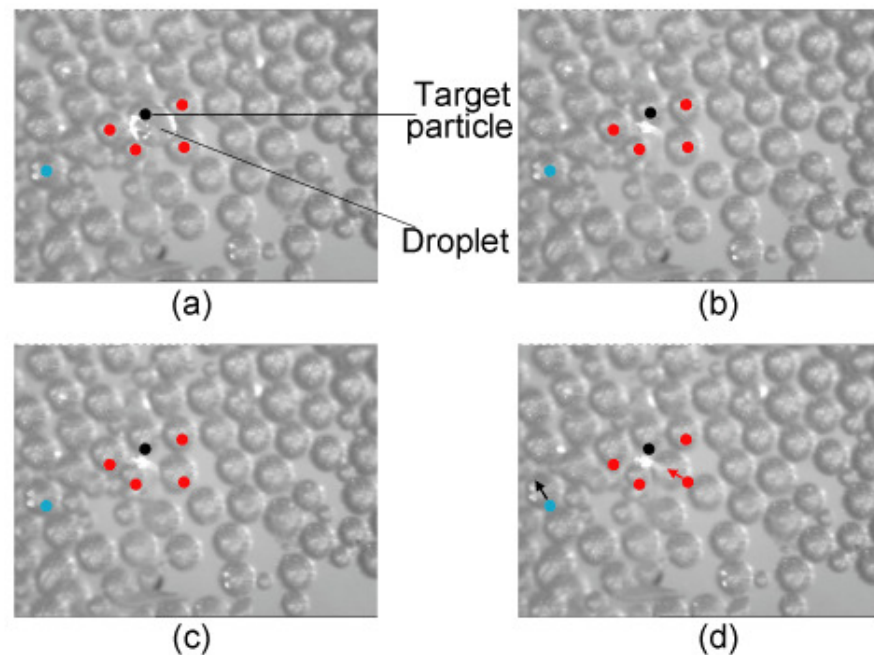


Figure 6.16: An experimental image sequence of a droplet misaligned with a particle fails to cause it to sink. A neighbour particles movement is shown with the arrows.

Surrounding particles sunk by continuous water droplet

By maintaining the height of the needle at a certain fixed value, and syringing excess fluid it should be possible to cause multiple droplets to form and release; each in turn growing until contact is made with the main fluid volume or with a floating particle before merging occurs and the next droplet forms. In this manner it is possible to remove multiple particles rapidly, as shown in Figure 6.17. Here, four particles were removed with four consecutive forming droplets (dotted circles). They are labelled with red, yellow, blue and green dots (listed in order of removal) to more clearly identify them. A black centre is added to the dots to indicate that the particle is sinking (and so moving out of the focal plane). The sequence of particle sinking is dependant on the movements of the particle after each sinking event. In Fig. 6.17 (a) the needle was aligned in the vicinity of the red labelled particle, subsequently (b), a

water droplet was produced to cause sinking to occur (c) and (d). As this particle sinks the yellow labelled particle moves under the next drop due to the ensuing capillary forces, such that by the time the second drop is large enough to merge (f) it sits most closely aligned with this particle. Again the result is sinking (g). A repeat of the process with a drift toward the bottom right (in a diagrammatic sense) causes the blue particle to sink next (i), with the green particle sinking with the fourth and final drop (j). In the context of application, a scheme of using dielectrophoretic force to keep a cluster fixed – as neatly demonstrated by Aubry *et al.* [121] – releasing it for selective particle removal, and then re-engaging it is conceivably possible.

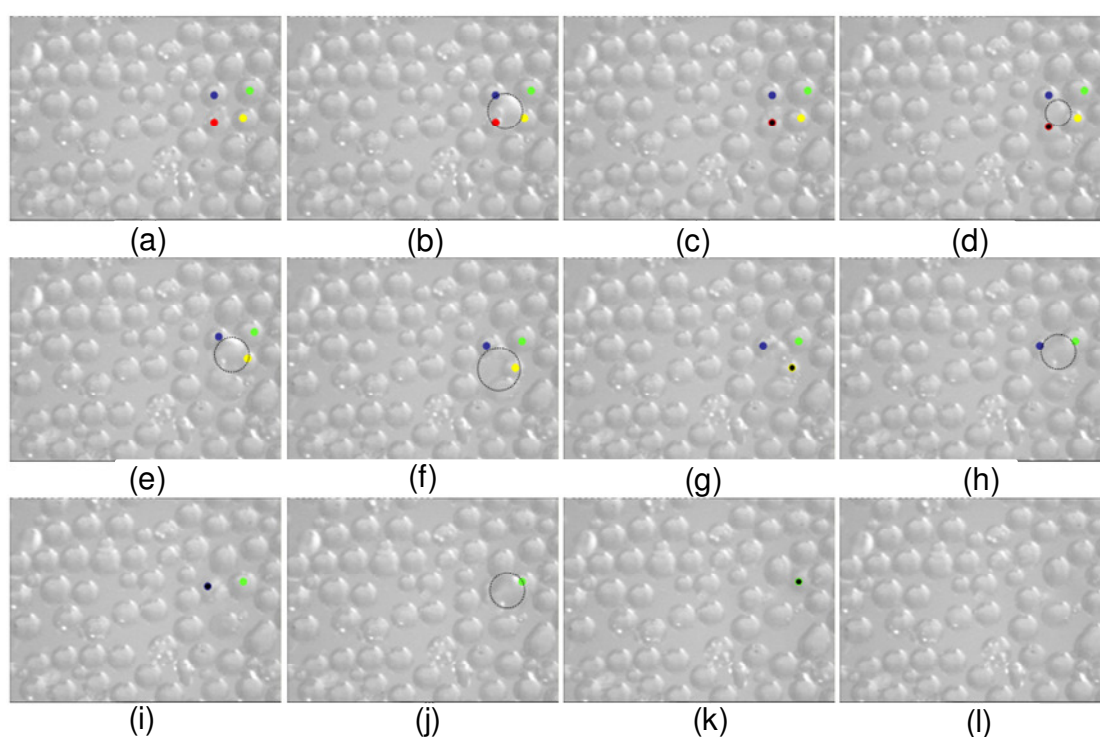


Figure 6.17: Image sequences of surrounding particles sunk by continuous water droplet applied in a fixed position. Coloured dots presents target particles, and the sequence of the sinking particle is bottom left (red), bottom right (yellow), up left (blue) and up right (green).

6.5 Conclusions

In this chapter, a way of delicately handling selected single particles based on the sink-float principle has been demonstrated. This approach enables automation capabilities to be incorporated without difficulty. Furthermore, the use of careful droplet deposition has been investigated as a means of removing rogue particles from self assembled clusters on a fluid gaseous interface. It was found that when the droplets merged with the main fluid volume, the ensuing fluid flow could pass over

both sides of the particle and remove the capillary forces which cause floatation to be possible. Two key factors were considered. Firstly, a study conducted of droplets placed on a submerged fixed particle showed that that there was sinking was limited to the degree of misalignment between the droplet and floating particles. This process was also droplet size dependant, wherein a larger droplet was desirable. Secondly, the fluid merging was a rapid process and a local swell occurred. This process could be lessened if a smaller droplet was used. However, it was found that despite the counter demands on size that a droplet can be used to sink individual particles within a cluster, the neighbouring particles remained floating and the cluster itself stays largely undisturbed.

The work of selecting a single floating particle based on the sink-float was also demonstrated in the paper published in *Applied Physics Letters*, as in Appendix C. Alternative work of selecting particles from a floating cluster was presented in the paper published in *Journal of Colloid and Interface Science*, as in Appendix D.

Chapter 7

Conclusions and Recommended Future Work

In this chapter, the summarization of the research contributions and a discussion of future work are included.

7.1 Conclusions

The general efforts in this thesis pertain to advancements in the techniques of particle manipulation for life sciences. In this vein, aspects of ultrasonic technology, capillary force mechanism and sink-float schemes have been developed. In ultrasonic technology, the endeavour to create a two dimensional trapping plane resulted in the particle positioning technique development. An acoustic device has been examined by observing particular particle patterns when corresponding excitation frequency was applied: one particle line observation under 1.33 MHz, two particle line observation under 2.66 MHz, and three particle line observation under 4.17 MHz. Based on this, two-dimensional (2-D) particle manipulation resulting in particle clumps has been demonstrated by switching frequencies between 1.305 MHz and 0.98 MHz, or rapidly sweeping frequency from 0.97 MHz to 0.98 MHz. Nevertheless, 2-D manipulation as combination of particle focusing and particle levitation also has been demonstrated by exciting the single actuator device in the region of 2.66 MHz to 2.8 MHz. Such levitation can reduce particle wast due to adhesion to the surface.

By further developing ultrasonic technique with vibrating bubbles, the ability to use cavitation microstreaming created around the bubble for size-based particles sorting has revealed the key factors affecting particles performance in the acoustic field. Depending on the particle size, particles can be selectively attracted and sorted by comparing the secondary Bjerknes force and drag force. Drag dominated particle (1.9

μm) behaviour results in the particles simply following the microstreaming generated by the oscillating bubble. Secondary Bjerknes dominated particle ($6 \mu\text{m}$) behaviour, on the other hand, causes the particles to deviate from the streamlines and attach themselves to the bubble, overcoming the weaker drag force.

The success in demonstrating capillary force mechanism for particle assembly in a capillary cell has revealed the possibility in biological investigations. The capillary force method permits the particles to be hydrated constantly, which makes this technique suitable for cell manipulation. Furthermore, the particles can be assembled to be harvest in batches and rebuilt with additional particles using the same setup. Different sizes or types particles can also be assembled at specific compositions. Nevertheless, all efforts listed above can be achieved without active energy supply and in a mechanism in which forces are linearly dependant on particle radius. The manner of operation permits groups of particles to be moved to location of interest, held in place with delicateness, without any external energy sources needed to drive the process.

Furthermore, the introduction of the well known sink-float scheme from macro-sized process to micro-sized particle selection has conducted. Delicately handling selected single particles based on the sink-float principle has demonstrated by applying a droplet dispensed directly above the selected particle floating on the liquid surface. The mode of sinking appears to be based on the detachment of particle from the liquid interface with an applied force. This method offers the desired attributes of particle handling and is amenable to the incorporation of automation to speedily accomplish the selective handling of multiple particles.

Additionally, the sink-float scheme has further expanded for wider application with particle selection from a floating monolayer cluster. The capability of removing rogue particles from self assembled clusters on a fluid gaseous interface via the deposition of droplets in close vicinity to the rogue particle has been demonstrated. With the accurate dispensing of droplets now achievable using technologies developed around the ink jet printer, this portends a useful method of altering removing rouge particles from clusters that form naturally due to capillary forces.

On the whole, both contacting and non-contacting approaches are conducted in the thesis. Ultrasonic method has been exploited by achieving 2-D particle manipulation

while using single transducer; and demonstrated the particles size based sorting method by combining with a vibrating bubble in the acoustic field. Furthermore, the particles can be assembled in a capillary cell remaining hydrated by using capillary flow, which requires no external energy. Additionally, selected single particles can be delicately handled by using sink-float scheme.

7.2 Recommended Future Work

The results of the project of developing advanced particle manipulation techniques in microfluidic systems, point out to several interesting directions for future work.

The 2-D pressure field presented in a microfluidic channel has been demonstrated using ultrasonic technique. However, the generation of such a pressure field was not able to be verified by numerical simulations over the range of actuation frequencies applied in the project research. More experiments are required in further investigations over a wider range of actuation frequencies together with simulation results. A more spatial controlled particle manipulation technique may be achieved.

Moreover, as with sonoporation based on oscillating bubble methods, the strong microstreaming and bubble deformation can lead to rupture cell membrane, further investigation need be conducted on the force effects on the particle in the acoustic field. Future research will be directed to applying this sorting technique to biological applications.

Bibliography:

1. Vilknær, T., D. Janásek, and A. Manz, *Micro Total Analysis Systems. Recent Developments*. Analytical Chemistry (Washington), 2004. **76**: p. 3373-3386.
2. Erickson, D. and D. Li, *Integrated microfluidic devices*. Analytica Chimica Acta, 2004. **507**(1): p. 11-26.
3. Petersson, F., et al., *Continuous separation of lipid particles from erythrocytes by means of laminar flow and acoustic standing wave forces*. Lab on a Chip, 2005. **5**(1): p. 20-22.
4. Haber, C. and D. Wirtz, *Magnetic tweezers for DNA micromanipulation*. Review of Scientific Instruments, 2000. **71**(12): p. 4561-4570.
5. Shao, F.F., A. Neild, and T. Alan, *Controlled particle self-assembly in an evaporating droplet*. Applied Physics Letters, 2011. **Submitted**.
6. Ferrari, E., et al., *Biological samples micro-manipulation by means of optical tweezers*. Microelectronic Engineering, 2005. **78-79**(1-4): p. 575-581.
7. Chiou, A. *Cellular mechanics and DNA mechanics via optical manipulation*. in *Conference Proceedings - Lasers and Electro-Optics Society Annual Meeting-LEOS*. 2005. Sydney.
8. Block, S.M., D.F. Blair, and H.C. Berg, *Compliance of bacterial flagella measured with optical tweezers*. Nature 1989. **338**: p. 514-518.
9. Ashkin, A., et al., *Force generation of organelle transport measured in vivo by an infrared laser trap*. Nature, 1990. **348**(6299): p. 346-348.
10. Ashkin, A., *History of optical trapping and manipulation of small-neutral particle, atoms, and molecules*. IEEE Journal on Selected Topics in Quantum Electronics, 2000. **6**(6): p. 841-856.
11. König, K., et al., *Cell damage by near-IR microbeams [9]*. Nature, 1995. **377**(6544): p. 20-21.
12. Tanase, M., N. Biais, and M. Sheetz, *Magnetic Tweezers in Cell Biology*, in *Methods in Cell Biology*, Y.L. Wang and D.E. Discher, Editors. 2007. p. 473-493.
13. Gosse, C. and V. Croquette, *Magnetic tweezers: Micromanipulation and force measurement at the molecular level*. Biophysical Journal, 2002. **82**(6): p. 3314-3329.
14. Nilsson, A., et al., *Acoustic control of suspended particles in micro fluidic chips*. Lab on a Chip - Miniaturisation for Chemistry and Biology, 2004. **4**(2): p. 131-135.
15. Neild, A., S. Oberti, and J. Dual, *Design, modeling and characterization of microfluidic devices for ultrasonic manipulation*. Sensors and Actuators, B: Chemical, 2007. **121**(2): p. 452-461.
16. Neild, A., et al., *Finite element modeling of a microparticle manipulator*. Ultrasonics, 2006. **44**(SUPPL.).
17. Neild, A., et al., *A micro-particle positioning technique combining an ultrasonic manipulator and a microgripper*. Journal of Micromechanics and Microengineering, 2006. **16**(8): p. 1562-1570.
18. Pohl, H.A., *Dielectrophoresis: The Behaviour of Neutral Matter in Nonuniform Electric Fields*. Cambridge University Press, 1978: p. 1-579.
19. Gascoyne, P., R. C. and J. Vykoukal, *Particle separation by dielectrophoresis*. Electrophoresis, 2002. **23**: p. 1973-1983.
20. Vyawahare, S., K.M. Craig, and A. Scherer, *Patterning lines by capillary flows*. Nano Letters, 2006. **6**(2): p. 271-276.
21. Maxwell, R.B., et al., *A microbubble-powered bioparticle actuator*. Journal of Microelectromechanical Systems, 2003. **12**(5): p. 630-640.

22. Taylor, R.S. and C. Hnatovsky, *Trapping and mixing of particles in water using a microbubble attached to an NSOM fiber probe*. Optics Express, 2004. **12**(5): p. 916-928.
23. Beyeler, F., et al. *Design of a micro-gripper and an ultrasonic manipulator for handling micron sized objects*. in *IEEE International Conference on Intelligent Robots and Systems*. 2006. Beijing.
24. Gattiker, F., et al., *Novel ultrasound read-out for a wireless implantable passive strain sensor (WIPSS)*. Sensors and Actuators A: Physical. **145-146**: p. 291-298.
25. Xia, Y. and G.M. Whitesides, *Soft Lithography*. Annual Review of Materials Science, 1998. **28**(1): p. 153-184.
26. Rathgeber, A., et al., *Planar microfluidics-liquid handling without walls*. eprint arXiv:physics/0104079, 2001. **04**.
27. Chabreyrie, R., et al., *Robustness of tuned mixing within a droplet for digital microfluidics*. Mechanics Research Communications, 2009. **36**(1): p. 130-136.
28. Wixforth, A., *Acoustically driven planar microfluidics*. Superlattices and Microstructures. **33**(5-6): p. 389-396.
29. Oberti, S., A. Neild, and J. Dual, *Manipulation of micrometer sized particles within a micromachined fluidic device to form two-dimensional patterns using ultrasound*. Journal of the Acoustical Society of America, 2007. **121**(2): p. 778-785.
30. Oberti, S., et al., *The use of acoustic radiation forces to position particles within fluid droplets*. Ultrasonics, 2009. **49**(1): p. 47-52.
31. Nguyen, N.-T. and Z. Wu, *Micromixers-a review*. Journal of Micromechanics and Microengineering, 2005. **15**(2).
32. Geng, X., et al., *Bubble-based micropump for electrically conducting liquids*. Journal of Micromechanics and Microengineering, 2001. **11**(3): p. 7.
33. Sato, M., M. Levesque, and R. Nerem, *Micropipette aspiration of cultured bovine aortic endothelial cells exposed to shear stress*. Arteriosclerosis, Thrombosis, and Vascular Biology, 1987. **7**(3): p. 11.
34. Wu, Z., et al., *Adhesion of normal and carcinoma hepatic cells on the membrane containing collagen IV using a micropipette technique*. Colloids and Surfaces B: Biointerfaces, 1998. **11**(5): p. 273-279.
35. Kumar, R., A. Kapoor, and R.H. Taylor. *Preliminary experiments in robot/human cooperative microinjection*. in *Intelligent Robots and Systems, 2003. (IROS 2003). Proceedings. 2003 IEEE/RSJ International Conference on*. 2003.
36. Jager, E.W.H., O. Inganäs, and I. Lundström, *Microrobots for micrometer-size objects in aqueous media: Potential tools for single-cell manipulation*. Science, 2000. **288**(5475): p. 2335-2338.
37. Chronis, N. and L. Lee, P., *Electrothermally Activated SU-8 Microgripper for Single Cell Manipulation in Solution*. Journal of Microelectromechanical Systems, 2005. **14**(4): p. 857-863.
38. Colinjivadi, K.S., J.B. Lee, and R. Draper, *Viable cell handling with high aspect ratio polymer chopstick gripper mounted on a nano precision manipulator*. Microsystem Technologies, 2008. **14**(9-11): p. 1627-1633.
39. Lin, L., *Microscale Thermal Bubble Formation: Thermophysical Phenomena and Applications*. Microscale Thermophysical Engineering, 1998. **2**(2): p. 71 - 85.

40. Okamoto, T., T. Suzuki, and N. Yamamoto, *Microarray fabrication with covalent attachment of DNA using Bubble Jet technology*. Nat Biotech, 2000. **18**(4): p. 438-441.
41. Liu, R.H., et al., *Bubble-induced acoustic micromixing*. Lab on a Chip, 2002. **2**(3): p. 151-157.
42. Tan, W.-H. and S. Takeuchi, *Dynamics microarray system with gentle retrieval mechanism for cell-encapsulating hydrogel beads*. Lab on a Chip, 2008. **8**: p. 259-266.
43. Ashkin, A., *Acceleration and Trapping of Particles By Radiation Pressure*. Physical Review Letters, 1970. **24**(4): p. 156-159.
44. Rawson, E.G. and A.D. May, *Propulsion and Angular Stabilization of Dust Particles in a Laser Cavity*. Applied Physics Letters, 1966. **8**(4): p. 93-95.
45. Ashkin, A. and J.M. Dziedzic, *Internal cell manipulation using infrared laser traps*. Proceedings of the National Academy of Sciences of the United States of America, 1989. **86**(20): p. 7914-7918.
46. Chiou, P.Y., A.T. Ohta, and M.C. Wu, *Massively parallel manipulation of single cells and microparticles using optical images*. Nature, 2005. **436**(7049): p. 370-372.
47. Dholakia, K., *Micromanipulation: Optoelectronic tweezers*. Nat Mater, 2005. **4**(8): p. 579-580.
48. Padgett, M. and R. Di Leonardo, *Holographic optical tweezers and their relevance to lab on chip devices*. Lab on a Chip. **11**(7): p. 1196-1205.
49. Crick, F.H.C. and A.F.W. Hughes, *The physical properties of cytoplasm: A study by means of the magnetic particle method, Part I Experiment*. Experimental Cell Research, 1950. **1**(37-80).
50. Yan, J., D. Skoko, and J.F. Marko, *Near-field-magnetic-tweezer manipulation of single DNA molecules*. Physical Review E - Statistical, Nonlinear, and Soft Matter Physics, 2004. **70**(1 1).
51. Gor'kov, L.P., *Forces acting on a small particle in an acoustic field within an ideal fluid*. Doklady Akademii Nauk, 1961. **140**: p. 88-92.
52. Hawkes, J.J., et al., *Ultrasonic deposition of cells on a surface*. Biosensors and Bioelectronics, 2004. **19**(9): p. 1021-1028.
53. Hill, M., Y. Shen, and J.J. Hawkes, *Modelling of layered resonators for ultrasonic separation*. Ultrasonics, 2002. **40**(1-8): p. 385-392.
54. Martin, S.P., et al., *Spore and micro-particle capture on an immunosensor surface in an ultrasound standing wave system*. Biosensors and Bioelectronics, 2005. **21**(5): p. 758-767.
55. Hill, M., R.J. Townsend, and N.R. Harris, *Modelling for the robust design of layered resonators for ultrasonic particle manipulation*. Ultrasonics, 2008. **48**(6-7): p. 521-528.
56. Haake, A. and J. Dual, *Micro-manipulation of small particles by node position control of an ultrasonic standing wave*. Ultrasonics, 2002. **40**(1-8): p. 317-322.
57. Dougherty, G.M. and A.P. Pisano. *Ultrasonic particle manipulation in microchannels using phased co-planar transducers*. in *TRANSDUCERS, Solid-State Sensors, Actuators and Microsystems, 12th International Conference on, 2003*. 2003.
58. Lilliehorn, T., et al., *Dynamic arraying of microbeads for bioassays in microfluidic channels*. Sensors and Actuators, B: Chemical, 2005. **106**(2): p. 851-858.

59. Kapishnikov, S., V. Kantsler, and V. Steinberg, *Continuous particle size separation and size sorting using ultrasound in a microchannel*. Journal of Statistical Mechanics: Theory and Experiment, 2006.
60. Courtney, C.R.P., et al., *Manipulation of microparticles using phase-controllable ultrasonic standing waves*. The Journal of the Acoustical Society of America. **128**(4): p. EL195-EL199.
61. Manneberg, O., et al., *Wedge transducer design for two-dimensional ultrasonic manipulation in a microfluidic chip*. Journal of Micromechanics and Microengineering, 2008. **18**(9).
62. Manneberg, O., et al., *A three-dimensional ultrasonic cage for characterization of individual cells*. Applied Physics Letters, 2008. **93**(6): p. 063901-3.
63. Manneberg, O., et al., *Spatial confinement of ultrasonic force fields in microfluidic channels*. Ultrasonics, 2009. **49**(1): p. 112-119.
64. Wiklund, M., et al., *Ultrasonic standing wave manipulation technology integrated into a dielectrophoretic chip*. Lab on a Chip, 2006. **6**(12): p. 1537-1544.
65. Kirby, B.J., *Micro- and Nanoscale Fluid Mechanics: Transport in Microfluidic Devices*. 2010, Cambridge University Press.
66. Jones, T.B. and M. Washizu, *Multipolar dielectrophoretic and eletrorotation theory*. Electrostatics, 1996. **37**: p. 121-134.
67. Wang, X., W.B. Wang, and P.R.C. Gascoyne, *General expressions for dielectrophoretic force and eletrorotational torque derived using the Maxwell stress tensor method*. Electrostatics, 1997. **39**: p. 277-295.
68. Deegan, R.D., et al., *Capillary flow as the cause of ring stains from dried liquid drops*. Nature, 1997. **389**(6653): p. 827-829.
69. Hagsater, S.M., et al., *Acoustic resonances in microfluidic chips: full-image micro-PIV experiments and numerical simulations*. Lab on a Chip, 2007. **7**(10): p. 1336-1344.
70. Yosioka, K. and Y. Kawasima, *Acoustic Radiation Pressure on a Compressible Sphere*. Acustica, 1955. **5**.
71. WP, M., ed. *Acoustic Streaming*. Physical Acoustic, ed. W.L. Nyborg. Vol. II-Part B. 1965, Academic Press: New York.
72. Steven, M.W., D.B. Bruce, and M.P. James, *Measurement of ultrasonic forces for particle-liquid separations*. American Institute of Chemical Engineers. AIChE Journal, 1997. **43**(7): p. 1727.
73. Petersson, F., et al., *Carrier Medium Exchange through Ultrasonic Particle Switching in Microfluidic Channels*. Analytical Chemistry (Washington), 2005. **77**: p. 1216-1221.
74. Hawkes, J.J. and W.T. Coakley, *Force field particle filter, combining ultrasound standing waves and laminar flow*. Sensors and Actuators B: Chemical, 2001. **75**(3): p. 213-222.
75. Townsend, R.J., et al., *Investigation of two-dimensional acoustic resonant modes in a particle separator*. Ultrasonics, 2006. **44**(Supplement 1): p. e467-e471.
76. Saito, M., S.-y. Izumida, and J. Hirota, *Ultrasonic trapping of paramecia and estimation of their locomotive force*. Applied Physics Letters, 1997. **71**(14): p. 1909-1911.
77. Saito, M., N. Kitamura, and M. Terauchi, *Ultrasonic manipulation of locomotive microorganisms and evaluation of their activity*. Journal of Applied Physics, 2002. **92**(12): p. 7581-7586.

78. Neild, A., et al., *Simultaneous positioning of cells into two-dimensional arrays using ultrasound*. *Biotechnology and Bioengineering*, 2007. **97**(5): p. 1335-1339.
79. Manneberg, O., et al., *Flow-free transport of cells in microchannels by frequency-modulated ultrasound*. *Lab on a Chip*, 2009. **9**(6): p. 833-837.
80. Oberti, S., et al., *Towards the automation of micron-sized particle handling by use of acoustic manipulation assisted by microfluidics*. *Ultrasonics*, 2008. **48**(6-7): p. 529-536.
81. Glynn-Jones, P., et al., *Mode-switching: A new technique for electronically varying the agglomeration position in an acoustic particle manipulator*. *Ultrasonics*. **50**(1): p. 68-75.
82. Elder, S.A., J. Kolb, and W.L. Nyborg, *Small-Scale Acoustic Streaming Effects in Liquids*. *The Journal of the Acoustical Society of America*, 1954. **26**(5): p. 933.
83. Elder, S.A., *Cavitation Microstreaming*. *The Journal of the Acoustical Society of America*, 1959. **31**(1): p. 54-64.
84. Tho, P., R. Manasseh, and A. Ooi, *Cavitation microstreaming patterns in single and multiple bubble systems*. *Journal of Fluid Mechanics*, 2007. **576**: p. 191.
85. Marmottant, P. and S. Hilgenfeldt, *Controlled vesicle deformation and lysis by single oscillating bubbles*. *Nature*, 2003. **423**(6936): p. 153(4).
86. Marmottant, P. and S. Hilgenfeldt, *A bubble-driven microfluidic transport element for bioengineering*. *Proceedings of the National Academy of Sciences of the United States of America*, 2004. **101**(26): p. 9523-9527.
87. van Wamel, A., et al., *Vibrating microbubbles poking individual cells: Drug transfer into cells via sonoporation*. *Journal of Controlled Release*, 2006. **112**(2): p. 149-155.
88. Glasgow, I. and N. Aubry, *Enhancement of microfluidic mixing using time pulsing*. *Lab on a Chip*, 2003. **3**(2): p. 114-120.
89. Ahmed, D., et al., *A millisecond micromixer via single-bubble-based acoustic streaming*. *Lab on a Chip*, 2009. **9**(18): p. 2738-2741.
90. Sakamoto, S.-i. and Y. Watanabe, *Effects of Existence of Microbubbles for Increase of Acoustic Streaming*. *Jpn. J. Appl. Phys.*, 1999. **38**: p. 3.
91. Okabe, T., S.-i. Sakamoto, and Y. Watanabe, *Experimental Study on Acoustic Streaming in Water Containing Microcapsules*. *Jpn. J. Appl. Phys.*, 2001. **40**: p. 40.
92. Nomura, S., et al., *Cavitation Bubble Streaming in Ultrasonic-Standing-Wave field*. *Jpn. J. Appl. Phys.*, 2005. **44**(5A): p. 3161-3164.
93. Eller, A.I. and L.A. Crum, *Instability of the Motion of a Pulsating Bubble in a Sound Field*. *The Journal of the Acoustical Society of America*, 1970. **47**(3B): p. 762-767.
94. DOINIKOV, A.A., *Translational motion of a bubble undergoing shape oscillations*. *Journal of Fluid Mechanics*, 2004. **501**: p. 1-24.
95. Watanabe, T. and Y. Kukita, *Translational and radial motions of a bubble in an acoustic standing wave field*. *Physics of Fluids A: Fluid Dynamics*, 1993. **5**(11): p. 2682-2688.
96. Gac, S.L., et al., *Sonoporation of suspension cells with a single cavitation bubble in a microfluidic confinement*. *Lab on a Chip*, 2007. **7**(12): p. 1666-1672.
97. Kornfeld, M. and L. Suvorov, *On the Destructive Action of Cavitation*. *Journal of Applied Physics*, 1944. **15**(6): p. 495-506.

98. Matsumoto, K. and I. Ueno, *Oscillating bubbles in ultrasonic acoustic field*. Journal of Physics: Conference Series, 2009. **147**(1).
99. Miles, J. and D. Henderson, *Parametrically Forced Surface Waves*. Annual Review of Fluid Mechanics, 1990. **22**(1): p. 143-165.
100. Neppiras, E.A., *Acoustic cavitation*. Physics Reports, 1980. **61**(3): p. 159-251.
101. Ashokkumar, M., et al., *The detection and control of stable and transient acoustic cavitation bubbles*. Physical Chemistry Chemical Physics, 2009. **11**(43): p. 10118-10121.
102. Calvisi, M.L., et al., *Shape stability and violent collapse of microbubbles in acoustic traveling waves*. Physics of Fluids, 2007. **19**(4): p. 047101.
103. Rooney, J.A., *Hemolysis Near an Ultrasonically Pulsating Gas Bubble*. Science, 1970. **169**(3948): p. 869-871.
104. Lewin, P.A. and L. Bjorno, *Acoustically induced shear stresses in the vicinity of microbubbles in tissue*. The Journal of the Acoustical Society of America, 1982. **71**(3): p. 728-734.
105. Wu, J., *Theoretical study on shear stress generated by microstreaming surrounding contrast agents attached to living cells*. Ultrasound in Medicine & Biology, 2002. **28**(1): p. 125-129.
106. Kao, J., et al., *A bubble-powered micro-rotor: conception, manufacturing, assembly and characterization*. Journal of Micromechanics and Microengineering, 2007. **17**(12): p. 2454-2460.
107. Plesset, M.S. and A. Prosperetti, *Bubble Dynamics and Cavitation*. Annual Review of Fluid Mechanics, 1977. **9**(1): p. 145-185.
108. Leighton, T.G., A.J. Walton, and M.J.W. Pickworth, *Primary Bjerknes forces*. European Journal of Physics, 1990. **11**(1): p. 4.
109. Crum, L.A., *Bjerknes forces on bubbles in a stationary sound field*. The Journal of the Acoustical Society of America, 1975. **57**(6): p. 1363-1370.
110. Mettin, R., et al., *Bjerknes forces between small cavitation bubbles in a strong acoustic field*. Physical Review E, 1997. **56**(3): p. 2924.
111. Oguz, H.N. and A. Prosperetti, *A generalization of the impulse and virial theorems with an application to bubble oscillations*. Journal of Fluid Mechanics, 1990. **218**: p. 143-162.
112. Ilinskii, Y.A., M.F. Hamilton, and E.A. Zabolotskaya, *Bubble interaction dynamics in Lagrangian and Hamiltonian mechanics*. The Journal of the Acoustical Society of America, 2007. **121**(2): p. 786-795.
113. Hay, T.A., et al., *Model of coupled pulsation and translation of a gas bubble and rigid particle*. The Journal of the Acoustical Society of America, 2009. **125**(3): p. 1331-1339.
114. Coakley, W.T. and W.L. Nyborg, *Cavitation dynamics of gas bubbles*. Applications in Ultrasound : Its Applications in Medicine and Biology ed. F.J. Fry. 1978, New York: Elsevier. 77-159.
115. TRINH, E.H., D.B. THIESSEN, and R.G. HOLT, *Driven and freely decaying nonlinear shape oscillations of drops and bubbles immersed in a liquid: experimental results*. Journal of Fluid Mechanics, 1998. **364**: p. 253-272.
116. Longuet-Higgins, M.S., *Monopole emission of sound by asymmetric bubble oscillations. Part 1. Normal modes*. Journal of Fluid Mechanics, 1989. **201**: p. 525-541.
117. Xu, L., et al., *Continuous particle assembly in a capillary cell*. Applied Physics Letters, 2009. **95**(15).
118. Malaquin, L., et al., *Controlled particle placement through convective and capillary assembly*. Langmuir, 2007. **23**(23): p. 11513-11521.

119. Dimitrov, A.S. and K. Nagayama, *Continuous convective assembling of fine particles into two-dimensional arrays on solid surfaces*. Langmuir, 1996. **12**(5): p. 1303-1311.
120. Bowden, N., et al., *Self-Assembly of Mesoscale Objects into Ordered Two-Dimensional Arrays*. Science, 1997. **276**(5310): p. 233-235.
121. Aubry, N., et al., *Micro- and Nanoparticles Self-Assembly for Virtually Defect-Free, Adjustable Monolayers*. Proceedings of the National Academy of Sciences of the United States of America, 2008. **105**(10): p. 3711-3714.
122. Tang, Z., et al., *Self-Assembly of CdTe Nanocrystals into Free-Floating Sheets*. Science, 2006. **314**(5797): p. 274-278.
123. Ye, Y.H., et al., *Self-assembling three-dimensional colloidal photonic crystal structure with high crystalline quality*. Applied Physics Letters, 2001. **78**(1): p. 52-54.
124. Marmur, A., *Line tension and the intrinsic contact angle in solid-liquid-fluid systems*. Journal of Colloid and Interface Science, 1997. **186**(2): p. 462-466.
125. Douglas-Hamilton, D.H., et al., *Particle Distribution in Low-Volume Capillary-Loaded Chambers*. J Androl, 2005. **26**(1): p. 107-114.
126. Berke, A.P., et al., *Hydrodynamic attraction of swimming microorganisms by surfaces*. Physical Review Letters, 2008. **101**(3).
127. Young, T., *An Essay on the Cohesion of Fluids*. Philosophical Transactions of the Royal Society of London, 1805. **95**: p. 65-87.
128. Extrand, C.W., *Model for Contact Angles and Hysteresis on Rough and Ultraphobic Surfaces*. Langmuir, 2002. **18**(21): p. 7991-7999.
129. Extrand, C.W., *Encyclopedia of Surface and Colloid Science*, ed. A. Hubbard. 2002, New York: Marcel Dekker. P2414.
130. Oliver, J.F., C. Huh, and S.G. Mason, *Resistance to spreading of liquids by sharp edges*. Journal of Colloid and Interface Science, 1977. **59**(3): p. 568-581.
131. J. W. Gibbs, *The Scientific Papers of J. Willard Gibbs*. Vol. 1. 1906, London: Longmans-Green.
132. White, L.R., *The equilibrium of a liquid drop on a nonhorizontal substrate and the Gibb's criteria for advance over a sharp edge*. Journal of Colloid and Interface Science, 1980. **73**(1): p. 256-259.
133. Bhaduri, B., A. Neild, and T.W. Ng, *Directional Brownian diffusion dynamics with variable magnitudes*. Applied Physics Letters, 2008. **92**(8).
134. Singh, P. and D. Joseph, *Fluid dynamics of floating particles*. Journal of Fluid Mechanics, 2005. **530**: p. 31.
135. Chen, X., S. Mandre, and J.J. Feng, *Partial coalescence between a drop and a liquid-liquid interface*. Physics of Fluids, 2006. **18**(5).
136. Chateau, X. and O. Pitois, *Quasistatic detachment of a sphere from a liquid interface*. Journal of Colloid and Interface Science, 2003. **259**(2): p. 346-353.
137. O'Brien, S.B.G. and B.H.A.A. Van Den Brule, *A mathematical model for the cleansing of silicon substrates by fluid immersion*. Journal of Colloid and Interface Science, 1991. **144**(1): p. 210-221.
138. Shao, F.F., A. Neild, and T.W. Ng, *Hydrophobicity effect in the self assembly of particles in an evaporating droplet*. Journal of Applied Physics. **108**(3): p. 034512.
139. Kralchevsky, P.A. and K. Nagayama, *Capillary forces between colloidal particles*. Langmuir, 1994. **10**(1): p. 23-36.
140. Nicolson, M.M., *The interaction between floating particles*. Mathematical Proceedings of the Cambridge Philosophical Society, 1949. **45**(02): p. 288-295.

141. Chan, D.Y.C., J.D. Henry, and L.R. White, *The interaction of colloidal particles collected at fluid interfaces*. Journal of Colloid and Interface Science, 1981. **79**(2): p. 410-418.
142. Gifford, W.A. and L.E. Scriven, *On the attraction of floating particles*. Chemical Engineering Science, 1971. **26**(3): p. 287-297.
143. Kralchevsky, P.A., et al., *Capillary meniscus interaction between colloidal particles attached to a liquid--fluid interface*. Journal of Colloid and Interface Science, 1992. **151**(1): p. 79-94.
144. Kralchevsky, P.A., et al., *Energetical and Force Approaches to the Capillary Interactions between Particles Attached to a Liquid-Fluid Interface*. Journal of Colloid and Interface Science, 1993. **155**(2): p. 420-437.
145. Kralchevsky, P.A. and K. Nagayama, *Capillary interactions between particles bound to interfaces, liquid films and biomembranes*. Advances in Colloid and Interface Science, 2000. **85**(2-3): p. 145-192.
146. Thoroddsen, S.T. and K. Takehara, *The coalescence cascade of a drop*. Physics of Fluids, 2000. **12**(6): p. 1265-1267.
147. Blanchette, F. and T.P. Bigioni, *Partial coalescence of drops at liquid interfaces*. Nat Phys, 2006. **2**(4): p. 254-257.
148. Falkovich, G., et al., *Surface tension: Floater clustering in a standing wave*. Nature, 2005. **435**(7045): p. 1045(2).

Publications arising from the work

1. Xu, L., T.W. Ng, and A. Neild, *Delicate selective single particle handling with a float-sink scheme*. Applied Physics Letters, 2009. **94**(3).
2. Xu, L., A. Neild, and T.W. Ng, *Continuous particle assembly in a capillary cell*. Applied Physics Letters, 2009. **95**(15).
3. Xu, L., A. Neild, and T.W. Ng, *Selective removal of micro-particles from a floating monolayer cluster*. Colloids and Surfaces A: Physicochemical and Engineering Aspects, **In Press, Available online**
4. Xu, L., P. R. Rogers, A. Neild, T.W. Ng, *Bubble excitation using standing waves for particle sorting*. Journal of Acoustical Society of America, 2011. **Submitted**
5. Xu, L., A. Neild, *Two dimensional acoustic manipulation in microfluidic channels*, International Conference on Applied Mechanics, Materials and Manufacturing (ICSMMM 2011). **Accepted**

Appendices:

- A. Bubble excitation using standing waves for particle sorting**

Bubble excitation using standing waves for particle sorting

Lin Xu, Priscilla R. Rogers, Adrian Neild[§], Tuck Wah Ng

Department of Mechanical & Aerospace Engineering, Monash University, Clayton VIC 3800
Australia.

Ultrasonic standing waves are shown to be suitable for exciting bubbles in a manner which induces microstreaming patterns. These patterns can be used to sort suspended particle matter based on size. The use of such standing waves means that the frequency of excitation is dependant on device geometry, and hence fixed for a given system, this is much more convenient than exciting bubble resonances which are dependent on the size of individual bubbles.

[§] Corresponding author: 

Introduction

Ultrasonic vibration as an actuation mechanism is used in a multitude of applications in microfluidic systems. The main mechanisms are acoustic radiation force^{1, 2} and acoustic streaming³. Both arise due to second order terms in the Navier-Stokes equation which time average (over a vibration cycle) to non-zero values. In the case of the former, the result is a net force acting on particles suspended in the fluid, whilst the latter results in a body force acting on the fluid itself. Acoustic radiation forces, created by ultrasonic standing waves, form time invariant force fields in which particles are usually (depending on stiffness and density parameter combinations for the particle and fluid) trapped at the acoustic pressure nodes. As such, these standing waves have been used to collect particles in lines along the length of a channel⁴ in grids of multiple points in two dimensional fields⁵ or in a 3-dimensional cage⁶. They also allow the coating of surfaces with suspended particles⁷, transporting particles within reach of external manipulating tools⁸ and moving certain particles preferentially⁹. In microfluidic systems with bulk fluid movement, concentration has been demonstrated^{10, 11}, as has sorting by compressibility¹². Acoustic streaming has been used to achieve rapid fluidic mixing¹³ and controlled droplet translation¹⁴. These applications have the commonality that they utilize an ultrasonic standing wave, a resonant field with pressure nodes and antinodes, within such standing wave field, both acoustic radiation forces and acoustic streaming coexist¹⁵, it is such a field which will be used to excite bubble motion in the work presented here.

Whilst ultrasonic standing waves can induce streaming to cause large scale mixing, without the use of very high frequency (>50MHz) it is increasingly difficult to induce fluid flow at the microscale¹⁶. To alleviate this difficulty, vibrating gas bubbles, suspended within a liquid sound field, can be used to sufficiently focus ultrasonic energy for fluid actuation at micrometer scales, typically of an order similar to the bubble radius R . Marmottant and Hilgenfeldt showed that acoustic excitation of tethered air bubbles can effect strong acoustic microstreaming in the vicinity

of the bubble¹⁷, which arises due to the frictional forces generated at the air/liquid interface¹⁸. Bubble vibration and acoustic microstreaming has been shown useful for many applications, including controlled vesicle deformation¹⁷, jetting¹⁹, propulsion²⁰, pumping¹⁶, rotor actuation²¹, mixing²² and recently for particle sorting²³. Using bubbles for particle sorting involves a balance between the drag forces acting on the particles due to the microstreaming and the Bjerknes force attracting the particle to the bubble, such a balance is particle size dependant, hence the sorting mechanism. Bubbles have been suggested as a useful mechanism for holding biological matter²⁴, hence the interest in controlling what becomes attached to the bubble. There are two key issues with this approach, firstly microstreaming near the bubble is a localized effect, hence for the particles to undergo the sorting mechanism they must be within close proximity of the bubble, so a method is needed to ensure this is the case. Secondly, the actuation of a bubble at resonance requires the correct frequency, however over time bubbles undergoing ultrasonic excitation tend to grow due to enhanced diffusion as the microstreaming constantly changes the surrounding fluid²⁵,²⁶. Furthermore, it would be advantageous to be able to excite multiple bubbles simultaneously to increase the rate of sorting, this would require the production of multiple identical sized bubbles, or the possibility of exciting bubble over a range of sizes, when taken with the expected bubble growth the latter option would clearly be beneficial. In this work, we demonstrate that rather than exciting a bubble at it's own resonant frequency, an ultrasonic standing waves can be excited at device resonance, this has the effect of aligning the bubbles and suspended particles, and also to excite the bubbles such that the ensuing microstreaming captures particles selectively, resulting in sorting.

Device Description

The device used for experimentation is depicted in Fig. 1. It consisted of a 5 mm square piezoelectric transducer bonded to a 20 mm square piece of silicon wafer. A 0.5 mm diameter wire was used to define the fluidic chamber height and lateral dimensions of 4.7 mm × 4 mm. These

values were different so that the resonant frequencies causing mode shapes of one-dimensional pressure fields occur at different frequencies in each of the two lateral directions. The fluid chamber was filled with 9.3 μL of copolymer microsphere solution (1.9 μm and 6 μm diameter particles, Bangs Laboratories), into which an air microbubble was subsequently injected using a microliter syringe (Gastight syringe, Hamilton). The chamber was covered with a 2 mm thick glass coverslip (5 mm square) to which the bubble adhered. Electrical inputs were supplied to the upper and lower surfaces of the piezoelectric element analogous to Neild et al.²⁷, and were driven by a signal generator (Stanford Research SDR 345) via a power amplifier (Amplifier Research 25A250A). The particles suspended in the enclosed fluidic chamber were viewed using an Olympus BX51 upright microscope fitted with a charge coupled device camera (Hitachi HV-D30) operating at 25 frames per second. Videos and still images were captured accordingly.

Results and Discussion

Two resonant frequencies of the device were determined by the observation of the behaviour of suspended particles. When a strong standing wave is established the 6 μm copolymer microspheres will align along the pressure nodes. At 939.5 kHz a quasi one-dimensional standing waves across the shorter lateral dimension of the chamber was found, resulting in lines of parallel particles, as shown in Fig. 2(a). When a bubble is introduced into the chamber it becomes located close to the nodal line as seen in Fig. 2(b). At 673 kHz strong particle alignment was also observed, the pattern formed was not one of parallel lines (as are usually sought), but a more complicated arrangement of aligned particles, to demonstrate this accurately a composite image has been formed in Fig. 3, again it can be seen that the bubbles present, four in this case, are located close to the pressure node.

Acoustic radiation forces are known to align particles of this density and compressibility along the pressure node, the bubbles also align along the same lines, however in their case the behaviour is

dependant on the frequency of excitation and how that relates to the bubbles resonance. When a permanent gas bubble is placed in a sound field, it may undergo several different types of oscillatory motion, recently reviewed by Tho et al.²⁸. Radial expansion and contraction of the bubble wall, whilst maintaining its spherical shape, is known as a volume oscillation. Largely a function of the bubble's resonant characteristics, the microstreaming generated is strongest when the bubble is excited near its natural frequency ω_0 , given by:

$$\omega_0 = 3\kappa \frac{p_g}{\rho R_0^2} - \frac{2\sigma}{\rho R_0^3}, \quad (1)$$

where R_0 is the corresponding resonant radius of the bubble, κ is the polytropic exponent, p_g is the pressure of the gas at rest, σ is the surface tension and ρ is the density of the liquid. Within a standing pressure field, Watanabe and Kukita found that a bubble of radius R , sufficiently smaller than the volumetric resonant radius ($R/R_0 < 0.87$), would move to the pressure antinode within the standing wave, whilst a bubble larger than the resonant size ($R/R_0 > 1.03$) would move to the pressure node²⁹. At a frequency of 939.5 kHz an air bubble suspended in water, where κ takes a value of between 1 and 1.4, $p_g = 100$ kPa, $\sigma = 72.5$ N/m and $\rho = 1000$ kg/m³, the resonant radius is approximately 3 μ m. Accordingly, when a 25 μ m bubble radius, well above the resonant radius, is introduced into the 939.5 kHz pressure field, it moves towards the pressure node. As can be seen, the bubble just falls short of reaching the node, which can be attributed to the capillary forces, arising between the bubble and substrate due to surface tension, exceeding the increasingly small acoustic radiation force amplitudes exerted on the bubble as it translates towards the node. However the motion of the bubble can result in perfect alignment with the particles as shown in Figure 4.

By alignment of the bubble and particles, the first goal is accomplished, that of ensuring a higher degree of interaction between the bubble (whose sphere of influence through microstreaming is relatively small) and the particles. However, no microstreaming, usually excited by resonant excitation of the bubble, has been demonstrated. This is seen in Figure 5, were the bubbles have

attracted large quantities of particles to their surfaces in this highly concentrated (allowing easy visualization of the nodal lines) sample, the motion of the particles which results in attraction is characterized by the looping trajectories of microstreaming.

A key advantage of using device resonances to excite the bubbles is that a strong pressure field, and also solid surface vibration, is exerted on any bubble present. This means that a range of bubble sizes can be excited using one frequency. Figure 6 shows the ability to excite different bubble sizes, each of the bubbles acts to attract particles, again the trajectories being those synonymous with a streaming field. More importantly, many bubbles can be excited simultaneously; an image of this is seen in Figure 7 in which the 6 μm particles are collected on the surface of the bubbles.

Whilst collection of 6 μm particles has now been demonstrated at pressure nodal lines, for different sized bubbles at a single frequency and for multiple bubbles simultaneously, all using a device resonance as actuation of the bubble, no sorting has been shown. For this we compare the behavior of the 6 μm (used for preceding results due to their easy visualization) with 1.9 μm . In Figure 8 two bubbles of similar sizes are excited in a 939.5 kHz standing wave in separate experiments, the first with 6 μm particles and the second with 1.9 μm particles. For the larger particles it can be seen that they follow a curved trajectory before collecting on the surface of the bubble, whilst the small particles appear to be repelled from the surface of the bubble, though in fact they are simply following the streamlines. The observed smaller particle behavior is analogous to that reported by Marmottant and Hilgenfeldt, where the particles follow vertical loop-like trajectories attributed to the combined volume and translational oscillations¹⁷, under the influence of a steady Stokes drag. It is the behaviour of the larger particles then; that requires more explanation as they break away from the streamlines, this is due to Bjerknes forces. Indeed, it has been previously demonstrated that this size selective behaviour is due to a balance between the drag forces arising from the

streaming flow and the Bjerknes forces arising between the bubble and particle in the ultrasonic field. The secondary Bjerknes force was first discovered by Bjerknes who observed a translational force between two pulsating bubbles³⁰, which was further extended to that between a pulsating bubble and solid object³¹. In a more recent study, Hay et al. showed that particles more dense than the fluid will experience an attractive Bjerknes force³², and furthermore that the force is a function of the particle size R_p cubed, defined by:

$$F_B = 4\pi\rho \left(\frac{\rho - \rho_p}{\rho + 2\rho_p} \right) \frac{R^4 R_p^3}{d^5} \omega^2 \zeta^2, \quad (2)$$

where ρ_p is the density of the particle, d is the separation distance between the particle and the bubble, ω is the angular frequency of the bubble pulsations and ζ is the amplitude of the radial displacement of the bubble's wall during vibration. As the Stokes drag force, defined by $6\pi\mu UR_p$, where μ is the dynamic viscosity of the liquid and U is the relative velocity of the fluid, only scales with R_p , larger particles will experience a larger relative Bjerknes force, where the Bjerknes force will be sufficient to overcome the drag force for larger particle sizes as the particle approaches the bubble. This makes it increasingly difficult for the larger particles to continue to follow the streamlines. Note also that the Bjerknes force scales inversely with the separation between the bubble and particle, d , to the fifth power, meaning that the sphere of influence of this force is small. It is the acoustic streaming which brings all the particles within close proximity to the bubble, when there the Bjerknes forces is large enough to pull the larger particles out of the streamlines and onto the bubble's surface. It is this process which has occurred in collecting the particles as shown in Figures 5 to 7.

The differing behavior of the two particle sizes clearly demonstrates the possibility of a sorting mechanism using a vibrating bubble excited by a standing wave. This is demonstrated in Fig. 9, where, using an excitation frequency of 939.5 kHz, the 6 μm and 1.9 μm particles are captured and repelled, respectively. In addition, as seen in the final frame of Fig. 9, the particles fell away from the bubble once the vibration ceased, which would allow the system to be refreshed and

recommence anew. It is also worth noting that the trapped particles in the bubble are held at a hydrated state³³, which is useful if the approach is translated to the case of cells.

Conclusion

Ultrasonic standing waves have been shown to be effective in actuating bubbles, this is achieved at frequencies much in excess of the natural resonant frequency of the bubbles themselves. This removes the necessity to tune excitation to the resonant frequency of a given bubble, allowing excitation of multiple bubble sizes simultaneously. Upon initial excitation of the device resonance which yields a standing wave, the captured bubbles along with suspended particles are collected at the pressure nodes. The particles come under the influence of microstreaming which is produced by the oscillating bubble, this can cause smaller particles to come into very close proximity to the bubble prior to continuing on the streamlines away from the bubble, whilst larger particles diverge from the streamlines under the influence of Bjerknes forces, becoming trapped on the bubble/fluid interface.

References

1. K. Yosioka, Y. Kawasima, *Acustica*, 5,167–173, (1955).
2. L. P. Gor'kov, *Doklady Akademii Nauk Sssr*, 140, 88–92, (1961).
3. W. L. Nyborg. Acoustic streaming. In W. P. Mason, editor, *Physical Acoustics*, volume II-Part B, chapter 11. Academic Press (New York), 1965.
4. M. Wiklund, C. Günther, R. Lemor, M. Jäger, G. Fuhr, H. M. Hertz, *Lab Chip*, 6, 1537-44 (2006).
5. A. Neild, S. Oberti, G. Radziwill, J. Dual, *Biotechnol. Bioeng*, 97, 1335-1339 (2007).
6. O. Manneburg, B. Vanherberghen, J. Svennebring, H. M. Hertz, B. Onfelt, M. Wiklund, *Applied Physics Letters*, 93, 063901, (2008).

7. S.P. Martin, R.J. Townsend, L.A. Kuznetsova, K.A.J Borthwick, M. Hill, M.B. McDonnell, W.T. Coakley, *Biosens. Bioelectron.*, **21**, 758-767 (2005).
8. A. Neild, S. Oberti, F. Beyeler, J. Dual, B. J. Nelson, *Journal of Micromechanics and Microengineering*, **16**, 1562–1570, (2006).
9. O. Manneberg, B. Vanherberghen, B. Önfelt, M. Wiklund, *Lab Chip*, **9**, 833–837, (2009).
10. V. Yantchev, J. Enlund, I. Katardjiev, L. Johansson L, *Journal of Micromechanics and Microengineering*, **20**, 035031 (2010).
11. A. Nilsson, F. Petersson, H. Jonsson, and T. Laurell. *Lab Chip*, **4**, 131–135, (2004).
12. F. Petersson, A. Nilsson, C. Holm, H. Jonsson, T. Laurell, *Lab Chip*, **5**, 20–22, (2005).
13. G. Yaralioglu, I. O. Wygant, T. C. Marentis, B. T. Khuri-Yakub, *Anal. Chem.*, **76**, 3694-3698 (2004).
14. K. Sritharan, C. J. Strobl, M.F. Schneider, A. Wixforth, Z. Guttenberg, *Appl. Phys. Lett.*, **88**, 054102 (2006).
15. S. M. Hagsater, T. G. Jensen, H. Bruus, J. P. Kutter, *Lab Chip*, **7**, 1336–1344, (2007).
16. P. Marmottant, and S. Hilgenfeldt, *PNAS*, **101**, 9523 (2004)
17. P. Marmottant, and S. Hilgenfeldt, *Nature*, **423**, 153 (2003)
18. W. Nyborg, *J. Acoust. Soc. Am.*, **30**, 329 (1958)
19. S.H. Ko, S.J Lee, and K.H Kang, *Appl. Phys. Lett.*, **94**, 194102 (2009)
20. R. J. Dijkink, J. P. Van der Dennen, C. D. Ohl, and A. Prosperetti, *J. Micromech. Microeng.*, **16**, 1653 (2006)
21. J. Kao, X. Wang, J. Warren, J. Xu, and D. Attinger, *J. Micromech. Microeng.*, **17**, 2454, (2007)
22. R. Liu, J. Yang, M. Pindera, M. Athavale, and P. Grodzinski, *Lab Chip*, **2**, 151 (2002)
- 23.
24. Bubbles for bio capture cite
25. E. A. Calvisi, et al., *Physics of Fluids*, **19**, 047101 (2007)
26. P. Tao, R. Manasseh, and A. Ooi, *J. Fluid Mech.*,

27. A. Neild, S. Oberti, and J. Dual, *Sensor. and Actuat. B- Chem*, 121, 452 (2007)
28. P. Tho, R. Manasseh, and A. Ooi, *J. Fluid Mech.*, 576, 191 (2007)
29. T. Watanabe, and Y. Kukita, *Phys. Fluids A*, 5, 2682 (1993)
30. V.F.K. Bjerknes, *Fields of force*, Columbia University Press (1906)
31. W. Coakley and W. Nyborg, in *Ultrasound: It's applications in medicine and biology*, edited by F.J. Fry, (Elsevier, New Yorl, 1978), p.77
32. T. Hay, M. Hamilton, Y. Ilinski and E. Zabolotskaya, *J. Acoust. Soc. Am.*, 125, 1331 (2009)
33. L. Xu, A. Neild, T. W. Ng, F. F. Shao, *Applied Physics Letters*, 95, 153501 (2009)

List of Figure Captions

Figure 1: Schematic description of experiment setup, (a) the cross-section view of the device used in the experiment, and (b) the top view of the device.

Figure 2: Lines forming in one dimensional standing pressure field at 939.5 kHz. (a) Two of the lines shown straight without any bubble presented. (b) The effect of a bubble, circled in blue, causing one of the lines to bow around.

Figure 3: Complex patterns forming in one dimensional standing pressure field at 673 kHz.

Figure 4: Experimental image sequences of the bubble moving towards to the pressure node.

Figure 5: Experimental images of bubbles attracted large group of particles at the nodal line. (a) and (b) is 0.8s apart. (c) and (d) is 0.76s apart.

Figure 6: Experimental images of different size bubbles excited by the standing waves.

Figure 7: Experimental images of particles collected by many bubbles excited simultaneously. (a) Five bubbles are attached at the glass surface; directly below (b) two bubbles are attached on the silicon surface. Each of the two bubbles is attached on the glass surface (c) and silicon surface (d).

Figure 8: Experimental image sequences of the bubble acting as a mechanism in two cases: (a) At 939.5 kHz, 6.0 μm particles were captured by the 25 μm radius bubble. (b) At 939.5 kHz, 1.9 μm particles were repelled from the similar size bubble instead captured.

Figure 9: Experimental image sequences of particles' motion affected by the bubble at 939.5 kHz: 6.0 μm particles circled in red were captured by the bubble; and 1.9 μm particles circled in white were repelled from the bubble. The last image shows that

the 6.0 μm particles were falling from the bubble when the power was turned off for 42 seconds.

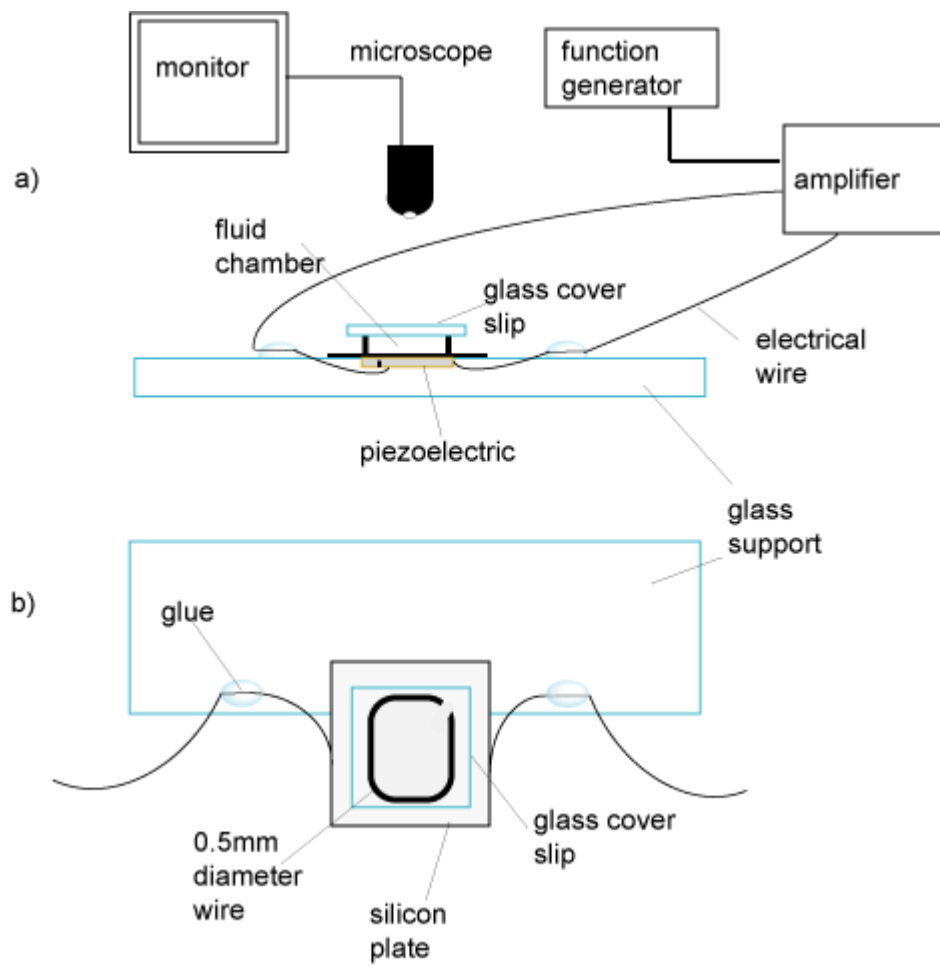
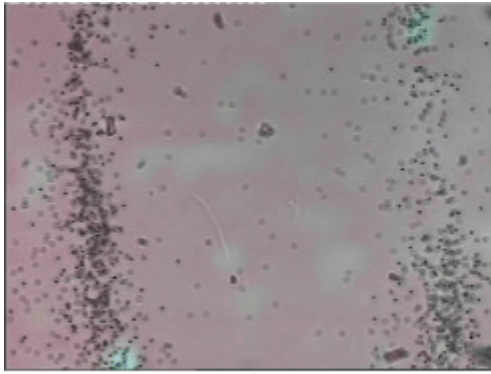
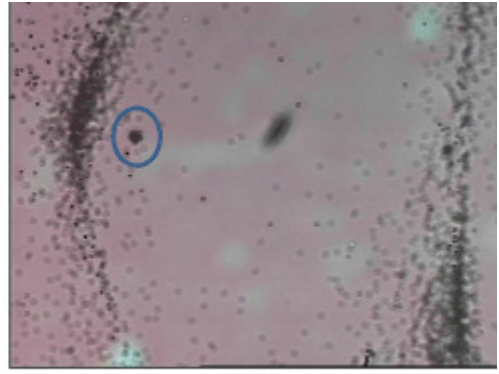


Fig 1



(a)



(b)

Fig 2

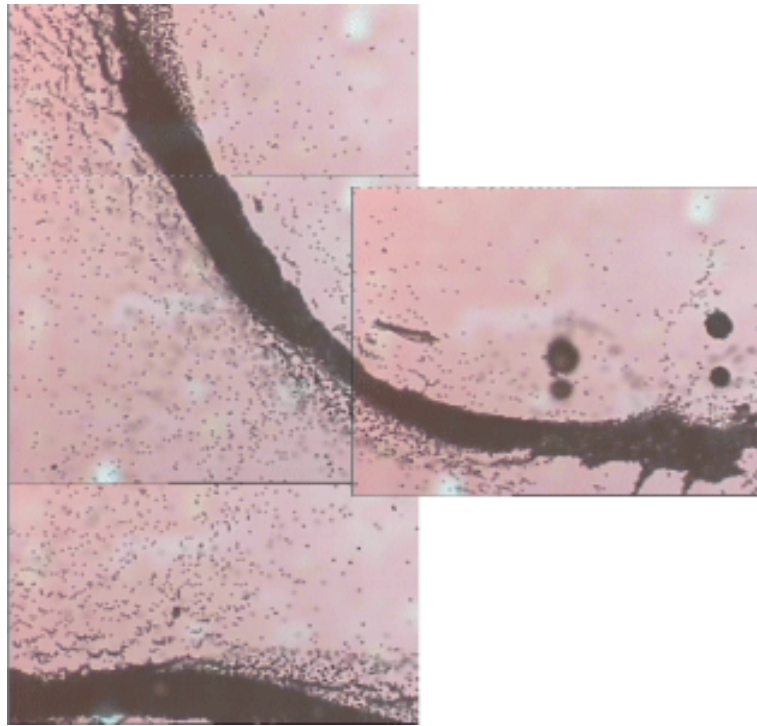


Fig 3

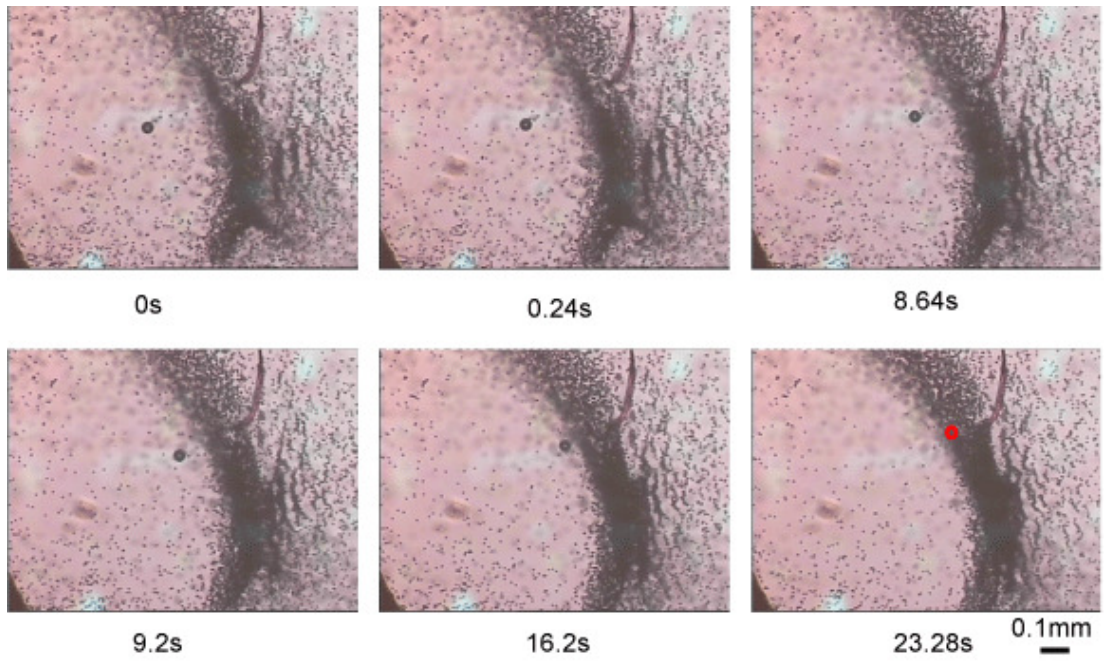


Fig 4

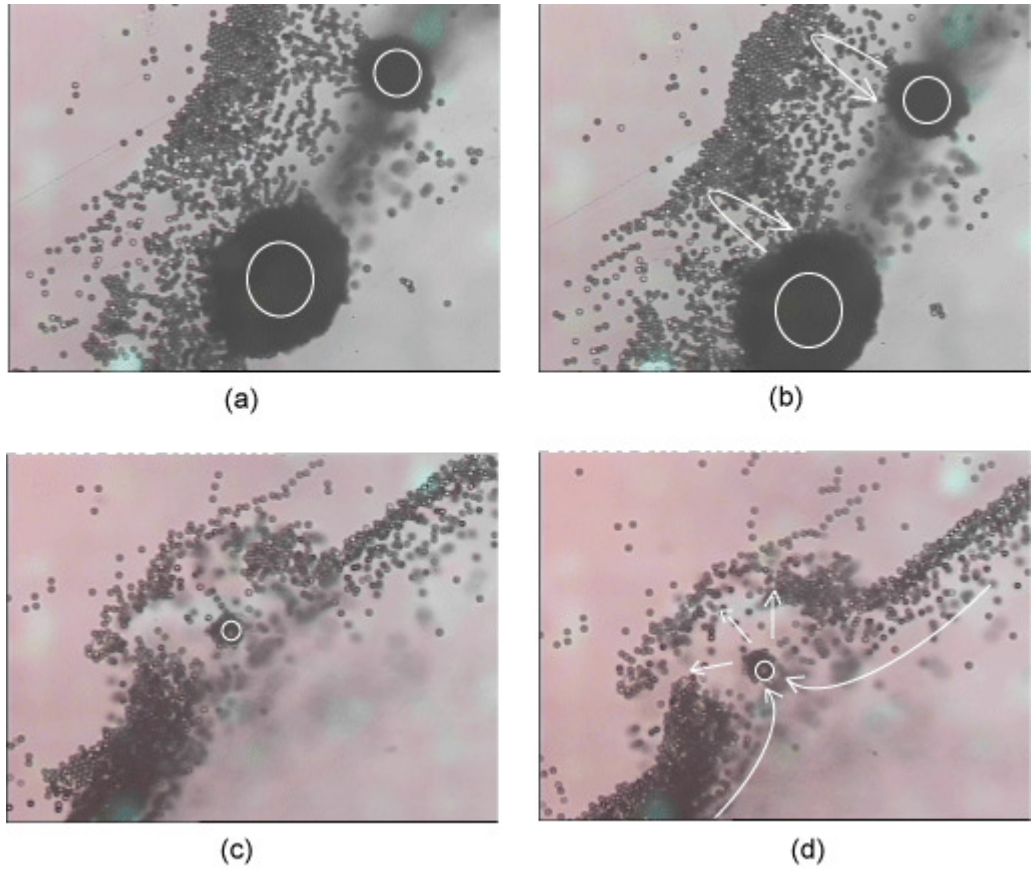
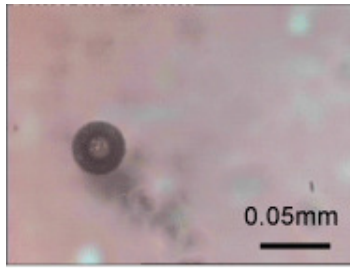
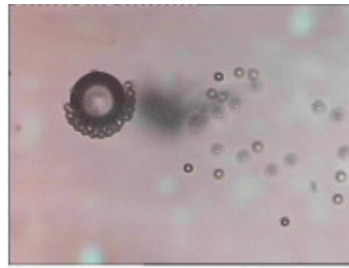


Fig 5



(a)



(b)



(c)

Fig 6

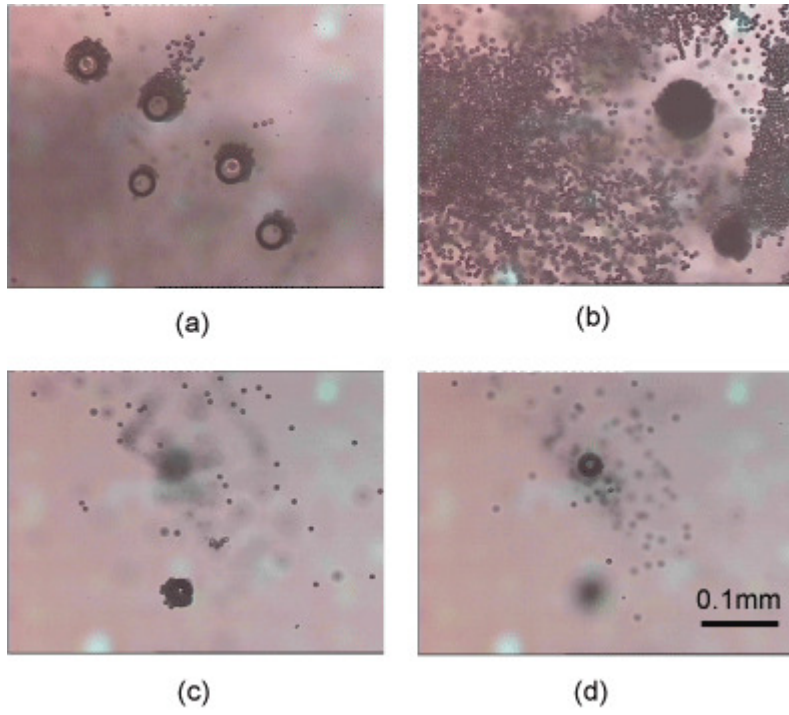


Fig 7

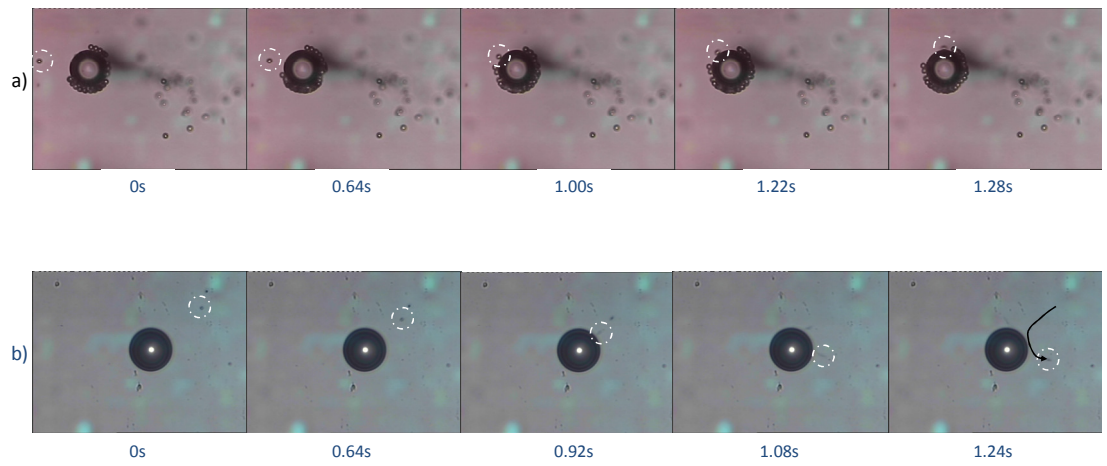


Fig 8

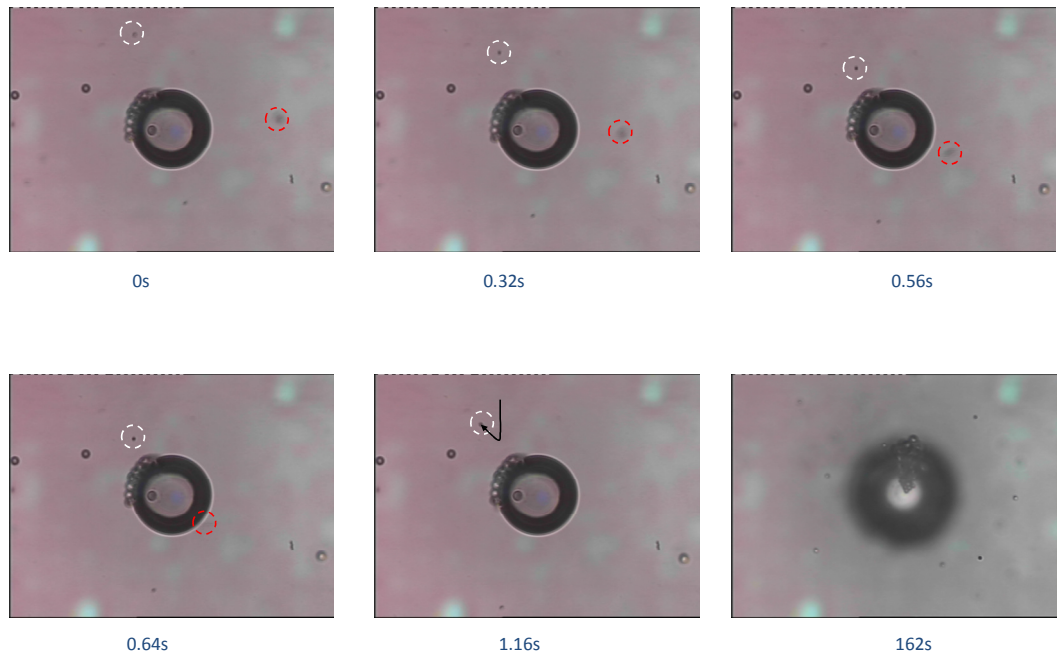


Fig 9

B. Continuous particle assembly in a capillary cell

Continuous particle assembly in a capillary cell

Lin Xu, Adrian Neild,^{a)} Tuck Wah Ng, and Fen Fen Shao

Department of Mechanical and Aerospace Engineering, Monash University, Clayton, Victoria 3800, Australia

(Received 13 July 2009; accepted 22 September 2009; published online 12 October 2009)

Capillary force mechanisms have the advantages of providing the motive force to move groups of particles to locations of interest while holding them in place, offering delicateness, and obviating the use external energy sources. We report a capillary force method that permits particles to remain hydrated, while assembled and harvested in batches using a single setup, furthermore assembly of different sizes/types is possible. The physics behind the process is described and the technique demonstrated with the formation of an ensemble of 6 μm particles. © 2009 American Institute of Physics. [doi:10.1063/1.3249582]

The ability to accomplish controlled assembly of particles has many practical applications. Efforts to achieve this have been relatively recent¹ compared to the knowledge gained on the behavior of particles and fluids in the micro-scale which date back to the 19th century.^{2,3} The techniques reported to control particle arrangement can be broadly classified as either contacting or noncontacting. The former include the use of grippers⁴ or for more delicacy “soft media” such as hydrogel beads,⁵ bubbles,⁶ or droplets.⁷ Noncontacting approaches include the generation of ultrasonic^{8,9} or dielectrophoretic¹⁰ forces, both offering delicacy and a means to move and hold groups of particles at certain locations. Alternatively, obviating the need for external energy sources, capillary forces can allow controlled particle assembly,¹¹ or cause droplets to fill cavities forming micro-plate wells.¹² As such, capillary forces have intriguing potential in low power applications, such as hand-held diagnostic systems especially in remote locations.

Particles in an evaporating droplet are moved preferentially toward the contact line (liquid, vapor, solid interface). As the contact line recedes, particles can pin naturally¹³ or at induced points¹⁴ to create patterned assemblies. Limitations exist when the assembled structures require rebuilding with additional particles, the particles (e.g., cells) need to remain hydrated, or particles of different sizes/types at specific compositions need to be assembled. We describe here a capillary based scheme that possesses these capabilities. Furthermore, in contrast to natural pinning which depends on particle size, concentration, and surface properties,¹⁵ the proposed method clearly defines a single region in which the particle assembly occurs.

In optical manipulation the relationship between force and particle radius is cubic (gradient forces) or to the sixth power (scattering forces),^{16–18} the acoustic radiation forces has a cubic relationship in ultrasonic standing waves¹⁹ (all assuming the wavelength far exceeds the radius). Particles in a flowing fluid experience drag, which has a linear relationship with radius, with particles of low inertia typically simply follow fluid flow [the principle of particle image velocimetry (PIV)]. Consequently, when acoustic streaming (flow patterns) and acoustic radiation forces are present the behav-

ior of small and large particles are dominated by the former and latter, respectively.²⁰ Being flow based, the method presented will be suitable for manipulation of very small particles, furthermore it is unusual in that the flow leads to a stable end location without swirling.

A fluid cell was prepared by depositing a set volume of deionized water on a glass slide and lowering a cut cover slip until fully wetted, giving a cell height of 10 μm .^{21,22} Three sides of the cell were sealed [Fig. 1(a)]. A small opening was left at the center of the sealed edge opposite the free side at which a droplet of particles in suspension can be introduced; this creates a continuous fluid body combining the droplet and the cell contents. This body must re-establish equilibrium, clearly observed by a movement of the contact line at the free edge of the cell [depicted as being from A' to B' in Fig. 1(b)]. The sharp edge of the cover slip (C) allows a large range in the contact angle, hence the meniscus can deform as shown.²³ As evaporation progresses, the droplet free surface and meniscus combination will recede gradually before eventually falling back to the original position of A and A', respectively. In the intervening time a flow occurs within the cell which causes particle collection and assembly, which is governed by two effects, the quasistatic maintenance of equilibrium of surface forces acting on the fluid, and the replacement of evaporated fluid. We consider them separately, though they are interrelated.

The addition of a droplet causes a short time scale flow through the chamber, as equilibrium is sought. Subsequently, as fluid evaporates this equilibrium needs to be maintained resulting in further flow. The equilibrium of a small scale

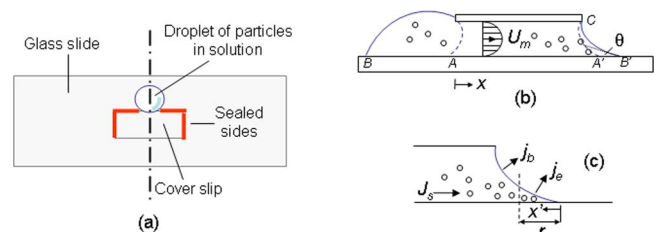


FIG. 1. (Color online) Schematic description of the proposed method to locate particles in position using capillary force, (a) the top view of the device used in the experiment, (b) the cross-section view about X–X with description of flow mechanics from droplet the meniscus, and (c) the evaporation mechanics from the meniscus causing a flow that will carry particles toward it.

^{a)}Author to whom correspondence should be addressed. Electronic mail: adrian.neild@eng.monash.edu.au.

open fluid system is most easily considered as the minimization of the surface energies of the liquid vapor interface and the solid liquid interface, and the line energy related to the movement of the contact line (during which the equilibrium contact angle θ_0 , may alter through a range between the receding angle θ_R , and the advancing angle, θ_A). This can be expressed as²⁴

$$\delta w = 0 = \gamma_{LV} dA_{LV} + (\gamma_{SL} - \gamma_{SV}) dA_{SL} - 2\pi k dr, \quad (1)$$

where δw represents the work change, γ_{LV} , γ_{SL} , and γ_{SV} are the surface energies (subscripts being liquid, solid, and vapor), and k is the line energy. The other variables are geometric, dA_{LV} and dA_{SL} are the changes in interface areas, and r is the radius of the wetted area of the solid surface. So the fluid will seek to minimize surface areas and contact line length.

The second important physical mechanism, evaporation, also affects the flow rate. We consider this, by idealizing the bottom tip of the meniscus B' as a wedge similar to a droplet rim, with a length r typically order 1 mm,²⁵ Fig. 1(c), the equation for the evaporative flux in a droplet at some distance x' ($< r$) from the contact line is

$$j_e(x') = j_o x'^{-[(\pi-2\theta)/(2\pi-2\theta)]}, \quad (2)$$

where j_o is an evaporative constant. The evaporation flux outside this region j_b is a constant for the bulk suspension in which x' is replaced by r . In a quasistatic situation of a flow at reasonably low speeds, the shape of the meniscus at the rim of a droplet is kept by a fluid flow J_s toward the contact line in which¹³

$$J_s = \int_0^r (j_e - j_b) \eta(x'), \quad (3)$$

where $\eta(x')$ is the arc length of the meniscus surface.

The varying ability of vapor to diffuse (allowing further vapor to be removed) causes the changes in evaporative rates across a droplet,¹³ so the addition of the cell which creates a wedge of narrow width (ideal for enhanced diffusion) and a long length should prove to be an efficacious evaporative structure.

In the case of the cell, we see that a shift in the meniscus shape from B' to A', while the contact angle at the lower edge remains the same, causes the surface area of the meniscus to vary greatly. We can thus expect that the evaporation to be faster in the case of B' (possessing the larger area), so the change of meniscus shape causes a varying J_s (which drives particle deposition capability), in contrast to methods such as vertical evaporation colloidal deposition.²⁶ In our approach, the continual droplet deposition at the inlet ensures that particle collection and concentration can be maintained at a fixed location; making it also accessible for harvesting and without the need for drying.

The particles chosen were 6 μm diameter copolymer microspheres, as they are clearly visible under magnification levels offering a suitable field of view. A droplet of 1.3 μl milli-Q water was released on the middle of a glass slide this forms a thin film when a cut cover slip (3 by 22 mm) is placed on top of it [Fig. 1(b)] creating the liquid cell. Varnish was used carefully to seal the sides of the cover slip, leaving one length side free and opening in the middle of the opposite side. Then a 1.4 μl solution droplet was placed carefully at this opening. A charge coupled device camera (Hitachi

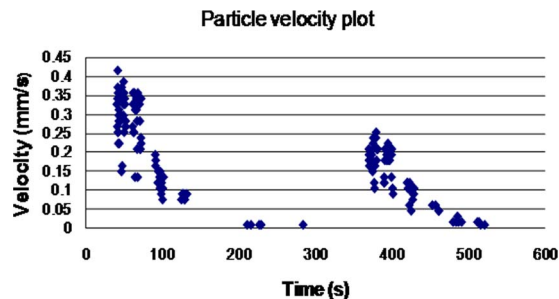


FIG. 2. (Color online) Plot of velocity of individual particles in the cell against the time, at the location of 2.2 mm away from the free edge. A second water droplet was added at 350 s.

HV-D30) attached to a microscope permitted viewing and recording from the top of the device [Fig. 1(a)].

Figure 2 tracks individual particle speeds over time at a distance of 2.2 mm from the free edge. Speeds of about 0.4 mm/s were measured initially, reducing to 0.007 mm/s, as evaporation progressed over the next 312 s. At 350 s, another particle solution droplet of 1.3 μl volume was placed at the input, the speed was restored to 0.2 mm/s and again reduced rapidly. It is evident that no backflow (into the droplet) occurs.

Figure 3 gives a spatial plot of particle concentration at 1.9 mm from the free edge after 100 s, approximately uniform concentration was achievable across a span length of about 165 mm. Outside this span the particle concentration fell to almost zero this is attributed to the limit of the flow fanning out from the narrow entry opening. These results illustrate the suitability of the technique in providing a steady throughput of particles to be collected, concentrated or assembled.

Figure 4 shows the particles collected at the meniscus. As, in this demonstration, the particles are introduced to the system via the droplet deposited externally to the cell, the aligned particles have passed from this droplet through the cell. It is easily conceivable that assemblies of multiple particles sizes can be achieved by changing the suspensions added in each subsequent droplet. It is clear that the surface tension is able to hold the particles in place. Figures 4(a) and 4(b) have the time difference of 2.4 s apart. Note the minor retraction of the particles back into the solution region in Fig. 4(b), as they follow the retreating meniscus due to water evaporation. That the particle concentration appears somewhat unchanged between the two illustrates that the retreating meniscus is not dominant in the particle collection. The

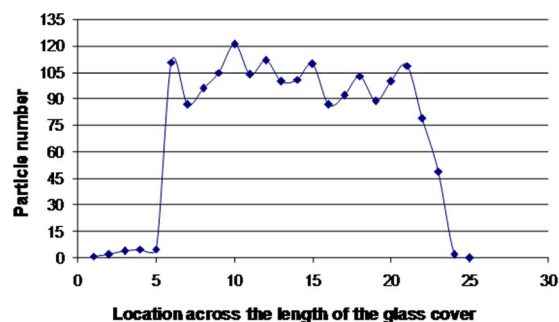


FIG. 3. (Color online) Plot of particle concentration along the length of 1.9 mm away from the free edge after a time of 100 s. The distribution is approximately a uniform top hat function.

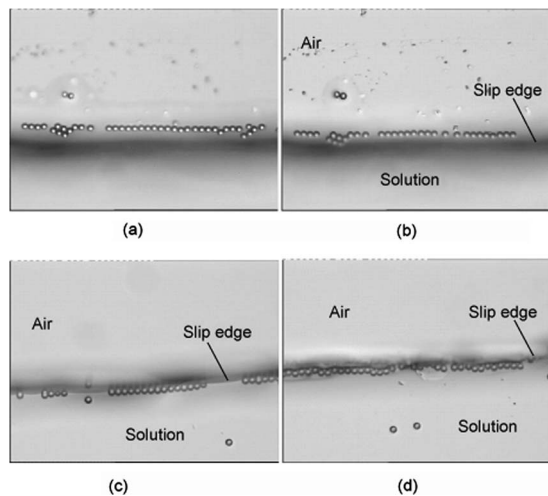


FIG. 4. Images with particles formed in lines. (a) and (b) show particles forming lines at the free opening, and the second image (b) occurring 2.4 s later than (a), clearly showing a slight retraction or the contact line toward the coverslip. (c) and (d) show particles forming lines just under the coverslip edge with (d) having an undulating edge.

ability to line the particles following the coverslip edge, Fig. 4(c), even when this is not smooth as in Fig. 4(d) implies the capability to shape the assembly of particles.

The results shown enlighten the interplay between the two mechanisms governing the fluid flow. We note that the maximum flow detected was 0.4 mm/s, furthermore from Fig. 4(a) we conclude the meniscus moves over a distance of approximately 60 μm , shown by the deposition of two particles at this outermost extent (something we observed rarely), the volume of liquid required for this change (approximating a triangular cross section for the meniscus change) can be estimated to be transferred in less than a tenth of a second at a flow rate of 0.4 mm/s. So, clearly flow arising from maintaining quasistatic equilibrium is negligible, instead evaporation rates dominates. Of course, the evaporation may be greater in the droplet, but this will not affect flow in the chamber other than by equilibrium maintenance.

In summary, we demonstrate a capillary force method that permits (a) the particles (e.g., cells) to be hydrated con-

stantly, (b) the assembled particles to be harvested in batches and rebuilt with additional particles using the same setup, and (c) particles of different sizes or types to be assembled at specific compositions. This can be achieved without active energy supply (rather environmental) and in a mechanism in which forces are (only) linearly dependant on particle radius. The manner of operation permits groups of particles to be moved to locations of interest, held in place with delicateness, without any external energy sources needed to drive the process.

¹J. Atencia and D. J. Beebe, *Nature (London)* **437**, 648 (2005).

²G. Hagen, *Ann. Phys. Chem.* **46**, 423 (1839).

³J. L. M. Poiseuille, *Compt. Rend.* **11**, 961 (1840).

⁴E. W. H. Jager, O. Ilganas, and I. Lundstrom, *Science* **288**, 2335 (2000).

⁵W. H. Tan and S. Takeuchi, *Lab Chip* **8**, 259 (2008).

⁶R. S. Taylor and C. Hnatovsky, *Opt. Express* **12**, 916 (2004).

⁷L. Xu, T. W. Ng, and A. Neild, *Appl. Phys. Lett.* **94**, 034104 (2009).

⁸S. P. Martin, R. J. Townsend, L. A. Kuznetsova, K. A. J. Borthwick, M. Hill, M. B. McDonnell, and W. T. Coakley, *Biosens. Bioelectron.* **21**, 758 (2005).

⁹A. Neild, S. Oberti, F. Beyeler, J. Dual, and B. J. Nelson, *J. Micromech. Microeng.* **16**, 1562 (2006).

¹⁰P. R. C. Gascoyne and J. Vykoukal, *Electrophoresis* **23**, 1973 (2002).

¹¹L. Malaquin, T. Kraus, H. Schmid, E. Delamarque, and H. Wolf, *Langmuir* **23**, 11513 (2007).

¹²T. W. Ng, Y. Yu, H. Y. Tan, and A. Neild, *Appl. Phys. Lett.* **93**, 174105 (2008).

¹³R. D. Deegan, O. Bakajin, T. F. Dupont, G. Huber, S. R. Nagel, and T. A. Witten, *Nature (London)* **389**, 827 (1997).

¹⁴S. Vyawahare, K. M. Craig, and A. Scherer, *Nano Lett.* **6**, 271 (2006).

¹⁵T. Kajiyama, D. Kaneko, and M. Doi, *Langmuir* **24**, 12369 (2008).

¹⁶A. Neild, T. W. Ng, and W. M. S. Yui, *Opt. Express* **17**, 5321 (2009).

¹⁷Y. Harada and T. Asakara, *Opt. Commun.* **124**, 529 (1996).

¹⁸P. Zemanek, A. Jonas, L. Sramek, and M. Liska, *Opt. Commun.* **151**, 273 (1998).

¹⁹L. P. Gor'kov, *Sov. Phys. Dokl.* **6**, 773 (1961).

²⁰S. M. Hagsäter, T. G. Jensen, H. Bruus, and J. P. Kutter, *Lab Chip* **7**, 1336 (2007).

²¹A. P. Berke, L. Turner, H. C. Berg, and E. Lauga, *Phys. Rev. Lett.* **101**, 038102 (2008).

²²B. Bhaduri, A. Neild, and T. W. Ng, *Appl. Phys. Lett.* **92**, 084105 (2008).

²³J. W. Gibbs, *The Scientific Papers of J. Willard Gibbs* (Longmans-Green, London, 1906), Vol. 1, p. 55.

²⁴A. Marmur, *J. Colloid Interface Sci.* **186**, 462 (1997).

²⁵A. S. Dimitrov and K. Nagayama, *Langmuir* **12**, 1303 (1996).

²⁶Y.-H. Ye, F. LeBlanc, A. Haché, and V.-V. Truong, *Appl. Phys. Lett.* **78**, 52 (2001).

C. Delicate selective single particle handling with a float sink scheme

Delicate selective single particle handling with a float-sink scheme

Lin Xu, Tuck Wah Ng, and Adrian Neild^{a)}

Department of Mechanical Engineering, Monash University, Clayton, Victoria 3800, Australia

(Received 26 November 2008; accepted 24 December 2008; published online 23 January 2009)

Selective single particle handling with high degrees of controllability, precision, and delicateness is sought after for operations such as sorting, isolation, and placement. Here, we describe and demonstrate an approach that operates based on a droplet dispensed directly above a selected particle floating on the liquid surface to cause it to sink. The mode of sinking appears to be based on the detachment of the particle from the liquid interface with an applied force. This method offers the desired attributes of particle handling and is amenable to the incorporation of automation to speedily accomplish the selective handling of multiple particles. © 2009 American Institute of Physics. [DOI: 10.1063/1.3073864]

The selective handling of fragile single particles is a challenging task. Cells, for example, have membranes that damage easily and are susceptible to environmental conditions. The ability to handle fragile single particles in a repeatable and convenient manner is vital in the context of operations such as sorting, isolation, and placement. The various techniques reported to achieve controlled particle handling can be broadly classified as either noncontacting or contacting. The noncontacting approaches typically apply the use of optical,^{1,2} magnetic,^{3,4} ultrasonic,⁵ or dielectrophoretic⁶ principles. Optical methods arguably offer the highest degrees of controllability, precision, and delicateness, albeit it can result in cell phototoxicity.⁷ The most generally used contacting approach employs vacuum suction via micropipettes. The degrees of controllability and precision with this method are generally low. Probes and grippers based on MEMS technology offer improved performance in these aspects,^{8,9} although the degree of delicateness achievable with them will be lower than the noncontacting schemes. Contacting “soft medium” approaches based on hydrogel beads¹⁰ or bubbles¹¹ offer solution to the delicateness problem but will likely incur some difficulties in particle harvest when the operation is complete. The float-sink principle—which we utilize in this work—is well known and widely used in the large scale separation of macrosized items, particularly in the recycling industry. We envisage a method whereby droplets can be released on selected micron-sized single particles floating on the surface of a liquid in order to cause them to sink [Fig. 1(a)]. This handling approach intuitively benefits from high degrees of controllability, precision, and delicateness without the difficulty of particle harvest when the process is complete.

A spherical particle placed in a large reservoir of liquid surmounted by gas has an axis-symmetric meniscus forming around the surrounding liquid. The solid-fluid-gas interface [Fig. 1(b)] obeys the classical capillarity equation of

$$\frac{\rho g}{\sigma} z - \frac{P_0}{\sigma} = \frac{z'}{r(r'^2 + z'^2)^{1/2}} - \frac{r''z' - r'z''}{(r'^2 + z'^2)^{3/2}}, \quad (1)$$

where $r(s)$ and $z(s)$ are cylindrical polar coordinates of the interface, r' and r'' denote the respective first and second

derivative of r (similarly for the case of z , z' , and z'') with respect to the curvilinear abscissa s along the radial profile of the interface, σ is the surface tension, P_0 is the liquid pressure at $z=0$, and ρg is the volumetric weight of the liquid. When the particle is at rest, the sum of F_t (total force required to maintain the particle), F_c (capillary force), and F_b (buoyancy force) are equal to zero. The work necessary to detach the particle downward from the surface under an applied force has been found to be¹²

$$E = 2\pi\sigma R_s^2 \left[\frac{1}{4} \left(1 - \cos \frac{\theta}{2} \right)^2 \left(7 \cos^2 \frac{\theta}{2} + 8 \cos \frac{\theta}{2} + 3 \right) + \frac{1}{2} \sin^4 \frac{\theta}{2} \left(\log \frac{4}{\varepsilon \sin \frac{\theta}{2} \left(1 + \cos \frac{\theta}{2} \right)} - \gamma \right) \right], \quad (2)$$

where R_s is the radius of the particle, θ is the contact angle, ε is the Bond number, and γ is the Euler’s constant. This approximation is valid for $\varepsilon < 1$. Equation (2) provides us with the intuitive knowledge that smaller particles will detach with lower amounts of energy applied. The application of a water droplet on the floating spherical particle can result in sinking in two ways. Any droplet of water of radius R_d located at a height h above the liquid surface will possess a potential energy of $V = 4\pi\rho ghR_d^3/3$. The release of this droplet directly above the particle will cause sinking when V

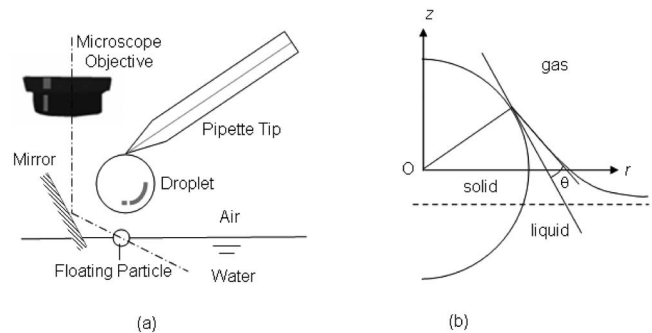


FIG. 1. Schematic description of (a) the proposed method to delicately handle single particles delicately using a float-sink principle and (b) a depiction of the important parameters for a solid spherical particle in a solid-liquid-gas interface.

^{a)}Author to whom correspondence should be addressed. Electronic mail: adrian.neild@eng.monash.edu.au.

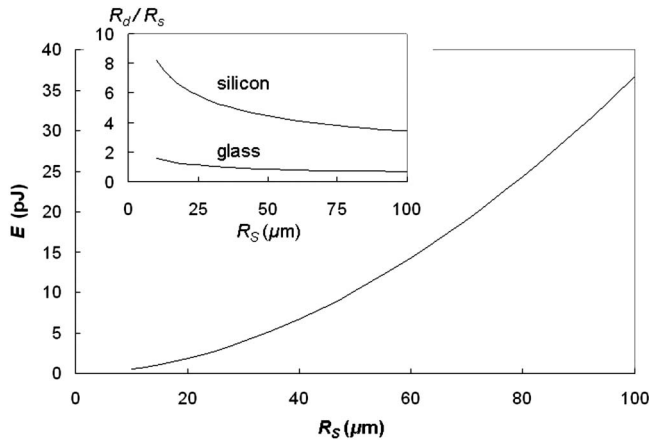


FIG. 2. Plot of work needed E to detach a spherical glass (hydrophilic) particle downward in water against the particle radius R_s . The inset presents the minimum values of R_d/R_s needed to sink glass (hydrophilic) and silicon (hydrophobic) particle of radius R_s in water, which is based on perfect transfer of energy from droplet to the particle.

$> E$, assuming that all the potential energy of the droplet is transferred to the particle. In reality, higher V values will be needed due to factors such as viscous dissipation by the surrounding fluid and imperfect transfer of energy from droplet to the particle. Similarly, particle-droplet misalignment will necessitate a larger radius droplet or greater height of release to be used for sinking to occur. Logically, sinking will altogether not be possible if there is a sufficiently high degree of misalignment between particle and droplet. Figure 2 presents a plot of E against R_s for hydrophilic glass ($\theta=27^\circ$) spherical particles in water. The trend is the same with hydrophobic silicon ($\theta=110^\circ$) but with the detachment energy some 130–140 times higher. It can be seen thus that hydrophilic particles are more readily sinkable in this mode. The inverse relationship between E and θ imputes that the addition of surfactants—which reduces θ —will cause the floating particles to sink more readily. This offers an added degree of parameter control in the selection and handling of particles. Suppose that we consider a reasonable case of the droplet being released at a height of 3 mm above the water surface. Equating E and V allows us to determine the minimum R_d/R_s ratios needed to sink particles of various radii, as depicted in the inset of Fig. 2. In the case of glass spherical particles, we find that droplet radii roughly in the order of the particle radii will suffice to cause sinking. The values with silicon particles are higher and more varying, ranging from a value of 6.3 for $R_s=20 \mu\text{m}$ to 3.4 for $R_s=100 \mu\text{m}$.

Another conceivable mode of sinking may arise out of the released droplet wetting the region of floating particle exposed to air. This has the effect of eliminating the capillary force that acts to keep the particle floating. It is clear that a more hydrophilic particle, with contact lines closer to the top, should have a greater propensity to sink in this mode. This is similar in behavior as the case of the mode of detachment using the applied force. It is conceivable that there will be a higher droplet particle misalignment tolerance to accommodate sinking in this mode.

We devised an experiment in which single particles were placed carefully in the viewable region of a microscope attached to a charge coupled device camera [Fig. 1(a)]. The particles were glass microspheres with diameters of 106–125 μm (Whitehouse Scientific GP0116). These par-

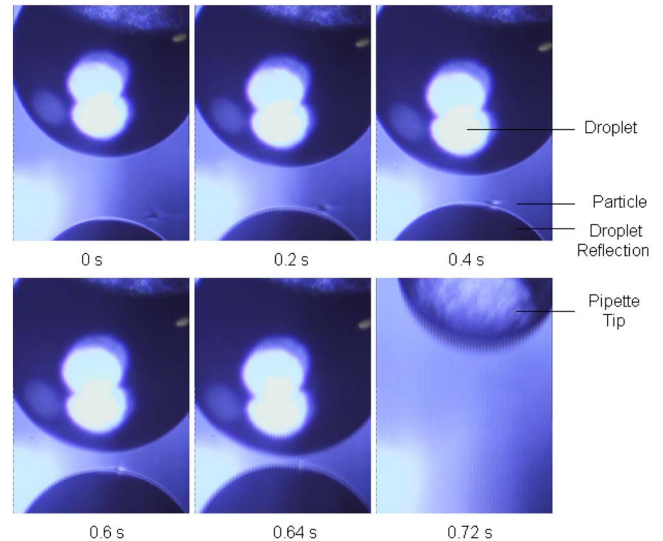


FIG. 3. (Color online) Image sequences of a dispensed droplet that caused sinking of an originally floating glass particle in water.

ticles were floated on the surface of Milli-Q water filled in a Petri dish. A flat end needle connected to a microinjector was fixed in position to produce small water droplets. The flat needle was positioned using a manual three-axis optomechanical translator. The output from the camera was sent to a computer to monitor the process and a mirror placed under the CCD camera at an angle in order to be able to visualize both the particle and water droplet at the same time. To minimize splashing, the needle was placed as close as possible to the water surface. Nevertheless, placing the needle too close to the water may cause the droplet to prematurely attach to the water surface. In the experiments, we estimated the droplet dispensed to be $0.3 \mu\text{l}$ giving a radius of $415 \mu\text{m}$. Some points were noteworthy in the recording process. As the mirror was submerged in the liquid, it tended to create a liquid meniscus that caused particles to migrate toward it. This effect was mitigated by submerging the mirror only slightly and to have it tilted closer to the vertical. As the mirror and camera were not moved as one unit and coupled with the difficulty of handling the particles with mechanical tweezers, the observation of particles within the field of view required careful manipulation and often simply just patient waiting for the particle to arrive. We have found that placing the particle and fluid medium on a typical microscopic stage was not suitable as it would cause the particles to move violently on the liquid surface even with gentle translations.

Figure 3 presents image sequences of an originally floating particle that was sunk with a droplet placed above it. The particle was clearly moving toward the needle apex during the first 0.64 s of observation. From 0.4 s after observation, the droplet began to be ejected from the needle tip. At 0.72 s, both the droplet and particle were seen to disappear from view, indicating that the particle had sunk into the liquid as a result of a droplet released close to just above it. As the center of the droplet was approximately 0.5 mm above the liquid surface, this amounted to a potential energy V of $14.7 \times 10^{-10} \text{ J}$. This was clearly higher than values of E depicted in Fig. 2 for particle radii between 50 and 60 μm , confirming sufficiency of the $V > E$ condition for sinking by droplet-particle energy transfer. Figure 4 presents image se-

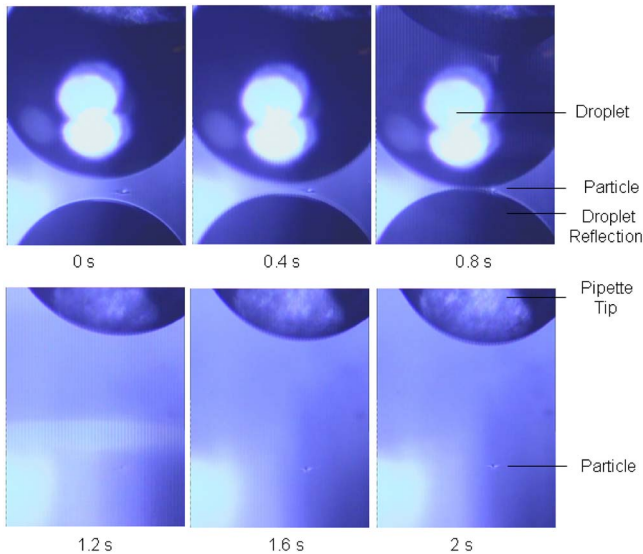


FIG. 4. (Color online) Image sequences of a dispensed droplet that failed to cause sinking of an originally floating glass particle in water.

quences of an originally floating particle that did not sink when a droplet was dispensed. The particle in this case was visibly more misaligned to the droplet than in Fig. 3. Nevertheless, sinking via wetting—if it was the mode of operation—should have occurred considering that the droplet was much larger than the particle, and the particle was located well within its vicinity of influence. This result appears to indicate that detachment with an applied force is the domi-

nant mode of action. If so, this offers considerably greater resolution in selecting which particles to remove from the liquid surface. The results shown indicate the viability of using this scheme in selectively sink particles from the liquid surface. Receptacles placed under the selected particle can be used as a convenient collection tool. We envisage that a liquid dispenser mounted on a motorized two-axis displacement translator—operating akin to an ink-jet printer—can be developed to rapidly select and handle particles this way.

In summary, we demonstrate a way of delicately handling selected single particles based on the float-sink principle. This approach enables automation capabilities to be incorporated without difficulty.

This work has been supported by Australian Research Council (ARC) Discovery under Grant No. DP0878454.

¹A. Ashkin and J. M. Dziedzic, *Science* **235**, 1517 (1987).

²P. Y. Chiou, A. T. Ohta, and M. C. Wu, *Nature (London)* **436**, 370 (2005).

³V. Gosse and V. Croquette, *Biophys. J.* **82**, 3314 (2002).

⁴C. Haber and D. Witz, *Rev. Sci. Instrum.* **71**, 4561 (2000).

⁵A. Neild, S. Oberti, F. Beyeler, J. Dual, and B. J. Nelson, *J. Micromech. Microeng.* **16**, 1562 (2006).

⁶P. R. C. Gascoyne and J. Vykoukal, *Electrophoresis* **23**, 1973 (2002).

⁷K. Konig, H. Liang, M. W. Berns, and B. J. Tromberg, *Nature (London)* **377**, 20 (1995).

⁸E. W. H. Jager, O. Ilganas, and I. Lundstrom, *Science* **288**, 2335 (2000).

⁹K. S. Colijnivadi, J.-B. Lee, and R. Draper, *Microsyst. Technol.* **14**, 1627 (2008).

¹⁰W. H. Tan and S. Takeuchi, *Lab Chip* **8**, 259 (2008).

¹¹R. S. Taylor and C. Hnatovsky, *Opt. Express* **12**, 916 (2004).

¹²X. Chateau and O. Pitois, *J. Colloid Interface Sci.* **259**, 346 (2003).

D. Selective removal of micro-particles from a floating monolayer cluster



Contents lists available at SciVerse ScienceDirect

Colloids and Surfaces A: Physicochemical and
Engineering Aspectsjournal homepage: www.elsevier.com/locate/colsurfa

Selective removal of micro-particles from a floating monolayer cluster

Lin Xu, Adrian Neild*, Tuck Wah Ng

Department of Mechanical and Aerospace Engineering, Monash University, Clayton, Australia

ARTICLE INFO

Article history:

Received 19 July 2011
Received in revised form
14 September 2011
Accepted 16 September 2011
Available online xxx

Keywords:

Self assembly
Monolayer
Capillary forces
Sorting

ABSTRACT

Self assembly is a very attractive way of creating two dimensional arrays of particles. One convenient method is to use the inter-particle forces which occur between particles of similar characteristics which float at a fluid gaseous interface. However, within populations of particles it is often beneficial to be able to remove rogue units. This work demonstrates that such selectivity is possible via the deposition of droplets in close vicinity to the particle whilst leaving the rest of the cluster largely undisturbed. With the accurate dispensing of droplets now achievable using technologies developed around the ink jet printer, this portends a useful method of sorting or removing rogue particles from clusters that form naturally due to capillary forces.

© 2011 Elsevier B.V. All rights reserved.

1. Introduction

The formation of ordered two dimensional particle arrays has important uses in the creation of desired surface structures in materials, and sensors in biomedicine. The ability to do this in the form of a floating monolayer via self assembly from inter-particle forces possesses distinct advantages [1,2]. Capillarity offers a convenient means of congregating particles. This arises because particles floating close to each other deform the interface around them to minimize the interfacial energy [3–9]. Capillarity induced clustering, whilst advantageous in that no external energy source need be applied, suffers from the inability to achieve the assembly features mentioned earlier (lattice spacing control, defect-free and long range order) effectively. One approach that can overcome this somewhat is via the use of surface standing waves [10]. However, a method that is more amenable for particles in the micro and nano scale involves applying an external electric field normal to the interface after capillary induced clustering has occurred [11]. This work examines the selective removal of single particles from a self assembled cluster, this has uses for removing rogue particles in order to either mould the shape of the cluster, remove incorrectly sized particle which may form dislocations in the lattice or to perform sorting within the particle population.

An energy barrier exists between floating particles and those submerged in the fluid body, particles in either of these states are kept separated. Hence the removal of a rogue particle will not be

reversed naturally, in terms of sorting this means that two distinct populations can be created. The requirement then is for a mechanism to effect a movement from one state to the other. A recent approach which applies the float-sink method has been demonstrated to accomplish the sinking of selected isolated particles [12]. Typically, a droplet that is significantly larger is dispensed directly above the particle to do this. An issue is that isolated particles on a fluid surface tend to move relatively quickly along the surface, by having clusters of particles this movement is largely removed, but it does introduce other issues. The question of whether this is workable in terms of removing one particle from a cluster formed by capillarity is intriguing as well as functionally important; and on the surface appears unlikely in view that the droplet to particle size ratio used has to be rather large. Yet, we conclusively show that this is possible to remove individual particles from an otherwise unaffected cluster.

2. Underlying mechanisms

2.1. Capillary forces of floating particles

For a particle to sit in equilibrium at a fluid/gaseous interface three forces must be balanced in the vertical direction, these are the capillary force, F_C , the pressure force F_p and the weight of the particle F_g . In balancing these forces a deformation of the fluid surface normally occurs, characterized by h , and depicted in Fig. 1. The ratios between the relevant forces are given by [9]:

$$\frac{F_C}{F_g} = -\frac{3\rho_L}{2Bo\rho_p} \sin(\theta_C) \sin(\theta_C + \alpha) \quad (1a)$$

* Corresponding author. Tel.: +61 3 9905 3545; fax: +61 3 9905 1825.
E-mail address: adrian.neild@eng.monash.edu.au (A. Neild).

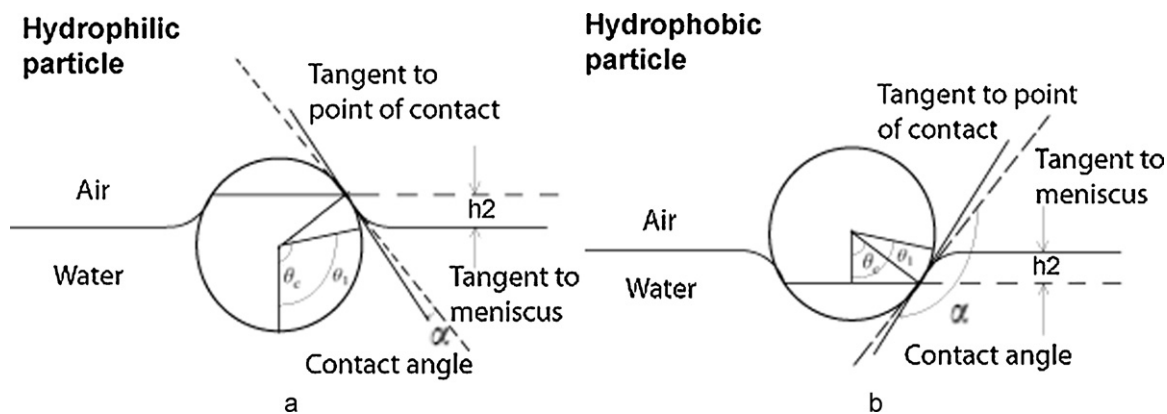


Fig. 1. (a) Hydrophilic and (b) hydrophobic particle floating on the liquid surface.

$$\begin{aligned} \frac{F_p}{F_g} = & \frac{3\rho_L}{4\rho_p} \left(\frac{2}{3} - \cos(\theta_C) + \frac{1}{3} \cos^3(\theta_C) \right) \\ & + \frac{3\rho_g}{4\rho_p} \left(\frac{2}{3} + \cos(\theta_C) - \frac{1}{3} \cos^3(\theta_C) \right) \\ & - \frac{3(\rho_L - \rho_g)h}{4\rho_p R} \sin^2(\theta_C) \end{aligned} \quad (1b)$$

where R is the particle radius, θ_C is termed the filling angle, α is the contact angle of the particle and ρ_L , ρ_g and ρ_p are the densities of the liquid, gas and particle respectively. The term Bo refers to the Bond number, given by $\rho_L g R^2 / \gamma$, where γ is the surface tension. The deformation, h , itself being given by [13]:

$$h \approx R \sin(\theta_C) \sin(\theta_C + \alpha) \left[\ln \left\{ \frac{4}{\varepsilon \sin(\theta_C) (1 - \cos(\theta_C + \alpha))} \right\} - e \right] \quad (2)$$

where $\varepsilon = R/L_c$ is the square root of the Bond number with L_c the capillary length ($= \sqrt{\gamma/\rho_L g}$), and e is the Euler constant. Such an approach allows both unknowns, θ_C and h , to be found, and has been applied for example to surface cleaning [14] and coffee stain deposits [15]. The parameters for experiments presented in this work are γ for water is 72 mN/m, the particle radius is 60 μm giving a Bond number of 5×10^{-4} . In addition the particle density is 2.19 g/ml and the particle contact angle is 27°.

When more than one particle is present at the surface, the deformation causes a capillary force between the particles to occur [16]. The capillary force between two floating bubbles has been analyzed analytically using a range of approaches [3–7]. The lateral force acting of particles of radii R_1 and R_2 separated by a distance L is equal in magnitude and opposite in sign and is given, for small Bond numbers by [8]

$$F_{12} = -\frac{2\pi\gamma Q_1 Q_2}{L} \quad (3)$$

In this equation, $Q_k = r_k \sin(\psi_k)$, where r_k is the radius of the particle for $k=1$ or 2 and ψ_k is the interface slope with the horizontal plane at the point of contact. The dynamical behavior of particles floating on fluid can be analyzed using Eq. (3) by incorporating the relevant drag forces. Simulations of these have been performed [9]. The result of this lateral force is an attractive force developed between hydrophilic particles [8].

2.2. Drop coalescence at fluid interfaces

When a drop is gently placed on a reservoir of the same fluid, gravity draws the drop downwards and eventually the drop and

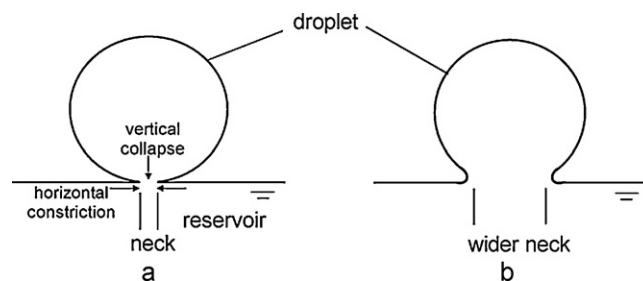


Fig. 2. (a) Initial contact of a droplet with liquid reservoir with a neck (bridge) joining the two liquid bodies, and competition develops from horizontal constriction of the interface driven by surface tension on the sides of the drops, and vertical collapse driven by the curvature at the top of the drop the interfaces. (b) The neck joining the two liquid bodies experiences widening when the drop is continuously merging to the reservoir.

reservoir interfaces become sufficiently close such that attractive Van der Waals forces initiate coalescence. The ensuing coalescence involves a fluid neck or bridge forming that rapidly opens up (see Fig. 2a). When the liquid has low viscosity, capillary waves propagate away from the initial point of contact [17]. This induces two possible outcomes; total coalescence in which the drop merges completely with the reservoir after experiencing a widening neck (Fig. 2b), or a fraction of the drop merges with the reservoir and a daughter drop is left behind. For the latter (partial coalescence) to occur, the horizontal constriction of the interface, which is driven by surface tension on the sides of the drops, must overcome the vertical collapse driven by the curvature at the top of the drop. When capillary waves are able to reach the drop's summit before being damped, they interfere with the vertical collapse and allow the horizontal stretch to dominate and cause the daughter droplet to form [18,19]. A similar process proceeds with the daughter droplet until coalescence completes. The process of coalescence is extremely fast (in the order of milliseconds) and can only be viewed using high speed cameras. The fluid flow during coalescence is dependent on the density, surface tension and viscosity (for water this is 0.001 N s/m²).

3. Methods

Two sets of experiments were conducted. In the first set (Fig. 3a), a hollow glass microspheres with diameter of 120 μm (Whitehouse Scientific GP0116) was attached to the side of a 100 μm thick cover slip in order to create a pin head. This glass slide was then fixed vertically onto a Petri dish filled with Milli-Q water. The water covered the slide and approximately half of the particle, therefore the pin head can be observed above the water surface. The liquid

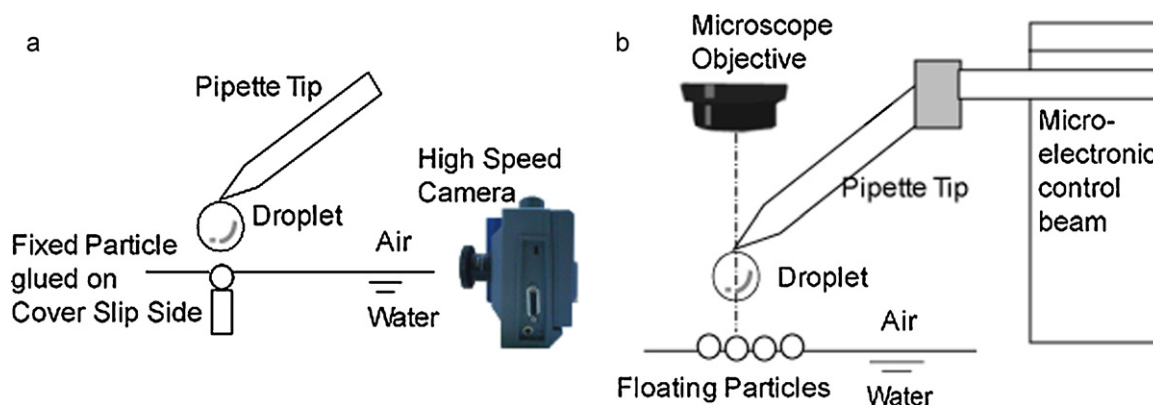


Fig. 3. Schematic description of experiment setups: (a) a high speed camera was conducted to view the liquid coalescence pattern created by the droplet and the pin head and (b) a droplet was applied to sink a certain particle from clustered floating particles.

coalescence pattern was investigated by releasing the droplet (of the same fluid) gently on the pin head. The entire process was monitored by a high speed camera (Fastec Imaging) at [500 frames/s] and saved as a digital video file in a computer. The purpose of making the particle static was to align the droplet more accurately with the particles. Such an alignment is especially necessary in the sense perpendicular to the focal plane as video detection is not possible in this direction. This setup also allowed the lighting and alignment of the camera to be better controlled so that high speed images from the side can be recorded for experiments that are inherently difficult to perform. A flat ended needle (Eppendorf AG) with inner diameter of $10\ \mu\text{m}$ was positioned using a manual three-axis mechanical translator. A droplet was then produced at the needle tip and lowered gently towards the pin head. Varied size droplets were introduced in a series of tests that allowed investigation of the nature of liquid coalescence over a particle at the fluid interface.

In the second set of experiments (Fig. 3b), clusters of the same hollow glass microspheres were set floating on the surface of Milli-Q water contained in a small Petri dish. A droplet (of the same fluid) generated from the needle was positioned carefully on them by using a Micro-controller (Newport). The output from the CCD camera integrated with a microscope was sent to a computer to monitor the process. The needle was left static in the vertical direction with the tip of the needle positioned $30\ \mu\text{m}$ from the fluid surface. This allowed the distance between needle tip and liquid surface to approximately define the size of the droplet formed, and ensured that the tip will not contact the fluid surface as doing so will cause a sudden movement of nearby particles. Whilst the distance defined the droplet size, it should be noted that the droplet will tend to move up from the tip of the needle, rather than simply hang downwards, thereby causing the resulting drop size to be slightly larger than a diameter of $30\ \mu\text{m}$.

4. Results and discussion

We consider first results investigating the coalescence of the droplet with the fluid surface with a fixed particle. Fig. 4 provides images taken using backlighting which allows the edge of the droplet to be more defined. The smaller shape at the center of the droplet is the bright spot due to light focused through the droplet, whilst the hump at the bottom of each image (outlined in red) is the particle protruding through the liquid surface. The bulk fluid surface which partially submerges the particle is aligned with the lower edge of the image. In terms of causing a given particle to sink in a given fluid, there are two key parameters: the alignment and size of the drop.

In the image sequences of Fig. 4, the centers of the descending droplet and particle were closely aligned (the offset much lower than one particle diameter distance). As the droplet was lowered slowly towards the fluid surface, it first met the particle and then merged with the fluid itself. This process occurred much faster than the speed with which the needle was moved. It can be seen from Fig. 4, that a contact line was formed for both the 17 nl and 103 nl droplets on the static particle as they descended until contact was made with the fluid surface itself. After this, the droplet quickly merged with the bulk fluid volume. The transient liquid swells above the surface that appeared on both sides of the static particle clearly demonstrate that fluid from the droplet had passed over both the left and right (with reference to the images) sides of the particle. From this process, one can infer that the particle is enveloped by liquid (no contact with the fluid/air interface) and should submerge fully underwater. Under such conditions, the capillary forces assisting a free particle to remain at the fluid surface will disappear and the downward momentum imparted onto the particle due to the rapid fluid motion that occurs as the two unequal fluid volumes merge.

Cases of three droplets that were not sufficiently aligned to cause fluid to cover both sides of the tethered particle are shown in Fig. 5. A droplet of 4.1 nl (Fig. 5(a)) positioned such that its center aligned with the particle's center to a degree slightly higher than the cases in Fig. 4 did not produce the same outcome. With the droplet lowered to a height close enough to the particle and fluid below such that merging started to take place, the contact line formed between the droplet and the particle was seen to descend on one side (right).

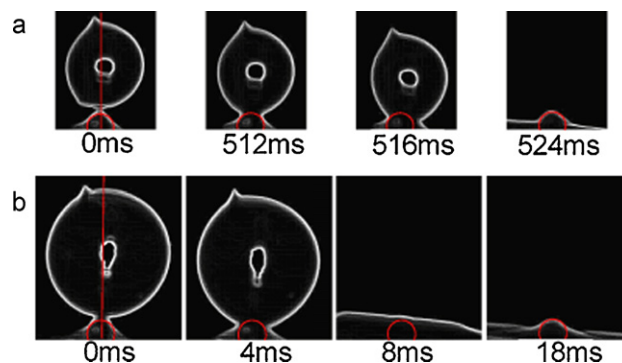


Fig. 4. Experimental image sequences of the liquid coalescence patterns directly over a pin head by varied droplet size. (a) Time evolution of a droplet with approximate 17 nl approached to the pin head. (b) Time evolution of a 103 nl droplet approached to the pin head.

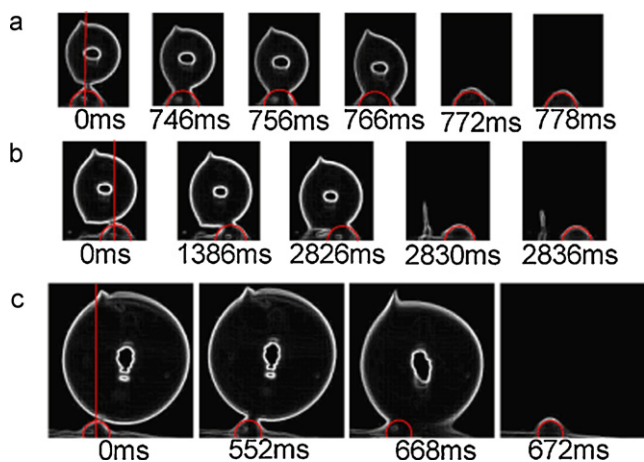


Fig. 5. Experimental image sequences of the liquid coalescence pattern over a pin head by (a) a 4.1 nl droplet from right, (b) a 7.1 nl droplet from left, and (c) a 103 nl droplet from right approach.

The swell of fluid formed as merging completed was entirely to the same side of the particle. This result showed the dependence of the sinking process on the alignment between particle and droplet centers. The second sequence with a 7.1 nl droplet, shows the liquid merging asymmetrically more clearly as the misalignment was increased. With the droplet offset to the left by a distance of 55 μm , the descending droplet made a contact line on the particle which remained high up on the right hand side. When merging began, this contact line remained stationary and the fluid passed to the left of the particle. The third sequence shows the same process with a much larger 103 nl droplet. Even with this volume that was well in excess of the particle size, an offset of 110 μm was sufficient for the fluid to merge almost entirely on one side. Once again the contact line remained high on the particle and ensured that the swell was predominately on the right hand side of the particle.

For the experiments the static particle was aligned such it was half submerged when compared with the fluid surface. However, Eq. (2) shows that at the vicinity of the particle itself, the fluid surface will deform to the extent that it interfaces with the particle at its contact angle. For example, a 60 μm radius particle, with 27° contact angle can exact a local deformation of as much as 36 μm in the vertical direction. As the droplet is lowered, a second contact line is produced on the particle. A local deformation can also be expected, though it would be expected to be considerably lower than from that of a flat surface, since any deformation of the spherical droplet will involve a larger surface area change and as such a larger surface energy gradient is associated with this case. It can be seen from the images that there is indeed a tight curve as the droplet meets the particle; again this deformation being such that the contact angle formed is dictated by the three phases present (air, water, and solid). It is when these contact lines meet that merging between the droplet and main fluid body occurs. Such a consideration is largely one of geometry and can be treated as quasi-static. However, it can be seen from the images, that once one side merges, two options can occur, either liquid flowing to one side or on both sides (within the image plane). It can be seen from Fig. 4(a) that prior to merging, the height of the droplet contact line on the particle is slightly higher on the left than on the right. This meant that flow had occurred on both sides. It can also be seen between the second and third images of Fig. 5(c) that the droplet merged with the liquid such that its contact line drops downwards on the left hand side without allowing flow to develop. Hence whilst the two contact lines must meet to effect merging on that respective sides, this geometrical consideration is not sufficient to predict how merging will take place. In Fig. 4(a) it would predict flow to the right,

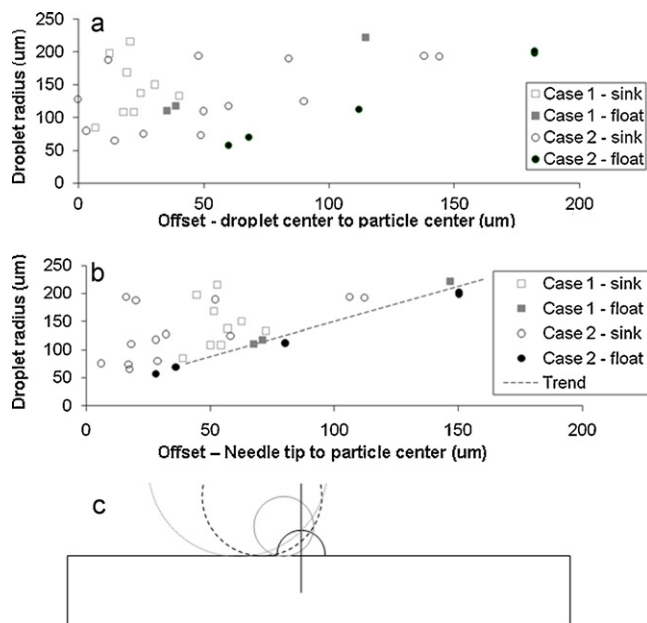


Fig. 6. (a) Plot of the droplet size against the offset distance measured from the center of the drop to the center of the particle, (b) plot of the droplet size against the offset distance measured from the needle tip to the center of the particle, and (c) schematic diagram of the alignment for the fluid contact line merges on one side at the critical offset.

whilst in Fig. 5(c) the contact line changed on the left such that a bit greater merging could have occurred on both sides. Clearly, it is the widening of the neck forming between the two fluids which ultimately dictates the nature of the merging process.

It is clear that for the contact line to be removed from the particle by the droplet, which eliminates the capillary forces maintaining the particle at the interface and ensures downward momentum transferred to the particle from the liquid, the alignment has to exceed critical maximum offset value. Not surprisingly, this value is droplet size dependant. To examine this dependency further, a series of experiments were performed with varying alignment and droplet size, again using a fixed particle in the same arrangement. The needle used had a hooked end this provided additional control over the droplet. When a droplet of small size is produced at the tip of a needle, surface tension can cause the droplet to form around the needle tip rather than dangle from it as would be expected at the macro scale. By using a needle with a slight bend, the way in which the droplet clung to the needle was more repeatable (always preferring, based on surface energy minimization, one side). Fig. 6a shows the behavior of the various droplet and offset (measured as the distance from the center of the drop to the center of the particle) combinations, the outcomes have been classed as either causing sinking (fluid passes over both sides of the particle) or allowing floating (fluid passing over one side only) these outcomes were again determined from inspection of images taken with a high speed camera. It can be seen that for both needle arrangements (bent leftwards – case 1, and bent rightwards – case 2) a change of behavior occurs once a critical value of offset is exceeded and that this critical value is droplet size dependant. In Fig. 6b we correct for the bend of the needle, which causes the tip of the needle to be offset by 32 μm from the shaft (measured from images of the needle after the droplet has coalesced). Hence in this image the offset of the droplet with respect to the particle is measured from the tip of the needle producing the droplet, it can be seen that the data sets now map over each other. Effectively what this shows is that the offset should be measured with respect to the needle tip. When the droplet merges with the bulk fluid it remains attached to the needle

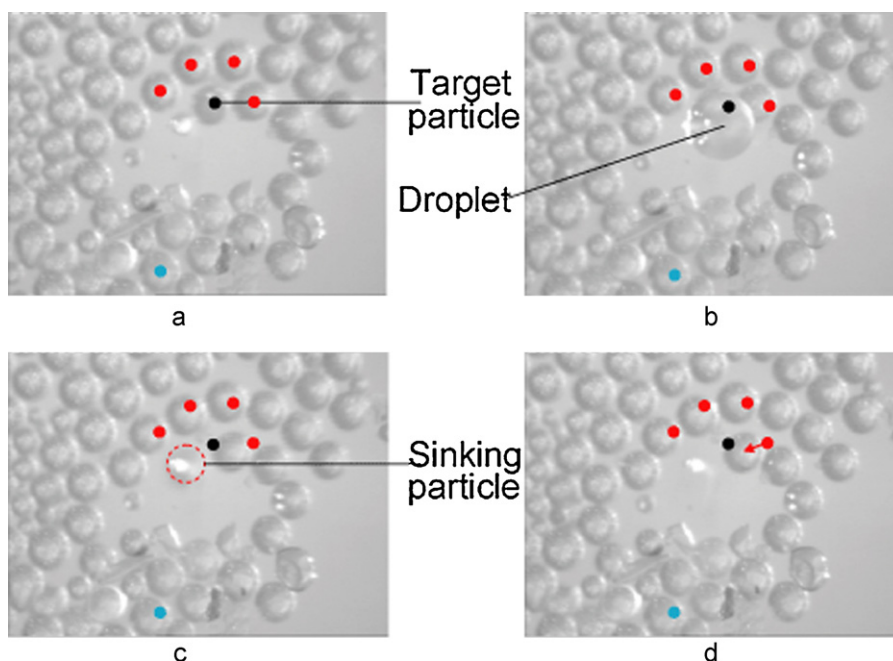


Fig. 7. An experimental image sequence showing the sinking of a single particle from a floating cluster sunk by a droplet. A neighbor particles movement is shown with the arrows.

tip until the last moment, hence it is the location of the tip which is critical. In Fig. 6c a diagram of the alignment for cases in which the fluid contact line merges on only one side is shown, it can be seen that the contact line (with no surface deformation) is higher up the particle for larger droplets indicating that in these cases, in which a greater fluid volume is involved, the momentum of the flow which occurs when the fluids merges is sufficient to displace the contact line further than for the small droplet cases.

In extrapolating the preceding consideration to that of a free particle within a cluster, we must examine three factors. Firstly, in fixing the particle we have reduced it to a zero degree of freedom object, whilst a particle on the fluid/air interface has 5 degrees of freedom (our aim here is to selectively overcome the sixth direction, that perpendicular to the interface). For a particle in a cluster, the proximity of other particles means that translation within the plane of the interface is hindered; however the three rotational degrees of freedom remain. The effect of the asymmetric flow of fluid over the particle as described above will be to cause some rotation of the particle due to shear forces. In terms of the contact line, this will cause a change in contact line angle based on the contact angle hysteresis of the solid surface. However, as the main body of fluid contact line advances (recedes) due to rotation the droplet contact line will recede (advance), limiting the role that rotation plays. The second key difference is that due to the presence of the surrounding particles, a limit must be imposed on the maximum droplet size. This is to ensure that contact is predominantly made on the particle selected for removal. As a limit is also imposed on the minimum size due to the need to create flow around the whole particle to cause sinking, it is not assured that removal of individual particles would be possible. Thirdly, it is clear from the previous experiments that as the fluid volumes merge the air/bulk fluid interface raises, whilst for the case of the static particle this plays no major role, the effect will be more sensitive when the particle to be sunk is part of a cluster, possibly hindering the removal of individual particles. Despite these factors, the following experiments demonstrate that the goal of single particle removal is in fact possible.

To investigate the effectiveness of this method in removing individual particles from a cluster, single droplets are used to sink

single particles and then multiple droplets used for multiple targets. In each case the needle is not moved in height, rather the merging of the fluid volumes occurs due to the droplet's growth (at a droplet volume of 3.5 nl). In the case of the multiple targets, this simply means that a larger liquid volume is syringed in to create the multiple droplets continuously.

In Fig. 7(a) a target particle is labeled with a black dot, and is surrounded by four almost adjacent particles denoted with red dots. The dots remain static across the images to allow easy comparison. Again from (a) it can be seen that the neighboring particle furthest to the right is closest to the target. As the drop grows prior to merging as shown in (b) it can be seen that the particles drifted leftwards. There is a net shift by most particles in this direction even by those well away from the droplet, as can be seen from the particle labeled with a blue dot. The shift of the closest particle to the target however is significantly greater, showing a degree of interaction with the droplet (perhaps with a contact line being formed). As the fluid volumes merge the target particle disappears (c). The erstwhile closest neighbor continues to drift leftward, with the other red labeled particles also moving towards the original location of the target. The most significant movement was made by the red dot labeled particle second from the left, which is also the least constrained by the neighboring particles in contact. It seems that, as well as the standard drift of the whole cluster, there is also a net movement towards the location from which the target was removed. Clearly, this was most significant for particles in closest proximity.

Fig. 8 shows a similar sequence, in this instance three of the surrounding particles move significantly towards removed target particle once it has sunk. The fourth of the adjacent particles continues its drift after the merging without a change in direction. This is likely caused by collisions with the other particles. This sequence of events includes a very small particle, which despite its small size does not sink due to the brief rise in the fluid interface height associated with the fluids merging.

Fig. 9 shows a sequence of images from an experiment in which the droplet was misaligned with the nominal target particle, again labeled with a black dot. It can be seen in (a) that the droplet is formed above five particles, labeled with black and red dots, and

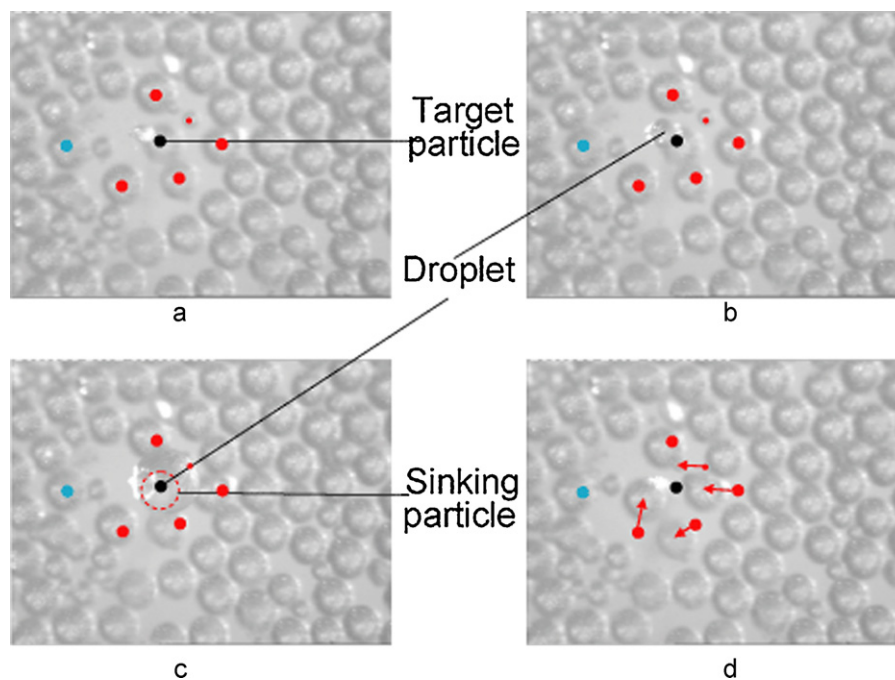


Fig. 8. An experimental image sequence of a single particle from a floating cluster sunk by a droplet. A small particle can still be seen after the process showing the relatively small effect that the swell of fluid after merging has on the ability of nearby particles to float even when the particle in question is much smaller than the droplet.

is aligned close with the center point between these particles. The droplet merges with the fluid in (b) without sinking any of the particles. Instead the surrounding particles remain in their position. Note that the bright spot initially appears in (b) is the needle tip. Through images (c) and (d) the drifting demeanor of the cluster labeled with a black arrow with reference to the particle labeled with a blue dot is clearly shown. This steady drift meant that the droplet was further misaligned to the black dot particle when the fluid merged in image (b) as opposed to when it first appeared to be the case in (a). At the time of merging, the droplet was in the middle of the red and black labeled particles. It can be seen in (d)

that the neighboring particle labeled with a red arrow, naturally moves inwards with subsequent fluid merging. This experiment shows that accurate alignment is required, as was expected from the static particle experiments. Whilst the drifting shown in the experiments can cause misalignment to occur during the process of droplet formation, we see from this experiment that the initial alignment must be poor. Furthermore, droplets can be created rapidly and accurately using technologies developed around the application of ink-jet printing.

By maintaining the height of the needle at a certain fixed value, and syringing excess fluid it should be possible to cause multiple

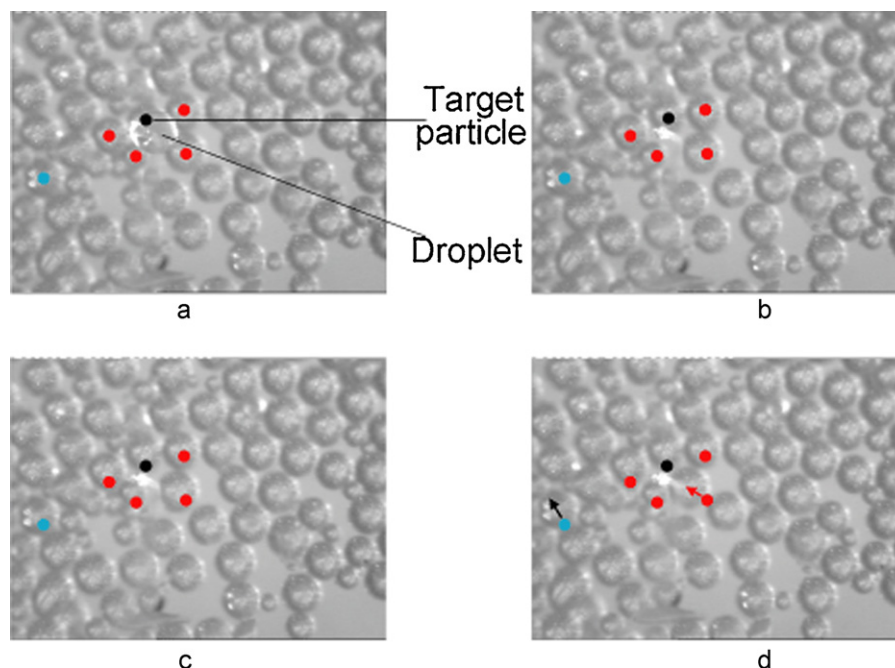


Fig. 9. An experimental image sequence of a droplet misaligned with a particle fails to cause it to sink. A neighbor particles movement is shown with the arrows.

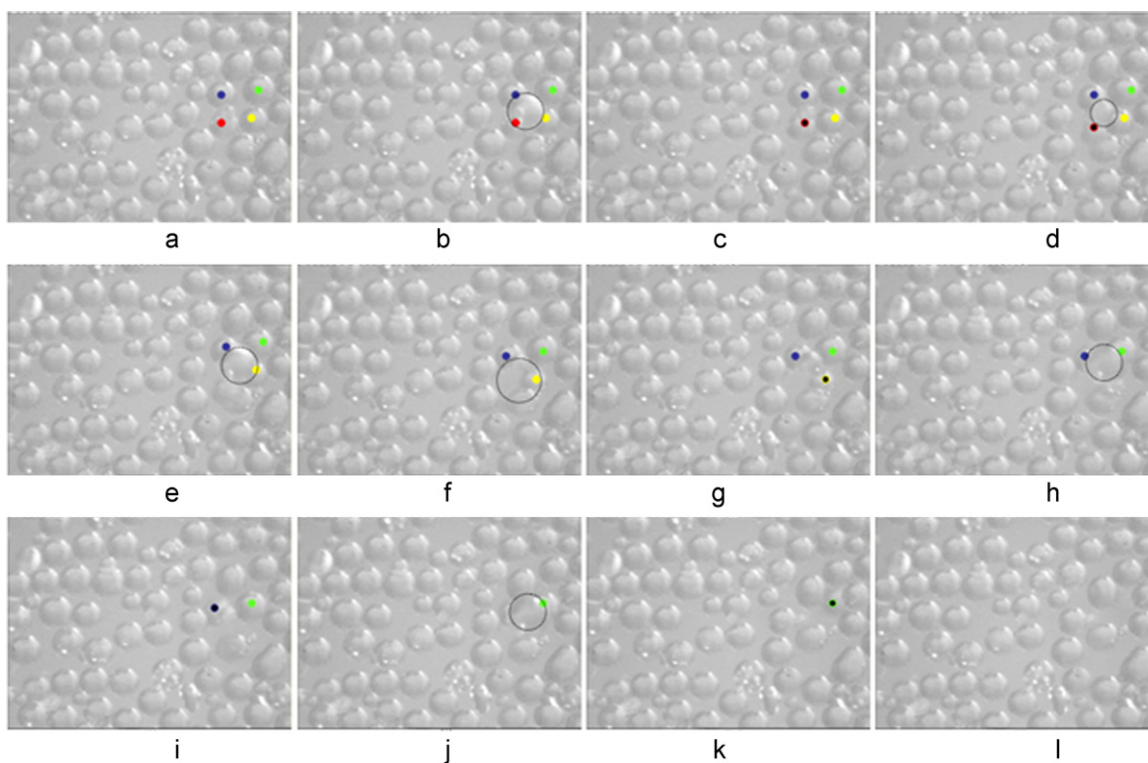


Fig. 10. Images sequences of surrounding particles sunk by continuous water droplet applied in a fixed position. Colored dots presents target particles, and the sequence of the sinking particle is bottom left (red), bottom right (yellow), up left (blue) and up right (green). (For interpretation of the references to color in this figure legend, the reader is referred to the web version of the article.)

droplets to form and release; each in turn growing until contact is made with the main fluid volume or with a floating particle before merging occurs and the next droplet forms. In this manner it is possible to remove multiple particles rapidly, as shown in Fig. 10. Here, four particles were removed with four consecutive forming droplets (dotted circles). They are labeled with red, yellow, blue and green dots (listed in order of removal) to more clearly identify them. A black center is added to the dots to indicate that the particle is sinking (and so moving out of the focal plane). The sequence of particle sinking is dependant on the movements of the particle after each sinking event. In Fig. 10(a) the needle was aligned in the vicinity of the red labeled particle, subsequently (b), a water droplet was produced to cause sinking to occur (c) and (d). As this particle sinks the yellow labeled particle moves under the next drop due to the ensuing capillary forces, such that by the time the second drop is large enough to merge (f) it sits most closely aligned with this particle. Again the result is sinking (g). A repeat of the process with a drift towards the bottom right (in a diagrammatic sense) causes the blue particle to sink next (i), with the green particle sinking with the fourth and final drop (j). In the context of application, a scheme of using dielectrophoretic force to keep a cluster fixed – as neatly demonstrated by Aubry et al. [11] – releasing it for selective particle removal, and then re-engaging it is conceivably possible.

Should a different fluid be used, the way the particle sits at the air/fluid interface will change, so for example if the particle sits higher in the fluid (depends on surface tension contact angle and the fluid density) then a better alignment of the drop with the particle will be required. It is this height in the fluid which is critical when the drop touches the particle as it dictates how far around the particle the contact line must move, a secondary consideration is the contact angle as that will dictate the degree of localized curvature of the droplet where it touches the particle. When coalescences occurs the major aspect effecting the sinking of the particle is the broadening which occurs as merging progresses, causing a

shift around the particle, this can be expected to be effected by the flow characteristics of the droplet and so the viscosity and surface energy.

5. Conclusion

The use of careful droplet deposition has been investigated as a means of removing rogue particles from a population of self assembled particles on a fluid gaseous interface. It was found that when the droplets merged with the main fluid volume, the ensuing fluid flow could pass over both sides of the particle and remove the capillary forces which cause floatation to be possible. Two key factors were considered. Firstly, a study conducted of droplets placed on a submerged fixed particle showed that that there was sinking was limited to the degree of misalignment between the droplet and floating particles. This process was also droplet size dependant, wherein a larger droplet was desirable. Secondly, the fluid merging was a rapid process and a local swell occurred. This process could be lessened if a smaller droplet was used. However, it was found that despite the counter demands on size that a droplet can be used to sink individual particles within a cluster, the neighboring particles remained floating and the cluster itself stays largely undisturbed.

Acknowledgement

Portions of this work were made possible by funding support from the Australian Research Council Discovery Grant DP0878454.

References

- [1] N.A. Bowden, I.S. Choi, B.A. Grzybowski, G.M. Whitesides, *Science* 276 (1997) 233.
- [2] Z. Tan, Zhang, Y. Wang, S.C. Glotzer, N.A. Kotov, *Science* 314 (2006) 274.
- [3] M.M. Nicholson, *Proc. Cambridge Philos. Soc.* 45 (1949) 288.
- [4] D.Y.C. Chan, J.D. Henry, L.R. White, *J. Colloid Interface Sci.* 79 (1981) 410.

- [5] W.A. Gifford, L.E. Scriven, Chem. Eng. Sci. 26 (1971) 287.
- [6] P.A. Kralchevsky, V.N. Paunov, N.D. Denkov, K. Nagayama, J. Colloid Interface Sci. 151 (1992) 79.
- [7] P.A. Kralchevsky, V.N. Paunov, N.D. Denkov, N.B. Ivanov, K. Nagayama, J. Colloid Interface Sci. 155 (1993) 420.
- [8] P.A. Kralchevsky, K. Nagayama, Adv. Colloid Interface Sci. 85 (2000) 145.
- [9] P. Singh, D.D. Joseph, J. Fluid Mech. 530 (2005) 31.
- [10] G. Falkovich, A. Weinberg, P. Denissenko, S. Lukaschuk, Nature 435 (2005) 1045.
- [11] N. Aubry, P. Singh, M. Janjua, S. Nudurupati, Proc. Natl. Acad. Sci. U. S. A. 105 (2008) 3711.
- [12] L. Xu, T.W. Ng, A. Neild, Appl. Phys. Lett. 94 (2009) 034104.
- [13] X. Chateau, O. Pitois, J. Colloid Interface Sci. 259 (2003) 346.
- [14] S.B.G. O'Brien, B.H.A.A. van der Brule, J. Colloid Interface Sci. 144 (1991) 210.
- [15] F. Shao, A. Neild, T.W. Ng, J. Appl. Phys. 108 (2010) 034512.
- [16] P.A. Kralchevsky, K. Nagayama, Langmuir 10 (1994) 23.
- [17] S.T. Thoroddsen, K. Takehara, Fluids Phys. 12 (2000) 1265.
- [18] X. Chen, S. Mandre, J.J. Feng, Fluids Phys. 18 (2006) 051705.
- [19] F. Blanchette, T.P. Bigioni, Nat. Phys. 2 (2006) 254.

